**UNIVERSIDAD DE JAÉN**

**FACULTAD DE CIENCIAS EXPERIMENTALES**

**DEPARTAMENTO DE GEOLOGÍA**

**TESIS DOCTORAL**

# CARACTERIZACIÓN MINERAL DE ZONAS DE FALLA RICAS EN MINERALES FIBROSOS DE LA ARCILLA: UNA APROXIMACIÓN EXPERIMENTAL Y TERMODINÁMICA

**PRESENTADA POR:**

**DIANA CATALINA SÁNCHEZ ROA**

**DIRIGIDA POR:**

**DR. D. JUAN JIMÉNEZ MILLÁN**

**DR. D. FERNANDO NIETO GARCÍA**

**DR. D. DANIEL ROY FAULKNER**

**JAÉN, 3 DE JULIO DE 2017**

**ISBN 978-84-9159-089-7**

# Caracterización mineral de zonas de falla ricas en minerales fibrosos de la arcilla:

## Una aproximación experimental y termodinámica

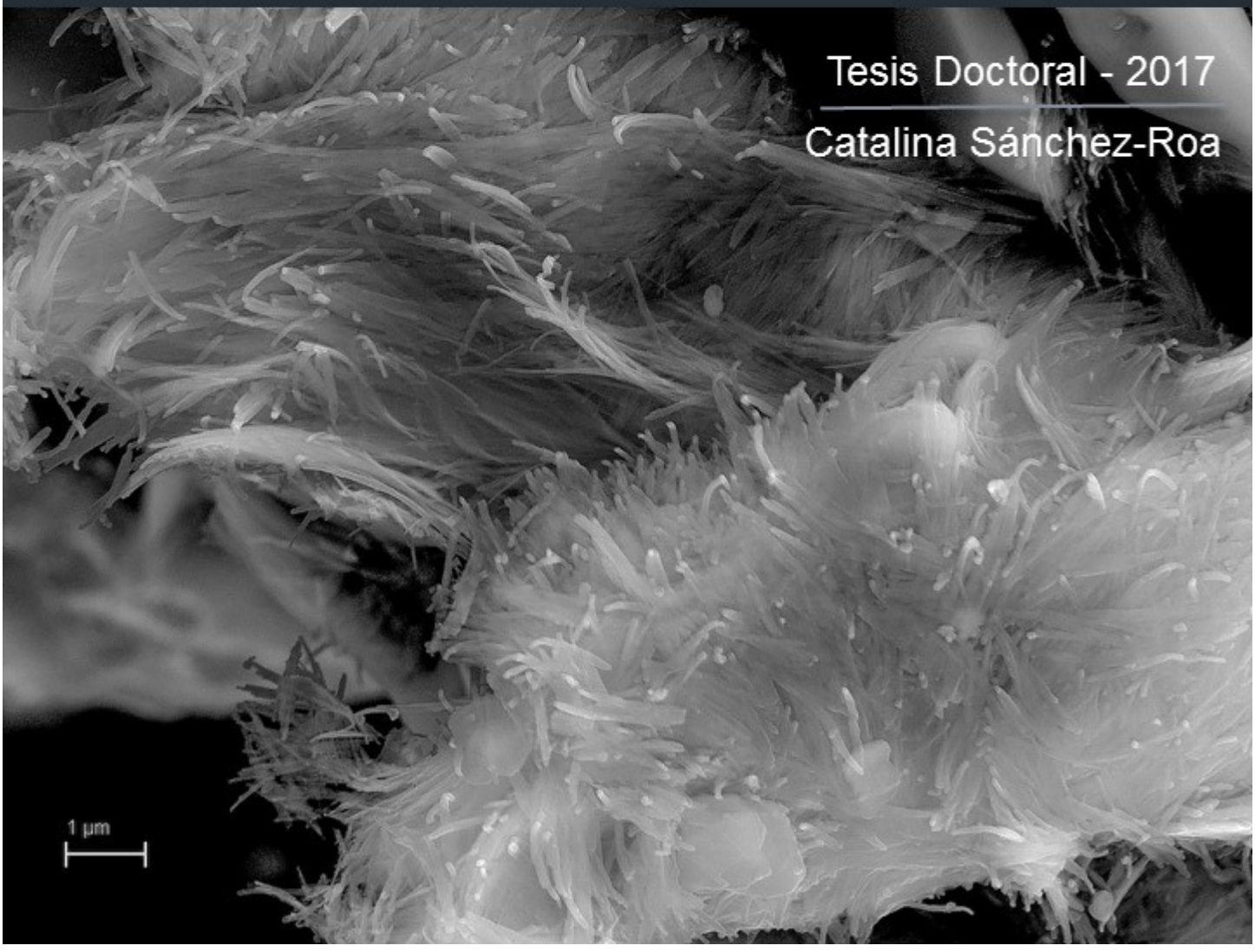


Tesis Doctoral - 2017

Catalina Sánchez-Roa

*Zona de estudio: Sismitas en el área de Galera.*

**Universidad de Jaén**

**Departamento de Geología**
**Centro de Estudios Avanzados en Ciencias de La Tierra**

# Caracterización mineral de zonas de falla ricas en minerales fibrosos de la arcilla: una aproximación experimental y termodinámica

**…**

# Mineral characterization of fibrous clay-rich fault zones: a thermodynamic and experimental approach

**Catalina Sánchez-Roa**

Programa de Doctorado en Ciencia y Tecnología de la Tierra y del Medio Ambiente

Tesis Doctoral con Mención Internacional

Jaén, junio de 2017

**Universidad de Jaén**

**Departamento de Geología**
**Centro de Estudios Avanzados en Ciencias de La Tierra**

**Programa de Doctorado en Ciencia y Tecnología de la Tierra**

# Caracterización Mineral de Zonas de Falla Ricas en Minerales Fibrosos de la Arcilla: una Aproximación Experimental y Termodinámica

…

# Mineral Characterization of Fibrous Clay-Rich Fault Zones: a Thermodynamic and Experimental Approach

Memoria de Tesis presentada por Catalina Sánchez-Roa para optar al grado de Doctor por la Universidad de Jaén, con mención de Doctorado Internacional.

Esta Tesis Doctoral ha sido dirigida por el Dr. Juan Jiménez Millán (Departamento de Geología y Centro de Estudios Avanzados en Ciencias de la Tierra de la Universidad de Jaén), el Dr. Fernando Nieto García (Departamento de Mineralogía y Petrología e IACT (CSIC-UGR), Facultad de Ciencias, Universidad de Granada), y el Dr. Daniel Roy Faulkner (Laboratorio de Deformación de Rocas, Departamento de Ciencias de la Tierra y el Océano, Universidad de Liverpool).

Jaén, Junio de 2017

Visto Bueno de los Directores:

Juan Jiménez Millán  Fernando Nieto García  Daniel Roy Faulkner

La Doctoranda

Catalina Sánchez-Roa

Esta tesis se presenta como una recopilación de los siguientes artículos científicos:

This thesis is presented as a collection of the following journal articles:

Sánchez-Roa, C., Jiménez-Millán, J., Abad, I., Faulkner, D.R., Nieto, F., García-Tortosa, F.J., 2016. Fibrous clay mineral authigenesis induced by fluid-rock interaction in the Galera fault zone (Betic Cordillera, SE Spain) and its influence on fault gouge frictional properties. *Applied Clay Science*. doi:10.1016/j.clay.2016.06.023

Sánchez-Roa, C., Bauluz, B., Nieto, F., Abad, I., Jiménez-Millán, J., Faulkner, D.R. Micro- and nano-scale study of deformed phyllosilicate-rich gouges from the Galera Fault Zone (Betic Cordillera, SE Spain). This manuscript will be submitted for consideration to *American Mineralogist*.

Sánchez-Roa, C., Vidal, O., Jiménez-Millán, J., Nieto, F., Faulkner, D.R. Implications of sepiolite dehydration for earthquake nucleation in the Galera Fault Zone: a thermodynamic approach. This manuscript was sent for consideration to *Applied Geochemistry* on 18 April 2017.

Sánchez-Roa, C., Faulkner, D.R., Boulton, C., Jiménez-Millán, J., Nieto, F., 2017. How phyllosilicate mineral structure affects fault strength in Mg-rich fault systems. *Geophysical Research Letters*. doi:10.1002/2017GL073055

*Dedicado a mi madre, por su infinita fortaleza*
*y su apoyo incondicional*

## Agradecimientos

Mis más profundos agradecimientos para mis directores de tesis, Juan, Fernando y Dan. Nada hubiese sido posible sin su constante dirección, apoyo y comprensión. A Juan Jiménez quiero agradecer muy especialmente por haber confiado en mí para la ejecución de este proyecto, desde el primer día recogiéndome en el aeropuerto hasta el último día de correcciones de este manuscrito he podido contar con el apoyo absoluto de un magnifico supervisor del que he aprendido no solo ciencia sino valiosas lecciones de vida. A Fernando, mil gracias por recomendarme para esta beca pre-doctoral, por tener siempre entera disposición para discutir el maravilloso mundo de la mineralogía de arcillas y por todos los cafés y la inmensa sabiduría que ha compartido conmigo durante los últimos cuatro años. Y a Dan muchas gracias por unirse a este proyecto con gran entusiasmo, por hacer del día a día momentos divertidos y por poder contar con sus palabras de apoyo en los momentos difíciles, sobre todo gracias por compartir su contagiosa pasión por la ciencia. Ha sido un gran honor trabajar bajo la supervisión de estos tres grandiosos científicos y excelentes personas, de corazón gracias.

Quiero expresar mi especial gratitud hacia los coautores de los artículos de los que se compone esta tesis doctoral, que han contribuido enormemente a mi formación y generosamente dedicado su tiempo y esfuerzo a este proyecto. A Isabel Abad por su grandiosa colaboración con la preparación de muestras, el análisis de datos de difracción de rayos-X, por acogerme cariñosamente a mi llegada a Jaén y dar los primeros pasos de mi carrera investigadora junto a mí. A Fran García Tortosa por su amor al campo, por presentarme la hermosa área de la Falla de Galera y por su ayuda con la geología estructural. A Blanca Bauluz por su ayuda con la impregnación de los minerales fibrosos que realmente presentaban un reto, por su disposición y colaboración en la microscopia electrónica de transmisión y especialmente por su gran amabilidad. A Olivier Vidal por su invaluable ayuda

en la construcción del modelo termodinámico, por todas sus enseñanzas, su paciencia, y por acogerme calurosamente en Grenoble. A Carolyn Boulton por compartir conmigo sus amplios conocimientos en la deformación de rocas y por sus constantes palabras de ánimo.

A todos los técnicos que colaboraron en la adquisición de datos de microscopia, especialmente a María del Mar Abad, Amparo Martínez-Morales, María Ángeles Laguna, Alfonso Ibarra, Rodrigo Fernández-Pacheco. A James Utley por su colaboración en la adquisicion de estandares y difraccion de rayos-X. Y A Antonio Piedra por la preparacion de muestras.

Al departamento de Geología de la Universidad de Jaén y al CEAC-Tierra a los que he pertenecido durante los ultimos años y todos sus integrantes que siempre han hecho todo lo posible para colaborar con éste proyecto, Chari, Africa, Matias, José Manuel, Pedro, Pilar y Cristina.

Al Laboratorio de deformación de Rocas de la Universidad de Liverpool, por su calurosa acogida, y a todos aquellos colaboraron con el trabajo experimental y analítico, especialmente quiero agradecer a Betty Mariani y John Wheeler por las discusiones científicas y a Gary, Oshaine, Henri, Pam, Mike and John por su ayuda en solucionar cualquier problema con los equipos experimentales, el SEM y muchos otros. A Stephen Crowly por su ayuda en el montaje del sistema de vacío para ensayos de fricción.

Al Institute de Ciences de la Terre y a todas las maravillosas personas con las que pude compartir en los meses en que Grenoble fue mi segundo hogar. Especialmente a Margarita por siempre estar dispuesta a resolver dudas termodinámicas y a Katia, Igor, Ellie, Frans, Maor y todos los que hicieron de la estancia una experiencia muy enriquecedora.

A todos los referees y editores asociados que contribuyeron en el proceso de peer-review de los artículos científicos, mejorando la calidad científica de esta tesis, especialmente Dr. Diane Moore, Dr Ake Fagereng, Telemaco Tesei y aquellos que prefirieron ser anónimos.

A todos mis amigos, los viejos y los nuevos y todos los compañeros de despacho que han estado ahí desde para compartir una noche de cervezas hasta para dar las mejores palabras de aliento en los momentos más difíciles. A mis primos, especialmente a Julio, Dani y Caro, y a Ale, Ana, Lu, Cata, Irene, Julia, Joe y Mike que han sido algunos de los mejores *cheerleaders*.

A mis padres, mis abuelos y mi familia, por siempre impulsarme a seguir mis sueños, por enseñarme la importancia del trabajo constante y por sembrar la curiosidad científica que me ha traído hasta aquí. A todos los que ocupan un lugar especial en mi vida y que no he podido ver tanto como me hubiera gustado durante estos últimos años.

A Rich, por su constante ayuda lingüística, tecnológica, de diseño, culinaria, logística y muchas más. Por haber estado apoyándome incondicionalmente en los buenos y malos momentos, por siempre tener una buena razón para seguir adelante, por animarme a creer en mí, pero sobre todo, por hacerme feliz. Por todas estas y muchas otras razones, este trabajo, es también suyo.

A todos aquellos que de alguna forma hicieron parte de este proyecto.

Financiación:

Quiero expresar mi gratitud a todas las fuentes de financiación de este proyecto. Esta Tesis Doctoral ha sido posible gracias a la financiación obtenida del programa de becas predoctorales FPI, beca BES-2012-052562 del Ministerio de Economía y competitividad. Los proyectos de investigación del Ministerio de Economía y competitividad CGL2011-30153-C02-01 y CGL2011-30153- C02-02 y CGL2013-46169-C2-1-P, los proyectos de investigación UJA2014/06/17, UJA2015/07/10 de la Universidad-Caja Rural de Jaén, los grupos de investigación RNM-179 y RNM-325 de la Junta de Andalucía, UK NERC grant NE/J024449/1. Gracias a las becas para estancias cortas del MINECO que financiaron tres de mis estancias de investigación EEBB-I-14-07975, EEBB-I-15-09955 y EEBB-I-16-10797, y a las ayudas para estancias cortas y para participación en congresos de la Universidad de Jaén que financió una más. Por ultimo quiero agradecer la importante labor de las sociedades científicas, incluyendo a la Sociedad Española de Mineralogía (SEM), Sociedad Española de Arcillas (SEA) y la American Geophysical Union (AGU) que financiaron mi participación en congresos nacionales e internacionales.

# Table of Contents

## Resumen

Las zonas de falla constituyen una pequeña, pero crítica parte de la corteza terrestre. Estas zonas, controlan procesos importantes como el flujo de fluidos o la energía geotérmica y son la fuente principal de los terremotos. El estudio de las rocas de falla es fundamental para comprender los procesos físicos y químicos que ocurren dentro de estas importantes estructuras geológicas. El objetivo de esta tesis es determinar el papel de los minerales fibrosos de la arcilla en zonas de falla, utilizando la Falla de Galera (Sur de España), una zona de falla sísmicamente activa, como área de estudio.

En esta memoria se combinan tres enfoques principales para identificar el origen, la estabilidad termodinámica y el comportamiento mecánico de los minerales fibrosos de la arcilla en zonas de falla. En primer lugar, la caracterización mineralógica y geoquímica de las rocas se realiza, hasta la escala nanométrica, mediante técnicas analíticas, que incluyen XRD, SEM, TEM y XRF. En segundo lugar, se desarrolló un modelo termodinámico para la deshidratación de sepiolita, que se aplica a la predicción de los cambios de hidratación, volumen, y fases minerales estables con el aumento de profundidad de la falla. Por último, se integran experimentos de fricción en rocas ricas en minerales planares y fibrosos de la arcilla, que permiten caracterizar las propiedades mecánicas de los materiales presentes en las rocas de falla.

El análisis mineralógico y geoquímico permitió la identificación de diferencias significativas en las asociaciones de minerales de la arcilla y en la composición química de las rocas de la Zona de Falla de Galera, incluyendo el enriquecimiento en Mg y la consecuente presencia de minerales fibrosos de la arcilla autigénicos: sepiolita y palygorskita concentrados y limitados a las principales zonas de deslizamiento de la falla. La microscopia electrónica de alta resolución (HRTEM) y analítica (AEM) han mostrado evidencias de transformaciones minerales continuas desde sepiolita hasta esmectita magnésica dioctaédrica, pasando por palygorskita dentro de las rocas de falla. Estos resultados indican que las rocas ricas en minerales fibrosos de la arcilla se formaron por alteración hidrotermal durante períodos de interacción fluido-roca concentrados en zonas de fracturación y deslizamiento. Se han interpretado las transformaciones minerales sucesivas como el resultado de una posterior interacción de las rocas de falla con fluidos meteóricos que promueven un aumento del contenido de Al en el sistema. Además, el análisis textural de las rocas a escala micro y nanométrica reveló una diferencia radical en la orientación de los granos entre las rocas de falla ricas en filosilicatos planares y las rocas de falla ricas en filosilicatos fibrosos, lo que afecta a la permeabilidad de la roca que componen.

Dado el importante papel de los minerales fibrosos de la arcilla en la Zona de Falla de Galera, se estimó necesario caracterizar la estabilidad termodinámica de estos minerales en rocas de falla. Para ello, se desarrolló un nuevo modelo termodinámico para la deshidratación de la sepiolita, que se empleó en el cálculo de sus condiciones de estabilidad Presión-Temperatura, cambios de volumen y contenido de agua para la composición ideal de sepiolita y composiciones de rocas naturales. Los resultados indican que el campo de estabilidad de la sepiolita está limitado por la reacción sepiolita → talco + cuarzo + $H_2O$, que ocurre aproximadamente a 325ºC y a una presión de 1 a 500 MPa. Este campo de

estabilidad sugiere que la sepiolita podría controlar el comportamiento mecánico de las fallas de la corteza hasta aquellas profundidades que presenten temperaturas menores a 325°C. El modelo termodinámico se aplicó al caso natural de la Zona de Falla de Galera (SE de España) utilizando datos de fluorescencia de rayos X (XRF) de la composición de las rocas de falla compuestas principalmente por sepiolita. La deshidratación de la sepiolita a T<300°C es modesta en comparación con la que se produce durante su descomposición, en la que pierde el 62% de agua y el 31% del volumen sólido original.

Se ha diseñado y llevado a cabo un estudio que permite evaluar el efecto de los minerales fibrosos de la arcilla en la resistencia a la fricción de fallas activas, mediante ensayos de fricción triaxial. El estudio se realizó sobre un grupo de minerales ricos en Mg que comparten el espacio composicional Mg-Al-Si-O y permite una comparación directa con minerales planares magnésicos. La selección de minerales incluyó: talco, saponita, sepiolita y palygorskita. Los resultados indican que los filosilicatos magnésicos fibrosos presentan una resistencia al deslizamiento significativamente mayor que sus equivalentes planares. En el caso tratado, la resistencia a la fricción está fuertemente influida por la estructura cristalina de los minerales estudiados, que determina la fuerza de los enlaces atómicos, la continuidad de las capas de agua dentro de los cristales y las posibles interacciones de las superficies minerales con moléculas de agua.

Los resultados obtenidos en esta tesis doctoral sugieren que la presencia de minerales fibrosos de la arcilla en zonas de falla puede producirse como consecuencia del enriquecimiento en Mg catalizado por la deformación y la circulación de fluidos, los cuales promovieron múltiples reacciones y transformaciones minerales dentro de la roca de falla. La presencia de sepiolita y sus cambios de hidratación, volumen y reacciones minerales en zonas de falla, pueden tener importantes implicaciones en el estado de esfuerzo de la falla y afectar drásticamente a las propiedades de resistencia al deslizamiento de la falla, lo que afectaría a la distribución de áreas sismogénicas en sistemas de falla ricos en Mg.

## Summary

Fault zones are a small but critical part of the Earth's crust. They control important processes such as fluid flow, geothermal energy, and are the primary source of earthquakes. The study of fault rocks is fundamental to understand the physical and chemical processes that occur within these important geological structures. This thesis aims to explore the role of fibrous clay minerals in fault zones using the seismically active Galera Fault (South Spain) as a case study.

Three main approaches are combined in this manuscript to identify the origin, thermodynamic stability, and frictional behaviour of fibrous clay minerals in fault zones. First, analytical techniques including XRD, SEM, TEM and XRF were used to complete the mineralogical and geochemical characterization of the gouges up to the nanometric scale. Secondly, a thermodynamic model of sepiolite dehydration was developed and used to predict changes in hydration and volume changes, and mineral reactions with increasing depth in the fault. Lastly, friction experiments were conducted to characterize the mechanical properties of the fault rock materials.

Mineralogical and geochemical analysis led to the identification of significant differences in clay mineral assemblages and chemical composition in the Galera Fault Zone samples, including Mg-enrichment and the presence of authigenic fibrous clay minerals: sepiolite and palygorskite concentrated within and limited to the main sliding planes of the fault. Further in depth mineralogical analysis of the gouge materials through HR-TEM and AEM showed evidence of mineral transformations occuring from sepiolite to Mg-dioctahedral smectites, with intermediate stages including palygorskite within the fault gouges. These results indicate that fibrous clay-rich gouges were formed by hydrothermal alteration during periods of fluid-rock interaction that was concentrated in fault planes and fractures. Mineral transformations were interpreted as the result of a later stage of fluid-rock interactions that promoted an Al increase in the system. Furthermore, textural analysis of the rocks at the micro- and nano-scale revealed a radical difference in grain alignment between the planar phyllosilicate-rich gouge and the fibrous phyllosilicate-rich gouge that influences rock permeability.

Based on the mineralogical findings and the important role of the fibrous clay minerals in the Galera Fault, a new thermodynamic model for sepiolite dehydration was developed and used to calculate its P-T stability conditions, and changes in volume and water content for including the ideal sepiolite composition and natural rock compositions. Results show that the stability field of sepiolite is ultimately limited by the reaction sepiolite → talc + quartz + $H_2O$, which is located at about 325°C at 1 to 500 MPa. This stability field suggests that sepiolite could control the mechanical behaviour of crustal faults to 325°C. The refined model was applied to the natural case of the Galera Fault Zone (SE Spain) using X-ray fluorescence (XRF) data of the bulk rock composition of the fault core gouge, which is mainly composed of sepiolite. The dehydration of sepiolite at T<300°C is modest compared to that occurring during its breakdown, loosing 62% of water molecules and 31% of the original solid volume.

A study was designed and conducted to evaluate the effect of the fibrous clay minerals on the frictional strength of active faults. Triaxial frictional tests were performed on a group of Mg-rich minerals common in the Mg-Al-Si-O compositional space in order to permit a direct comparison with Mg planar minerals. The minerals selected included talc, saponite, sepiolite and palygorskite. . Results show fibrous Mg-rich phyllosilicates present a significantly stronger slip resistance than their planar equivalents and have the potential for earthquake nucleation. In this case, their frictional strength is highly influenced by the crystal structure of the minerals studied, which determine the strength of the atomic bonds, continuity of water layers within the crystals, and the possible interactions of mineral surfaces with water molecules.

The results gathered in this doctoral thesis suggest that the presence of fibrous clay minerals in fault zones can occur as a consequence of Mg-enrichment favoured by deformation and fluid circulation, which promotes several mineral reactions and transformations within the fault gouge. The significant hydration and volume changes of sepiolite and its related mineral reactions can have important implications on the state of stress and strength of the Galera Fault and other sepiolite-bearing gouges. Furthermore, the formation and stability of the fibrous clay minerals in fault gouges can lead to significant changes in the mineralogy and produce noticeable differences in fault strength, affecting the distribution of seismogenic areas in Mg-rich fault systems.

# Chapter 1 Introducción

## 1.1 Motivación general y alcance de este estudio

Las zonas de falla y las zonas de cizalla que se desarrollan en la corteza terrestre son áreas de concentración de esfuerzos en las que tienen lugar un gran número de procesos físico-químicos. Las fracturas interconectadas en las zonas de falla actúan como conductos de fluidos que interactúan activamente con grandes volúmenes de roca. Estos procesos mecánicos y químicos provocan el desarrollo de diferentes tipos de rocas con propiedades características que, a menudo, se diferencian claramente de las propiedades de la roca original, o protolito (incluyendo cohesión, fabrica, tamaño de grano y mineralogía). Un resultado común de los procesos mecánicos y químicos que ocurren en las rocas de falla es la presencia de una mayor cantidad de minerales de la arcilla en el núcleo de la falla. Las paragénesis minerales, las microestructuras y la composición química de las rocas de falla aportan información valiosa sobre los procesos que sufrieron, tales como evidencias químicas de la interacción fluido-roca y las propiedades de fricción de los materiales sobre la superficie de deslizamiento. La paragénesis de los minerales de la arcilla y sus propiedades de fricción han sido previamente estudiadas en la literatura (Behnsen y Faulkner, 2012; Moore y Lockner, 2004; Sakuma y Suehara, 2015), sin embargo, sólo unos pocos estudios han descrito anteriormente la presencia de filosilicatos fibrosos (sepiolita y palygorskita) en fallas (Haines y van der Pluijm, 2012; Post y Crawford, 2007).

Esta tesis integra una caracterización mineralógica y geoquímica minuciosa de los minerales de la arcilla y de los filosilicatos fibrosos de zonas de falla con observaciones de campo sobre su aparición, la modelización termodinámica de sus condiciones de estabilidad y experimentos de fricción que aclaren su comportamiento mecánico. La conexión de los diferentes tipos de datos obtenidos permitirá identificar algunos de los procesos que suceden dentro de la zona sismogénica. Para este trabajo se ha seleccionado la Zona de Falla de Galera, sísmicamente activa, ubicada en la Cordillera Bética al SE de España, como caso natural de estudio. Su óptima exposición y estado de conservación proporciona un laboratorio natural para el estudio de minerales fibrosos en zonas de falla.

## 1.2 Problema de investigación

La zona de Falla de Galera presenta una gran concentración de minerales fibrosos de la arcilla, sepiolita y palygorskita, dentro de sus principales planos de deslizamiento. Hasta el momento, no existen estudios que profundicen en los procesos físico-químicos que conducen a la formación de estos minerales en las zonas de falla. Por otra parte, la estabilidad termodinámica de los minerales fibrosos de la arcilla ha sido poco explorada y, por ahora, se carece de datos y modelos termodinámicos capaces de predecir su estabilidad en zonas de falla. Asimismo, la caracterización del comportamiento de fricción de los minerales fibrosos no se ha realizado y, por tanto, se desconoce el comportamiento mecánico de estas fases minerales o su evolución en profundidad. Por ello, los tres problemas principales planteados en este estudio buscan expandir el estado del conocimiento sobre: 1. El origen de los minerales fibrosos de la arcilla en las zonas de falla; 2. Su estabilidad termodinámica en las zonas de falla; y 3. Su influencia sobre los procesos

de deformación en fallas activas y sobre su régimen mecánico y sísmico: modelo de deslizamiento estable (procesos de arrastre) *vs* deslizamiento inestable que provoque la nucleación y propagación de terremotos.

## 1.3 Introducción a los contenidos del estudio

### 1.3.1 Autigénesis mineral en zonas de falla

Los minerales de la arcilla son un grupo de alumino-silicatos hidratados, abundantes en la corteza terrestre, que forman parte del grupo de los filosilicatos y se caracterizan por tener un tamaño de grano pequeño, menor de 2 μm. La estructura básica de los minerales de la arcilla está formada por capas de coordinación tetraédrica ocupadas por átomos de silicio o de aluminio y capas octaédricas en las que un catión central ($Mg^{2+}$, $Fe^{2+}$, $Al^{3+}$, etc.) se une a átomos de oxígeno y grupos hidroxilo. Estas capas básicas se organizan en diferentes configuraciones para producir los diversos tipos de minerales de la arcilla. Las estructuras compuestas de una capa tetraédrica y una octaédrica conforman el tipo 1:1, algunos ejemplos de este grupo incluyen la caolinita y el grupo de minerales de la serpentina. Las estructuras 2:1 están compuestas de dos capas tetraédricas y una capa octaédrica. Dentro de este grupo se encuentran la illita, las esmectitas, etc. La clorita es el ejemplo más importante del tipo 2:1:1, las cuales incluyen una capa de hidróxido entre dos paquetes con estructura 2:1. Finalmente, el grupo de minerales fibrosos de la arcilla presenta una inversión de los oxígenos apicales en los tetraedros de silicio, con una periodicidad determinada, dependiendo del mineral del que se trate, sepiolita o palygorskita (Fig. 1.1). El pequeño tamaño y la estructura cristalina defectuosa de los minerales de la arcilla contribuyen a que estos minerales presenten propiedades físicas particulares, por ejemplo, áreas superficiales más grandes que las de otros minerales. Por otra parte, la estructura cristaloquímica interna de los minerales de la arcilla les confiere características específicas de reactividad química, que permite la incorporación de sustancias químicas en sus superficies o dentro de su estructura, convirtiéndose en agentes importantes de transferencia de materia y/o transformación (Velde, 1995).

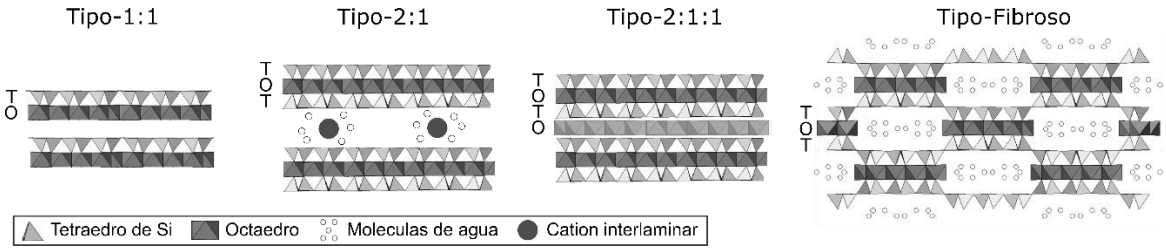


Figura 1.1. Grupos de los minerales de arcilla.

Los minerales de la arcilla se forman en ambientes variados que incluyen, entre otros, procesos superficiales que dan lugar a suelos (Schulze, 2002), procesos diagenéticos (Abad et al., 2002; Nieto et al., 2005, 1996) o alteraciones hidrotermales de rocas preexistentes

(Inoue, 1995). En todos los casos, la formación de minerales de la arcilla está fuertemente ligada a la presencia de agua, la cual constituye una parte fundamental de la estructura de este grupo de minerales. Por otra parte, los minerales de la arcilla son componentes frecuentes de las rocas de falla (Haines y van der Pluijm, 2012; Haines et al, 2013; Vrolijk y Van Der Pluijm, 1999). La abundancia de este grupo de minerales en áreas de fuerte deformación esta frecuentemente relacionada con procesos mecánicos tales como la trituración continua de la roca que produce la reducción del tamaño de grano. Más importante aún es que su presencia está fuertemente relacionada con la circulación de fluidos que favorecen transformaciones minerales por procesos de disolución y posterior precipitación, disolución asistida por la presión y otros procesos que potencian la formación de filosilicatos y en particular de minerales de la arcilla.

La circulación de fluidos dentro de la corteza terrestre está fundamentalmente concentrada en áreas de deformación que contienen redes de fracturas interconectadas que facilitan su flujo (Faulkner et al., 2010). Los fluidos que circulan en las rocas de la corteza pueden ser de naturaleza meteórica, infiltrados en la roca a través de las fracturas que alcanzan la superficie (Burkhard y Kerrich, 1990) o de origen interno, de naturaleza hidrotermal o metamórfica, que migran hacia áreas de menor presión, llevando consigo elementos en solución (McCaig, 1988). La interacción de fluidos que transportan cantidades importantes de iones y elementos disueltos con el gran volumen de roca fracturada puede producir cambios químicos, mineralógicos y procesos de transferencia de masa; estos se evidencian en las rocas alteradas que presentan una composición química y mineral significativamente diferente a la de las rocas del protolito (Haines y Van der Pluijm, 2012; Solum et al., 2003). Por esta razón, se han desarrollado técnicas geoquímicas que comparan la composición de rocas de falla con su protolito, como herramienta para reconocer las reacciones químicas y de neoformación de minerales inducidos por la interacción fluido-roca. Estas técnicas de balance de masas permiten también investigar la naturaleza del fluido circulante (McCaig, 1984; Ferry, 1986).

La presencia de minerales de la arcilla en zonas de falla es de gran importancia debido a su capacidad de hinchamiento, intercambiar cationes y transformarse a bajas temperaturas (Ahn y Peacor, 1986; Cuadros y Altaner, 1998). Además de su comportamiento reactivo, la combinación de un alto contenido de agua dentro de su estructura y baja permeabilidad permite que los minerales de la arcilla actúen como agentes lubricantes del plano de falla. Por esta razón, se ha sugerido que la presencia de rocas de falla con alto contenido en minerales de la arcilla contribuye al debilitamiento de las fallas (Wang, 1984) y que, posiblemente, constituye un factor fundamental en el control de los mecanismos de deslizamiento sísmico frente a los movimientos reptantes de planos de falla activos (Faulkner et al., 2011; Solum et al., 2003). Dentro de los estudios que relacionan la aparición de minerales de arcilla con una mayor debilidad de los planos de falla, muchos se han concentrado en filosilicatos ricos en Mg, como por ejemplo, los minerales del grupo de la serpentina y las esmectitas ricas en Mg, como la saponita (Irwin y Barnes, 1975; Reinen et al., 1991; Lockner et al., 2011; Wintsch et al., 1995). Sin embargo, el número de estudios sobre el origen en las zonas de falla de los minerales fibrosos de la arcilla (también filosilicatos ricos en Mg, como sepiolita y palygorskita) es muy escaso (García-Romero et al.,

2006) y no se ha determinado la influencia de su contenido en el comportamiento mecánico de fallas, tales como la Zona de Falla activa de Galera. Ello motiva buena parte de los contenidos de este estudio.

La determinación de la formación, distribución, estabilidad termodinámica y propiedades mecánicas de los filosilicatos en las rocas de falla son algunos de los principales factores que ayudan a comprender el papel de los minerales de la arcilla en el comportamiento mecánico de las rocas de falla (Schleicher et al., 2013, 2012). La identificación de los minerales de la arcilla se realiza en gran medida mediante la difracción de rayos-X (XRD), método analítico, basado en la Ley de Bragg, que permite la determinación del espaciado entre planos equivalentes del cristal a partir del ángulo específico en el que difractan rayos-X incidentes sobre la muestra, de longitud de onda conocida. La Ley de Bragg se expresa matemáticamente como: [$n\lambda = 2dsin\theta$ ], donde $n$ es un número entero positivo, $\lambda$ es la longitud de onda del haz de rayos X incidente, $d$ es la distancia entre capas atómicas en el cristal y $\theta$ es el ángulo de difracción (Bragg, 1913). La identificación de minerales se lleva a cabo comparando los grupos de picos de difracción que son característicos de cada estructura cristalina.

La naturaleza de las asociaciones de minerales de la arcilla relacionadas con fallas, su composición química y su influencia en la circulación de fluidos son algunos de los factores que controlan los procesos de deformación activa en zonas de falla. Por lo tanto, su caracterización es esencial para interpretar la historia de zonas de deformación a gran escala. Sin embargo, el tamaño de grano de los minerales de arcilla es uno de los mayores obstáculos en este tipo de estudios. Por este motivo, la microscopía electrónica se convierte en una herramienta esencial para explorar las relaciones texturales y microestructurales de rocas con alto contenido en minerales de la arcilla, y, por lo tanto, una técnica óptima para explorar zonas de falla a escalas microscópicas y nanoscópicas. La microscopía electrónica de barrido (SEM) proporciona datos texturales y microanalíticos, particularmente importantes en la determinación de minerales neoformados en rocas de falla. Sin embargo, esta técnica puede tener límites de resolución y carece de información estructural sobre los cristales presentes (Viti, 2011). En los casos en que el SEM no es suficiente para caracterizar las rocas de falla, la microscopía electrónica de transmisión (TEM) se convierte en una herramienta fundamental. Viti (2011) ha expuesto algunos de los casos específicos en los que el TEM es particularmente útil: la determinación del tamaño de grano en rocas de grano ultrafino; la detección y caracterización de minerales poco cristalinos o amorfos; la identificación de nuevos minerales producto de procesos de deformación (por ejemplo, los productos de reacciones de deshidratación) y las observaciones de nanotexturas de deformación en filosilicatos.

La microscopía electrónica de barrido se utiliza en este trabajo principalmente como una herramienta para la obtención de imágenes que proporcionan información sobre la topografía y composición de la muestra. El SEM utiliza un haz de electrones acelerados que producen diferentes señales al interactuar con la muestra. Las señales producidas incluyen, entre otras, los electrones secundarios, los electrones retrodispersados y los rayos-X (Joy, 1984). Estas señales son recogidas por una serie de detectores y se utilizan para examinar

diferentes aspectos de las muestras. Los electrones secundarios presentan condiciones ideales para estudiar la topografía de la muestra. Los electrones retrodispersados son desviados de su trayectoria original como consecuencia de la interacción del haz de electrones con los núcleos de los átomos de la muestra y proporcionan información significativa de su composición, al producir imágenes cuya intensidad de gris es función del número atómico medio del material analizado (Nieto et al. 2010). Por otra parte, los microscopios electrónicos de barrido están generalmente equipados con detectores de espectroscopia de dispersión de energía de rayos-X (EDS o EDX) que recogen los rayos X emitidos por la muestra y se utilizan para determinar la composición elemental del material.

La Microscopía Electrónica de Transmisión es una técnica que proporciona imágenes y análisis químicos de muy alta resolución, llegando a producir datos a escala nanométrica y, en casos óptimos, la resolución puede alcanzar la escala atómica. El TEM utiliza un haz altamente energético de electrones que se enfocan por medio de un conjunto de lentes condensadoras para atravesar una muestra muy delgada. Los electrones dispersados por los átomos de la muestra pasan a través de una lente electromagnética que los enfoca en un punto para formar el patrón de difracción. Si la parte transmitida del haz es posteriormente enfocada por la lente objetivo produce una imagen. La combinación del modo de imagen más la información del espacio recíproco (difracción) permite una caracterización completa del mineral en cuanto a su morfología, estructura cristalográfica, defectos cristalinos, etc (Nieto et al., 2010). Finalmente, la Microscopía Electrónica Analítica se basa en la detección de señales de rayos X generadas por la muestra a través de la técnica de espectroscopia de dispersión de energía de rayos-X (EDX) y permite la identificación de los elementos presentes en áreas muy pequeñas con una resolución de 1 nm o mejor (Botton, 2007). Este estudio tiene como objetivo aplicar técnicas de microscopia electrónica (SEM y TEM) para caracterizar los materiales de falla en la Zona de Falla de Galera, que requieren el uso de microscopía de alta resolución debido al pequeño tamaño de grano de los minerales que constituyen la matriz de la roca.

### 1.3.2 Estabilidad termodinámica de los minerales de la arcilla en zonas de falla

Uno de los mayores factores limitantes de la descripción y caracterización de la estabilidad y resistencia de planos de falla a profundidades sismogénicas radica en la dificultad de conocer con certeza las condiciones de presión, temperatura y fases minerales presentes. Estudios recientes que incluyen campañas de perforación atravesando y tomando muestras de núcleos de zonas activas de falla, tales como el proyecto SAFOD llevado a cabo en la Falla de San Adres y la perforación dentro de la zona de la Falla Alpina en Nueva Zelanda, han proporcionado las primeras evidencias en cuanto a reacciones minerales y circulación de fluidos en profundidad. Sin embargo, este tipo de perforaciones no superan los 3500 m de profundidad, por lo que la mineralogía de fallas activas a profundidades sismogénicas mayores de 3.5 km es aun desconocida. La estimación real de la resistencia al deslizamiento de un plano de falla en profundidad requiere una predicción acertada de las fases minerales estables en dichas condiciones. Las reacciones de deshidratación y transformación de fases minerales dentro del plano de falla pueden inducir cambios en el volumen de las fases

solidas y alterar la cantidad de agua en el sistema. En estos casos, las reacciones minerales influyen en la presión de fluidos, el esfuerzo normal sobre la falla y el sistema de esfuerzos en general, llegando a tener importantes efectos en el desarrollo de áreas sismogénicas dentro de la corteza terrestre (Bousquet et al., 2009). Los fluidos de este tipo de sistemas pueden tener fuentes externas o formarse como producto de la deshidratación *in situ* de fases minerales ricas en $H_2O$. Los minerales de la arcilla contienen grandes cantidades de agua en su estructura, por lo tanto sus reacciones químicas en el contexto de zonas de falla son de especial interés para estimar su contribución a la presión de fluidos en fallas activas. Asimismo, la variación en el volumen de los minerales de la arcilla durante la deshidratación con el aumento de la temperatura o la disminución de la actividad de $H_2O$ son funciónes escalonadas (Vidal y Dubacq, 2009), que presentan variaciones discontinuas de volumen a determinadas temperaturas o actividades de $H_2O$ resultantes de la pérdida de capas de agua. Por ejemplo, la naturaleza discontinua de la deshidratación de la esmectita tiene importantes implicaciones geológicas, ya que se acompaña de grandes cambios en el volumen de roca que pueden llegar hasta el 30% y pueden estar ligados a una liberación de agua de aproximadamente 150 kg por cada metro cúbico de esmectita (Vidal y Dubacq 2010). Estas variaciones son muy importantes y pueden tener un fuerte impacto en el comportamiento de las rocas de falla ricas en minerales de la arcilla, ya que podrían controlar procesos tales como las propiedades de fricción y la sismicidad en zonas de falla. Vidal y Dubacq (2009) han propuesto una solución termodinámica que permite la construcción de un modelo que reproduce las transiciones del número de capas de agua observadas experimentalmente; de igual forma este modelo termodinámico permite calcular los cambios de volumen asociados a la deshidratación y a las relaciones de estabilidad y compatibilidad de la esmectita con otros minerales, en un amplio rango de presión y temperatura. El modelo prevé cambios grandes y abruptos dentro de la zona sismogénica, lo que sugiere que la deshidratación de minerales de la arcilla puede llegar a tener un papel importante en el inicio de la sismicidad a profundidades menores de 30 km. Las transformaciones minerales y las reacciones de deshidratación pueden llegar por lo tanto a producir cambios significativos en la cantidad y presión de agua en el sistema, es por esta razón que la identificación y modelización de estos procesos son de gran importancia en la determinación de áreas sismogénicas dentro de la corteza terrestre (Bousquet et al., 2007).

La identificación de las posibles reacciones de formación o transformación de sepiolita en zonas de falla es un tema no tratado previamente y que tiene una aplicación directa en la Zona de Falla de Galera. En este estudio se pretende modelizar el comportamiento termodinámico de las rocas de falla incluyendo a los minerales fibrosos de la arcilla como componentes del sistema termodinámico, con el fin de conocer los limites de estabilidad de las asociaciones minerales presentes en la Falla de Galera. En primer lugar, es necesario establecer las propiedades termodinámicas de los minerales fibrosos de la arcilla para conseguir realizar una minimización de la energía libre de Gibbs, utilizando el software Theriyak-Domino (De Capitani y Petrakakis, 2010). Los resultados del modelo pueden servir como una primera aproximación al cálculo de las proporciones minerales en equilibrio a lo largo de la zona de falla, la determinación de las condiciones de presión y temperatura a las que se producen su deshidratación y transformaciones minerales, la evaluación de los cambios en el volumen de solidos y del agua liberada al sistema, a partir de

composiciones de roca total de muestras reales de la zona de falla de Galera. Establecer estos parámetros permitirá, como objetivo final, predecir las fases minerales estables y sus proporciones en la zona sismogénica de la Falla de Galera que, junto con medidas experimentales del comportamiento de fricción de las rocas de falla, nos permitirán establecer la resistencia de la falla al deslizamiento, su potencial para nuclear terremotos y la influencia de los minerales fibrosos de la arcilla en estos procesos.

### 1.3.3 Comportamiento mecánico de las fallas: implicaciones para la sismicidad

Los terremotos son fenómenos naturales que han sido objeto de numerosos estudios científicos. Sin embargo, aún no se pueden predecir con certeza y, frecuentemente, producen grandes desastres naturales con efectos devastadores para la sociedad. La mayoría de los terremotos de gran magnitud se producen en zonas de subducción o bordes de placas tectónicas. Algunos ejemplos son el terremoto y tsunami de Sumatra en el año 2004 de Magnitud 9.1 (Lay et al., 2005) y el terremoto en Japón en el año 2011 de Magnitud 9.0 (Lay et al., 2013). Sin embargo los terremotos más catastróficos, o de mayor riesgo, no son necesariamente los de mayor magnitud sino aquellos producidos a poca profundidad por fallas muy próximas a grandes ciudades, como es el caso de los recientes terremotos en los montes Apeninos en la región de Amatrice. Los estudios enfocados a descifrar las causas y factores que producen la nucleación de un terremoto y su propagación continúan siendo de gran importancia para la sociedad, ya que amplían el conocimiento y la precisión en la evaluación del riesgo sísmico.

Existen diversos enfoques en el estudio de los terremotos y sus causas. Algunos de ellos consideran factores puramente mecánicos y otros involucran un gran rango de factores que pueden llegar a influir en la sismicidad de una falla. Para lograr entender los mecanismos que conducen a la generación de terremotos, es necesario llevar a cabo un estudio detallado de la fuente sísmica. Estudios recientes que modelizan los mecanismos de producción de terremotos están construidos bajo la teoría de que la mayoría de los terremotos ocurren por deslizamientos repentinos a lo largo de fallas preexistentes en lugar de suceder como resultado de rupturas nuevas en la roca (Scholz, 1998). De este razonamiento, se deduce que el estudio detallado y global de las zonas de falla y de los procesos de fricción que allí ocurren, puede proporcionar información esencial para entender los factores que controlan la nucleación y propagación de terremotos.

Los terremotos ocurren cuando la fuerza de cizalla que se aplica al plano de deslizamiento excede la fuerza de fricción estática del mismo plano, liberando una acumulación de energía elástica. Dentro de este proceso de acumulación y liberación de energía, basada en la teoría del rebote elástico (Reid, 1910), se pueden describir tres periodos dentro del llamado ciclo sísmico (Fig. 1.2): el primero es el comienzo de un ciclo sísmico, donde no existe acumulación de energía; el segundo es el periodo inter-sísmico, durante el cual la energía elástica se almacena en las rocas de la falla de acuerdo con sus propiedades físicas y el tercero es el periodo post-sísmico cuando la energía elástica se ha liberado (Fagereng y Toy, 2011).


Figura 1.2. El ciclo sísmico. Según Fagereng y Toy (2011).

La resistencia de una falla y, por tanto, la cantidad de energía elástica que se puede almacenar en la roca está condicionada por interacciones entre tres factores principales: la fuerza normal, la presión de poro y el coeficiente de fricción (μ). La resistencia de la falla se aproxima al esfuerzo de cizalla en el momento del inicio del desplazamiento ($\tau_f$), que a su vez se define según la ley de Amonton como:

$$\tau_f = C_o + \mu_s (\sigma_n - P_f)$$

Donde $C_o$ es la resistencia cohesiva, $\mu_s$ es el coeficiente de fricción estático, $\sigma_n$ es el esfuerzo normal y $P_f$ es la presión del fluido (Fagereng and Toy, 2011).

Con el fin de profundizar en los procesos mecánicos que suceden en las zonas de falla y en particular la forma en la que interactúan los factores que afectan a los procesos de fricción ($C_o$, $\mu_s$, $\sigma_n$, y $P_f$), se han desarrollado instrumentos que permiten reproducir las condiciones de presión y temperatura estimadas para zonas sismogénicas dentro de la corteza terrestre. Estos instrumentos incluyen la posibilidad de deslizar una superficie contra otra controlando la fuerza necesaria para iniciar y mantener el movimiento a una tasa de desplazamiento determinada, de este tipo de experimentos se deduce el coeficiente de fricción estático ($\mu_{ss}$), asi como también, la fuerza necesaria para continuar deslizando las superficies una contra otra, que es proporcional al coeficiente de fricción cinético ($\mu_k$). Dentro de los instrumentos que permiten este tipo de condiciones se encuentran los aparatos de cizalla de rotación, instrumentos de compresión uniaxial e instrumentos de compresión triaxial. En este estudio se ha empleado un instrumento de deformación triaxial (Mitchell and Faulkner, 2008) y los experimentos de fricción han sido posibles gracias a un ensamblaje en configuración de fuerza cortante directa (*direct shear*) (Sánchez-Roa et al., 2016). Las especificaciones del equipo permiten alcanzar desplazamientos desde 0.05 μ/s hasta 10 μ/s que equivalen a velocidades de desplazamiento sub-símicas empleadas previamente en la investigación de nucleación de terremotos. Estos equipos de deformación permiten reproducir las condiciones de presión de la corteza terrestre a los que están sometidos los materiales de la Zona de Falla de Galera y permiten aplicar a estos materiales una fuerza de cizalla a velocidades sub-sísmicas como clave para comprender la deformación en minerales fibrosos de la arcilla y otros procesos implicados en el deslizamiento de fallas.

Se han empleado múltiples experimentos de laboratorio para intentar definir las propiedades reológicas de rocas y minerales, con el objetivo de caracterizar el comportamiento mecánico de la litosfera y el efecto que la heterogeneidad mineralógica tiene sobre la resistencia al deslizamiento de las fallas (Byerlee, 1978; Marone, 1998). Byerlee (1978). Un amplio estudio de diferentes tipos de rocas y minerales bajo un amplio rango de presión, reveló que cuando las superficies deslizantes de una falla están separadas por rocas de falla que contienen filosilicatos, la fricción puede llegar a ser muy baja y concluyó que debido a que las fallas naturales suelen contener minerales de alteración, la fricción de las fallas naturales puede estar fuertemente condicionada por la composición de la roca de falla. Estudios posteriores han demostrado que los filosilicatos suelen presentar una baja resistencia a la cizalla y por lo tanto se caracterizan por presentar bajos coeficientes de fricción (Moore y Lockner, 2004; Shimamoto y Logan, 1981). Los coeficientes de fricción ($\mu$) para los filosilicatos se encuentran principalmente en el rango de $\mu$ = 0.2-0.5 (Behnsen y Faulkner, 2012), aunque algunos estudios muestran $\mu$ <0,1 dependiendo de la presencia y composición de los fluidos de poro, la velocidad de cizallamiento, la temperatura y el tipo de estructura cristalina del mineral (Ikari et al., 2007, Saffer y Marone, 2003). La presencia de materiales de roca de falla con $\mu$ <0,6 han sido sugeridos como un mecanismo de debilitamiento de zonas de falla en la corteza media a superior (Moore y Lockner, 2004; Morrow et al., 2000). Algunos de los estudios mencionados, basados en experimentos de laboratorio en filosilicatos, han demostrado una relación directa entre el coeficiente de fricción en seco y la energía de enlace o cohesión entre las capas de cada mineral (Moore y Lockner, 2004), esto indica que el cizallamiento en estos minerales se centra principalmente en el espacio entre capas TO o TOT. Sin embargo, esta relación no siempre es directa (Behnsen y Faulkner, 2012; Sakuma y Suehara, 2015) e indica que otros factores como la estructura de los minerales y la distribución del agua dentro de ellas pueden tener efectos importantes en el coeficiente de fricción de los filosilicatos.

Los experimentos de fricción en el laboratorio simulan el desplazamiento de una superficie rocosa contra otra. Estos desplazamientos pueden suceder a velocidades sub-sísmicas, simulando los procesos que ocurren durante el periodo inter-sísmico ($\mu$m/s) o a velocidades sísmicas en equipos como los de rotación que permiten un desplazamiento infinito de las superficies (m/s). Con el fin de simular el ciclo sísmico es posible realizar intervalos secuenciales en los que la superficie se desplaza a velocidades sub-sísmicas y un incremento en la velocidad de desplazamiento es impuesto repentinamente simulando un terremoto. La respuesta del material a estas variaciones involucra un aumento inmediato de la fuerza de cizalla necesaria para desplazar las superficies (*shear stress*), seguido de una evolución de la fuerza necesaria para continuar el desplazamiento, que depende de varios factores incluyendo la naturaleza del material.

La interpretación de los resultados de experimentos de este tipo revela que los procesos que ocurren durante estos "terremotos" simulados son complejos e involucran un gran número de factores. La modelización matemática de los procesos que suceden durante la fricción de superficies de roca o materiales granulares es necesaria para hallar ecuaciones constitutivas que definan el comportamiento esperado de zonas de falla activas. Las ecuaciones que hasta el momento reproducen con mayor exactitud los resultados de fricción experimentales han

sido definidas como las leyes de tasa y estado de la fricción o "*Rate and state friction equations*" (Dieterich, 1979; Ruina, 1983).

Durante los últimos casi 40 años se han implementado las ecuaciones de fricción "Rate and state" para comprender los datos experimentales que simulan la nucleación de terremotos y se han convertido en una herramienta de gran importancia en el estudio de la mecánica de fallas y terremotos (Marone, 1998). Este conjunto de leyes incluyen una variable de estado que permite incluir procesos complejos que ocurren durante la fricción tales como, los efectos de memoria de las superficies y la evolución de familias de micro-contactos en la superficie deslizante durante todas las etapas de ciclo sísmico. De esta manera logran reproducir casi todos los comportamientos de una falla en la corteza terrestre con deformación frágil, durante las diferentes etapas de acumulación y liberación de energía elástica (Marone, 1998).

Los regímenes de estabilidad de la fricción y su relación con la sismogénesis dependen del parámetro combinado *(a - b)* y el parámetro $D_c$. Según las leyes constitutivas de la fricción se consideran dos escenarios posibles: deslizamiento estable o deslizamiento inestable. Los valores positivos de (a-b) corresponden a un régimen de deslizamiento estable (Fig. 1.3, izq.), en la que la roca de falla se hace más difícil de deslizar (o más resistente) con el incremento de la velocidad, lo que significa que los terremotos no se nuclean. En el caso contrario, los valores negativos de (a-b) corresponden a un régimen inestable (Fig. 1.3, dcha.); en este régimen, la roca de falla se hace más fácil de deslizar con el incremento de la velocidad y los terremotos pueden nuclear dentro de estos materiales (Scholz, 1998; Marone, 1998).

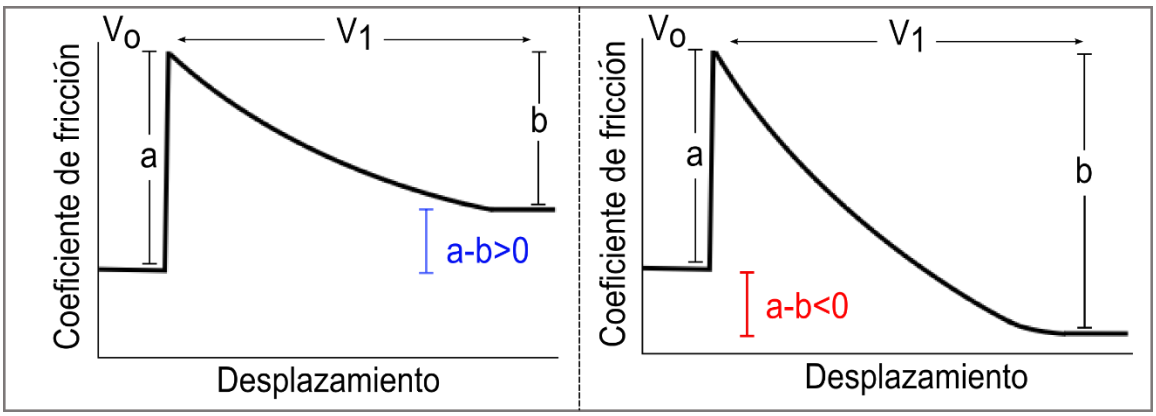


Figura 1.3. Parámetro de estabilidad del deslizamiento *(a-b)*, según Scholz (1998).

El grupo de los minerales fibrosos de la arcilla no ha sido incluido aún en los estudios de fricción aplicados a fallas activas de la corteza terrestre. Sin embargo su abundante presencia dentro de la Falla de Galera sugiere que estos minerales pueden tener un papel importante en los procesos de deformación de la zona. Por lo tanto, su estudio es de gran importancia no sólo para la falla de Galera, sino también para comprender los vínculos fundamentales entre la mineralogía y la mecánica de las fallas.

# 2. Selección del área de estudio y materiales empleados en este estudio

## 2.1 Sismicidad en el sur de España

El sur de España se localiza en un área de actividad sísmica baja a moderada en un contexto global. Sin embargo, el área del oeste mediterráneo, donde se encuentra Andalucía, constituye el área de mayor riesgo sísmico de la península Ibérica (Figura 1.4).

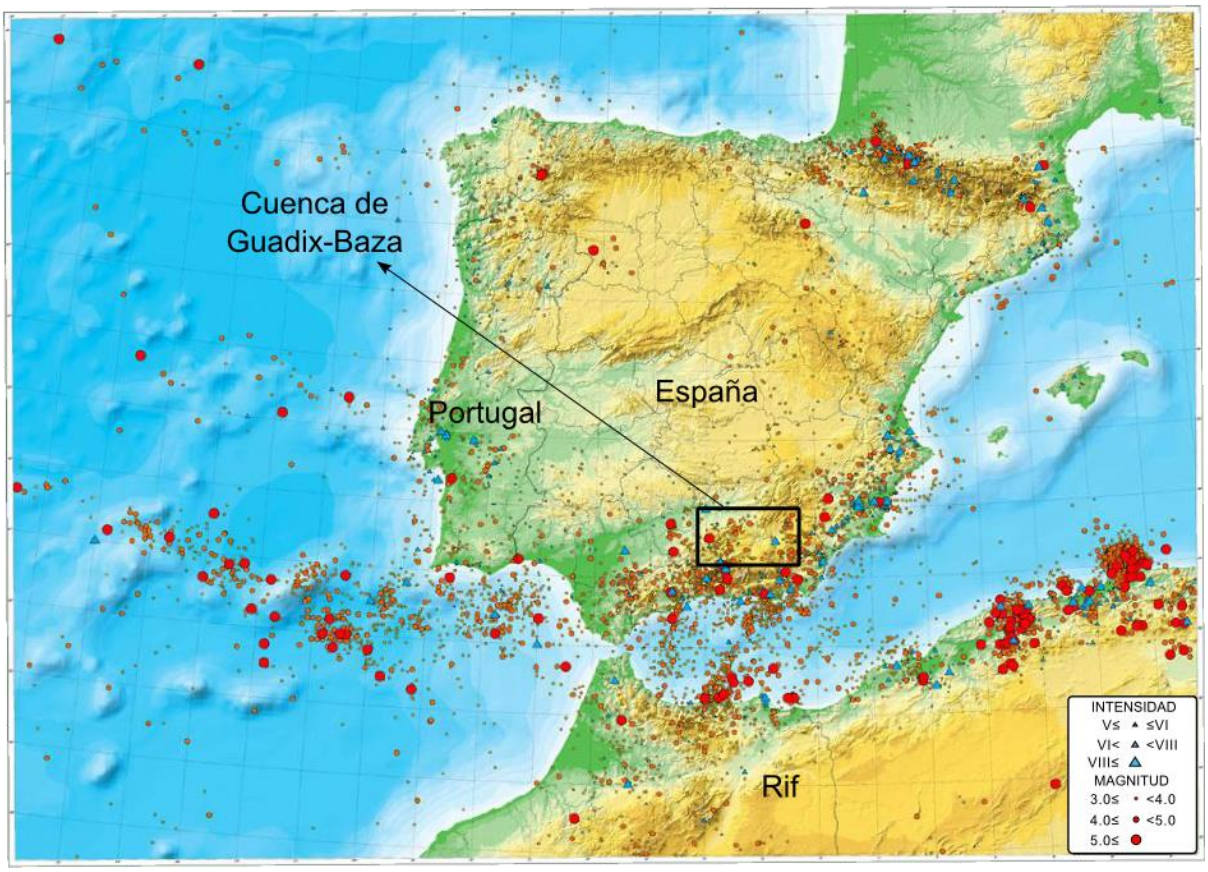


Figura 1.4. Mapa general de la sismicidad en la península Ibérica: La información sísmica proviene de la base de datos del Instituto Geográfico Nacional, actualizada al año 2003. Los epicentros del periodo histórico entre los años 1048 y 1919 están representados mediante valores de intensidad sísmica, mientras que los correspondientes al periodo instrumental 1920-2003, se representan por valores de magnitud.

Los esfuerzos de compresión entre las placas Africana y Euroasiática, con una tasa de movimiento relativo de aproximadamente 5 mm/año (DeMets et al., 1994), condujeron a la formación de las cordilleras Béticas y El Rif (Alfaro et al., 2008). La deformación dentro de este límite de placas difuso es absorbida por numerosas fallas distribuidas en un área de gran extensión. La mayoría de estas fallas tienen bajas tasas de desplazamiento y largos periodos de recurrencia que exceden los periodos cubiertos por los registros históricos e instrumentales.

La cordillera Bética forma parte de este régimen geodinámico de esfuerzo compresivo en dirección NNW-SSE con extensión asociada en dirección ENE-WSW (Galindo-Zaldivar et al., 1993). Esta extensión es acomodada principalmente por fallas normales de alto ángulo en sentido NNW-SSE (Galindo-Zaldivar et al., 1989).

## 2.2 Área de estudio

El área de estudio de esta tesis esta localizada dentro del área central de la Cordillera Bética en la cuenca de Guadix-Baza (Fig. 1.5), la más grande de las cuencas neógenas intramontañosas del este de la cordillera Bética (Libarren et al., 2003).

La Falla de Galera (García Tortosa et al., 2007) es una falla de salto en dirección, de 23 km de longitud y con orientación N48ºE. La zona de falla presenta 1,5 km de ancho con varios planos de falla paralelos entre si buzando entre 40º y 60º hacia el NW y que cortan una secuencia sedimentaria compuesta en su mayoría por areniscas, lutitas y margas. La falla está localizada en un área con escasa vegetación y bajas precipitaciones, de aproximadamente 423 mm/año (datos de la Agencia Estatal de Meteorología Española, AEMET). Las condiciones meteorológicas y geográficas de la zona de falla facilitan el acceso a los afloramientos de sus planos de falla, lo que permite el muestreo de rocas de falla poco alteradas y representativas de su mineralogía. Estas condiciones suponen un escenario favorable para el estudio.

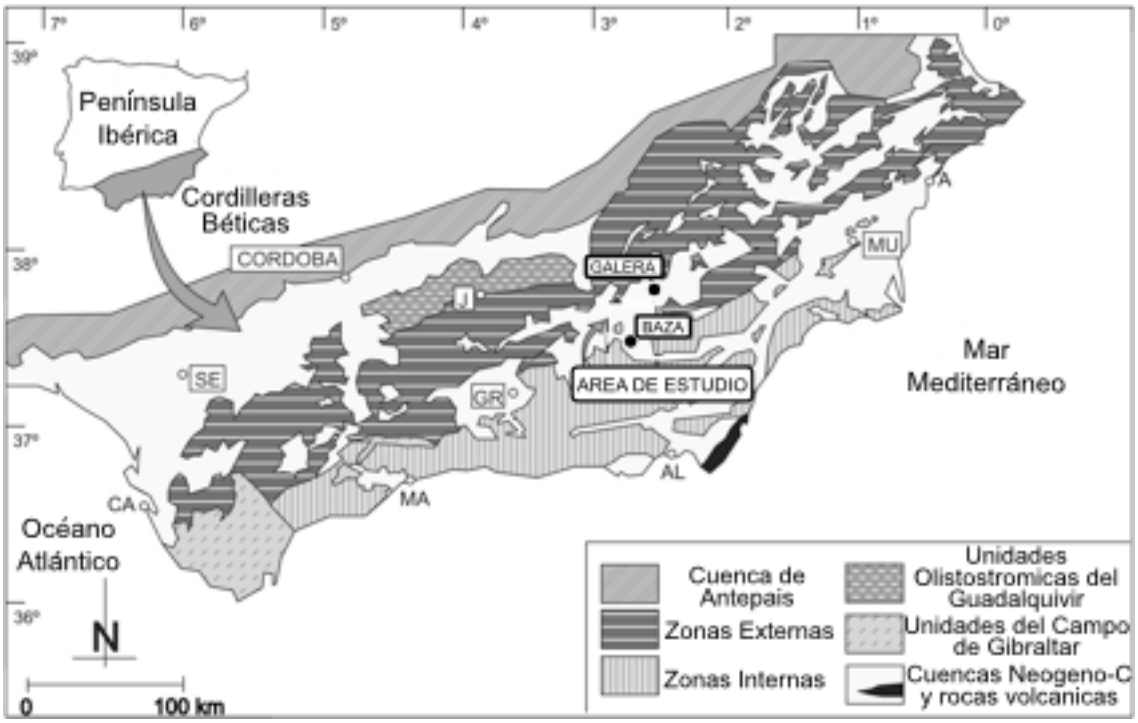


Figura 1.5. Ubicación de la Cuenca de Guadix-Baza, Cordillera Bética Central, Sur de España. Modificado de García-Tortosa et al. (2008).

La falla de Galera es una falla activa. Las fallas de Galera y Baza están asociadas a actividad sísmica consistente en terremotos recientes de magnitud inferior a 4,7, que incluyen enjambres sísmicos de magnitudes inferiores, como el reciente del 16 de febrero de 2004 en Benamaurel, cuando se registraron seis terremotos con magnitudes de 1,0 a 1,3 (Alfaro et al., 2008, García-Tortosa et al., 2011). Dentro de los terremotos más notables originados en

la Falla de Galera se encuentra el del 4 de junio de 1964, con una magnitud de 4.8 $m_{bLg}$ y una intensidad sentida de VIII en los pueblos de Galera y Orce (García-Tortosa et al., 2011). Como consecuencia de este sismo, más de la mitad de los techos y chimeneas de Galera quedaron destruidas y hasta el 70% de los de Orce quedaron afectados (Fig. 1.6).

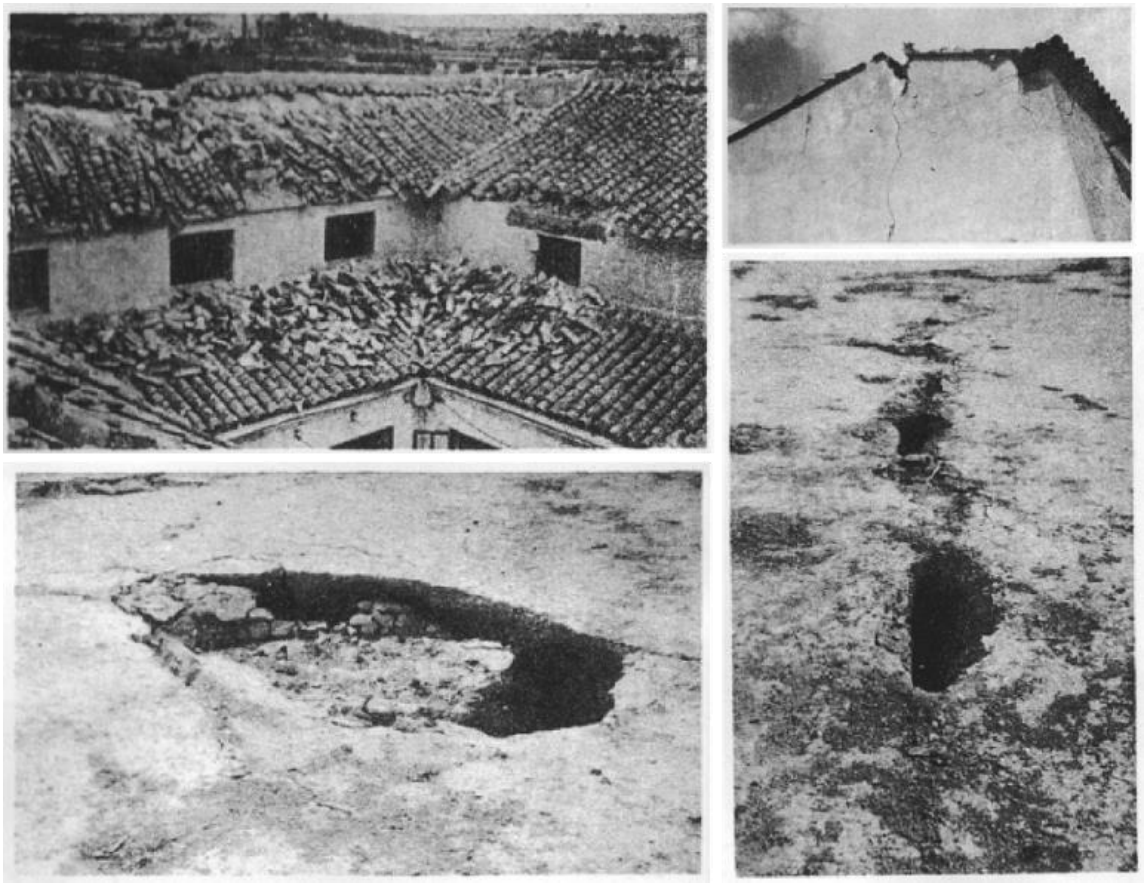

Figura 1.6. Daños reconocidos como consecuencia del terremoto de Galera en junio de 1964. (Fotografías extraídas del Boletín de sismos del IGN). Modificado de García-Tortosa et al. (2009).

Jiménez Millán et al. (2009) revelaron la presencia de indicios de minerales fibrosos en el área de la Falla de Galera. La presencia de sepiolita y palygorskita es, en general, poco común y aun menos frecuente en contextos de deformación y zonas de falla. La identificación de los patrones de distribución de minerales de la arcilla en la zona de falla de Galera debe contribuir a clarificar la relación de los minerales fibrosos de la arcilla con la falla. La presencia de sepiolita y palygorskita en esta zona de falla ha motivado el planteamiento del estudio de su comportamiento reológico durante procesos frágiles, así como investigar sus condiciones de estabilidad, con el objetivo de expandir desde diferentes perspectivas nuestro conocimiento acerca del papel de los minerales fibrosos de la arcilla en la estabilidad sísmica de zonas de falla.

## 2.3 Materiales

### Los minerales fibrosos de la arcilla (Sepiolita y Palygorskita)

La presencia de minerales fibrosos de la arcilla dentro de áreas de deformación caracterizan a la Falla de Galera y son una de las principales motivaciones de los estudios incluidos en esta tesis doctoral. Los materiales incluidos en este estudio son principalmente aquellos que componen la secuencia sedimentaria lacustre de la sub-cuenca de Baza y las rocas de falla de la Falla de Galera dentro de la cuenca de Guadix-Baza. Además, se incluye un estudio sobre un conjunto de materiales monominerálicos de filosilicatos, con el fin de estudiar en profundidad los efectos de la estructura mineral sobre la resistencia de la falla al deslizamiento. La Tabla 1.1. presenta una lista de los materiales utilizados:

| | **Nombre** |
|---|---|
| **a. Falla de Galera** | |
| Rocas de Falla | Pueblo de Galera (rica en esmectita y palygorskita) |
| | Rambla de los Pilares (rica en sepiolita) |
| Protolito | Lútitas oscuras |
| | Margas blancas |
| **b. Materiales estándar** | |
| Fibrosos | Palygorskita Florida (PIF-1) |
| | Sepiolita Vicalvaro (SV) |
| Planares | Talco (Wards) |
| | Saponita (separada de la Falla Alpina (NZ)) |

Tabla 1.1. Materiales utilizados en este estudio.

Tanto la sepiolita como la palygorskita son filosilicatos fibrosos compuestos de láminas continuas de tetraedros de silicio que tienen el oxígeno apical periódicamente invertido (García-Romero y Suárez, 2013). Como resultado de estas inversiones periódicas, los minerales del grupo de la palygorskita-sepiolita tienen una morfología fibrosa y canales que contienen moléculas de $H_2O$ y cationes intercambiables, tales como $Na^+$, $K^+$ y $Ca^{2+}$ (Guggenheim y Krekeler, 2011).

La palygorskita ideal tiene un carácter dioctaédrico (con el 80% de las posiciones octaédricas ocupadas) mientras que la sepiolita es un mineral puramente trioctaédrico (Suárez y García-Romero, 2011). Suárez y García-Romero (2011) demostraron que las composiciones químicas de los dos minerales presentan un rango de intersección. Este hallazgo derivó en la

identificación de minerales intermedios tales como la sepiolita-alumínica y la palygorskita-magnésica. En un estudio posterior, Suárez y García-Romero (2013) propusieron la existencia de una serie polisomática para explicar la serie continua de composiciones químicas a través del intercrecimiento de polisomas de sepiolita y palygorskita. El estudio de los procesos minerales y sus relaciones genéticas en zonas de falla es un campo de investigación activa, con posibles aplicaciones enfocadas a descifrar los efectos que los cambios en las propiedades físico-químicas de los minerales de la roca de falla pueden tener sobre el plano de deslizamiento.

La estructura cristalográfica y la deshidratación de los minerales fibrosos de la arcilla han sido explorados en estudios experimentales haciendo uso de análisis termogravimétricos (Nagata et al., 1973) y difracción de rayos X, con radiación de sincrotrón, sobre muestras de polvo (Post et al., 2007; Post and Heaney, 2008). Estos estudios confirmaron el modelo de estructura inicial propuesto por Brauner y Preisinger (1956), donde el estado cristaloquímico del agua en los minerales fibrosos de la arcilla se agrupa en tres situaciones: el primer grupo consiste en los grupos hidroxilo (OH) dentro de las capas octaédricas; el segundo grupo se refiere al agua de cristalización, que consiste en moléculas de agua que completan la coordinación 6 de los átomos de Mg en los bordes de las capas octaédricas; y el tercer grupo es el agua zeolítica, que se encuentra dentro de los canales de la estructura fibrosa. Además, los estudios citados revelaron la existencia de diferentes estados de deshidratación de los minerales fibrosos en etapas subsecuentes a temperaturas elevadas. El primer paso de la deshidratación de sepiolita implica la pérdida del agua zeolítica acompañada de una ligera disminución en los parámetros de la celda unitaria a y c (Post et al., 2007). La pérdida del agua de cristalización se produce en dos etapas, perdiendo la mitad del agua ligada estructuralmente en cada una de las etapas y disminuyendo continuamente los parámetros de la celda unitaria con el aumento de la temperatura. La pérdida del agua de cristalización provoca un cambio de fase, en el que la estructura se pliega por rotación de las cintas del filosilicato (Post et al., 2007). Es importante señalar que las variedades deshidratadas de los minerales fibrosos de la arcilla mencionadas anteriormente han sido generadas exclusivamente de forma experimental y bajo condiciones no hidrotermales.

Los filosilicatos fibrosos (sepiolita y palygorskita) se encuentran dentro de la parte superior de la corteza terrestre. Existen concentraciones de estos minerales en España y el área mediterránea en general, especialmente notables; están asociados a ambientes áridos. Estos minerales aparecen ampliamente como depósitos sedimentarios en ambientes evaporíticos (Akbulut y Kadir, 2003), así como en depósitos hidrotermales de sistemas relacionados con fluidos de alta salinidad y enriquecidos en Mg, como resultado de la alteración de minerales ricos en este elemento (Bach, 2002). Los minerales fibrosos de la arcilla y la esmectita rica en $Mg^{2+}$ pueden formarse en asociación con minerales tales como sulfatos y carbonatos en cuencas restringidas poco profundas con condiciones evaporíticas (Jones, 1986). De igual manera, los minerales fibrosos de la arcilla pueden formarse como producto de la des-dolomitización en ambientes lacustres (Pozo y Martin, 1989), como producto de la transformación diagenética de la magnesita en presencia de aguas ricas en sílice (Thiry y Pletsch, 2011), o a partir de esmectitas como resultado de un proceso de disolución-precipitación (Weaver y Beck, 1977). Este grupo de minerales de la arcilla ricos en Mg

también puede ser el resultado de la alteración de basaltos oceánicos (Trauth, 1977; Jones, 1986). Sin embargo, la mayoría de los depósitos de palygorskita y sepiolita en el mundo son autigénicos, formados por neoformación o cristalización de geles de sílice amorfo o por transformación de esmectita o illita en ambientes lacustres y perimarinos (Murray et al., 2011).

En cuanto a las condiciones químicas para su formación, la literatura mineralógica coincide en que los valores altos de $pH^+$ favorecen la estabilidad de la sepiolita y la palygorskita. Por ejemplo, en la transformación de montmorillonita en palygorskita, los valores de $pH^+$ deben estar entre 8 y 9 (Weaver y Beck, 1977). A altos valores de $pH^+$ (10,5-11,5) la sepiolita puede ser producto de la transformación diagenética de la magnesita (Ece, 1998). Otros autores convergen en la teoría de que para temperaturas bajas, la cristalización de la sepiolita requiere un $pH^+>8$ (Siffert y Wey, 1962, Wollast et al, 1968, La Iglesia, 1978). El límite inferior de $pH^+$ para la cristalización de palygorskita en suelos requiere una solución con $pH^+$ superior a 5,9 (Singer, 1979). Según Weaver y Beck (1977), los minerales fibrosos de la arcilla se ven favorecidos por salinidades inferiores a la normal de aguas marinas y por temperaturas altas. Desde el punto de vista termodinámico, sólo se requieren ligeras modificaciones de las condiciones normales del agua de mar para formar sepiolita y palygorskita. Las apariciones de sepiolita-palygorskita se asocian comúnmente con sílice amorfa, sin embargo, es común identificar asociaciones con cuarzo (Leguey et al., 1984), talco (Isphording 1984), kerolita (Stoessell y Hay, 1978) y saponita (Birsoy, 2002; Galan y Castillo, 1984).). La sepiolita también se presenta como un mineral secundario asociado con minerales del grupo de la serpentina, con dolomita y ópalo.

La importancia del estudio de los minerales fibrosos de la arcilla deriva del amplio abanico de ambientes geológicos en los que aparecen y su relación con áreas de deformación. El estudio de estos minerales de la arcilla es fundamental para comprender el comportamiento mecánico de las fallas activas donde puedan predominar.

## 3. Objetivos

Los objetivos principales de esta tesis doctoral son:

a. Determinar el origen y las relaciones genéticas de las asociaciones minerales de rocas de falla ricas en minerales fibrosos de la arcilla a través de la caracterización mineral y geoquímica.
b. Desarrollar un modelo termodinámico que describa las condiciones de estabilidad de la sepiolita y sus reacciones de deshidratación, con el fin de identificar procesos susceptibles de influir en el régimen sísmico de zonas de falla.
c. Evaluar las propiedades mecánicas de los filosilicatos fibrosos (sepiolita y palygorskita) como fases mono-minerálicas y comparar su comportamiento con el de filosilicatos planares con el fín de determinar su influencia en la dinámica de las fallas.
d. Estimar los procesos mecánicos y el estado de deformación de las fases minerales en las rocas de la Falla de Galera, a través de un amplio análisis a escala micro y nanométrica.
e. Integrar los datos minerales, geoquímicos, termodinámicos y de fricción para mejorar nuestro conocimiento sobre los procesos que tienen lugar durante el ciclo sísmico de la Zona de Falla de Galera como consecuencia de la deformación activa.

## 4. Estructura de la tesis

La presente tesis doctoral se presenta para su evaluación como un conjunto de trabajos publicados de acuerdo con lo establecido en el Reglamento de Estudios de Doctorado de la Universidad de Jaén (artículo 23). De este modo, el manuscrito se organiza en seis capítulos. Cuatro capítulos se corresponden con los artículos publicados o en proceso de publicación o revisión redactados en inglés. Se incluye, además, un capitulo de introducción y capítulo de conclusiones redactados en castellano.

En el capítulo I se presenta una introducción a la autigénesis de los minerales de la arcilla en las zonas de falla, la importancia de la modelización termodinámica y del estado de hidratación de filosilicatos, así como también, la importancia de los cambios minerales en la roca de falla. Finaliza con una introducción a las propiedades de fricción de las zonas de falla ricas en arcilla.

El capítulo II consiste en un análisis detallado de los materiales ricos en minerales de la arcilla identificados en la Zona de Falla de Galera, generados como consecuencia de los procesos de deformación activa que afectan a la cuenca de Guadix-Baza. En este capitulo se emplea una combinación de técnicas analíticas y experimentales, incluyendo difracción de rayos X, microscopía electrónica (SEM y TEM) y análisis químico (fluorescencia de rayos X, XRF, y espectrometría de masas por plasma de acoplamiento inductivo, ICP-MS) con el fin de establecer el origen de las asociaciones de minerales y su relación con el desarrollo de estructuras de deformación y eventos sísmicos en la falla de Galera. Este estudio resalta la importancia de la identificación y análisis de las arcillas en zonas de falla como una

herramienta valiosa en la interpretación de procesos geológicos que conducen a la autigénesis de minerales fibrosos de la arcilla y su influencia en la estabilidad mecánica de las zonas de falla. El contenido de este capítulo se recoge en el artículo titulado: Autigénesis de minerales fibrosos de la arcilla inducida por la interacción fluido-roca en la Zona de Falla de Galera (Cordillera Bética, SE de España) y su influencia en las propiedades de fricción de sus rocas de falla, *(Fibrous clay mineral authigenesis induced by fluid-rock interaction in the Galera Fault Zone (Betic Cordillera, SE Spain) and its influence on fault gouge frictional properties),* publicado en la revista *Applied Clay Science.*

El capítulo III consiste en un estudio a escala micro- y nano-métrica de muestras de rocas de falla, de la Zona de Falla de Galera, deformadas natural y experimentalmente. El objetivo del estudio es identificar los procesos químicos y físicos que contribuyen a las diferencias en la resistencia al cizallamiento entre las dos superficies principales de deslizamiento de la Zona de Falla de Galera, identificadas en el Capítulo II. Este estudio examina mediante SEM y TEM las transformaciones minerales y los procesos físicos relacionados con la alineación y deformación de granos, con el fin de identificar los factores que contribuyen a propiedades de fricción tan diferenciadas entre rocas de falla ricas en filosilicatos planares y las ricas en fibrosos. Los contenidos de este capítulo forman parte del manuscrito: Estudio de las rocas de falla deformadas en la Zona de Falla de Galera (Cordillera Bética, SE de España) a escalas micro y nanométrica, *(Micro- and nano-scale study of deformed phyllosilicate-rich gouges from the Galera Fault Zone (Betic Cordillera, SE Spain))* que será enviado a la revista *American Mineralogist*.

El capítulo IV presenta el desarrollo de un nuevo modelo termodinámico para la sepiolita como una herramienta para definir cómo se comporta este mineral bajo condiciones químicas y mecánicas variables. Este estudio adopta un enfoque termodinámico para responder a la limitación impuesta por la escasez de datos sobre la estabilidad de la sepiolita y las transformaciones minerales que la involucran. Los cálculos de minimización de energía libre de Gibbs, fueron ejecutados haciendo uso del software Theriyak-Domino, e incluyen las propiedades termodinámicas calculadas para la sepiolita. Este modelo permite la identificación de reacciones minerales y relaciones de compatibilidad de la sepiolita con otras fases minerales en una amplia gama de condiciones de presión y temperatura. Finalmente, se ha integrado el modelo termodinámico con ensayos de fricción que evalúan la resistencia al deslizamiento de las fallas. Estos métodos se aplican a un ejemplo natural como estrategia para explorar la relación entre la deshidratación de sepiolita y la nucleación de terremotos en la Zona de Falla de Galera. Este trabajo constituye el manuscrito: Implicaciones de la deshidratación de sepiolita en la nucleación de terremotos en la Zona de Falla de Galera: Un enfoque termodinámico, *(Implications of sepiolite dehydration for earthquake nucleation in the Galera Fault Zone: a thermodynamic approach),* que ha sido enviado a la revista *Applied Geochemistry.*

En el capítulo V se compara el comportamiento de fricción de un grupo de filosilicatos magnésicos tanto planares como fibrosos. Los experimentos de fricción fueron llevados a cabo a diferentes velocidades de nucleación con el objetivo de explorar los posibles efectos de la estructura cristalina sobre la resistencia a la fricción, así como evaluar la estabilidad

mecánica de minerales químicamente similares y estructuralmente diferentes. En este capitulo se emplea una comparación entre los experimentos saturados en agua y aquellos saturados en argón con el fin de explorar el papel del agua en su comportamiento de fricción. Los resultados del estudio se combinan con una revisión de los controles termodinámicos sobre la distribución de estos filosilicatos ricos en Mg en zonas de falla, para describir las implicaciones de los resultados sobre la resistencia al deslizamiento de fallas ricas en Mg. El manuscrito que recoge estos contenidos fue publicado en la revista *Geophysical Research Letters* como: Efectos de la estructura mineral de filosilicatos sobre la fuerza de fricción de fallas en sistemas ricos en magnesio, *(How phyllosilicate mineral structure affects fault strength in Mg-rich fault systems).*

Finalmente, en el capítulo VI se presentan las principales conclusiones y aportes científicos de esta tesis doctoral.

## Referencias

Abad, I., Nieto, F., Velilla, N., 2002. Chemical and textural characterisation of diagenetic to low-grade metamorphic phyllosilicates in turbidite sandstones of the South Portuguese Zone: A comparison between metapelites and sandstones. Schweizerische Mineral. und Petrogr. Mitteilungen 82, 303–324.

Ahn, J.H., Peacor, D.R., 1986. Transmission and Analytical Electron Microscopy of the Smectite-to-Illite Transition. Clays Clay Miner. 34, 165–179.

Akbulut, A.C., Kadir, S., 2003. The geology and origin of sepiolite, palygorskite and saponite in Neogene lacustrine sediments of the Serinhisar-Acipayam basin, Denizli, SW Turkey. Clays Clay Miner. 51, 279–292. doi:10.1346/CCMN.2003.0510304

Alfaro, P., Delgado, J., Galdeano, C.S., Galindo-Zaldíevar, J., García-Tortosa, F.J., López-Garrido, a. C., López-Casado, C., Marín-Lechado, C., Gil, a., Borque, M.J., 2008. The Baza Fault: A major active extensional fault in the central Betic Cordillera (south Spain). Int. J. Earth Sci. 97, 1353–1365. doi:10.1007/s00531-007-0213-z

Bach, W., 2002. Discovery of ancient and active hydrothermal systems along the ultra-slow spreading Southwest Indian Ridge 10°–16°E. Geochemistry Geophys. Geosystems 3, 1–14. doi:10.1029/2001GC000279

Behnsen, J., Faulkner, D.R., 2012. The effect of mineralogy and effective normal stress on frictional strength of sheet silicates. J. Struct. Geol. 42, 49–61. doi:10.1016/j.jsg.2012.06.015

Birsoy, R., 2002. Formation of sepiolite-palygorskite and related minerals from solution. Clays Clay Miner. 50, 736–745. doi:10.1346/000986002762090263

Bousquet, R., Arcay, D., Capitani, C. De, 2007. Do metamorphic reactions influence the subducting dynamic ? Geophys. Res. Abstr. EGU 9. doi:1607-7962/gra/EGU2007-A-08796

Bousquet, R., Vidal, O., de Capitani, C., 2009. Metamorphic reactions, fluids release and their influence on subduction earthquakes, in: EGU General Assembly 2009, Held 19-24 April, 2009 in Vienna, Austria http://meetings.copernicus.org/egu2009. p. p.12554.

Botton, G., 2007. Analytical electron microscopy. Sci. Microsc. doi:10.1007/978-0-387-49762-4_4

Bragg, W.H., 1913. The Reflection of X-rays by Crystals. (II.). Proc. R. Soc. A Math. Phys. Eng. Sci. 89, 246–248. doi:10.1098/rspa.1913.0082

Burkhard, M., Kerrich, R., 1990. Fluid-rock interactions during thrusting of the Glarus nappe - evidence from geochemical and stable isotope data. Schweiz. Miner. Pet. Mitt. 70, 77–82.

Byerlee, J., 1978. Friction of rocks. Pure Appl. Geophys. 116, 615–626. doi:10.1007/BF00876528

Cuadros, J., Altaner, S.P., 1998. Characterization of mixed-layer illite-smectite from bentonites using microscopic, chemical, and X-ray methods: constraints on the smectite-to-illite transformation mechanism. Am. Mineral. 83, 762–774.

De Capitani, C., Petrakakis, K., 2010. The computation of equilibrium assemblage diagrams with Theriak/Domino software. Am. Mineral. 95, 1006–1016. doi:10.2138/am.2010.3354

Fagereng, a., Toy, V.G., 2011. Geology of the earthquake source: an introduction. Geol. Soc. London, Spec. Publ. 359, 1–16. doi:10.1144/SP359.1

Faulkner, D.R., Jackson, C.A.L., Lunn, R.J., Schlische, R.W., Shipton, Z.K., Wibberley, C. a J., Withjack, M.O., 2010. A review of recent developments concerning the structure, mechanics and fluid flow properties of fault zones. J. Struct. Geol. 32, 1557–1575. doi:10.1016/j.jsg.2010.06.009

Faulkner, D.R., Lewis, a. C., Rutter, E.H., 2003. On the internal structure and mechanics of large strike-slip fault zones: Field observations of the Carboneras fault in southeastern Spain. Tectonophysics 367, 235–251. doi:10.1016/S0040-1951(03)00134-3

Galán, E. and Carretero, I., 1999. A new approach to compositional limits for sepiolite and palygorskite. Clays and Clay Minerals, 47, 4, 399–409.

Galan, E., Castillo, A., 1984. Sepiolite - Palygorskite in Spanish Tertiary Basins: Genetical Patterns in Continental Environments. Dev. Sedimentol. 37, 87–124. doi:10.1016/S0070-4571(08)70031-1

Galindo-Zaldivar, J., Gonzalez-Lodeiro, F., Jabaloy, A., 1989. Progressive extensional shear structures in a detachment contact in the Western Sierra Nevada (Betic Cordilleras, Spain). Geodin. Acta 3, 73–85. doi:10.1080/09853111.1989.11105175

García-Romero, E., Suárez, M., Oyarzun, R., López-García, J.A., Regueiro, M., 2006. Fault-hosted palygorskite from the Serrata de Nijar deformation zone (SE Spain). Clays Clay Miner. 54, 324–332. doi:10.1346/CCMN.2006.0540304

García-Romero, E., Suárez, M., 2013. Sepiolite-palygorskite: Textural study and genetic considerations. Appl. Clay Sci. doi:10.1016/j.clay.2013.09.013

García-Tortosa, F.J., Alfaro, P., Galindo-Zaldívar, J., Gibert, L., López-Garrido, A.C., Sanz de Galdeano, C., Ureña, M., 2008. Geomorphologic evidence of the active Baza Fault (Betic Cordillera, South Spain). Geomorphology 97, 374–391. doi:10.1016/j.geomorph.2007.08.007

García-Tortosa, F.J., Alfaro, P., Sanz de Galdeano, C., Galindo-Zaldívar, J., 2011. Glacis geometry as a geomorphic marker of recent tectonics: The Guadix-Baza basin (South Spain). Geomorphology 125, 517–529. doi:10.1016/j.geomorph.2010.10.021

Guggenheim, S., Krekeler, M.P.S., 2011. The structures and microtextures of the palygorskite-sepiolite group minerals, in: Galan, E., Singer, A. (Eds.), Developments in Clay Science. Elsevier B.V., pp. 3–32. doi:10.1016/B978-0-444-53607-5.00001-3

Haines, S.H., Kaproth, B., Marone, C., Saffer, D., Van der Pluijm, B., 2013. Shear zones in clay-rich fault gouge: A laboratory study of fabric development and evolution. J. Struct. Geol. 51, 206–225. doi:10.1016/j.jsg.2013.01.002

Haines, S.H., van der Pluijm, B.A., 2012. Patterns of mineral transformations in clay gouge, with examples from low-angle normal fault rocks in the western USA. J. Struct. Geol. 43, 2–32. doi:10.1016/j.jsg.2012.05.004

Ikari, M.J., Saffer, D.M., Marone, C., 2007. Effect of hydration state on the frictional properties of montmorillonite-based fault gouge. J. Geophys. Res. Solid Earth 112, 1–12. doi:10.1029/2006JB004748

Imber, J., Holdsworth, R.E., Butler, C.A., 2001. A reappraisal of the Sibson-Scholz fault zone model: The nature of the frictional to viscous ("brittle-ductile") transition along a long-lived, crustal-scale fault, Outer Hebrides, Scotland. Tectonics 20, 601–624.

Irwin, W.P., Barnes, I., 1975. Effect of geologic structure and metamorphic fluids on seismic behavior of the San Andreas fault system in central and northern California. Geology 3, 713–716. doi:10.1130/0091-7613(1975)3<713:EOGSAM>2.0.CO;2

Joy, D. C., 1984. Beam interactions, contrast and resolution in the SEM. J. Microsc. 136: 241–258. doi:10.1111/j.1365-2818.1984.tb00532.x

Lockner, D.A., Morrow, C., Moore, D., Hickman, S., 2011. Low strength of deep San Andreas fault gouge from SAFOD core. Nature 472, 82–85. doi:10.1038/nature09927

Marone, C., 1998. Laboratory-Derived Friction Laws and Their Application To Seismic Faulting. Annu. Rev. Earth Planet. Sci. 26, 643–696. doi:10.1146/annurev.earth.26.1.643

McCaig, A.M., 1988. Deep fluid circulation in fault zones. Geology 16, 867–870. doi:10.1130/0091-7613(1988)016<0867:DFCIFZ>2.3.CO;2

Moore, D., Lockner, D.A., 2007. Friction of the smectite clay montmorillonite: A review and interpretation of data, in: Dixon, T.H., Moore, C. (Eds.), The Seismogenic Zone of Subduction Thrust Faults, Margins Theor. Exp. Earth Sci. Ser., Vol 2. Columbia Univ. Press, New York, pp. 317–345.

Moore, D.E., Lockner, D.A., 2004. Crystallographic controls on the frictional behavior of dry and water-saturated sheet structure minerals. J. Geophys. Res. 109, 1–16. doi:10.1029/2003JB002582

Morrow, C. a, Moore, D.E., Lockner, D. a, 2000. The effect of mineral bond strength and absorved water on fault gouge frictional strength. Geophys. Res. Lett. 27, 815–818.

Nagata, H., Shimoda, S., Sudo, T., 1974. On dehydration of bound water of sepiolite. Clays Clay Miner. 22 (285), 293.

Nieto F, Jiménez Millán J, Gambogi G, Chiarini-García H, Correa Netto R (2010). Electron microscopy: SEM/ TEM. In: Physics in Medicine and Biology. Splinter R (ed.), CRC Press, Boca Raton. Ch. 40, 1-16.

Nieto, F., Mata, M.P., Bauluz, B., Giorgetti, G., Arkai, P., Peacor, D.R., 2005. Retrograde diagenesis, a widespread process on a regional scale. Clay Miner. 40, 93–104. doi:10.1180/0009855054010158

Nieto, F., Ortega-Huertas, M., Peacor, D.R., Arostegui, J., 1996. Evolution of illite/smectite from early diagenesis through incipient metamorphism in sediments of the Basque-Cantabrian Basin. Clays Clay Miner. 44, 304–323. doi:10.1346/CCMN.1996.0440302

Paquet, H., Duplay, J., Valleron-Blanc, M.M., and Millot, G., 1987. Octahedral compositions of individual particles in smectite-palygorskite and smectite-sepiolite assemblages. Pp. 73_77 in: Proceedings of the International Clay Conference. Denver, 1985 (L.G. Schultz, H. Van Olphen, and F.A. Mumpton, editors). The Clay Minerals Society, Bloomington, Indiana, USA.

Post, J.E., Bish, D.L., Heaney, P.J., 2007. Synchrotron powder X-ray diffraction study of the structure and dehydration behavior of sepiolite. Am. Mineral. 92, 91–97.

Post, J.L., Crawford, S., 2007. Varied forms of palygorskite and sepiolite from different geologic systems. Appl. Clay Sci. 36, 232–244. doi:10.1016/j.clay.2006.10.003

Post, J.E., Heaney, P.J., 2008. Synchrotron powder X-ray diffraction study of the structure and dehydration behavior of palygorskite. Am. Mineral. 93, 667–675.

Reid, H.F., 1910. The California earthquake of April 18, 1906 : report of the State Earthquake Investigation Commission., Vol. 2. ed, CARNEGIE INSTITUTION OF WASHINGTON: Publications 87. Washington, D.C. : Carnegie Institution of Washington, 1910.

Reinen, L.A., Weeks, J.D., Tullis, T.E., 1991. The Frictional Behavior of Serpentinite: Implications for Aseismic Creep On Shallow Crustal Faults. Geophys. Res. Lett. 18, 1921–1924.

Saffer, D.M., Marone, C., 2003. Comparison of smectite- and illite-rich gouge frictional properties: Application to the updip limit of the seismogenic zone along subduction megathrusts. Earth Planet. Sci. Lett. 215, 219–235. doi:10.1016/S0012-821X(03)00424-2

Sakuma, H., Suehara, S., 2015. Interlayer bonding energy of layered minerals: Implication for the relationship with friction coefficient. J. Geophys. Res. Solid Earth 2212–2219. doi:10.1002/2015JB011900

Sanz de Galdeano, C., 1990. Geologic evolution of the Betic Cordilleras in the Western Mediterranean, Miocene to the present. Tectonophysics 172, 107–119. doi:10.1016/0040-1951(90)90062-D

Schleicher, A.M., Hofmann, H., van der Pluijm, B.A., 2013. Constraining clay hydration state and its role in active fault systems. Geochemistry, Geophys. Geosystems 14, 1039–1052. doi:10.1002/ggge.20077

Schleicher, A.M., van der Pluijm, B.A., Warr, L.N., 2012. Chlorite-smectite clay minerals and fault behavior: New evidence from the San Andreas Fault Observatory at Depth (SAFOD) core. Lithosphere 4, 209–220. doi:10.1130/L158.1

Scholz, C.H., 1998. Earthquakes and friction laws. Nature 391, 37–42. doi:10.1038/34097

Shimamoto, T., Logan, J.M., 1981. Effects of simulated clay gouges on the sliding behavior of tennessee sandstone. Tectonophysics 75, 243–255.

Singer, A., 1979. Palygorskite in sediments: Detrital, diagenetic or neoformed - A critical review. Geol. Rundschau 68, 996–1008. doi:10.1007/BF02274683

Solum, J.G., van der Pluijm, B. a., Peacor, D.R., Warr, L.N., 2003. Influence of phyllosilicate mineral assemblages, fabrics, and fluids on the behavior of the Punchbowl fault, southern California. J. Geophys. Res. Solid Earth 108, 1–12. doi:10.1029/2002JB001858

Suárez, M., García-Romero, E., 2011. Advances in the crystal chemistry of sepiolite and palygorskite, Developments in Clay Science. doi:10.1016/B978-0-444-53607-5.00002-5

Velde, B., 1995. Origins and mineralogy of clays: clays and the environment.

Vidal, O., Dubacq, B., 2009. Thermodynamic modelling of clay dehydration, stability and compositional evolution with temperature, pressure and H2O activity. Geochim. Cosmochim. Acta 73, 6544–6564. doi:10.1016/j.gca.2009.07.035

Vidal, O., Dubacq, B., 2010. Water release and rock volume change associated with smectite dehydration in the < 30 km depth seismcity of subduction zones. American Geophysical Union, Fall Meeting 2010, abstract #V31D-07

Viti, C., 2011. Exploring fault rocks at the nanoscale. J. Struct. Geol. 33, 1715–1727. doi:10.1016/j.jsg.2011.10.005

Vrolijk, P., Van Der Pluijm, B. a., 1999. Clay gouge. J. Struct. Geol. 21, 1039–1048. doi:10.1016/S0191-8141(99)00103-0

Wang, C.-Y., 1984. On the constitution of the San Andreas Fault Zone in central California. J. Geophys. Res. Solid Earth 89, 5858–5866. doi:10.1029/JB089iB07p05858

Wintsch, R.P., Christoffersen, R., Kronenberg, a. K., 1995. Fluid-rock reaction weakening of fault zones. J. Geophys. Res. 100, 13021. doi:10.1029/94JB02622

# Chapter 2 Mineral and geochemical characterisation of fault gouges

**Highlights:**

- A concentration of fibrous clay minerals was identified in highly deformed areas of the Galera Fault Zone, an active fault within the Betic Cordillera of southern Spain.
- Authigenesis of fibrous clay minerals implies an open chemical system in which the fault acts as a conduit to bring in Mg-rich fluids.
- Variations in the fluid-rock interaction ratio can cause heterogeneities in the mineralogy of the fault gouge. The mineral properties of the new associations have implications for fault zone strength and their potential for earthquake nucleation.

# Fibrous clay mineral authigenesis induced by fluid-rock interaction in the Galera Fault Zone (Betic Cordillera, SE Spain) and its influence on fault gouge frictional properties

CATALINA SÁNCHEZ-ROA (1), JUAN JIMÉNEZ-MILLÁN (1), ISABEL ABAD (1), DANIEL R. FAULKNER (3), FERNANDO NIETO (2), FRANCISCO J. GARCÍA-TORTOSA (1).

(1) Departamento de Geología y CEACTierra, Unidad Asociada IACT (CSIC-UGR), Universidad de Jaén, Campus Las Lagunillas s/n 23071, Jaén, España.

(2) Departamento de Mineralogía y Petrología e IACT (CSIC-UGR), Facultad de Ciencias, Universidad de Granada, Avda. Fuentenueva s/n 18002, Granada, España.

(3) Rock Deformation Laboratory, Department of Earth, Ocean and Ecological Sciences, University of Liverpool, Liverpool, UK.

**This article has been published in *Applied Clay Science*, 2016**
**Volume 134, Pages 275–288**
**DOI: http://dx.doi.org/10.1016/j.clay.2016.06.023**
**Received: 30 March 2016; Accepted: 25 June 2016; Available online: 15 July 2016.**

## Abstract

This study presents a mineralogical and mechanical analysis of the clay-rich materials and structures identified in the Galera Fault Zone, southern Spain that formed as a consequence of active deformation processes affecting this seismically active region. Significant differences in clay mineral assemblages and chemical composition were identified in rocks from the Galera Fault Zone, through a series of analytical techniques including XRD, SEM, TEM and XRF. Three distinct mineral assemblages were identified: 1) wall-rock assemblages including white marls and dark lutite layers, with the latter also found in injection features. Their assemblage includes dolomite, gypsum, quartz, calcite and phyllosilicates 2) smectite- and palygorskite-rich fault gouges formed on materials from the upper part of the stratigraphic sequence at the NE area of the fault (Galera Village), and 3) sepiolite-rich gouges in areas of the lower part of the stratigraphic sequence at the central SW segment of the fault (Rambla de los Pilares). Fibrous clay-rich gouges were formed by hydrothermal alteration during periods of fluid-rock interaction that was concentrated in fault planes and fractures. Their mineralogy is dominated by authigenic Mg-rich fibrous clay minerals; sepiolite, precipitated directly from an Mg-rich fluid; and palygorskite as the product of the interaction of the fluid with the Al-rich host rock. Experimental data from frictional sliding experiments on these clay-rich fault gouges reveal strong differences in their mechanical properties. Towards the north-eastern areas of the fault, the smectite- and palygorskite-rich gouge has a low friction coefficient (0.17 wet and 0.59 under vacuum) and its values of the friction stability parameter (a-b) are always positive indicating a stable regime that could be related with creeping and stable-sliding processes. In the central-south-western segment, however, the gouge is rich in authigenic sepiolite and presents complete absence of smectite. The higher friction coefficient (0.47 wet and 0.68 under vacuum) and negative values of a-b for this gouge suggest a more neutral to unstable regime that could favour earthquake nucleation.

# 1. Introduction

Detailed studies of fault-zone clay minerals and deformation-induced structures in upper crustal areas are key to understanding the mechanical behaviour of fault zones and deformation processes in a seismically active region. Brittle (localised) deformation of rocks in these areas can produce enrichment of clay minerals (e.g. illite, chlorite, smectite, and interstratifications of these clay minerals) as the result of low-temperature fluid-rock interactions (Evans and Chester, 1995; Solum et al., 2003; Moore and Rymer, 2007). Less frequently but still significant, fibrous clay minerals are constituents of shallow crustal faults, associated with the alteration of ultra-basic rocks (Galán and Castillo, 1984; Gibbs et al., 1993; Suárez and García-Romero, 2011; Yalcin et al., 2004; García-Romero et al., 2006; Haines and van der Plujim, 2012; Morton et al., 2012). The formation of sepiolite and palygorskite, two Mg-rich fibrous clay minerals, has also been described as a product of hydrothermal systems related to highly saline Mg-rich fluids as the result of alteration of Mg-rich minerals (Bach et al., 2002; Arranz et al., 2008). Furthermore, in tectonically active systems, the formation of fibrous clay minerals has been related to a mineralisation mechanism involving Mg-rich hydrothermal fluids and active faulting (García-Romero et al., 2006).

The concentration of neoformed clay minerals localised in fault gouges plays a significant role in fault dynamics, creates characteristic deformation microstructures and is often associated with stable creeping processes and aseismic slip (Rutter et al., 1986; Moore et al., 2010). Fault gouges play a significant role in the nucleation and rupture propagation of earthquakes (Sibson, 1977). Therefore testing their mechanical properties can give as a better insight into their implications for fault stability. Even though several studies on the frictional strength of clay minerals exist (e.g. Moore and Lockner, 2004; Numelin et al., 2007; Behnsen and Faulkner, 2012), few have addressed the influence of minerals with a fibrous-like structure, such as chrysotile in the mechanical behaviour of fault gouges (Moore et al., 1996) and none have yet considered the fibrous clay mineral group sepiolite-palygorskite. In frictional experiments, phyllosilicates commonly exhibit weak frictional behaviour (Shimamoto and Logan, 1981; Moore and Lockner, 2004). Friction coefficients ($\mu$) for phyllosilicates are mostly in the range of 0.2–0.5 (Moore and Lockner, 2004; Numelin et al., 2007; Behnsen and Faulkner, 2012). The presence of fault gouge materials with $\mu<0.6$ has been suggested as a potential mechanism for fault-zone weakening in the middle to upper crust (Imber et al., 2001; Moore and Lockner, 2004; Morrow et al., 2000). The evaluation and analysis of frictional properties of fault gouges could significantly improve earthquake hazard evaluation in active faults (e.g. Niemeijer and Vissers, 2014).

This study compiles a detailed analysis of the clay-rich materials and structures identified in the Galera Fault Zone that formed as a consequence of active deformation processes affecting the Guadix-Baza Basin (García-Tortosa et al., 2008; 2011). Experimental data from frictional sliding experiments on clay-rich fault gouges from the Galera Fault Zone could explain the development of instabilities on the fault plane that led to the nucleation of seismic events such as the 1964 earthquake that affected the village of Galera (García-Tortosa et al., 2011) and earlier events that could have been the trigger of liquefaction structures such as Pleistocene seismites previously described in the area (Gibert et al., 2005;

Alfaro et al., 2010).

This study also highlights the clay mineralogy of the area as a valuable tool in identifying geological processes leading to the authigenesis of fibrous clay minerals in the fault zone and its influence on the mechanical stability of the fault. A variety of analytical and experimental techniques, including X-ray diffraction (XRD), electron microscopy; scanning electron microscopy (SEM) and transmission electron microscopy (TEM), chemical analysis; X-ray fluorescence (XRF) and inductively coupled plasma-mass spectrometer (ICP-MS), and friction experiments, are used to establish the origin of the mineral assemblages, and their relation to the development of deformation structures and seismic events in the Galera Fault.

## 2. Geological Setting and Materials

### 2.1 Geological context

The study area is located in the Guadix-Baza Basin, the largest of the Neogene intramontane basins in the eastern Betic Cordillera (SE Spain) (Fig. 2.1a). The basin was isolated from the other Betic basins in the Late Miocene (Vera, 1970; Vera et al., 1994). The non-marine sedimentary characteristics of the Guadix-Baza Basin show two domains: The Guadix sub-basin towards the SW, filled with alluvium and lake sediments, and the Baza sub-basin towards the NE which accumulated lake sediments (Viseras, 1991; Vera et al., 1994).

The Plio-Pleistocene deposits from the Baza sub-basin exhibit three concentric lithologies: the internal area, dominated by gypsum; the intermediate area mainly composed of dark lutites, carbonatic layers, frequent layers of gypsum and the presence of native sulphur; and the marginal area composed by marls with localised gypsum deposits. The internal and intermediate areas are defined as the Benamaurel Gypsum Unit. The marginal area is named the Galera Gypsum Unit and is interpreted as a mosaic of shallow lakes surrounding a central salt lake (Gibert et al., 2007).

From the Late Miocene until the present, the basin has been subject to N–S to NNW–SSE compression, combined with an orthogonal extension (García-Tortosa et al., 2011). In this regional stress field, the Guadix-Baza Basin sedimentary coverage and basement are affected by extension and compression structures, including normal faults with a NNW–SSE to N–S strike such as the Baza, Zamborino and Graena Faults, and the strike-slip Galera Fault (Fig. 2.1).

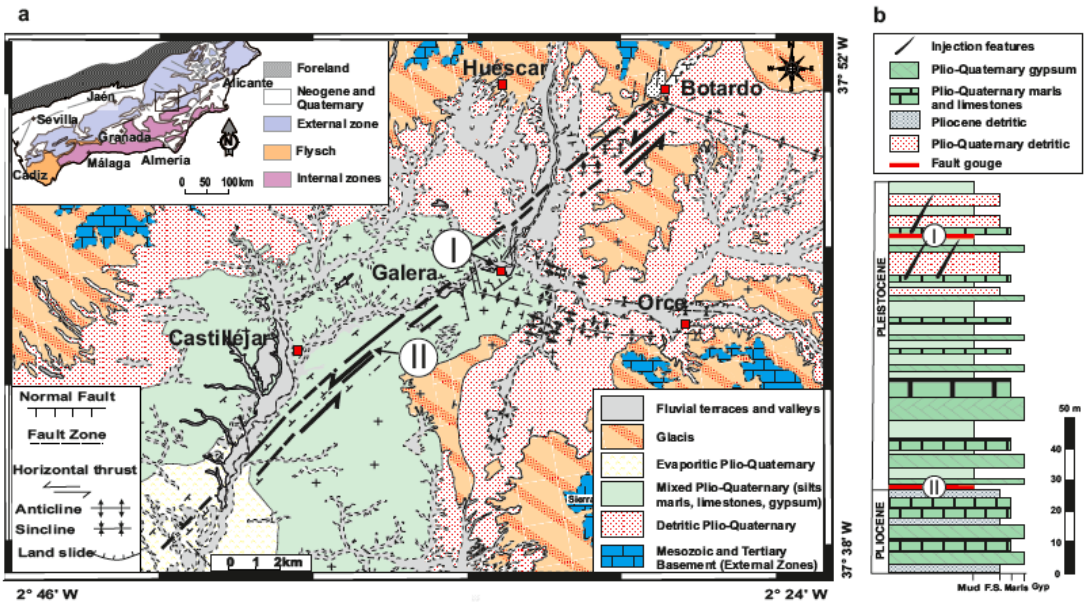


**Figure 2.1**. a. Location of the Galera Fault and geological map of the area of study in the Betic Cordilleras, modified from García-Tortosa et al. (2010). I: Sampling site by the Galera Village. II: Sampling site Rambla de los Pilares. b. Schematic profile illustrating the stratigraphic position of sampling points.

The Galera and Baza Faults are associated with seismic activity, consisting of recent earthquakes with a magnitude below 4.7, and including swarms of lower magnitudes such as the recent event on 16 February 2004 in Benamaurel when six earthquakes were registered with magnitudes from 1.0 to 1.3 (Alfaro et al., 2008; García-Tortosa et al., 2011).

The materials studied were collected from the Galera Fault, a 23-km-long strike-slip fault zone (N50°E), associated with a NE–SW elongated asymmetric anticline. The fault zone consists of a 1.5 km wide zone of deformation with several parallel splays dipping north-westwards between 40° and 60°, although local vertical dips have also been observed (Fig. 2.1a).

## 2.2 Study materials

Samples were collected from two outcrops of the Galera Fault: 1. Galera Village, located in a stratigraphically shallower section; and 2. Rambla de los Pilares, topographically and stratigraphically lower than the first outcrop (Fig. 2.1b). The systematic sampling involved a cross section perpendicular to the fault plane to obtain samples from the northern and southern blocks as well as the fault gouge from the fault core (Fig. 2.2).

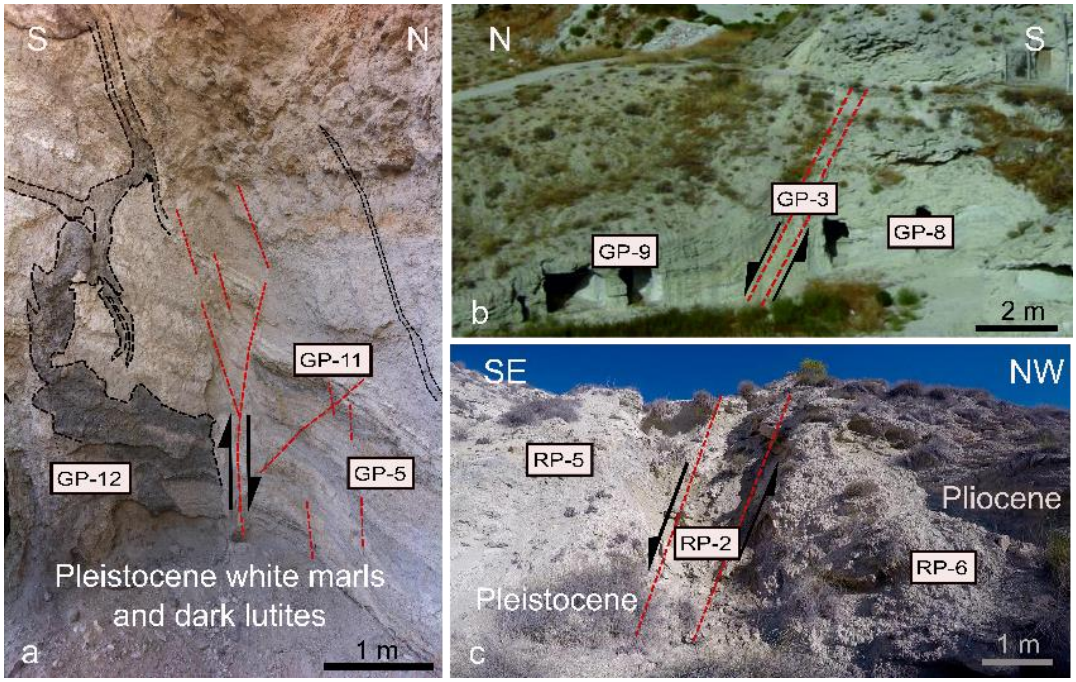


**Figure 2.2.** Photographs of sampling areas along the Galera Fault. a. Injection features crosscutting the Galera Gypsum Unit. b. Galera Village outcrop, sampling site I: Smectite- and palygorskite-rich shear zone affecting an alternation of Pleistocene white marls and dark lutites from the Galera Gypsum Unit. c. Rambla de los Pilares outcrop, sampling site II: Sepiolite-rich shear zone, the fault puts in contact Pleistocene white marls and dark lutites with Pliocene detritic rocks. The dashed red lines mark the limits of the compacted and foliated clay-rich fault gouge.

### 2.2.1 Sampling site I: Galera Village

This outcrop (Lat: 37.7377, Long: -2.5519, Alt: 900 m.a.s.l.), by the village of Galera, shows a main fault plane (N55°E/85°NW) associated with an asymmetric fold and a series of parallel fault planes accommodating minor extension (Fig. 2.2b). The stratigraphic column of the area is mainly composed of alternations of white marls and dark carbonatic lutites with a low degree of lithification and visible porosity, as well as silts, fine sands and gypsum. These sediments have been defined as part of the marginal area of the Baza Basin and denoted as the Galera Gypsum Unit by Gibert et al. (2007). However, the abundant gypsum strata in this sequence suggest a high evaporitic content, therefore in this work they are considered as part of the intermediate areas (Fig. 2.1b). Clay-rich mineral gouges were recognised associated with the fault structures. The fault gouge contains slickenside surfaces with striae with a pitch of 15° SW, and a thickness varying between 5 and 35 cm.

A series of grey structures crosscutting the stratification were identified in proximity to fault planes. The structures have a detritic filling, similar that described for the dark carbonatic lutites (Fig. 2.2a). The thickness of these injection features ranges from 5 to 30 cm. However, these materials are also found in irregularly shaped bodies close to the fault core and their thickness is very variable.

### 2.2.2 Sampling site II: Rambla de los Pilares

The Rambla de los Pilares area (Lat: 37.7205, Long: -2.6068, Alt: 800 m.a.s.l.) is located 5.5 km SE from Galera (Fig. 2.2c). One of the main geological features of the area is the presence of seismites, sedimentary deformation structures produced by liquefaction previously described by Alfaro et al. (2010). The occurrence of seismites towards the village of Galera is very scarce, contrasting with the high seismite population density in the Rambla de los Pilares area. The lithology of the wall rocks is very similar to sampling site I. The local stratigraphy is mainly formed of alternations of dark carbonatic lutites, gypsiferous sandstones, massive gypsum and white marls with varying proportions of clay minerals (Fig. 2.1b). These sediments are part of the intermediate areas of the Baza Basin described as defined by Gibert et al. (2007).

Samples were collected on one of the Galera Fault splays, showing a contact between Pleistocene sediments (carbonatic lutites, marls and silts) and Pliocene sediments (more cemented carbonatic lutites, massive gypsum, gypsiferous sandstones and marls) (Fig. 2.2c). In this locality, a 1-meter thick fault gouge layer containing fibrous clay minerals defines the fault zone. This deposit mainly consists of a green-grey concentration of clay minerals that show a fibrous fabric in hand specimen.

## 3. Methods

### 3.1 X-ray diffraction

X-ray diffraction (XRD) data were obtained from oriented aggregates from the whole sample and from the <2μm fraction, after washing with pure and ultrapure water to remove salts. Oriented aggregates were prepared by settling a dispersion in a glass holder. The <2μm fraction was separated by centrifugation. Ethylene glycol treatment was carried out to assist in the identification of expandable minerals (smectite, interstratified layers, etc.).

The diffractograms were obtained in a PANalytical X'Pert Pro diffractometer (CuKα radiation, 45 kV, 40 mA) equipped with an X'Celerator solid-state linear detector, using a step increment of 0.008° 2θ and a counting time of 10 s/step (Department of Mineralogy and Petrology, University of Granada). A sweep between 3º and 62º 2θ was made on the dry samples, while for the glycolated samples the sweep was done between 2º and 30º 2θ in order to confirm the identification of expandable minerals.

### 3.2 Electron microscopy

Textural and chemical observations in a scanning electron microscope (SEM) were made on polished thin sections using back-scattered electrons (BSE) in atomic number contrast mode, and on rock fragments in secondary electron mode (SE). The SEM study was carried out with a Merlin Carl Zeiss in the Centro de Instrumentación Científico-Técnica of the Universidad de Jaén (Spain).

For the textural and chemical characterisation at the nanometre scale, one sample of each

different mineral association defined by XRD analysis and SEM observations were prepared for transmission electron microscopy (TEM) study. Samples were prepared by dispersing finely ground sample particles, in alcohol or distilled water. The finest particles in the suspension were caught using Au and Cu grids coated with a perforated formvar resin. Additionally, very small amounts of the samples were impregnated in resin for later cutting with an ultramicrotome. The sections were then fixed on a Au or Cu grid for TEM analysis.

The TEM data were obtained using two electron microscopes at the Centro de Instrumentación Científica (C.I.C.) of the Universidad de Granada: the HAADF (high-angle annular dark field) FEI TITAN G2 microscope, operated at 300 kV, and the Philips CM20 (STEM) microscope, operated at 200 kV. Quantitative analyses (AEM) of particles were obtained in STEM mode with an EDAX microanalysis system in the Philips CM20. The monomineralic character of each grain is shown by its electron diffraction pattern that shows the existence of a single crystalline phase. The counting time used was 100 seconds except for Na and K, which were analysed for 15 seconds to try to minimise alkali-loss problems as short counting times improve reproducibility for K and Na (Nieto et al. 1996).

### 3.3 Chemical analysis and mass-balance calculations

The whole-rock analysis of major elements in the samples selected was carried out using X-ray fluorescence (XRF) and trace elements were analysed using an inductively coupled plasma-mass spectrometer (ICP-MS) at Activation Laboratories (Ontario, Canada).

Geochemical analyses of fault-related rocks allowed us to compare the relative concentration of constituents within the fault zone and their respective wall rock. The open system behaviour of most fault zones with respect to fluids requires a baseline to be established to convert variations in chemical composition into units of mass transfer (Gresens, 1967).

Based on the evidence of mineral changes related to fault activity, the Rambla de los Pilares area was selected to carry out a mass-balance calculation in order to understand the chemical and mineralogical reactions that occur during fault-zone development. Six samples of white marls from the stratigraphic column of this sampling area were selected as representative of wall rocks. Dark carbonatic lutites were not included in the calculation given that no evidence of chemical or mineral changes in these rocks caused by fault activity was found. Moreover, the chemical composition of four representative fault gouge samples from this area was determined. Whole-rock composition of the wall rock and fault rocks was calculated by averaging six intact white marls and four fault gouge compositions respectively (Table 2.1). The related $1\sigma$ standard deviation shows that wall rock and fault rocks are homogeneous in this area. The balance of element transport between fault rock and associated bulk wall rock was assessed using isocon graphs constructed according to the Gresens' equation (Gresens, 1967; Grant, 1986) using EASYGRESGRANT (López-Moro, 2012).

Grant (1986) modified the equations given by Gresens (1967) to develop the isocon method to calculate absolute and relative mass or volume changes associated with alteration or

mineralogical reaction. This method requires selection of immobile elements to define an isocon with which to compare mass gain or loss of elements. In an isocon diagram, immobile elements should be dispersed along a straight line passing through zero. The calculation usually uses high field strength elements (HFSE), such as Ti, P or Zr (see e.g. Schleicher et al., 2009; Duan et al., 2016), which are considered as immobile during geochemical alteration processes. In the case of faults in sedimentary sequences, Al is generally considered as an immobile element (e.g. Gratier et al., 2013; Trincal et al., 2014; Lacroix et al., 2015; Durand et al., 2015). In this study, the correlations between both $TiO_2$ and $Al_2O_3$ with the other elements in the rocks were compared to determine their mobility. Results of the statistical procedure show that $TiO_2$ and $Al_2O_3$ are positively correlated ($R^2$=0.9) to each other and negatively correlated to $SiO_2$, As or loss on ignition (L.O.I.) ($R^2$=0.7), thus both $TiO_2$ and $Al_2O_3$ can be regarded as a reliable proxy and were used to determine the isocon line.

**Table 2.1.** Bulk chemical compositions of representative samples and results of the mass balance calculations between the mean of the wall-rock marls and the mean of the fault gouges from the Rambla de los Pilares sampling site in the Galera Fault Zone.

| | Wall rocks | | | | | | Fault gouges | | | | | | | | |
|---|---|---|---|---|---|---|---|---|---|---|---|---|---|---|---|
| Major elements wt% | 080614_1 | 080614_3 | 080614_5 | 080614_6 | Mean | 1σ | 080614_12 | 080614_13 | 080614_16 | 080614_17 | 080614_18 | 080614_20 | Mean | 1σ | G/L |
| $SiO_2$ | 13.01 | 13.05 | 12.77 | 12.98 | 12.95 | 0.12 | 15.05 | 13.50 | 15.01 | 14.20 | 15.05 | 15.62 | 14.74 | 0.76 | 0.14 |
| $TiO_2$ | 0.53 | 0.59 | 0.55 | 0.57 | 0.56 | 0.02 | 0.45 | 0.49 | 0.46 | 0.48 | 0.46 | 0.48 | 0.47 | 0.02 | -1.42 |
| $Al_2O_3$ | 9.17 | 10.13 | 9.46 | 9.84 | 9.65 | 0.42 | 7.80 | 8.62 | 7.96 | 8.46 | 8.05 | 8.37 | 8.21 | 0.32 | -2.35 |
| $Fe_2O_3$ | 5.95 | 6.57 | 6.13 | 6.39 | 6.26 | 0.28 | 4.09 | 4.53 | 4.18 | 4.44 | 4.22 | 4.40 | 4.31 | 0.17 | -2.42 |
| MnO | 0.11 | 0.12 | 0.11 | 0.11 | 0.11 | 0.00 | 0.46 | 0.50 | 0.47 | 0.49 | 0.47 | 0.49 | 0.48 | 0.02 | -0.69 |
| MgO | 5.51 | 6.20 | 6.72 | 5.99 | 6.10 | 0.50 | 13.91 | 14.37 | 13.70 | 14.58 | 14.35 | 12.93 | 13.97 | 0.60 | 6.32 |
| CaO | 26.49 | 29.28 | 27.33 | 28.45 | 27.89 | 1.23 | 19.04 | 21.04 | 19.44 | 20.64 | 19.64 | 20.44 | 20.04 | 0.78 | -10.07 |
| $Na_2O$ | 4.37 | 4.83 | 4.51 | 4.69 | 4.60 | 0.20 | 5.51 | 6.09 | 5.63 | 5.97 | 5.68 | 5.92 | 5.80 | 0.23 | 0.56 |
| K2O | 2.59 | 2.86 | 2.67 | 2.78 | 2.73 | 0.12 | 1.09 | 1.20 | 1.11 | 1.18 | 1.12 | 1.17 | 1.14 | 0.04 | -1.71 |
| $P_2O_5$ | 0.80 | 0.88 | 0.82 | 0.86 | 0.84 | 0.04 | 0.34 | 0.38 | 0.35 | 0.37 | 0.35 | 0.37 | 0.36 | 0.01 | -0.52 |
| LOI | 31.71 | 24.91 | 29.32 | 27.10 | 28.26 | 2.92 | 32.24 | 29.02 | 32.01 | 29.50 | 30.70 | 30.45 | 30.65 | 1.30 | 2.39 |
| Density | 2.72 | 2.73 | 2.71 | 2.65 | 2.70 | 0.04 | 2.43 | 2.38 | 2.41 | 2.35 | 2.47 | 2.37 | 2.40 | 0.04 | |
| Minor elements ppm | | | | | | | | | | | | | | | |
| As | 6.6 | 5.9 | 6.4 | 5.8 | 6.2 | 0.38 | 11.8 | 10.8 | 11.6 | 11.0 | 12.1 | 12.0 | 11.6 | 0.54 | 4.11 |
| Rb | 22.8 | 25.2 | 23.5 | 24.5 | 24.0 | 1.06 | 6.5 | 7.1 | 6.6 | 7.0 | 6.7 | 6.9 | 6.8 | 0.27 | -17.96 |
| Ba | 27.6 | 30.5 | 28.4 | 29.6 | 29.0 | 1.28 | 8.6 | 9.5 | 8.7 | 9.3 | 8.8 | 9.2 | 9.0 | 0.35 | -21.00 |
| Sr | 21.9 | 24.2 | 22.5 | 23.5 | 23.0 | 1.01 | 12.7 | 14.1 | 13.0 | 13.8 | 13.1 | 13.7 | 13.4 | 0.52 | -11.09 |
| Pb | 11.6 | 12.8 | 12.0 | 12.4 | 12.2 | 0.54 | 5.2 | 5.8 | 5.3 | 5.7 | 5.4 | 5.6 | 5.5 | 0.21 | -7.31 |

| | | | | | | | | | | | | | | | |
|---|---|---|---|---|---|---|---|---|---|---|---|---|---|---|---|
| Cr | 26.6 | 29.4 | 27.4 | 28.6 | 28.0 | 1.23 | 5.0 | 5.6 | 5.1 | 5.5 | 5.2 | 5.4 | 5.3 | 0.21 | -23.29 |
| Ni | 20.9 | 23.1 | 21.6 | 22.4 | 22.0 | 0.97 | 5.7 | 6.3 | 5.8 | 6.2 | 5.9 | 6.1 | 6.0 | 0.23 | -16.67 |
| V | 20.9 | 23.1 | 21.6 | 22.4 | 22.0 | 0.97 | 12.4 | 13.7 | 12.6 | 13.4 | 12.7 | 13.3 | 13.0 | 0.51 | -10.44 |
| Sc | 12.7 | 14.1 | 13.1 | 13.7 | 13.4 | 0.59 | 7.8 | 8.6 | 8.0 | 8.4 | 8.0 | 8.4 | 8.2 | 0.32 | -6.11 |
| U | 21.9 | 24.2 | 22.5 | 23.5 | 23.0 | 1.01 | 7.7 | 8.5 | 7.9 | 8.3 | 7.9 | 8.3 | 8.1 | 0.32 | -15.80 |
| Zr | 24.7 | 27.3 | 25.5 | 26.5 | 26.0 | 1.14 | 6.8 | 7.6 | 7.0 | 7.4 | 7.1 | 7.3 | 7.2 | 0.28 | -19.60 |
| Y | 15.5 | 17.1 | 16.0 | 16.6 | 16.3 | 0.72 | 8.6 | 9.5 | 8.7 | 9.3 | 8.8 | 9.2 | 9.0 | 0.35 | -8.30 |
| Nb | 15.9 | 17.5 | 16.4 | 17.0 | 16.7 | 0.73 | 6.8 | 7.6 | 7.0 | 7.4 | 7.1 | 7.3 | 7.2 | 0.28 | -10.30 |
| La | 17.0 | 18.8 | 17.5 | 18.3 | 17.9 | 0.79 | 6.2 | 6.8 | 6.3 | 6.7 | 6.4 | 6.6 | 6.5 | 0.25 | -12.12 |
| Ce | 20.8 | 23.0 | 21.5 | 22.3 | 21.9 | 0.96 | 7.5 | 8.3 | 7.7 | 8.1 | 7.7 | 8.1 | 7.9 | 0.31 | -14.88 |
| Nd | 28.5 | 31.5 | 29.4 | 30.6 | 30.0 | 1.32 | 9.0 | 10.0 | 9.2 | 9.8 | 9.3 | 9.7 | 9.5 | 0.37 | -21.56 |
| Sm | 7.5 | 8.3 | 7.7 | 8.1 | 7.9 | 0.35 | 2.8 | 3.0 | 2.8 | 3.0 | 2.8 | 3.0 | 2.9 | 0.11 | -5.32 |
| Eu | 10.5 | 11.6 | 10.8 | 11.2 | 11.0 | 0.48 | 6.0 | 6.6 | 6.1 | 6.5 | 6.2 | 6.4 | 6.3 | 0.25 | -5.40 |
| Tb | 7.5 | 8.3 | 7.7 | 8.1 | 7.9 | 0.35 | 4.1 | 4.5 | 4.2 | 4.4 | 4.2 | 4.4 | 4.3 | 0.17 | -4.08 |
| Dy | 6.2 | 6.8 | 6.4 | 6.6 | 6.5 | 0.29 | 3.4 | 3.8 | 3.5 | 3.7 | 3.5 | 3.7 | 3.6 | 0.14 | -3.30 |
| Ho | 8.6 | 9.6 | 8.9 | 9.3 | 9.1 | 0.40 | 4.6 | 5.0 | 4.7 | 4.9 | 4.7 | 4.9 | 4.8 | 0.19 | -4.83 |
| Er | 25.7 | 28.4 | 26.5 | 27.5 | 27.0 | 1.19 | 12.1 | 13.3 | 12.3 | 13.1 | 12.4 | 13.0 | 12.7 | 0.50 | -15.71 |
| Yb | 23.8 | 26.3 | 24.5 | 25.5 | 25.0 | 1.10 | 11.2 | 12.4 | 11.4 | 12.2 | 11.6 | 12.0 | 11.8 | 0.46 | -14.51 |
| Lu | 3.4 | 3.8 | 3.5 | 3.7 | 3.6 | 0.16 | 1.8 | 2.0 | 1.8 | 2.0 | 1.9 | 1.9 | 1.9 | 0.07 | -1.91 |
| Be | 14.2 | 12.9 | 13.1 | 13.7 | 13.5 | 0.60 | 19.2 | 18.9 | 19.6 | 17.6 | 19.4 | 18.1 | 18.8 | 0.78 | 3.24 |
| Cu | 15.5 | 17.1 | 16.0 | 16.6 | 16.3 | 0.72 | 7.7 | 8.5 | 7.9 | 8.3 | 7.9 | 8.3 | 8.1 | 0.32 | -9.10 |
| W | 4.0 | 4.4 | 4.1 | 4.3 | 4.2 | 0.18 | 2.2 | 2.4 | 2.2 | 2.4 | 2.3 | 2.3 | 2.3 | 0.09 | -2.16 |

L.O.I.: Loss on ignition. G/L: Gain/Loss expressed in wt% or ppm of the result of the mass balance calculations between the mean of the wall-rock marls and the mean of the fault gouges from the Rambla de los Pilares site in the Galera fault zone.

### 3.4 Frictional strength and stability measurements

Friction tests were carried out on a triaxial deformation apparatus with a servo-controlled axial loading system and fluid pressure system (Mitchell and Faulkner, 2008; Faulkner and Armitage, 2013) in the Rock Deformation Laboratory in the University of Liverpool. The servo-controlled fluid systems control the confining- and pore-fluid pressure to a resolution of 0.01 MPa, while the axial loading system has a resolution better than +/- 0.05 kN. Frictional sliding experiments were conducted on fault gouges using a direct shear sample assembly (similar to that used by Verberne, 2014), which consists of a set of two cylindrical metal pistons 20 mm in diameter and 50 mm in length. The grooved piston face where the sample is placed has dimensions of 30 mm by 20 mm, and includes two sintered disks, which allow the distribution of the pore fluid along the sample layer (Fig. 2.3). The grooves ensure that no decoupling occurs between the sample sliders and gouge layer. Two silicon rubber spacers at the end of each grooved face allow the axial displacement to be accommodated within the assembly by shearing the sample layer. Experiments were performed on crushed and sieved powdered gouges to obtain a grain size < 53 μm, which was made into a paste using deionized water for water-saturated experiments and methanol for vacuum experiments. The layers were then constructed on the sliders using a precision levelling jig to ensure uniform thickness (Smith and Faulkner, 2010). For the vacuum tests, the samples were kept in a vacuum oven at 120°C for 5 hours before placing the powder in the sliders, and introduced in the pressure vessel while warm. The pore-fluid system was then evacuated overnight and kept under a vacuum of 4.2 x $10^{-4}$ mbar during the experiment to prevent water molecules being reabsorbed. Experimental conditions include: initial thickness of the layer = 2 mm; confining pressure (Pc) = 100 MPa; pore pressure (Pp) = 5 MPa; effective normal pressure ($\sigma n_{eff}$) = 95 MPa. These conditions simulate pressure conditions equivalent to 4.3 km depth calculated using a lithostatic gradient of 23 MPa/km, which is commensurate with the depth of earthquakes in the area, estimated between 1 and 10 km (according to data from the Seismological Network of the Instituto Geografico Nacional of Spain).

The values of friction coefficient ($\mu$) were determined for each experiment as the ratio of shear stress ($\tau$) to effective normal stress ($\sigma_n$); ($\mu=\tau/\sigma_n$). The "true shear stress" was calculated as a function of the displacement since the initial area of contact increases with displacement. The initial sliding velocity for the 1.5 mm run-in was 0.3 μm/s, a low loading rate to avoid the development of pore-fluid pressure within the layer. After the run-in, sliding velocity steps were imposed every 0.5 mm (0.3-3.0-0.3 μm/s) until a total displacement of 4 mm. The induced stepwise changes in slip velocity were modelled with an iterative numerical fitting of the experimental data (Noda and Shimamoto, 2009), using the ageing law (Dieterich, 1979) and two state variables for the fitting, as well as including the machine stiffness as a variable. The use of two state variables allows for a better approximation to the experimental curve, however, it is worth mentioning that the fitting of the data with one or two state variables does not affect the final values of the stability parameter (a-b). The method uses an inversion technique to find the best fit values for the constitutive parameters, a, $b_1$, $b_2$, $D_{c1}$, $D_{c2}$ (critical distances) and machine stiffness. The value of b for our calculations is taken as the addition of $b_1$ and $b_2$. The parameter (a-b)

describes the stability of the sliding surface differentiating a stable regime, in which the gouge is rate strengthening, meaning that a-b > 0 and earthquakes do not nucleate; and an unstable regime when a-b < 0 and the gouge is rate weakening indicating the potential for earthquake nucleation (Scholz, 1998).

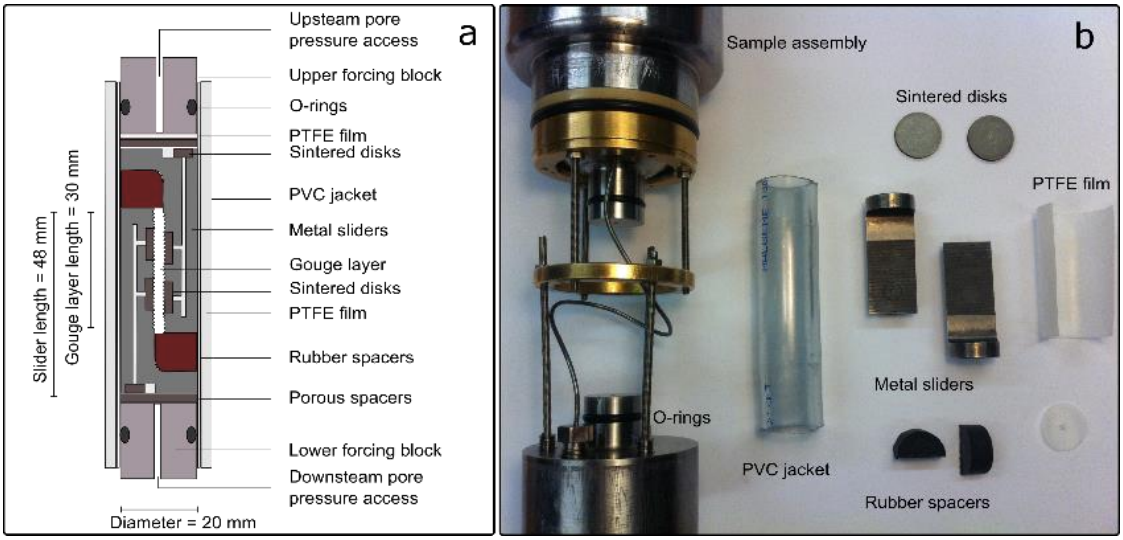


**Figure 2.3.** a. Schematic cross section of the direct shear sample assembly used in friction tests. b. Photograph of the sliders and other elements included in the direct shear sample assembly.

# 4. Results

## 4.1 Characterisation of mineral associations

Different types of mineral assemblages can be established according to the relationship with the deformation structures occurring in the study area: 1. Wall-rock assemblages for both sampling sites include a. white marls and b. dark carbonatic lutite and materials from the injection features, 2. Fault gouge assemblages from a. Galera Village and b. Rambla de los Pilares.

### 4.1.1. Wall-rock and injection features assemblages

#### a. White marls

These layers contain dolomite, gypsum, quartz, calcite and phyllosilicates. XRD studies of oriented aggregates of the <2 μm fraction reveal that the clay assemblage is dominated by K-white mica, smectite and minor amounts of kaolinite. XRD patterns of mica show a narrow (002) reflection at 1.008 nm. The intensity of these reflections changed only very slightly after heating and ethylene glycol solvation, indicating absence of expandable layers. In XRD powder patterns, non-basal reflections (020) and (130) are sharp and symmetric, while the (112) reflection is well developed, indicative of a well-ordered structure of $2M_1$ polytype.

Smectite was detected from its (001) reflection at 1.493 nm spacing expanding to 1.733 nm after ethylene glycol treatment (Fig. 2.4a). From a textural point of view, the micas are mostly present in the coarse size fraction, 60 μm on average, and show occasional bends within the larger crystals. In contrast, the smectite crystals are smaller (<10 μm) and form the matrix of the rock.

Dolomite and gypsum were interpreted by Gibert et al. (2007) as minerals precipitated from lake water with saline chemistry produced in an evaporitic paleoenvironment, in agreement with the depositional model of the Baza Basin as a shallow saline lake system. Both textural and X-ray diffraction data of phyllosilicates obtained in this study indicate a sedimentary origin for these minerals. Bent large crystals of mica with ordered structure and $2M_1$ polytype point to a detrital origin for the micas, whose source area is probably the metamorphic complexes of the inner part of Betic Cordillera in the Sierra Nevada. The presence of a rock matrix made of poorly crystalline smectite suggests that the formation of this mineral was linked to sedimentary processes that occurred in the basin and/or edaphic processes associated to soils developed in the source area. Therefore, these materials are characterised by the absence of authigenic precipitation related to the fault.

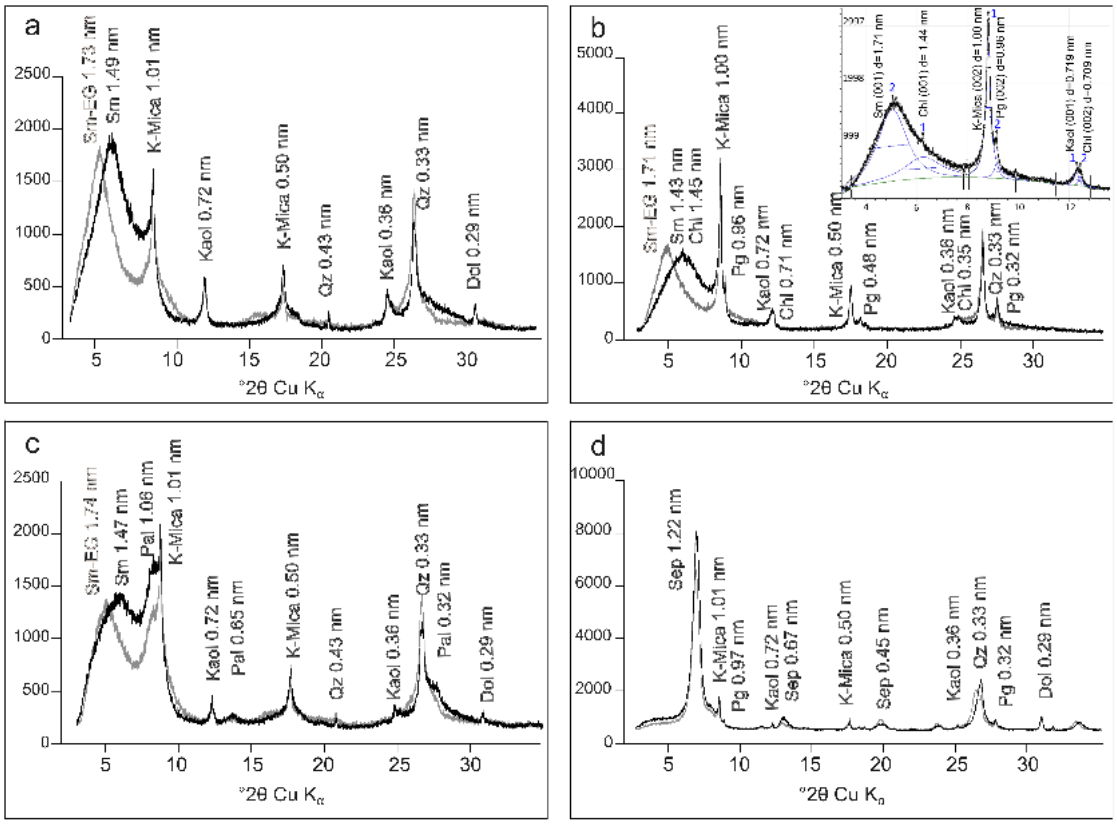


**Figure 2.4.** Representative diffractograms of oriented aggregates of the <2 μm fraction, air-dried (in black) and treated with ethylene glycol (in grey), for: a. White marls from the wall rock. b. Dark lutites and injection features, inset: Decomposition of the X-ray diffraction profile of samples from injection features to differentiate various mineral phases. c. Galera Village fault gouge (sampling point I). d. Rambla de los Pilares fault gouge (sampling point II). Mineral abbreviations for clay minerals according to Bergaya and Lagaly (2006), Kaol: kaolinite, K-Mica: white mica (including illite and muscovite), Sep: sepiolite, Sm: smectite, Pal: palygorskite. Non-clay minerals according to Whitney and Evans (2010), Chl: chlorite, Dol: dolomite, Pg: paragonite, Qz: quartz.

b. Dark lutites and injection features

The materials collected in the dark lutite strata as well as in the injection features have a mineral assemblage that includes smectite, paragonite and chlorite in addition to the minerals common to all rocks in the area: quartz, K-white mica, kaolinite, gypsum, calcite and dolomite (Fig. 2.4b). In order to identify accurately the mineral species present in the sediments, decomposition algorithms were applied to reflections selected from the X-ray diffractogram (Fig. 2.4b inset). The diagram revealed the presence of chlorite, which had been hidden by the (001) reflection of smectite. Paragonite, shaded by the 002 reflection of muscovite, was also recognised with this method. The operation on the reflections at 0.7 nm and 0.35 nm revealed the (001)/(002) reflections of kaolinite as well as the (002)/(004) reflections of chlorite. SEM observations with secondary electrons show high porosity within medium sand-size grains of chlorite and mica. Mica and chlorite crystals form the rock framework and appear as well crystallised grains with irregular pseudo-hexagonal sections and basal dimensions of around 100 μm (Fig. 2.5a and b). Prismatic siliceous grains are also seen in SEM observations, they were identified as fragments of diatoms and are aligned forming bands in samples from the injection features (Fig. 2.5c). TEM observations helped to identify smectite crystals with undulose morphologies and irregular edges as the main component of the matrix of the rock (Fig. 2.5d). The size of the smectite packets is less than 8 μm (Fig. 2.5). The chemical composition of phyllosilicates show phengitic micas with a sum of interlayer cations close to 1 atom per formula unit (a.f.u.) typical of evolved micas together with authigenic illites with a sum of interlayer cations < 0.8 a.f.u. (Table 2.2a). Some of the micas analysed were found to have Na contents up to 0.5 a.f.u. The AEM analyses of smectites from these materials show the existence of beidellite and montmorillonite with some nontronitic component (Table 2.2b).

The similarity of mineralogy and textural disposition between phyllosilicates in the wall rocks and injection features indicates that phyllosilicates in these clastic injections are not the result of clay growth in the fault zone during brittle deformation. The chemical composition of large crystals of mica and chlorite indicates a detrital origin from the metamorphic units in the core of the Betic Cordillera. The morphology and composition of smectite can be associated with the sedimentary processes occurring in the Guadix-Baza Basin. Therefore, the discordant injection features from the Galera Fault are similar to those described as injection clastic dikes formed by clastic material injected into fractures during transient fluid-pressure increases (Jolly and Lonergan, 2002).

**Table 2.2.** Structural formulae calculated from AEM data. Micas (75% of the Fe as $Fe^{3+}$, Guidotti et al., 1994) and smectites (all Fe as $Fe^{3+}$) normalised to $O_{10}(OH)_2$. $^{IV}Al = (4 - Si)$. Palygorskite normalised to $O_{20}(OH)_2$. and sepiolite to $O_{30}(OH)_4$.

a. Micas

| | Si | $Al^{IV}$ | $Al^{VI}$ | Fe | Mg | Ti | ∑ oct. | Ca | K | Na | ∑ inter. |
|---|---|---|---|---|---|---|---|---|---|---|---|
| Dark lutites and injection features | | | | | | | | | | | |
| GP-12- 8 | 3.15 | 0.85 | 1.49 | 0.23 | 0.32 | 0.04 | 2.08 | 0.00 | 0.82 | 0.16 | 0.98 |
| GP-12- 11 | 3.44 | 0.56 | 1.67 | 0.14 | 0.25 | 0.02 | 2.08 | 0.00 | 0.57 | 0.14 | 0.71 |
| GP-12- 12 | 3.18 | 0.82 | 1.65 | 0.13 | 0.29 | 0.02 | 2.08 | 0.00 | 0.45 | 0.49 | 0.94 |
| Galera Village gouge | | | | | | | | | | | |
| GP-3- 11 | 3.45 | 0.55 | 1.37 | 0.24 | 0.38 | 0.02 | 2.02 | 0.00 | 0.68 | 0.00 | 0.68 |
| Rambla de los Pilares gouge | | | | | | | | | | | |
| RP-2- 2 | 3.35 | 0.65 | 1.70 | 0.14 | 0.23 | 0.00 | 2.08 | 0.00 | 0.75 | 0.09 | 0.84 |
| RP-2- 3 | 3.36 | 0.64 | 1.59 | 0.21 | 0.23 | 0.02 | 2.04 | 0.00 | 0.68 | 0.00 | 0.68 |
| RP-2- 4 | 3.15 | 0.85 | 1.68 | 0.24 | 0.16 | 0.02 | 2.10 | 0.00 | 0.86 | 0.15 | 1.01 |
| RP-2- 9 | 3.32 | 0.68 | 1.72 | 0.11 | 0.25 | 0.02 | 2.09 | 0.02 | 0.57 | 0.07 | 0.66 |

b. Smectites

| | Si | $Al^{IV}$ | $Al^{VI}$ | Fe | Mg | Ti | ∑ oct. | Ca | K | Na | ∑ inter. |
|---|---|---|---|---|---|---|---|---|---|---|---|
| Dark lutites and injection features | | | | | | | | | | | |
| GP-12-5K | 3.99 | 0.01 | 1.03 | 0.60 | 0.51 | - | 2.14 | 0.02 | 0.07 | 0.00 | 0.09 |
| GP-12- 1 | 3.96 | 0.04 | 1.06 | 0.49 | 0.66 | - | 2.22 | 0.00 | 0.05 | 0.00 | 0.05 |
| GP-12- 4 | 3.65 | 0.35 | 1.74 | 0.24 | 0.17 | - | 2.15 | 0.00 | 0.07 | 0.00 | 0.07 |
| GP-5-3 | 3.92 | 0.08 | 1.40 | 0.23 | 0.45 | - | 2.08 | 0.00 | 0.30 | 0.00 | 0.30 |
| GP-5-9 | 3.89 | 0.11 | 0.64 | 1.02 | 0.52 | - | 2.17 | 0.00 | 0.10 | 0.00 | 0.10 |
| Galera Village gouge | | | | | | | | | | | |
| GP-3- 5 | 3.72 | 0.28 | 1.27 | 0.28 | 0.59 | - | 2.13 | 0.00 | 0.26 | 0.20 | 0.46 |
| GP-3- 6 | 3.90 | 0.10 | 1.24 | 0.44 | 0.44 | - | 2.12 | 0.03 | 0.12 | 0.00 | 0.15 |
| GP-3-14 | 3.70 | 0.30 | 1.19 | 0.30 | 0.58 | - | 2.07 | 0.00 | 0.30 | 0.30 | 0.60 |

c. Palygorskite

| | Si | $Al^{IV}$ | $Al^{VI}$ | Fe | Mg | Ti | ∑ oct. | Ca | K | Na | ∑ inter. |
|---|---|---|---|---|---|---|---|---|---|---|---|
| Galera Village gouge | | | | | | | | | | | |
| GP-3- 13 | 7.84 | 0.16 | 1.78 | 0.38 | 1.69 | - | 3.85 | 0.14 | - | 0.05 | 0.19 |
| GP-5- 2 | 7.77 | 0.23 | 1.58 | 0.53 | 2.01 | - | 4.12 | - | - | - | 0.00 |

d. Sepiolite

| | Si | $Al^{IV}$ | $Al^{VI}$ | Fe | Mg | Ti | ∑ oct. | Ca | K | Na | ∑ inter. |
|---|---|---|---|---|---|---|---|---|---|---|---|
| Rambla de los Pilares gouge | | | | | | | | | | | |
| RP-1-9K | 11.91 | 0.00 | 0.00 | 0.20 | 7.89 | - | 8.09 | - | - | - | 0.00 |
| RP-1-10K | 12.00 | 0.00 | 0.10 | 0.15 | 7.61 | - | 7.86 | - | - | - | 0.00 |

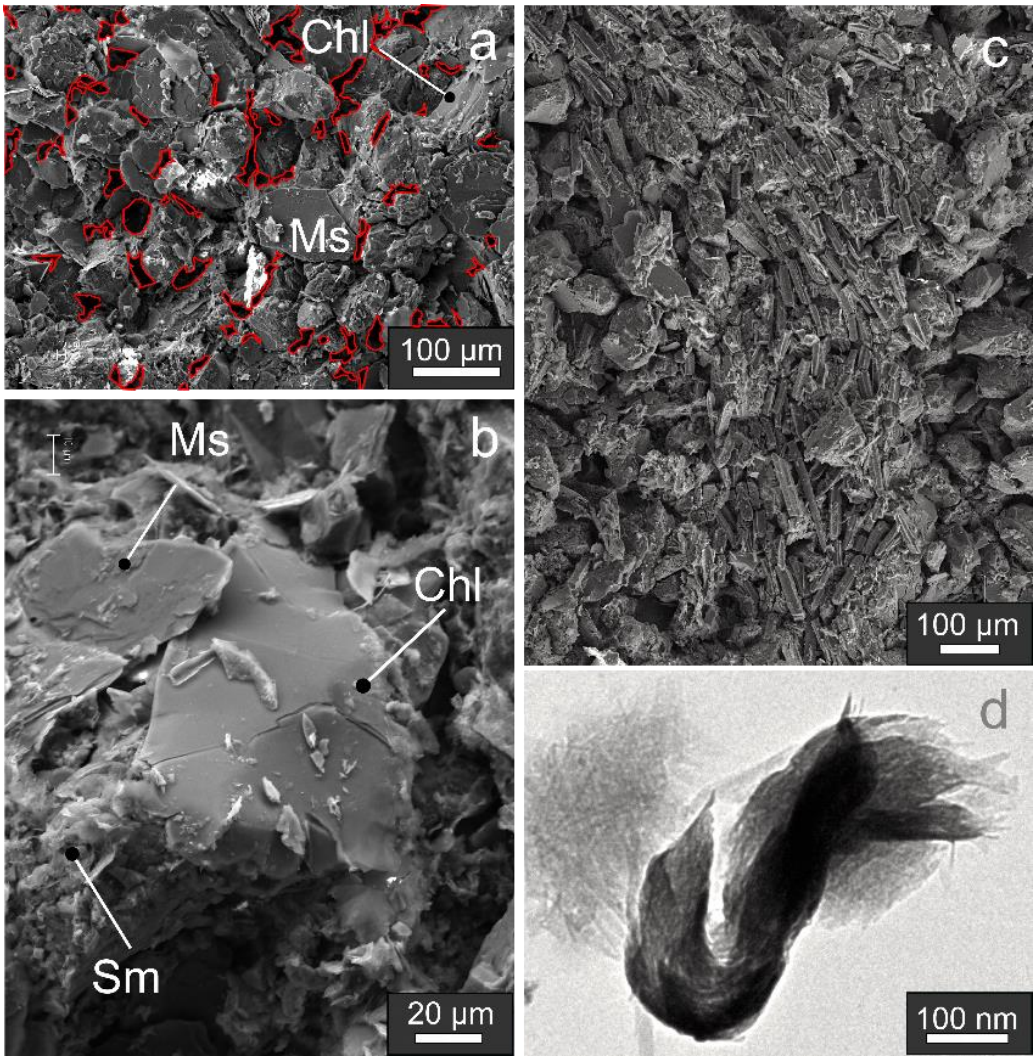


**Figure 2.5**. SE images of the materials in the injection features: a. Porous materials with a sandy texture. Pores are outlined in red. Chl: chlorite, Ms: muscovite b. Detail of the textural relations among phyllosilicates: Chl: chlorite, Ms: muscovite and Sm: smectite. c. Aligned fragments of diatoms. d) TEM image of a curved smectite crystal.

### 4.1.2. Fault gouges

a. Galera Village

A 10 to 30 cm thick layer of clay-rich gouge characterises the principal slip zone in the area. XRD analysis shows smectite and palygorskite as well as K-mica, kaolinite, quartz, gypsum and dolomite (Fig. 2.4c). Smectite was identified after ethylene glycol solvation where the (001) reflection originally at 1.474 nm increased to 1.735 nm. Palygorskite was identified by its typical reflections at 1.056 nm, 0.645 nm and 0.322 nm, which did not vary with ethylene glycol solvation.

In TEM images, palygorskite crystals can be observed as fibres 1 to 3 µm in length and 50 to 100 nm in width. The fibres group and are aligned in a preferential orientation forming bundles, which control the highly compacted fabric of the rock. Other crystals follow the same long-axis orientation pattern, and the clay fraction forms a coating around bigger crystals (Fig. 2.6).

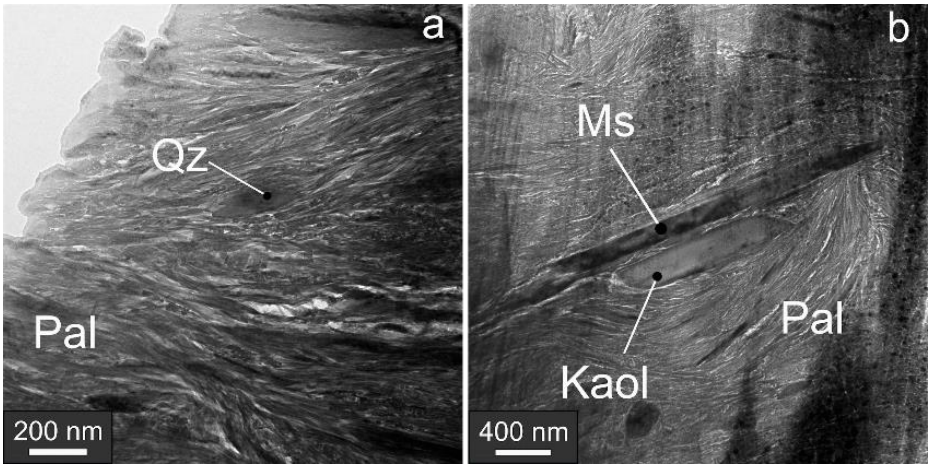


**Figure 2.6.** a. and b. Low-magnification images of fibrous crystals of palygorskite coating larger phyllosilicate crystals with the same orientation. Pal: palygorskite, Ms: muscovite, Kaol: kaolinite, Qz: quartz.

AEM analyses show the palygorskite composition, with significant amounts of Fe and occasionally of Na and Ca (Table 2.2c). This composition is within the range compiled from the literature by García-Romero and Suárez (2010) and, according to these authors, in the polysomatic series between this mineral and sepiolite corresponds to an ideal palygorskite. The presence of small fibres of palygorskite makes this gouge layer compositionally distinct to the wall rocks, suggesting that its formation could be related with deformation or fluid-rock interaction processes occurring in the area. Dioctahedral smectites are Al-dominant (beidellite and montmorillonite) or Fe-dominant (nontronite) (Table 2.2b), chemically similar to smectites in the wall rock. There is no strong chemical evidence to support an authigenic origin for smectite in this gouge.

b. Rambla de los Pilares

XRD analysis of the one metre-thick fault gouge revealed the presence of sepiolite, paragonite, illite/K-Mica, kaolinite, quartz and dolomite in the Rambla de los Pilares sampling area (Fig. 2.4d). Sepiolite was identified by its strong (110) reflection at 1.222 nm that shows no shift after ethylene glycol treatment. The diffraction pattern shows two strong 002 reflections corresponding to illite/K-Mica (d=1.008 nm) and paragonite (d=0.971 nm), respectively. Higher order basal reflections confirm the presence of illite/K-Mica and paragonite as distinct mineral phases. There were no significant changes in the intensity of the mica and chlorite (001) reflections after heating or ethylene glycol solvation, indicating absence of expandable clays.

Sepiolite appears in SEM images as groups of parallel bundles with closed porosity (of up to 150 μm in length and 30 μm in width), forming long and curved aggregates (Fig. 2.7a). The orientation of the fibres defines the linear-planar fabric of these rocks, as observed in BSE images (Fig. 2.7b). In TEM observations of the rock texture, individual crystals of sepiolite are perfectly straight (Fig. 2.7c and d) and sepiolite aggregates also appear in feather-like structures with one main orientation (Fig. 2.7e and f).

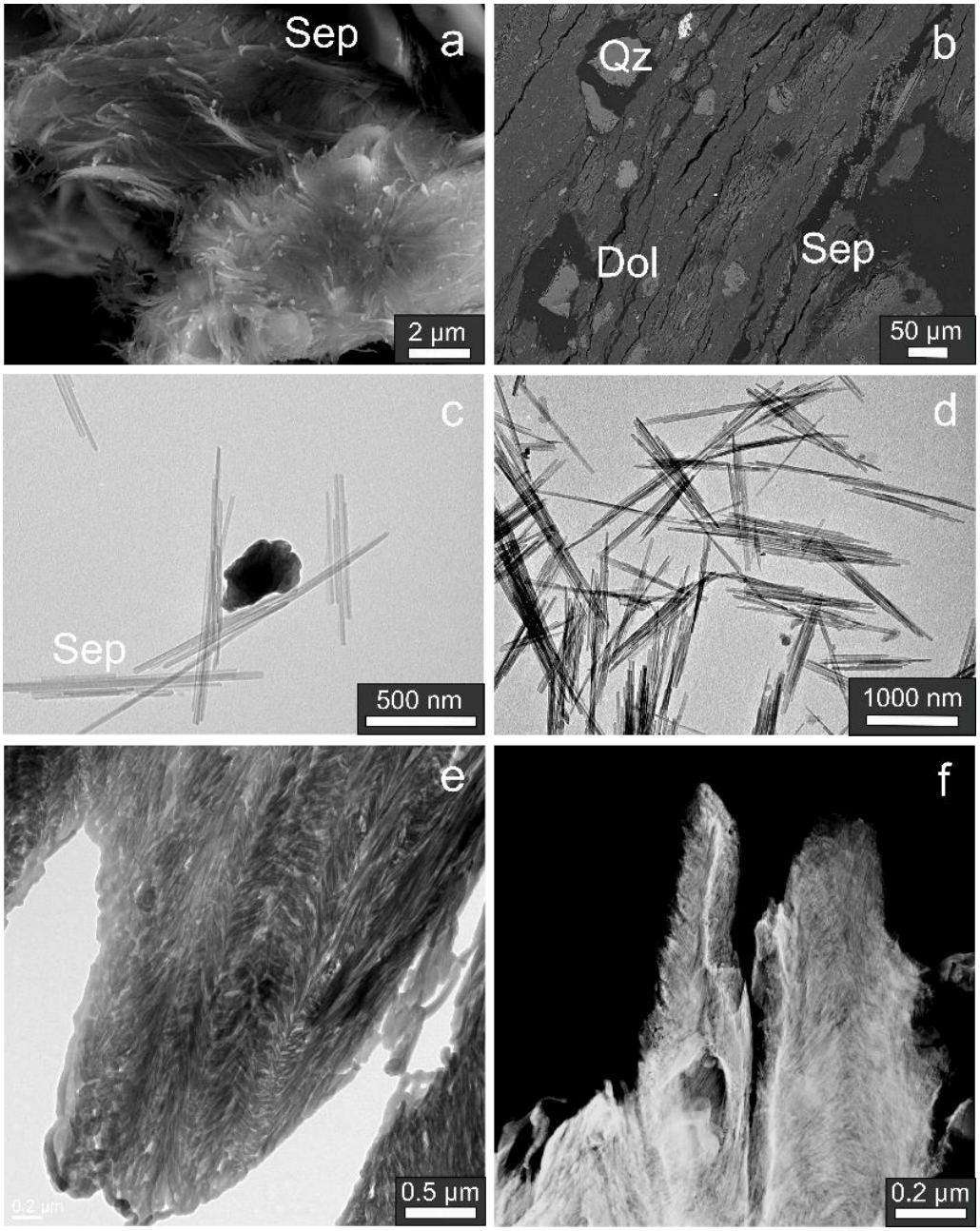


**Figure 2.7.** a. SEM image of secondary electrons from the sepiolite-rich fault gauge; b. BSE image of sepiolite bundles defining the fabric of the rock; c. and d. TEM images of bundles of single sepiolite crystals from the Rambla de los Pilares gouge; e. TEM images showing the feather-like structure of sepiolite; f. HAADF (high angle annular dark field) low-magnification images showing the feather-like structure of sepiolite crystals. Mineral abbreviations according to Whitney and Evans (2010), Dol: dolomite, Qz: quartz. Mineral abbreviations for clay minerals according to Bergaya and Lagaly (2006), Sep: sepiolite.

Chemical analyses of sepiolite crystals (Table 2.2d) show small contents of Fe and Al, while the normalised formula approaches the ideal, being in the field of sepiolite in the polysomatic series defined by Suárez and García-Romero (2013). Analyses of micas show the presence of phengite and illite (Table 2.2a) in both cases with the occasional presence of Na (< 0.20 a.f.u.) and K in the interlayer.

The restricted occurrence of this type of rock in the fault zone, its distinct phyllosilicate association and the presence of sepiolite as micrometric crystals indicate that sepiolite is an

authigenic phase. This gouge has shear indicators (linear-planar fabric), suggesting that the sepiolite formed prior to the end of slip on the fault plane.

### 4.2 Whole-rock compositions and mass-balance calculations

Based on the chemical analyses of the Rambla de los Pilares rocks, the concentration of a component in the altered rock was compared with the component in the original through a mass change term:

$$Ci_A = M_O / M_A (Ci_O + \Delta Ci)$$

Where: $Ci_A$ = concentration of component i in the altered rock; $M_O$ = mass of the original, fresh rock; $M_A$ = mass of the altered rock; $Ci_O$ = concentration of component i in the parent rock; and $\Delta Ci$ = change in concentration of component i.

Variations in element concentration values were detected from analyses of wall rock and deformed rocks. In the fault rocks corresponding to sample point II (Rambla de los Pilares), as a common trend, this comparison indicates strong gains of $Na_2O$ and MgO and moderate enrichment of the L.O.I., $Si_2O$ and Be (Fig. 2.8). Moderate REE losses can also be observed. Accordingly, $Na_2O$, MgO, $Si_2O$, L.O.I., and Be plot well above the immobile isocon for all the fault rocks from the Rambla de los Pilares, indicating that these elements are mass enriched in the rocks located in a deeper section of the fault (Fig. 2.8).

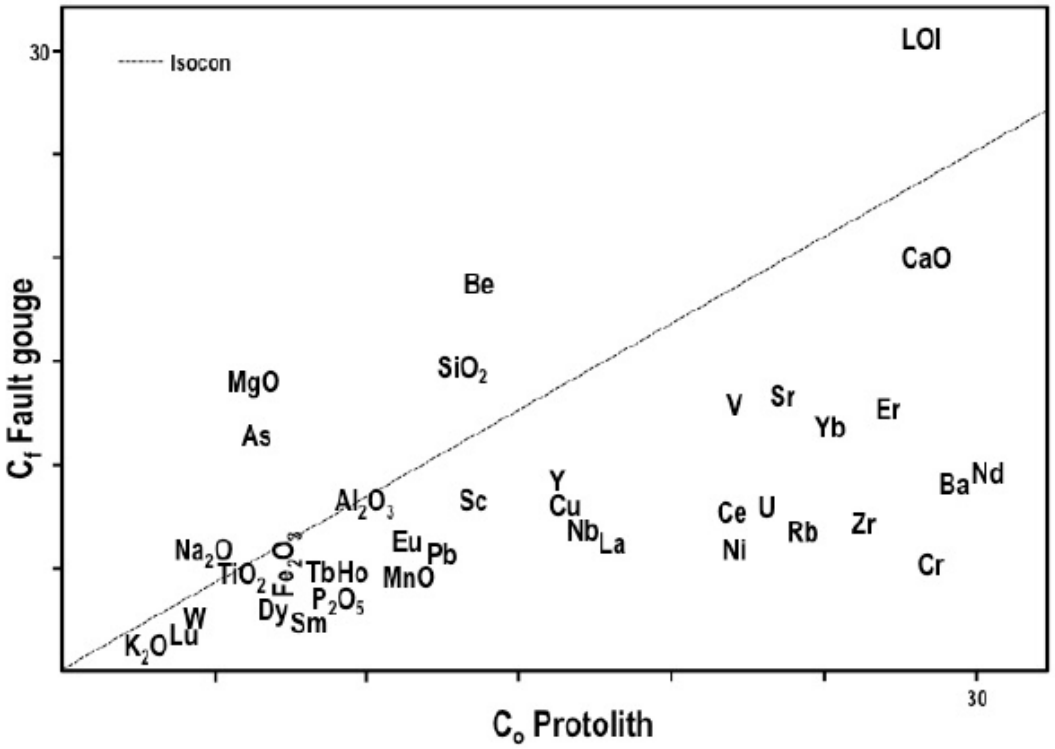


**Figure 2.8.** Isocon diagram comparing the mean chemical concentrations of elements in the wall rock and the fault gouge in the Rambla de los Pilares outcrop. Isocon: immobile isocon. Co: Wall-rock composition. Cf: Gouge composition.

## 4.3 Frictional properties of the fault gouges

Results of friction experiments under both water-saturated and vacuum conditions on the two fault gouge types from the Galera Fault are shown in Figure 2.9. For comparison purposes, the representative friction coefficient (μ) of each experiment was taken at 2.49 mm of axial displacement and is shown by a marker on each curve in Figure 2.9a.

All run-plots show an increase in shear stress (and therefore friction coefficient) during the run-in at a constant sliding velocity of 0.3 μm/sec up to the yield point when the material starts to deform permanently and the friction coefficient moves towards a steady-state value. All materials yielded before the start of the velocity steps at 1.5 mm of displacement.

Values of friction coefficient for the smectite- and palygorskite-rich gouge show a significant difference between wet and vacuum conditions (blue plots in Fig. 2.9a). Wet samples have a μ=0.177 while the vacuum samples are significantly stronger with μ=0.590. Values for the sepiolite-rich gouge are μ=0.472 and μ=0.686 for the wet and vacuum experiments respectively (red plots in Fig. 2.9a). For both gouges, friction coefficients in water-saturated experiments were lower than their equivalent vacuum experiment. However, the extent of this effect is variable between the two gouges, given that for the smectite- and palygorskite-rich gouge the difference between wet and vacuum conditions is $\Delta\mu = 0.41$, which is twice as much as for the sepiolite-rich gouge $\Delta\mu = 0.21$ (Fig. 2.9a).

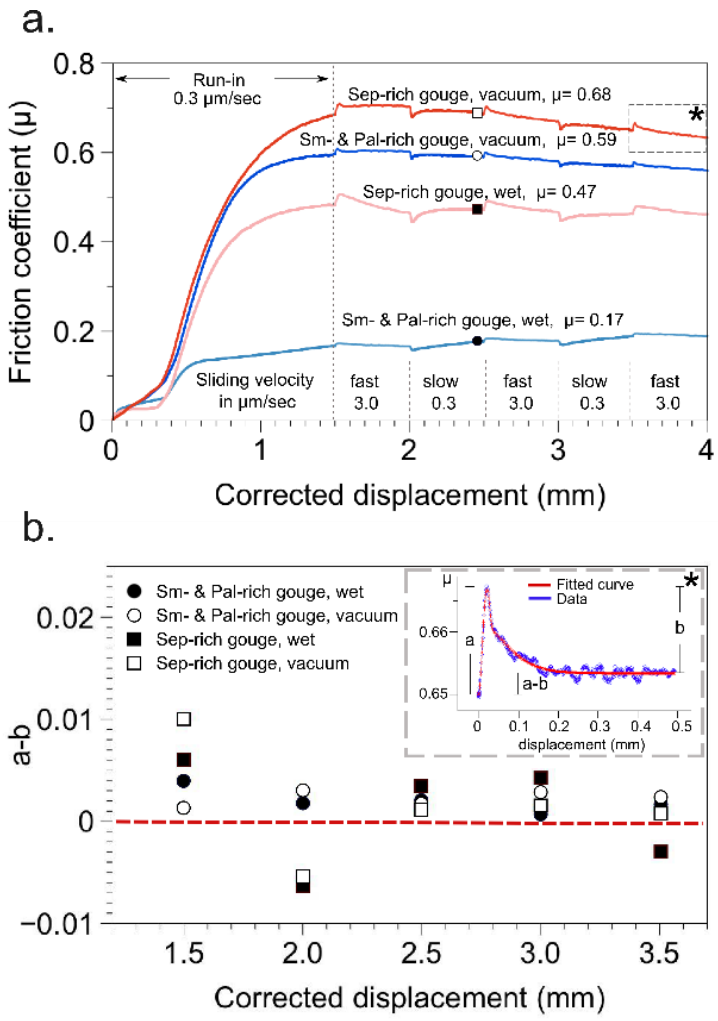


**Figure 2.9.** a. Experimental quantification of the frictional properties of two fault gouges from the Galera Fault Zone under vacuum and water-saturated conditions. The steps within the curves correspond to alternating changes in sliding velocity of one order of magnitude (0.3 to 3 μm/sec). Mineral abbreviations for clay minerals according to Bergaya and Lagaly (2006), Sep: sepiolite, Sm: smectite, Pal: palygorskite. b. Values of the stability parameter a-b for positive and negative velocity steps, inset: Enlargement of an individual positive velocity step at 3.5 mm of axial displacement from the sepiolite-rich experiment under vacuum conditions. The figure illustrates the fitting of the data with the aging law and the values of a, b and a-b.

Strain-hardening effects are primarily visible in the smectite- and palygorskite-rich gouge under water-saturated conditions where an increase in friction coefficient was observed after the yield point with increasing displacement. This increase of μ after yield accounts for 27% of the total gouge strength, (μ=0.138 at 0.7 mm displacement and μ=0.190 at 4 mm displacement).

The rate dependency of the friction coefficient has been tested experimentally, introducing 5 (positive and negative) velocity steps for each of the friction experiments, with variations in sliding velocity from 0.3 – 3.0 – 0.3 μm/sec (peaks after yield on run-plots in Fig. 2.9a). The resulting peaks that describe the rate and state effects of the imposed velocity variation have been linearly de-trended, to remove the overall trend of μ, and modelled to find the experimental variables a and b. An example of this procedure is illustrated in Fig. 2.9b inset.

Values for the stability parameter a-b for each test are shown in Fig 2.9b. All velocity steps for the smectite- and palygorskite-rich gouge are consistently positive for both the water-saturated and the experiment ran under vacuum. On the other hand, the values of a-b for the sepiolite-rich gouge yield occasional negative (potentially unstable) values both under water-saturated and vacuum conditions.

## 5. Discussion

The study documents significant differences in clay mineral assemblages and chemical composition of three rock types within the Galera Fault tectonic setting: 1) wall rocks including: white marls and dark lutite layers which also occur as injection features 2) smectite- and palygorskite-rich assemblages of gouges in shallow areas of the fault (Galera Village), 3) sepiolite-rich gouges in areas of higher fluid flux (Rambla de los Pilares) (See Fig. 2.1b). Textural, mineral and chemical evidence suggest the presence of both relict cataclastic and authigenic clay phases. The Mg-rich fibrous clay minerals were only observed within the fault zone as authigenic phases.

Wall-rock composition, fluid availability and temperature are some of the key factors controlling mineral transformations promoting the crystallisation of the authigenic phases during fault activity (Haines and van der Plujim, 2012; Solum et al., 2003). Haines and van der Plujim (2012) suggested that the low-temperature Mg-rich assemblages found in fault gouges are a response to external fluid fluxes. Our mineralogical and geochemical study provides data to discuss the origin of this fluid and to identify the influence of fluid-rock interactions during clay gouge authigenesis in the fault zone. The clay mineral assemblages found in the fault rocks indicate that mineral transformations in materials from the Galera Fault can be divided in two types: 1) Growth or concentration of Al-smectite and palygorskite in fault gouges, and 2) formation of a sepiolite-rich gouge.

There is no evidence of mineral authigenesis or transformations in the injection features crosscutting the sedimentary layering. Mineralogical features of these rocks are similar to those of the wall-rock lithologies and do not suggest growth of neoformed clays, although their linear fabric indicate a deformation-induced process that altered the sedimentary texture of the wall rock. Rocks associated with fault activity with absence of significant mineralogical transformations have also been reported in the literature (e.g. Engelder, 1974;

Brock and Engelder, 1977; Anderson et al., 1980; Haines and van der Plujim, 2012).

In the following sections we present an interpretation of the nature of the fluids and some of the mechanical and fluid-rock interaction processes due to the fault activity that explain the different type of rocks in the area of influence of the Galera Fault.

### 5.1 Nature of the fluids

Mineralogical and geochemical differences between fault gouges and wall rocks are likely to be the result of periods of fluid-rock interaction within the Galera Fault. The alteration assemblage is dominated by the formation of authigenic sepiolite and palygorskite. According to mass balance calculations, the present study reveals high mobility of elements promoted by processes occurring along the fault zone that appear to enhance fluid flux. Similar inferences have been made for other fault zones (e.g. Haines and van der Pluijm, 2012; Arancibia et al., 2014). Regarding major elements, the most mobile chemical components in the fault zone are MgO, the L.O.I. value (indicating the presence of $CO_2$ and $H_2O$) and CaO. The CaO loss (-10.01 wt.%), which can be associated to carbonate dissolution, as well as MgO and L.O.I. gains (6.32 and 2.39 wt.%) can be explained by fault-controlled fluid flow in the area. Haines and van der Pluijm (2012) recognised two distinct assemblages of Mg-rich phyllosilicates in fault gouges from western and southwestern USA, a sepiolite and other Mg-phyllosilicate-bearing assemblage and a palygorskite- and smectite-rich association. They suggested that both formed from mineral reactions associated to circulation of Mg-rich fluids along the fault plane at temperatures <<200 ºC. The isocon diagram (Fig. 2.8) also shows large gains of trace elements such as Be (3.24 ppm) and As (4.11 ppm) in the sepiolite-rich gouge. The As and Be enrichment also points to a circulation of hot deep fluids as the source of the Mg-rich fluid given that significant amounts of these elements have been found in rocks associated with hydrothermal processes (see e.g. Rancourt at al., 2001; Lubben et al., 2012; López and O´Connor, 2012). The sources for Arsenic (As) and its high concentration in groundwater have been previously related to thermal waters and fumaroles (Nordstrom, 2010). Reported cases of Be enrichment are scarce, however there are examples where the whole-rock geochemical data of rocks formed in geothermal systems are especially enriched in Be. These gains seem to be similarly distributed as As and Li enrichments in the Roosevelt Hot Springs KGRA, Utah (Bamford et al., 1980).

Regarding the source of the fluid for the Mg-rich assemblages in fault areas, factors such as the alkali-rich oxidizing conditions required for the growth of these assemblages (Jones and Galán, 1988), suggest a meteoric or basinal origin for the fluids (García-Romero et al., 2006; Haines and van der Pluijm, 2012). Hayman (2006) suggested that dolomitic marbles found in the fault-footwall were a likely source of Mg for fluid associated to the Mg-rich assemblages in the Black Mountains. In the Galera Fault, deep circulation of thermal fluids through fractures affecting the substratum could promote the dissolution of the thick dolostone sequences that form the Mesozoic carbonatic basement, explaining the Mg enrichment of the fluid. Sepiolite and palygorskite can be formed either directly from those Si-and Mg-rich alkali (pH 7-9) oxidized fluids at temperatures <<200 ºC (Siffert and Wey, 1962; Jones and Galán, 1988; Post and Crawford, 2007) or as a result of their interaction with fragmental phyllosilicates (Jacobs et al., 2006; Morton et al., 2012) (Fig. 2.10).

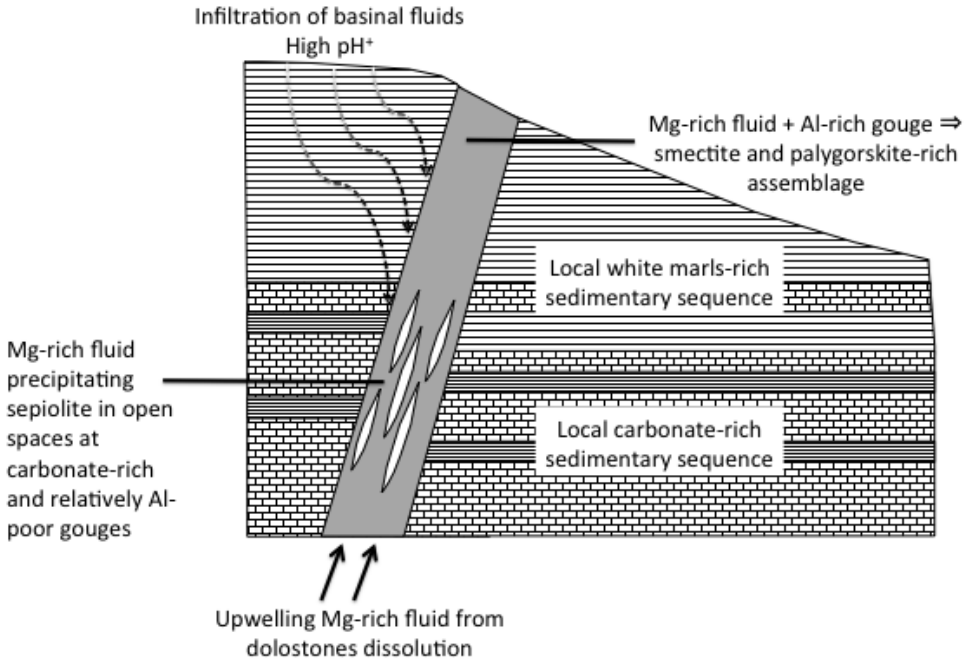


**Figure 2.10.** Schematic diagram illustrating the different processes responsible for Mg-rich phyllosilicate authigenesis during fault activity in the Galera Fault Zone.

## 5.2 Origin of the fibrous phyllosilicates

Based on the clay mineral assemblages found in fault gouges, Haines and van der Pluijm (2012) suggested four general mineral transformations associated with fault activity: 1) growth of authigenic 1Md illite; 2) 'retrograde diagenesis' of chlorite-rich gouge to authigenic chlorite/smectite and saponite; 3) growth of authigenic dioctahedral smectite from alteration of acidic volcanic wall rocks; 4) formation of Mg-rich phyllosilicate assemblages (sepiolite+saponite+talc+lizardite or palygorskite +/- chlorite +/- quartz) by reaction of phyllosilicate gouges with Mg-rich fluids. The illitic and dioctahedral smectite transformations appear to be near-isochemical and do not require large external fluid fluxes, whereas the low-temperature Mg-rich assemblages are a response to external fluid fluxes. In the Galera Fault Zone, sepiolite and palygorskite seem to be mineral markers of chemical changes during fluid-rock interaction processes, as illustrated by petrographic, geochemical and XRD results. Faulting or tectonic fracturing creating permeable zones may promote clay mineral reaction without significant heat addition (e.g. Uysal et al., 2000). In these cases, fluid composition can strongly influence the mineral assemblages of the fluid circulation zones. Mass balance calculations (Fig. 2.8) suggest that geochemical gain of Mg was associated to a hydrothermal fluid also enriched in As and Be. The crystallisation of the fibrous phyllosilicates must be associated to the circulation of the Mg-rich fluid flux through the fault zone.

This study has recognised Mg-rich phyllosilicates in two distinct mineral assemblages from the Galera Fault gouges. The smectite- and palygorskite-bearing assemblage appears in the NE fault segment between materials from the upper part of the stratigraphic column, whereas sepiolite-rich gouges occur in the central SW segment between stratigraphically

deeper levels. Moreover, chemical analyses of sepiolite show compositions close to the Mg-rich end-member composition, whereas palygorskite contains significantly higher amounts of Al and Fe. Based on these compositional differences and due to the spatial distribution of assemblages (palygorskite is never found in conjunction with sepiolite and both correspond to the end-members of the polysomatic series), it is likely that the two assemblages may be the result of the evolution of a common Mg-rich fluid interacting with fault rocks according to two distinct mineral transformations: 1) Mg-rich fluid + carbonate-rich Al-poor gouge ⇒ sepiolite-rich assemblage; 2) Mg-rich fluid + Al-rich gouge ⇒ palygorskite-rich assemblage. Thus, the two assemblages may be the result of a common Mg-rich fluid precipitating sepiolite in open spaces at carbonate-rich and relatively Al-poor gouges in the Rambla de los Pilares area and interacting with gouges derived from more Al-rich white marls wall rocks at Galera Village to form palygorskite.

The precipitation of sepiolite must be mainly controlled by the chemical properties of the Mg-rich fluid. An important factor in the sepiolite fluid equilibrium is its $pH^+$ dependency. Wollast et al. (1968) showed through their experiments how the rapid precipitation of sepiolite at higher pH values suggests that the rate of reaction depends on the concentration of OH- ions. In the case study presented here, an initially low pH value in the fluid could have been the trigger for dolomite dissolution in deep dolostones from the Mesozoic carbonatic basement and dolomite-bearing sediments from the evaporitic sequence of the Guadix-Baza Basin, and consequently Mg enrichment of the hydrothermal fluids. A later $pH^+$ increase possibly associated with active faulting and deformation, which could increase the interaction with highly saline brines from the basin, could be involved in the precipitation of sepiolite in the Rambla de los Pilares area at lower temperatures (Fig. 2.10). Haines and van der Plujim (2012) indicated that sepiolite and palygorskite are both fibrous Mg-rich phyllosilicates that can form at very low temperatures (25-150ºC).

Fibrous clay minerals have been associated with tension fracture zones (Thiry and Pletsch, 2011) where the sepiolite crystals show some syndeformational structures. The textural characteristics of sepiolite grains as long, well-formed crystals could suggest direct precipitation from a hydrothermal solution under alkaline and saline conditions controlled by Si, Mg, Al and Fe concentrations (Esteoule-Choux, 1984).

Sepiolite will remain stable within the fault zone up to temperatures of 325 ºC as determined in cold-seal pressure vessel experiments (Frank-Kamenetskiy et al., 1969). This indicates that the fault gouge could be stable at seismogenic depths in the Galera Fault and could affect mechanical processes of faults, including earthquake nucleation. Local occurrence of sepiolite and palygorskite in cores recovered from the SAFOD drilling project at depths close to 3 km (Bradbury et al., 2011, 2015) supports the argument that fibrous clay minerals are stable in fault zones and hence these could potentially be significant components of the gouge at the seismogenic depths of the Galera Fault.

The authigenesis of palygorskite, with higher amounts of Al in its structure, at the shallower and marginal part of the Galera Fault suggest an evolution of the conditions of the Mg-rich fluid circulating through the fault zone and/or the interaction of this fluid with Al-rich wall rocks (Fig. 2.10). Wall rocks in this area are characterised by the presence of a smectite-rich matrix, and include considerable amounts of dolomite and quartz. The palygorskite

disseminated through this gouge may be the result of a localised transformation of smectite-rich gouge reacting with Mg-rich fluids passing along a shear surface, where Al is available for authigenic formation. A similar formation process has been discussed in García-Romero et al. (2006) for palygorskite found in tension fractures of the Carboneras Fault. Haines and van der Pluijm (2012) proposed a similar process for the formation of palygorskite-rich gouges.

Differences between the sepiolite-rich and the smectite- and palygorskite-rich gouges could be explained by heterogeneity in the fluid-rock interactions along the fault. Pure smectite has been found to be stable up to 70°C in geothermal environments with complete water-rock interaction and an adequate supply of ions (Jennings and Thompson, 1986; Harvey and Browne, 1991), however in low permeability materials with an incomplete water-rock interaction, smectites may be present in the rock matrix up to 150°C (Gunderson et al., 2000). The absence of Al-smectite in the Mg-rich sepiolite deposit suggests that this gouge is a product of high fluid-rock interaction process in an area with increased flux rates, promoting hydrothermal processes that include direct precipitation of sepiolite. Meanwhile, the palygorskite-rich assemblage probably formed in areas of lower fluid flux where the related fluid interaction with the Al-rich wall rocks promotes the formation of palygorskite and concentrates smectites already present in the wall rock.

### 5.3 Fluid mobility and syndeformational structures

Deformation processes in the Guadix-Baza Basin favour fluid flow within the fault zone, including the formation of highly permeable paths through which fluids circulate and form new authigenic mineral associations. In addition to mineral authigenesis, sedimentary strata close to the fault core developed injection structures as a consequence of active deformation. The presence of the clastic-filled injection features provides evidence for fluid mobility in the Galera Fault Zone. The highly porous texture of these materials provides a suitable medium for the accumulation and circulation of aqueous interstitial fluids recharged through its connection with the fault. Seismites and clastic injection features are likely formed during seismic events when the pore-fluid pressure exceeds the pressure of an unconsolidated sand body creating fluidization (Jolly and Lonergan, 2002).

Smectite, the significant component of the matrix of the sediments of the basin, has a low liquid limit which favours the liquefaction and the transition of sediments to a fluid state (Azañón et al., 2010). The cyclical propagation of seismic waves thorough clay-rich sediments can trigger their liquefaction (McCalpin, 1996). The existence of bands of diatom fragments that exhibit preferred orientation can be interpreted as evidence of a flow texture associated with liquefaction of materials in the basin. The presence of clastic injection features and seismites, sedimentary deformation structures, described by Alfaro et al. (2010), confirm the impact of the seismic activity on the development of the deformation structures.

## 5.4 Implications of chemical and mineral reactions on the mechanical properties of the Galera Fault

The distribution of neoformed minerals in the fault core has implications for the mechanical behaviour of the different segments of the fault. According to Byerlee (1978), mineralogy, fluid activity, microfabric and volume changes have different effects on the mechanical properties and strength of shallow crustal faults. In the case of the Galera Fault, the hydrothermal alteration concentrates fibrous and platy (mainly smectite) phyllosilicates within the fault zone. These phyllosilicates constitute the majority of their respective fault gouges.

An interesting observation from the friction experiments is the marked difference in strength between the two clay-rich gouges. Differences in strength under water-saturated conditions highlight the important role of water in frictional strength of phyllosilicates, as previously shown (Moore and Lockner, 2004; Behnsen and Faulkner, 2012). However, in this set of experiments the effect of water seems to be more significant in the smectite- and palygorskite-rich gouge than in the sepiolite-rich gouge. Possible causes for this difference could include a higher percentage of stronger minerals such as quartz, feldspar and calcite in the sepiolite-rich gouge that are largely unaffected by the presence of water. Additionally, the mineral assemblage in the gouge from the Galera Village area is dominated by smectite instead of fibrous clay minerals. The dominance of smectite makes the gouge very weak and sensitive to the hydration state (Moore et al., 1982; Behnsen and Faulkner, 2013).

Alternatively, the crystallographic fibrous structure of the sepiolite-palygorskite group could promote a stronger framework that, coupled with the discontinuity of water layers, could make these minerals less sensitive to the effects of water. Analysing the intrinsic rheological properties of monomineralic samples of fibrous clay minerals would help to identify the mechanism promoting stronger friction coefficients in these gouges and is the focus of on-going work.

Concentration of clay minerals in the fault zone during slip will affect the overall frictional properties of the fault zone and favour creeping processes (Faulkner et al. 2003; Collettini et al., 2009a, 2009b; Haines and van der Pluijm, 2012). In the northern segment of the Galera Fault, the gouge is dominated by smectite, one of the mineral groups with the lowest friction coefficient and mostly frictionally stable behaviour in nature, with reported values of $\mu$ between 0.11 and 0.26 for montmorillonite with different interlayer cations (Behnsen and Faulkner, 2013), and as low as $\mu$=0.05 for saponite (Lockner et al., 2011). Results from our wet experiments for the smectite- and palygorskite-rich gouge collected from shallower segments of the fault show $\mu$=0.17 (Fig. 2.9a) and are therefore expected to weaken the fault. Furthermore, as shown by the consistently positive values of the a-b parameter (Fig. 2.9b), this gouge is velocity-strengthening and hence stable under the tested conditions. This implies earthquakes cannot nucleate within this material (Scholz, 1998). This gouge (and its mineral association) could therefore be related to fault creep and stable-sliding processes (Faulkner et al., 2003; Collettini et al., 2009). In the southern segment, however, the sepiolite-rich gouge shows higher friction coefficients: $\mu$= 0.47 under water-saturated conditions and $\mu$= 0.68 under vacuum (Fig. 2.9a). These values of strength are closer to those reported for quartzo-feldspathic rocks (0.6-0.85) (Byerlee, 1978) and do not

contribute to the weakening of the fault. On the contrary, fault gouges rich in sepiolite show inconsistent changes in a-b with intermittent negative values (Fig. 2.9b), which allow for the possibility of unstable slip, perhaps leading to earthquake nucleation (Scholz, 1998).

## 6. Conclusions

The mineralogical analysis of the rocks in the Galera Fault Zone reveals differences between the fault gouges and the sedimentary sequence affected by the fault. The most significant changes include mineral associations dominated by fibrous clay minerals, which are only present in highly deformed rocks and are a product of the geological processes triggered by the fault activity.

The progressive faulting and seismicity of the area mobilised fluids within the fault zones resulting in new mineral associations with a distinct chemical signature. The geochemical data show enrichments in As and Be, elements associated with hot fluid circulation. Interactions of the fluid with the Mesozoic carbonatic basement could be responsible for the dissolution of dolostones and consequently Mg enrichment of the thermal fluid. The precipitation of mineral assemblages that include fibrous clay minerals would result from the interaction of the aforementioned fluids with the wall-rock mineral associations and perhaps also with high $pH^+$ basinal fluids.

Highly porous strata from the sedimentary sequence also provide a suitable medium for the accumulation and circulation of the mobilised fluids. Fluid textures within clastic injection features in the Galera Fault Zone indicate that during seismic events, these sediments can become fluidised and highly mobile.

The identification of mineral authigenesis and heterogeneities in the mineralogy of the Galera Fault gouge is of great importance in the assessment of its mechanical behaviour. The change in mineralogy within the fault core results in low friction coefficients and a stable frictional regime for the smectite- and palygorskite-rich gouge, contrasting with the stronger friction coefficients and neutral to unstable frictional regime for the sepiolite-rich gouge. These results indicate that earthquakes in the Galera Fault are more likely to nucleate in sepiolite-rich areas of the fault assuming continuity of these deposits in depth, and highlights the importance of clay mineralogy studies for the evaluation of seismic risk linked to fault areas.

## Acknowledgments

The authors would like to thank Dr M.M. Abad-Ortega and A. Martinez-Morales for their support in electron microscopy data acquisition, Dr H. Noda for his code used in the numerical fitting of the experimental data, G. Coughlan for his technical support during the experimental work, and R. Lackey for his English language editing support. This manuscript has been greatly improved by comments and suggestions from two anonymous reviewers. This work has been financed by the research projects CGL2011-30153-C02-01 and CGL2011-30153-C02-02 from MINECO, research project UJA2014/06/17 from the Universidad-Caja Rural de Jaén, Research Groups RNM-179 and RNM-325 of the Junta de

Andalucía, UK NERC grant NE/J024449/1 and the F.P.I. Grant No. BES-2012-052 562 from the Spanish Government (Ministerio de Economía y Competitividad).

## References

Alfaro, P., Delgado, J., Sanz de Galdeano, C., Galindo-Zaldívar, J., García-Tortosa, F.J., López-Garrido, A.C., López-Casado, C., Marín, C., Gil, A., Borque, M.J., 2008. The Baza Fault: a major active extensional fault in the Central Betic Cordillera (South Spain). Int. J. Earth Sci. 97, 1353–1365.

Alfaro, P., Gibert, L., Moretti, M., García-Tortosa, F.J., Sanz de Galdeano, C., Galindo Zaldívar, J., López Garrido, A.C., 2010. The significance of giant seismites in the Plio-Pleistocene Baza palaeo-lake (S Spain). Terra Nova 22, 172–179.

Anderson, J.L., Osborne, R.H., Palmer, D.F., 1980. Petrogenesis of cataclastic rock within the San Andreas fault zone of southern California. Tectonophysics 67, 221–249.

Arancibia, G., Fujita, K., Hoshino, K., Mitchell, T.M., Cembrano, J., Gomila, R. Morata, D., Faulkner, D.R. and Rempe, M., 2014. Hydrothermal alteration in an exhumed crustal fault zone: Testing geochemical mobility in the Caleta Coloso Fault, Atacama Fault System, Northern Chile. Tectonophysics 623, 147–168.

Arranz, E., Lago, M., Bastida, J., Galés, C., Soriano, J., Ubide, T., 2008. Hydrothermal macroscopy Fe-sepiolite from Oujda mounts (Middle Atlas, Eastern Morocco). J. Afr. Earth Sci. 52, 81–88.

Azañón, J.M., Azor, A., Yesares, J., Tsige, M., Mateos, R.M., Nieto, F., Delgado, J., Lopez-Chicano, M., Martin, W., Rodriguez-Fernandez, J., 2010. Regional-scale high-plasticity clay-bearing formation as controlling factor on landslides in Southeast Spain. Geomorphology 120, 26–37.

Bach, W., Banerjee, N.R., Dick, H.J.B., 2002. Discovery of ancient and active hydrothermal systems along the ultra-slow spreading Southwest Indian Ridge 10 degrees-16 degrees E. Geochem. Geophy. Geosy. 3, 1044.

Bamford, R.W., Christensen, O.D., Gpuano R.M., 1980. Multielement Geochemistry of Solid Materials in Geothermal Systems and its Applications. Part 1: The Hot-Water System at the Roosevelt Hot Springs KGRA, Utah. U.S. Department of Energy.

Behnsen, J., Faulkner, D., 2011. Water and argon permeability of phyllosilicates powders under medium to high pressure. J. Geophys. Res. 116, B11203.

Behnsen, J., Faulkner D., 2012. Frictional strength of sheet silicates under medium to high pressure. J. Struct. Geol. 42, 49–61.

Behnsen, J., Faulkner D., 2013. Permeability and frictional strength of cation-exchanged montmorillonite. J. Geophys. Res. 118, 1-11.

Bergaya, F., Theng, B.K.G., Lagaly, G. (Eds.), 2006. Handbook of Clay Science. Elsevier, Developments of Clay Science, Volume 1, Amsterdam.

Bradbury, K.K., Evans, J.P., Chester, J.S., Chester, F.M., and Kirschner, D.K., 2011. Lithology and internal structure of the San Andreas fault at depth based on characterization of Phase 3 whole-rock core in the San Andreas Fault Observatory at Depth (SAFOD) borehole. Earth Planet. Sci. Lett. 310, 1-2, 131-144.

Bradbury, K.K., Davis C.R., Shervais J.W., Janecke S.U., Evans J.P., 2015. Composition, alteration, and texture of fault-related rocks from SAFOD core and surface outcrop analogs: evidence for deformation processes and fluid–rock interactions. Pure Appl. Geophys. 172 1053–1078.

Brock, A., Engelder, T., 1977. Deformation associated with the movement of the Muddy Mountain overthrust in the Buffington window, southeastern Nevada. Geol. Soc. Am. Bull. 88, 1667–1677.

Byerlee, J., 1978. Friction of rocks. Pure Appl. Geophys. 116, 615–626.

Collettini, C., Viti, C., Smith, S.A.F., Holdsworth, R.E., 2009a. The development of interconnected talc networks and weakening of continental low-angle normal faults. Geology 37, 567–570.

Collettini, C., Niemeijer, A., Viti, C., Marone, C., 2009b. Fault zone fabric and fault weakness. Nature 462, 907–910.

Dieterich, J.H., 1979a. Modelling of rock friction 1. Experimental results and constitutive equations. J. Geophys. Res. 84, B5, 2161–2168.

Duan, Q., Yang, X., Ma, S., Chen, J., Chen, J., 2016. Fluid–rock interactions in seismic faults: Implications from the structures and mineralogical and geochemical compositions of drilling cores from the rupture of the 2008 Wenchuan earthquake, China. Tectonophysics 666, 260–280.

Durand, C., Oliot, E., Marquer, D., Sizun, J.-P., 2015. Chemical mass transfer in shear zones and metacarbonate xenoliths: a comparison of four mass balance approaches. Eur. J. Mineral. 27, 731-754.

Engelder, J.T., 1974. Cataclasis and the generation of fault gouge. Geol. Soc. Am. Bull. 85, 1515–1522.

Esteoule-Choux, J., 1984. Palygorskite in the Tertiary deposits of the Armorican Massif. In: Singer, A., Galán, E. (eds.). Palygorskite-sepiolite occurrences. Genesis and uses. Elsevier, Amsterdam. 75–85.

Evans, J., Chester, F., 1995. Fluid-rock interaction in faults of the San Andreas system: Inferences from San Gabriel fault rock geochemistry and microstructures. J. Geophys. Res. 100, B7, 13007–13020.

Faulkner, D.R., Lewis, A.C. and Rutter, E.H., 2003. On the internal structure and mechanics of the large strike-slip fault zones: field observations of the Carboneras fault in southeastem Spain, Tectonophysics, 367 (3-4), 235-251.

Faulkner, D.R., Armitage, P.J., 2013. The effect of tectonic environment on permeability development around faults and in the brittle crust. Earth Planet. Sc. Lett. 375, 71–77.

Frank-Kamenetsky, V.A., Kotov, N.V., Klochkova, G.N., 1969. Phase transformations in sepiolite and palygorskite at different pressures under hydrothermal conditions. Geokhimiya 1, 14–21.

Galán, E., Castillo, A., 1984. Sepiolite-palygorskite in Spanish Tertiary Basins: Genetical patterns in continental environments. In: Singer, A., Galán, E. (eds.). Palygorskite-sepiolite occurrences. Genesis and uses. Developments in Sedimentology, 37, 87–124. Elsevier.

García-Romero, E., Suárez, M., Oyarzun, R., López-García, J.A., Regueiro, M., 2006. Fault hosted palygorskite from the Serrata de Nijar deformation zone (SE Spain). Clays Clay Miner. 54, 324–332.

García-Romero, E., Suárez, M., 2010. On the chemical composition of sepiolite and palygorskite. Clays Clay Miner. 58, 1, 1–20.

García-Tortosa, F.J., Alfaro P., Galindo-Zaldívar J., Gibert L., López-Garrido A.C., Sanz de Galdeano C., Ureña M., 2008. Geomorphologic evidence of the active Baza Fault (Betic Cordillera, South Spain). Geomorphology. 97, 374–391.

García-Tortosa, F.J., Alfaro, P., Galindo-Zaldívar J., Sanz de Galdeano, C., 2011. Glacis geometry as a geomorphic marker of recent tectonics: the Guadix-Baza Basin (South Spain). Geomorphology. 125, 517–529.

Gibbs, A.E., Hein, J.R., Lewis, S.D., McCulloch, D.S., 1993. Hydrothermal palygorskite and ferromanganese mineralization at a central California margin fracture zone. Mar. Geol. 115, 47–65.

Gibert, L., Sanz de Galdeano, C., Alfaro, P., Scott, G.R., López-Garrido, A.C., 2005. Seismic induced Pleistocene landslides in deltaic deposits of the Baza basin (SE Spain). Sediment. Geol. 179, 279–294.

Gibert, L., Ortí, F., Rosell L., 2007. Plio-Pleistocene lacustrine evaporites of the Baza Basin (Betic Chain, SE Spain). Sediment. Geol. 200, 89–116.

Grant, J.A., 1986. The Isocon diagram - A simple solution to Gresen's equation for metasomatic alteration. Econ. Geol. 81, 1976–1982.

Gratier, J.P., Dysthe D.K., Renard F., 2013. Chapter 2: The role of pressure solution creep in the ductility of the Earth's upper crust, in Advances in Geophysics, edited by R. Dmowska, pp. 47–179, Elsevier.

Gresens, P.L., 1967. Composition-volume relationships of metasomatism. Chem. Geol. 2, 47–65.

Guidotti, C.V., Yates, M.G., Dyar, M.D., and Taylor, M.E., 1994. Petrogenetic implications of the $Fe^{3+}$ content of muscovite in pelitic schists. Am. Mineral. 79, 793-795.

Gunderson, R., Cumming, W., Astra, D., Harvey, C., 2000. Analysis of smectite clays in geothermal drill cuttings by the methylene blue method: for well site geothermometry and resistivity sounding correlation. Proceedings World Geothermal Congress 2000, 1175–1181.

Haines, S., van der Pluijm, B., 2012. Patterns of mineral transformations in clay gouge, with examples from low-angle normal fault rocks in the western USA. J. Struct. Geol. 43, 2–32.

Harvey, C.C., Browne, P.R.L., 1991. Mixed-layer clay geothermometry in the Wairakei geothermal field, New Zealand. Clays Clay Miner. 39, 614–621.

Hayman, N., Housen, B., Cladouhos, T., Livi, K., 2004. Magnetic and clast fabrics as measurements of grain-scale processes within the Death Valley shallow crustal detachment faults. J. Geophys. Res. B 109. doi:10.1029/ 2003JB002902.

Imber, J., Holdsworth, R. E., Butler, C. A., Strachan, R. A., 2001. A reappraisal of the Sibson-Scholz fault zone model: The nature of the frictional to viscous ("brittle-ductile") transition along a long-lived, crustal-scale fault, Outer Hebrides, Scotland. Tectonics 20, 5, 601–624.

Jacobs, M., Kerr, P., 1965. Hydrothermal alteration along the Lisbon Valley fault zone, San Juan County, Utah. Geological Society of America Bulletin 76, 423–440.

Jennings, S., Thompson, G.R., 1986. Diagenesis in Plio-Pleistocene sediments in the Colorado River delta, southern California. J. Sed. Petr. 56, 89–98.

Jolly, R.J.H., Lonergan, L., 2002. Mechanisms and controls on formation of sand intrusions. J. Geol. Soc. Lond. 159, 605–617.

Jones, B., Galan, E., 1988. Sepiolite and palygorskite. In: Bailey, S. (Ed.), Hydrous Phyllosilicates (Exclusive of Micas). Rev. Mineral. 19, 631–674.

Lacroix, B., Tesei, T., Oliot, E., Lahfid, A., Collettini, C., 2015. Early weakening processes inside thrust fault. Tectonics 34, 1396-1411.

Lockner, D., Morrow, C., Moore, D., Hickman, S., 2011. Low strength of deep San Andreas fault gouge from SAFOD core. Nature 472, 82–85.

López D.L., O'Connor 2012. Arsenic in geothermal and mine drainage waters in the world. In "Understanding the Geological and Medical Interphase of Arsenic. Noller C.Ng, Nidu, R., Bundschuch, J. and Bhattacharya, P. (eds). Taylor and Francis. 477-480.

Lubben J.D., Cline J.S. & Barker S.L. (2012) Ore fluid properties and sources from quartz-associated gold at the Betze-Post Carlin-Type Gold Deposit, Nevada, United States. Economic Geology, 107, 1351–1385.

McCalpin, J.P., 1996. Paleoseismology. International Geophysical Series, 62nd ed. Academic Press, San Diego. 588 p.

Mitchell, T., Faulkner, D., 2008. Experimental measurements of permeability evolution during triaxial compression of initially intact crystalline rocks and implications for fluid flow in fault zones. J. Geophys. Res. 113, B11412.

Moore, D.E., Lockner, D.A., Summers, R., Ma, S., Byerlee, J.D., 1996. Strength of chrysotile-serpentinite gouge under hydrothermal conditions: Can it explain a weak San Andreas fault? Geology 24,11, 1041–1044.

Moore, D., Lockner, D., 2004. Crystallographic controls on the frictional behavior of dry and water-saturated sheet structure minerals. J. Geophys. Res. 109, B03401.

Moore, D., Morrow, C., Byerlee, J., 1982. Use of swelling clays to reduce permeability and its potential application to nuclear waste repository sealing, Geophys. Res. Lett., 9(9), 1009–1012.

Moore, D.E., Rymer, M.J., 2007. Talc-bearing serpentinite and the creeping section of the San Andreas fault. Nature 448, 10.1038.

Moore, D.E., Lockner, D.A., Ponce, D.A., 2010. Anomalously low strength of serpentinite sheared against granite and implications for creep on the Hayward and Calaveras Faults. In: K. Knudsen et al. (eds.). Proceedings of the Third Conference on Earthquake Hazards in the Eastern San Francisco Bay Area, California Geological Survey Special Reports, California Geological Survey (Dept. of Natural Resources), Sacramento, Calif. 219, 101–113.

Morrow, C., Moore, D., Lockner, D., 2000. The effect of mineral bond strength and adsorbed water on fault gouge frictional strength. Geophys. Res. Lett. 27, 815–818.

Morton, N., Girty, G.H., Rockwell, T.K., 2012. Fault zone architecture of the San Jacinto fault zone in Horse Canyon, southern California: a model for focused post-seismic fluid flow and heat transfer in the shallow crust. Earth Planet. Sc. Lett. 329, 71–83.

Niemeijer, A.R., Vissers, R.L.M., 2014. Earthquake rupture propagation inferred from the spatial distribution of fault rock frictional properties. Earth Planet. Sc. Lett. 396, 154–164.

Nieto F., Ortega-Huertas M., Peacor D.R., Aróstegui J., 1996. Evolution of illite/smectite from early diagenesis through incipient metamorphism in sediments of the Basque-Cantabrian Basin. Clays Clay Minerals, 44, 304–323.

Noda, H., Shimamoto, T., 2009. Constitutive properties of clayey fault gouge from the Hanaore fault zone, southwest Japan. J. Geophys. Res. 114. B04409.

Nordstrom, D.K., 2010. Geothermal Arsenic, Arsenic in Geosphere and Human Diseases. In: Jean, Bunddschuh, Bhattacharya (eds.). Taylor & Francis Group, London. 41–43.

Numelin, T., Marone, C., and Kirby, E., 2007. Frictional properties of natural fault gouge from a low-angle normal fault, Panamint Valley, California: Tectonics, v. 26, TC2004, doi: 10.1029/2005TC001916.

Post, J., Crawford, S., 2007. Varied forms of palygorskite and sepiolite from different geologic systems. Appl. Clay. Sci. 36, 232–244.

Rancourt, D.G., Fortin, D., Pichler, T., Thibault, P.J., Lamarche, G., Morris, V., Mercier, P., 2001. Mineralogy of a natural As-rich hydrous ferric oxide coprecipitate formed by mixing of hydrothermal fluid and seawater: Implications regarding surface complexation and color banding in ferrihydrite deposits. Am.Mineral. 86, 834–851.

Rutter, E.H., Maddock, R.H., Hall, S.H., White S.H., 1986. Comparative microstructures of natural and experimentally produced claybearing fault gouges. Pure Appl. Geophys. 124, 3–30.

Sanz de Galdeano, C., 1990. Geologic evolution of the Betic Cordilleras in the Western Mediterranean, Miocene to the present. Tectonophysics. 172, 107–119.

Schleicher, A.M., Tourscher, S.N., van der Pluijm, B.A., Warr L.N., 2009. Constraints on mineralization, fluid-rock interaction, and mass transfer during faulting at 2–3 km depth from the SAFOD drill hole. J. Geophys. Res. 114, B04202.

Scholz, C. H., 1998. Earthquakes and friction laws. Nature. 391, 37–42.

Shimamoto, T., Logan, J. M., 1981. Effects of simulated fault gouge on the sliding behavior of Tennessee sandstone: nonclay gouges. J. Geophys. Res. 86, 2902–2914.

Sibson, R. H., 1977. Fault rocks and fault mechanisms. J. Geol. Soc. Lond. 133, 191–213.

Siffert, B., Wey, R., 1962. Synthese d'une sepiolite a temperature ordinaire. C. R. Acad. Sci. Paris. 254, 1460–1463.

Smith, S.A.F., Faulkner, D.R., 2010. Laboratory measurements of the frictional properties of a natural low-angle normal fault: The Zuccale fault, Elba Island, Italy. J. Geophys. Res. 115, B02407.

Solum, J., Van der Pluijm, B., Peacor, D., Warr, L., 2003. Influence of phyllosilicate mineral assemblages, fabrics, and fluids on the behavior of the Punchbowl fault, southern California. J. Geophys. Res. 108, B5, 2233.

Suárez, M., García-Romero, E., 2011. Advances in the crystal chemistry of sepiolite and palygorskite. In: E. Galan and A. Singer (eds.). Developments in Palygorskite-Sepiolite Research. A New Look at these Nanomaterials. Developments in Clay Science, 3. Elsevier, Amsterdam, pp. 33–55.

Suárez, M., García-Romero, E., 2013. Sepiolite–palygorskite: a continuous polysomatic series. Clays Clay Miner. 61, 5, 461–472.

Trincal, V., Charpentier, D., Buatier, M.D., Grobety, B., Lacroix, B., Labaume, P., Sizun, J.-P., 2014. Quantification of mass transfers and mineralogical transformations in a thrust fault (Monte Perdido thrust unit, southern Pyrenees, Spain). Marine and Petroleum Geology. doi:10.1016/j.marpetgeo.2013.12.016

Thiry, M., Pletsch, T., 2011. Palygorskite clays in marine sediments: records of extreme climate. In: Galán, E., Singer, A. (eds.). Developments in Palygorskite and Sepiolite Research. A New Outlook on these Nanomaterials. Developments in Clay Science, vol. 3. Elsevier, Amsterdam, pp. 101–124.

Uysal, I.T., Golding, S.D., Audsley, F., 2000. Clay Mineral Authigenesis in the Late Permian Coal Measures, Bowen Basin, Queensland, Australia. Clays Clay Miner. 48, 351–365.

Vera, J.A., 1970. Estudio estratigráfico de la depresión de Guadix–Baza. Boletín Geológico y Minero 91, 429–462.

Vera, J.A., Rodriguez, J., Guerra, A., Viseras, C., 1994. La cuenca de Guadix-Baza. Documents et travaux de I'IGAL 14, 1–17.

Verberne, B.A., Spiers, C.J., Niemeijer, A.R, De Bresser, J.H.P., De Winter, D.A.M., Plümper, O., 2014. Frictional Properties and Microstructure of Calcite-Rich Fault Gouges Sheared at Sub-Seismic Sliding Velocities. Pure Appl. Geophys. 171, 2617–2640.

Viseras, C.A., 1991. Estratigrafía y sedimentología del relleno aluvial de la cuenca de Guadix (Cordilleras Béticas). Ph.D. Thesis, Univ. Granada, Spain.

Whitney, D.L., Evans, B.W., 2010. Abbreviations for names of rock-forming minerals. Am. Mineral. 95, 185-187.

Wollast, R., Mackenzie, P.T., Bricker, D.P., 1968. Experimental precipitation and genesis of sepiolite at earth-surface conditions. Am. Mineral. 53, 1645–1661.

Yalcin, H., Bozkaya, O., 2004. Ultramafic-Rock-Hosted vein Sepiolite occurrences in the Ankara Ophiolitic Mélange, Central Anatolia, Turkey. Clays Clay Miner. 52, 2, 227–239.

# Chapter 3 Micro- and nano-scale study of clay-rich fault gouges

**Highlights:**

- Naturally- and experimentally-deformed gouges containing planar and fibrous clay minerals were studied using scanning and transmission electron microscopy (SEM, TEM).
- The two gouges present radically different microstructures. The smectite-rich gouge crystals are aligned, whereas the sepiolite-rich gouge exhibits a grid-like microfabric in which the needle-like crystals are bent into "feather-like" structures. This phenomenon strongly influences gouge permeability.
- Chemical results suggest two ongoing transformations between the phyllosilicates in the gouges: from sepiolite to palygorskite, and from palygorskite to smectite. These transformations affect important chemical and physical properties of the gouge including their mechanical properties.

# Micro- and nano-scale study of deformed phyllosilicate-rich gouges from the Galera Fault Zone (Betic Cordillera, SE Spain)

CATALINA SÁNCHEZ-ROA (1) *, BLANCA BAULUZ (2), FERNANDO NIETO (3), ISABEL ABAD (1), JUAN JIMENÉZ-MILLÁN (1) DANIEL FAULKNER (4).

(1) Departamento de Geología and CEACTierra, Unidad Asociada IACT (CSIC-UGR), Universidad de Jaén, Campus Las Lagunillas s/n, 23071 Jaén, Spain, (2), IUCA-Facultad de Ciencias, Universidad de Zaragoza, Pedro Cerbuna 12, Zaragoza, Spain, (3) Departamento de Mineralogía y Petrología and IACT (CSIC-UGR), Facultad de Ciencias, Universidad de Granada, Avda. Fuentenueva s/n, 18002 Granada, Spain, (4) Rock Deformation Laboratory, Department of Earth, Ocean and Ecological Sciences, University of Liverpool, Liverpool, UK.

**This manuscript will be submitted for consideration to *American Mineralogist*.**

## Abstract

Naturally- and experimentally-deformed gouges from sliding surfaces within the Galera Fault Zone were analysed using scanning and transmission electron microscopy (SEM, TEM) to identify changes in the fault rocks as a consequence of ongoing deformation. The two gouges studied have a particular mineral association that includes planar (mainly smectite and illite) and fibrous clay minerals (sepiolite and palygorskite). Mechanical findings include a radical difference grain alignment between the two gouges, a phenomenon that strongly influences gouge permeability. Smectite crystals are aligned on the same orientation and show a great number of layer terminations and delamination on the basal planes that contribute to a distributed mode of deformation in the gouge. In contrast, the sepiolite-rich gouge exhibits a grid-like microfabric that results in localised deformation limited to small areas where the needle-like crystals are bent and broken producing "feather-like" structures, without the presence of lattice distortions. Meanwhile, significant chemical results include: 1. Al content identified in some of the sepiolite fibres through AEM, together with variability in the (110) d-spacing of sepiolite across single fibres, suggest the existence of a progressive transformation from sepiolite to palygorskite; 2. Authigenic Mg-rich smectite identified in the smectite-rich gouge suggests an ongoing transformation between smectite and palygorskite; 3. Chemical continuity of Mg-decrease and Al+Fe-increase in the octahedral cation content of the sepiolites, palygorskites and smectites within the gouges indicate a sequence of mineral transformations that is favoured by an increase of Al content. Partial or total transformations between smectites and fibrous clay minerals affect important chemical and physical properties of the gouge including their mechanical properties. We propose that the extent of the palygorskite to smectite transformation in the Galera Fault is an important controlling factor that can progressively change both the permeability and weakness of the fault.

## 1. Introduction

Active faulting is an important phenomenon triggering chemical and physical processes in the rocks involved (Hickman et al., 1995; Faulkner et al., 2010). Chemical processes involve element mobility and redistribution assisted by fluids running through the faults. These fluids can either come from deep sources as hydrothermal fluids or meteoric waters infiltrating through the newly-formed cracks in the rock. Significant evidence of the chemical reactions occurred in this setting include changes in the mineralogy of the fault gouge (Schleicher et al., 2006; 2012). Physical processes on the other hand are related to how minerals accommodate deformation under high levels of stress, commonly experienced on fault planes. A previous study of the mineralogy of the Galera Fault (SE Spain) documented the presence of authigenic fibrous clay minerals within the fault planes as a consequence of the fluid-rock interactions favoured by active faulting (Sánchez-Roa et al., 2016). The two types of fault gouge in the Galera Fault present different resistance to shear due to the authigenic minerals concentrated in each section of the fault: the gouge to the south-west rich in fibrous clay minerals has a higher friction coefficient ($\mu$=0.47 under wet deformation); meanwhile the gouge recovered close to the town of Galera is rich in smectite with a small amount of fibrous minerals and has a lower friction coefficient ($\mu$=0.17 under wet deformation) (Sánchez-Roa et al., 2016). The contrasting mechanical behaviour between the two gouges motivates the study of the textural evolution and mineral transformations that can contribute to a different resistance to shear during active faulting. Due to the very small grain size (<2$\mu$m) of the authigenic minerals in the Galera Fault, this study requires a micro- to nano-scale examination through electron microscopy, that allows the identification of physical and/or chemical processes imperceptible through other mechanisms.

Fault zone permeability is an important parameter in fault zones and is affected by some essential parameters such as the host rock lithology, fault activity, magnitude of displacement (which will control the gouge's fabric and texture), pre-existing structures, the depth, the tectonic stress field and the width of the damage zone (Houwers et al., 2015). The rock texture and its influence in the permeability of the two gouge types of the Galera Fault Zone can only be explored through scanning and transmission electron microscopy (SEM and TEM). Furthermore, a micro and nano-scale study of these fault rocks could provide a deeper insight into the deformation mechanisms in phyllosilicates, which for planar phyllosilicates include delamination, fracturing, kinking and dislocation glide (Ibanez and Kronenberg, 1993; Mares and Kronenberg, 1993; Sánchez-Navas and Galindo-Zaldívar, 1993; French et al., 2015). Delamination often occurs during frictional sliding in phyllosilicates with low interlayer electrostatic separation energy (Moore and Lockner, 2004), as is the case for talc and pyrophyllite (Giese, 1978; Sakuma and Suehara, 2015). However little is known about the possible deformation mechanisms occurring in fibrous materials such as the fibrous clay minerals or a mixed regime where both fibrous and planar phyllosilicates are present.

The study of clay minerals by TEM has been reported to be difficult due to their susceptibility to electron-beam damage mainly related to the diffusion of alkali elements induced by the high voltages of the electron beam (Pluijm et al., 1988; Peacor, 1992). These

observations remain true for the fibrous clay mineral group (sepiolite and palygorskite), where the cause of instability under the electron beam has been previously attributed to the high percentage of $H_2O$ and mobile cations within the zeolite-like channels (Krekeler and Guggenheim, 2008). Most of the work on the microscopic properties of these minerals has been achieved by separating individual particles, however the investigation of their mineral transformations and their contribution to the fabric of rocks is still to be explored. Thus, the study of these small grain size phyllosilicates in the context of active deformation is poorly understood and requires TEM exploration.

In this study we investigate by SEM and TEM naturally- and experimentally-deformed fault gouge samples collected from two main sliding surfaces within the Galera Fault Zone. The aim of the study is to identify the chemical and physical processes that contribute to differences in the resistance to shear between the two main sliding surfaces of the Galera Fault Zone, including chemical processes such as mineral transformations and physical processes related to grain alignment and deformation.

## 2. Geological setting

The Galera Fault Zone is an active strike-slip fault, located in the Betic Cordillera (SE Spain) within the Guadix-Baza Basin (García-Tortosa et al., 2011). The Galera Fault has an extension of approximately 23-km long and 1.5 km wide with orientation N50°E. The structure is associated with a NE–SW elongated asymmetric anticline and consists of several parallel splays dipping north-westwards between 40° and 60° (Sánchez-Roa et al., 2016). The sedimentary sequence of the wall rock presents an alternation of white marls and dark lutitic layers that contain dolomite, gypsum, quartz, calcite and phyllosilicates in their mineral assemblages. Meanwhile, two distinct minerals assemblages have been identified within the fault planes and are the two materials focus of this study. The first consist of smectite- and palygorskite-rich fault gouges at the NE area of the fault (Galera Village); the second consists of a sepiolite-rich gouge mainly at the central SW segment of the fault (Rambla de los Pilares). Fibrous clay-rich gouges are enriched in Mg due to hydrothermal alteration during periods of fluid-rock interaction that was concentrated in fault planes and fractures (Sánchez-Roa et al., 2016).

## 3. Methods

### 3.1. Sample preparation

The preparation of samples for High-Resolution (HR-) TEM observation had three different procedures:

3.1.1 Impregnation with London Resin White (LRW) and ion thinning

Samples selected for microstructural analysis were prepared using a method modified from Kim et al. (1995). The method involves a multi-step exchange of the sample material with ethanol (99.9%) and London Resin White under refrigeration. The aim of the impregnation

is to preserve the texture and the permanent expansion of smectite interlayers for TEM observation.

Impregnation
Hydration phase: Air dried rock pieces were placed on a grid suspended over water creating a water steam saturated atmosphere. The samples were left for rehydration over a period of 48 hours.

Embedding phase: The water in the clay is replaced by ultra-pure ethanol of 99.9% purity. The samples were immersed in 100% ethanol for two periods of two hours and one of four hours. The LRW is progressively added in different mixtures of ethanol and LRW with volume ratios of ½, ⅓ and ¼ each for two hours and then immersed in pure LRW overnight in a refrigerator. The next day the LRW was changed twice after periods of four hours.

Polymerization phase: Fresh LRW was added to the samples and placed in an oven at 60° C for 24h to polymerize and harden the LRW. The vacuum desiccator step (Kim et al., 1995), was not fully carried out due to the fragile nature of the samples.

The cured samples were cut perpendicular to the shear plane, in the direction of shear and an ordinary thin section was then prepared using a diamond saw with oil as lubricant to shape the samples. Sticky wax was used as an adhesive to bond the sample and the thin section glass.

Thinning
Several 3 mm copper rings with a 1 mm hole in diameter were glued with an epoxy resin to the areas selected for further study. After drying for 24 hours, the rings were removed by heating the thin section. The rings were cleaned and ion-thinned to a suitable thickness for TEM study in a Fischione-1010 ion mill (Universidad de Jaén). The initial conditions for the ion thinning were 12°, 5Kv and 5mA until the first hole opened, from there they had an intermediate stage with 8°, 4Kv and 5mA, followed by a final stage with 5°, 3Kv and 5mA.

### 3.1.2 Impregnation with Epothin resin and FIB-SEM

Sample preparation through the second method included an impregnation of the samples in Epothin resin and hardener in a ratio of 2:1 and hardened under vacuum. The blocks were polished using silicon carbide powder and both isopropanol and mineral oil as lubricant agent. The polished blocks were observed under a Dual Beam Ariga Zeiss FIB-SEM (Focused Ion Beam-Scanning Electron Microscope) mainly operated at 30kV (Universidad de Sevilla). The objective of using the technique is to identify the most interesting areas for observation while keeping the fabric and structural context of the extracted lamellae. The FIB-SEM technique combines imaging capabilities of the electron beam and milling capabilities of the ion beam allowing the selection of suitable sampling sites with signs of higher deformation and micro-scale sectioning of electron transparent foils for TEM analysis. The selected area is marked and trenched using a focused beam of $Ga^+$ ions (Overwijk, 1993), the initial intensity for trenching was set to 20 nA for one hour and then set to 4 nA until the end of the trenching process. The procedure leaves a narrow slice

standing and pending by one of the uncut edges. The slice was then welded by depositing a Pt-binding agent and was fixed to a half-copper-washer for TEM observation.

3.1.3 Particle dispersion

Powders of the natural samples were prepared using holey carbon-coated Cu grids. The powder was dispersed in ultra-pure ethanol and immersed in the ultrasonic bath for 15 seconds. This preparation disperses individual grains of minerals onto the grid surface. The analyses performed on individual crystals allow a larger area to be used in the scanning transmission electron microscopy (STEM) mode for the analysis and provides better reproducibility of data due to the decrease in alkali loss. Although the powdered samples offer better analytical quality, the ion-milled samples offer textural information of the analysed grains (Abad et al., 2002).

## 3.2. Analytical techniques

Scanning Electron Microscopy (SEM)
Textural observations were made on polished impregnated blocks in secondary electron mode (SE) and backscattered electron mode (BSE). The SEM study was carried out with a Merlin Carl Zeiss field emision (FE) SEM in the Centro de Instrumentación Científico-Técnica of the Universidad de Jaén.

High Resolution Transmission Electron Microscopy (HR-TEM)

The TEM images were obtained using three instruments: a JEOL-2000-FX-II TEM at the University of Zaragoza operated at 200 kV; a FEI TITAN G2 TEM in the Centro de Instrumentación Científica (C.I.C.) of the Universidad de Granada, operated at 300 kV, with XFEG emission gun, spherical aberration corrector and HAADF detector, with a resolution of 0.8 Å in the TEM mode and 2 Å in the scanning TEM mode; and a FEI TITAN High-base TEM in the Laboratorio de Microscopías avanzadas at the Universidad de Zaragoza, operated at 300 kV, with Schottky-FEG emission gun, spherical aberration corrector (CETCOR, CEOS company), HAADF detector, and a 2k x 2k CCD Gatan camera, with a resolution of 0.9 Å in the TEM mode.

Analytical Electron Microscopy (AEM)
Chemical analyses (TEM-AEM) were obtained with two instruments: a Philips CM20 (C.I.C., Universidad de Granada), operating at 200 kV in STEM mode, with an EDAX solid-state energy dispersive X-ray (EDX) detector and with a scan window of ~20 Å~ 100 nm for the analysis of individual clay particles; the second instrument is a FEI TITAN Low-base TEM in the Laboratorio de Microscopias Avanzadas at the Universidad de Zaragoza, operated at 300 kV, with a High brightness field emission gun (XFEG), a monochromator unit, a spherical aberration corrector (CETCOR, CEOS company), HAADF detector, and a 2k x 2k CCD Gatan camera, with a resolution of 0.9 Å. The analyses were obtained in the HRSTEM mode. The following minerals were used to obtain the k factors for the transformation of intensity radiuses towards concentration ratios in accordance with the approximation made by Cliff and Lorimer (1975): Albite, olivine, biotite, spessartine, moscovite, chlorite and titanite.

Structural formulae of smectites were calculated from AEM data after analysing 89 crystals. The results were normalised to $O_{10}(OH)_2$ and all Fe was considered as $Fe^{3+}$.The normalisation procedure shows a sum of octahedral cations higher than 2.1 per formula unit (a.f.u.) for 43% of the analysed crystals indicating a divergence from their dioctahedral character. In addition, the sum of interlayer cations is lower than 0.2 a.f.u. for 32.5% and lower than 0.3 for 53.9% of the analysed crystals. These results suggest the possibility that some of the $Mg^{2+}$ that was originally considered octahedral is instead located in the interlayer. Thus, the total $Mg^{2+}$ was redistributed within interlayer and octahedral positions to ensure that the octahedral sheet keeps a dioctahedral character and that the interlayer charge remains within the normal range for smectites (0.2 to 0.6).

### 3.3. Permeability measurements

Permeability tests were carried out on a triaxial deformation apparatus with a servo-controlled axial loading system and fluid pressure pump (Mitchell and Faulkner, 2008) in the Rock Deformation Laboratory in the University of Liverpool. The apparatus is capable of applying confining pressures of up to 250 MPa and pore pressures up to 200 MPa. It measures ultra-low permeability down to $10^{-22}$ $m^2$ and a sample volume change of 0.1 $mm^3$. The servo-controlled pore fluid system controls pore fluid pressure and serves as a high precision volumometer. This system can be used to measure permeability through various methods including the pulse transient technique (Brace et al., 1968) applied in this study to obtain values of permeability for the fault gouges with increasing confining pressure. The gouge powders were prepared by mixing 0.4 g of the sample with 0.5 mL of distilled water. The paste was then placed between to sintered disks with a known permeability of $10^{-13}$ $m^2$. The disks holding a cylindrical gouge layer of approximately 1 mm high were placed within a PVC jacket and coupled with the sample assembly. Once the sample was inside the pressure vessel the confining and pore pressure were increased alternately starting with a pore pressure value of 5 MPa that was kept for all measurements and a starting confining pressure of 10 MPa. The confining pressure was progressively increased in 20 MPa intervals to obtain permeability measurement at 5, 20, 40, 60 80, and 100 MPa effective pressure. The pressure was left to equilibrate after each pressure increase until no changes in either pore of confining pressure were observed. The samples were recovered after depressurization and carefully measured to determine the final sample thickness and calculate permeability values. The pulse transient technique imposes a 1 MPa pressure differential in the upstream after equilibrium is reached and bases the calculations in how the pressure increase is transmitted through the gouge sample to determine permeability (Brace et al., 1968).

# 4. Results

## 4.1 SEM observations

4.1.1 Naturally deformed fault rocks

a. Smectite- and palygorskite-rich fault gouge

SEM observations of the fault gouge from the Galera town area show that the rock is composed of a very fine grain phyllosilicate-rich matrix that constitutes the majority of the rock and surround micron-size clasts of dolomite, orthoclase and quartz. Deformation features in the sample include the presence of bands of very fine grain minerals alternated with bands of coarser minerals that insinuate cataclastic processes including grain rotation and grain size reduction (Fig. 3.1). The observed structural features of the sample include the alignment of platy clay minerals in an orientation similar to the shear direction, between 135° and 180° to the shear vector (Rutter et al., 1986), hereafter called the P-foliation after Logan et al. (1979). A set of shears that transect the P-foliation were also identified in the gouge and correspond with the definition of R1 (Riedel) shears according to Logan et al., (1979). The gouge also exhibits surfaces parallel to the shear zone and with the same sense of shear, here called Y surfaces (Logan et al., 1979).

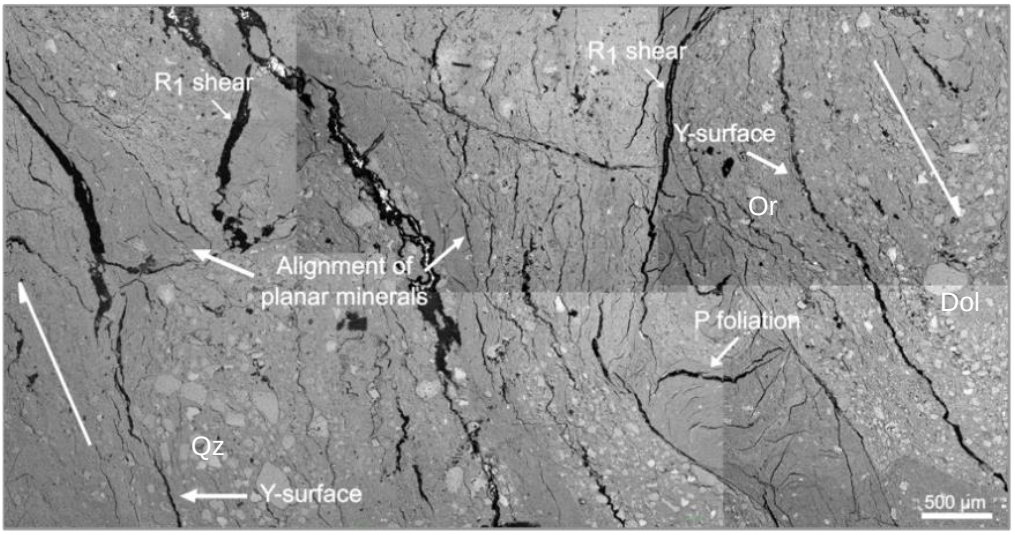


**Figure 3.1.** BSE image showing the deformation features of the naturally deformed smectite and palygorskite fault gouge, including P-foliation following the alignment of platy clay minerals, $R_1$ (Riedel) shears transecting the P-foliation, and Y surfaces parallel to the shear zone.

b. Sepiolite-rich fault gouge

Low magnification BSE images of the sepiolite-rich fault gouge show a homogeneous gouge with very fine grain size sepiolite that constitutes the majority of the sample (Fig. 3.2a). Deformation features are observed in the larger grain size phases that show mica-delamination and broken and aligned grains (Fig. 3.2a), however due to the clay size of the matrix further examination is restricted. Secondary electron image using in-lens detector of the gouge matrix shows fibrous sepiolite crystals with mainly two preferred orientations perpendicular to each other forming the majority of the gouge matrix (Fig. 3.2b).

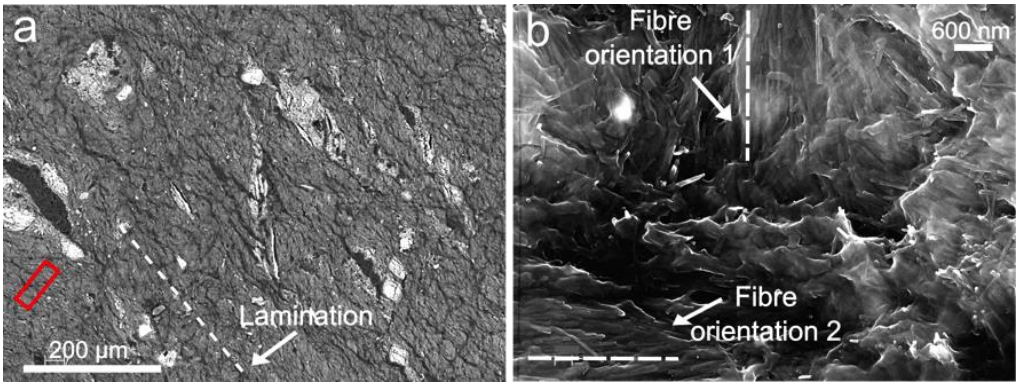


**Figure 3.2. a.** BSE image showing the deformation features of the naturally deformed sepiolite fault gouge and deformation in larger grains of mica and dolomite. The red rectangle indicates the area selected for FIB-SEM lamellae extraction for TEM analysis **b**. Secondary electrons image (in-lens detector) of the matrix of the rock showing the fibrous character of sepiolite.

### 4.1.2 Experimentally-deformed fault rocks

a. Smectite and palygorskite fault gouge material (wet deformation)

The examined gouge layers were recovered from the sliders and they keep some features related to the experimental assembly such as the grooved surface of the sliders (Fig. 3.3a), high deformation is visible towards the limit with the grooves, these type of shears have been described as boundary shears. The experimentally-deformed layers show microstructural features previously described for clay-rich fault gouges (Rutter et al., 1986), such as P-foliation (Fig. 3.3b) and $R_1$ shears, the deformation bands are markedly noticeable when affecting coarser grains of mica and dolomite (Fig. 3.3c).

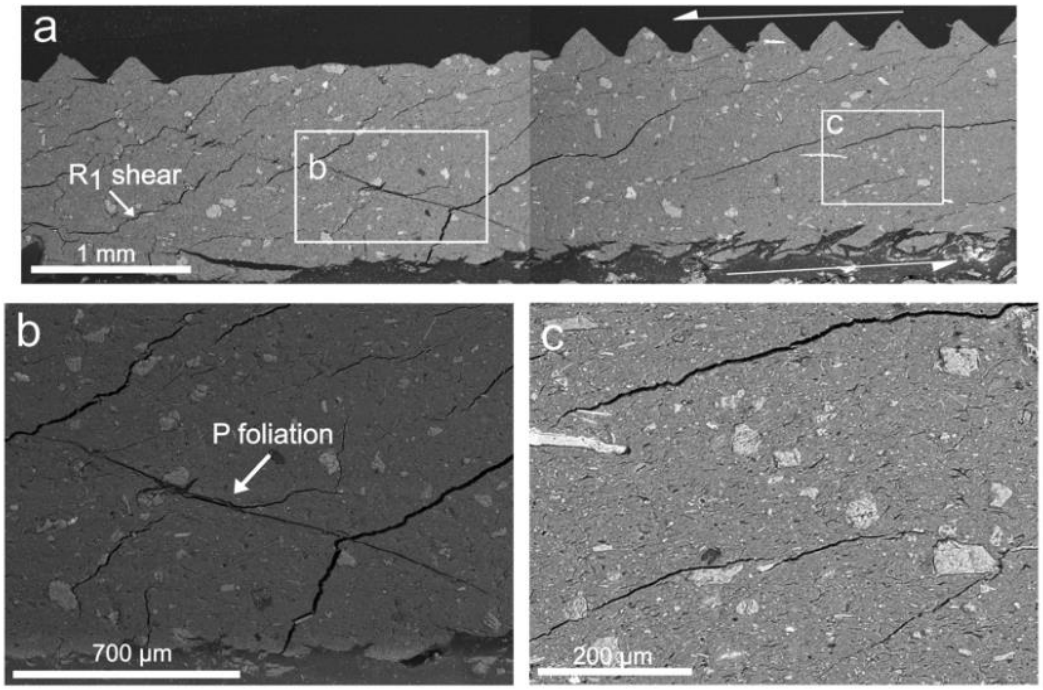


**Figure 3.3. a.** BSE image of the experimentally-deformed smectite and palygorskite fault gouge material under wet deformation**. b.** Enlarged view of the P-foliation. **c.** Enlarged view of the $R_1$ shears and alignment of dolomite and orthoclase grains.

b. Sepiolite fault gouge material (wet deformation)

Deformation microstructures in the experimentally-deformed sepiolite-rich gouge are highly pronounced in mineral phases with bigger grain size, however clay mineral alignment is hard to define (Fig. 3.4). The artificial grooves in the gouge were lost during the impregnation due to the highly localised strain in the boundary shears (Fig. 3.4). Larger gypsum crystals are deformed in domino –type asymmetric boudinage (Fig. 3.4b, 3.4c), while larger mica crystals align and delaminate in favour of $R_1$ shears (Fig. 3.4d, 3.4e). Dolomite crystals also appear highly fragmented due to the transection of $R_1$ and P surfaces with trail development (Fig. 3.4f).

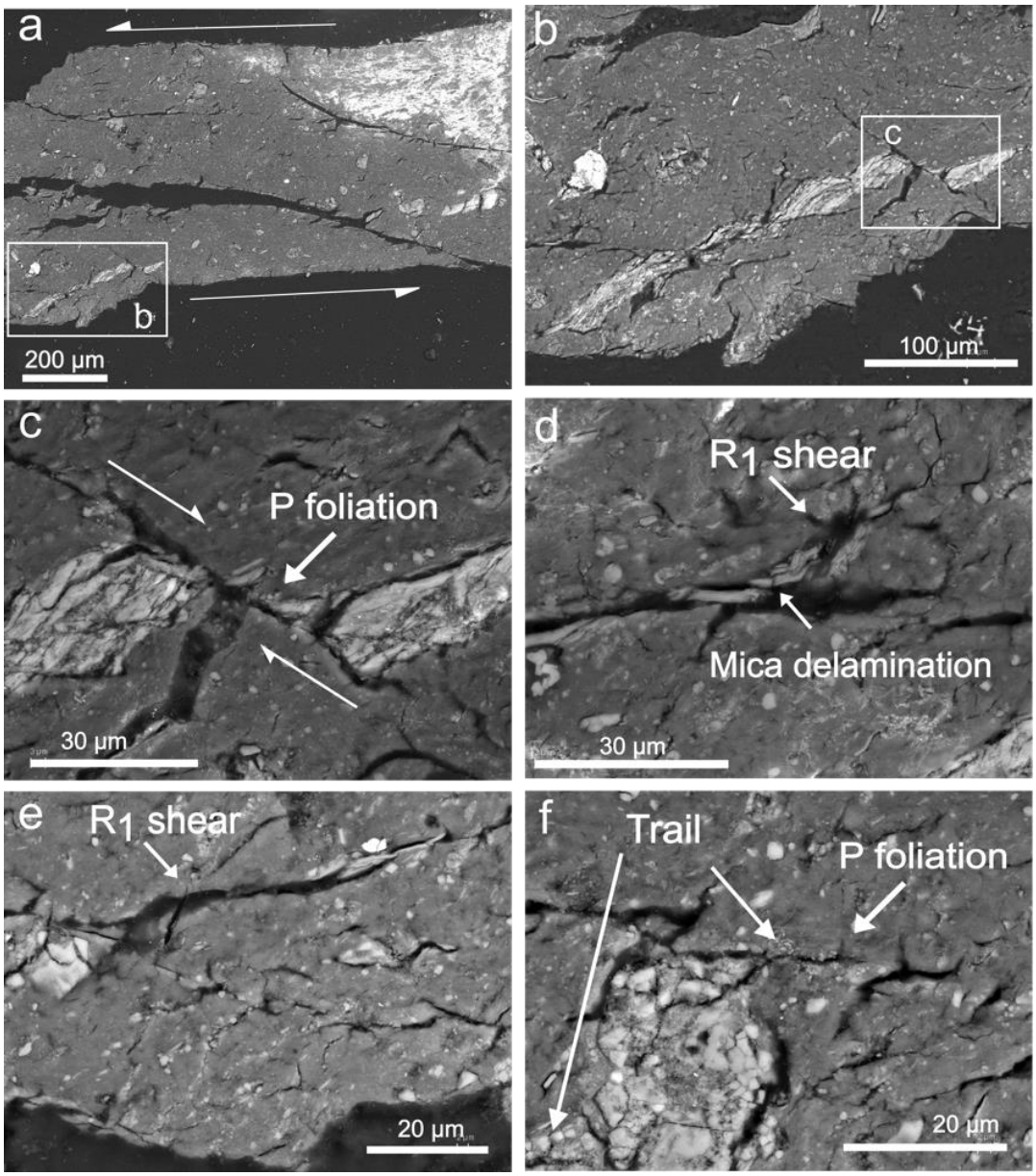


**Figure 3.4. a.** BSE image of the experimentally-deformed sepiolite fault gouge material under wet deformation. Shear direction indicated with half arrows. **b.** Enlargement of a boudinage structure on a gypsum crystal. **c** Enlargement of $R_1$ shear. Shear direction indicated with half arrows. d **to f.** Enlargement of structural features in the sample.

c. Smectite and palygorskite fault gouge material (dry deformation)

The experimentally-deformed gouge closely resembles the deformation structures identified in the natural gouge such as the $R_1$ shears, bands of clay minerals alternated with bands of bigger grain size (Fig. 3.5a to 3.5d). A view of the shear planes shows the polished slickenside surface and striae, result of the shear (Fig. 3.5e, 3.5f).

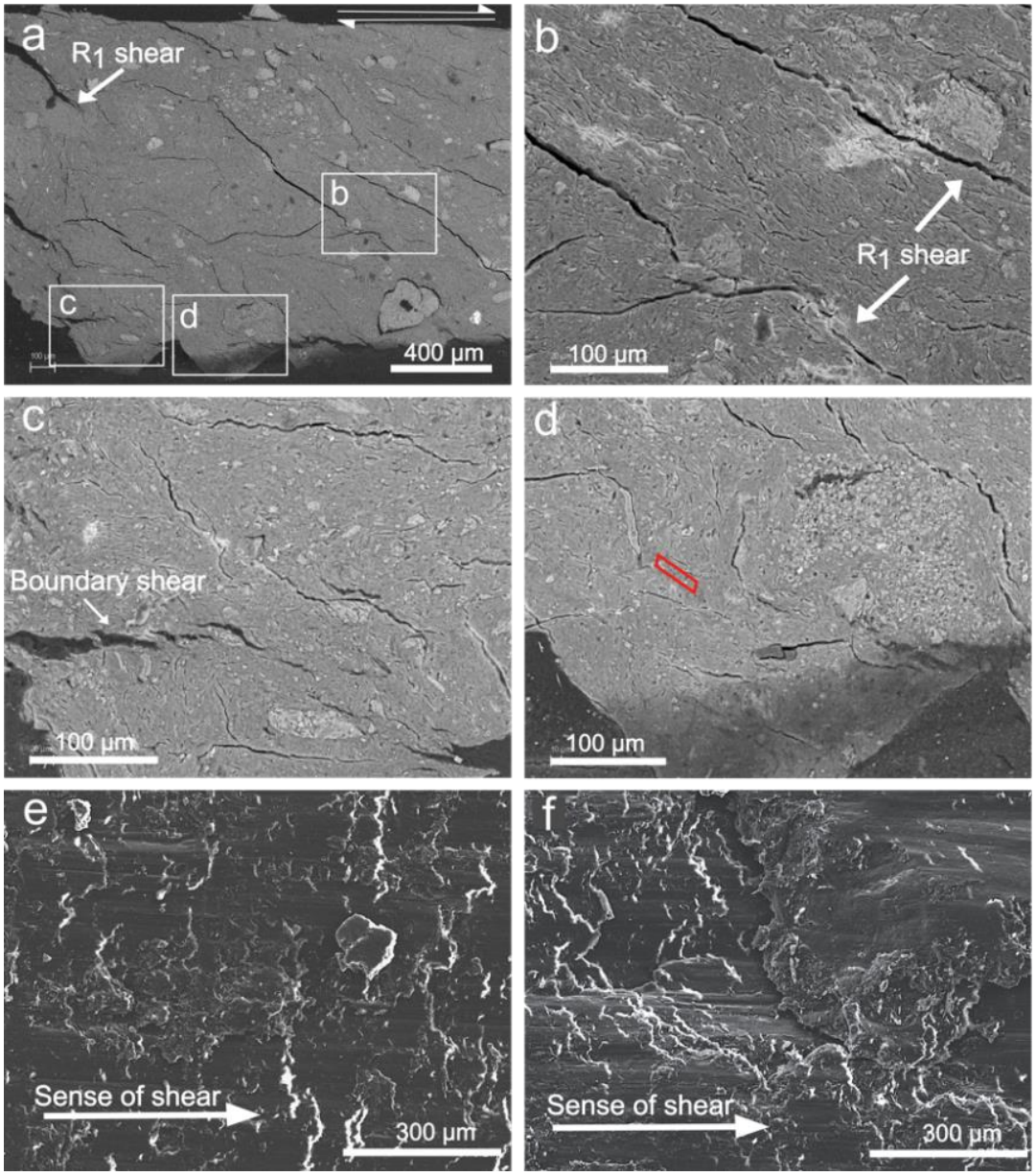


**Figure 3.5**. **a.** BSE image of the experimentally-deformed smectite and palygorskite fault gouge material under dry deformation. **b, c, and d.** Enlargement of structural features in the sample. The red rectangle indicates the area selected for FIB-SEM lamellae extraction for TEM analysis **e.** and **f.** Secondary electrons image of the shear planes after deformation with horizontal striae and polished slickenside surface.

d. Sepiolite fault gouge material (dry deformation)

SEM examination of the deformed gouge shows similar deformation microstructures to the ones observe in the gouge deformed naturally and under wet conditions (Fig. 3.6). Being noticeable a higher amount of small incipient $R_1$ shears that align in similar direction but are not connected between them (Fig. 3.6c). Figures 3.6d to 3.6f show the presence of a grid-

like microfabric of the deformed gouge caused by the two main preferred orientations of sepiolite fibres. The two orientations of the fibres persist even towards the R1 shears and on the shear planes (Fig. 3.6e, 3.6f).

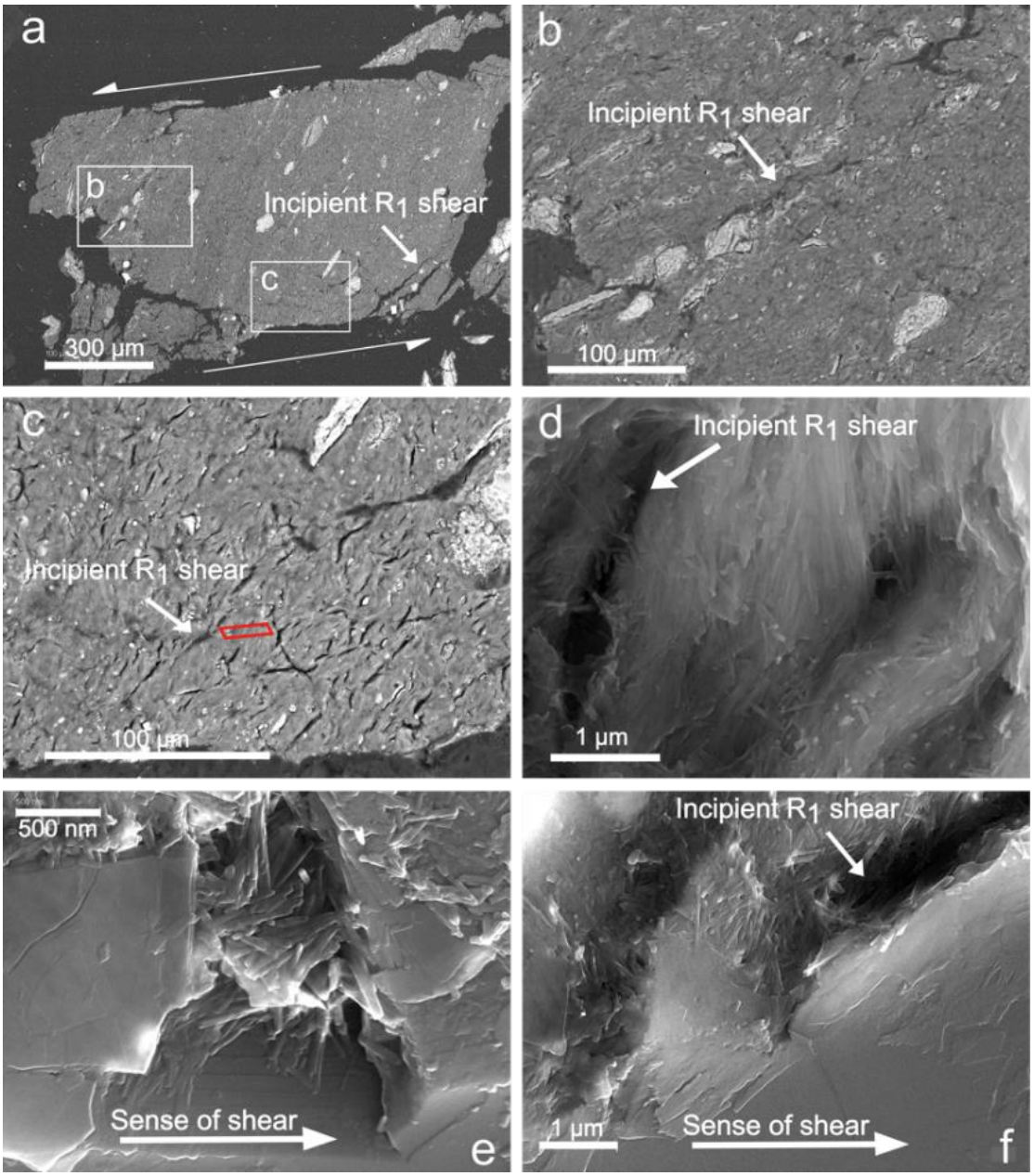


**Figure 3.6. a.** BSE image of the experimentally-deformed sepiolite fault gouge material under dry deformation. **b and c.** Enlargement of structural features in the sample. The red parallelogram indicates the site selected for FIB-SEM extraction for TEM analysis. **d.** Secondary electrons high-magnification image (in-lens detector) showing sepiolite crystals of the matrix **e.** and **f.** Secondary electrons image of the shear planes after deformation under dry conditions.

Summary of micro-scale observations:

- Naturally deformed rocks

Grain orientation for the two materials studied differs significantly. The smectite- and palygorskite-rich gouge shows grain alingment showing a series of parallel structures folowing similar orientations, on the other hand in the sepiolite-rich gouge it is noticeable the presence of two or more orientations of the fibres.

- Experimentally-deformed rocks

The differences for grain orientation identified in the two naturally deformed gouges studied remain noticeable in the experimentally-deformed rocks, grain alingment in the smectite- and palygorskite-rich gouge and grid microfabric in the sepiolite-rich gouge.

The preseence of water during deformation does not develop any significant differences in grain orientation for either gouge, showing a similar resulting microstructure under both wet and dry conditions.

## 4.2 TEM observations

### 4.2.1 Naturally deformed fault rocks

a. Smectite and palygorskite fault rock

The gouge has a matrix mainly composed of smectite, with minor amounts of palygorskite and illite, illite shows lattice fringes with 1.00 nm spacing and is the most crystalline phase on the basis on Selected Area Electron Diffraction (SAED) patterns, however illite crystals are embedded in smectite crystals with a similar orientation, which hinders the chemical analysis of a single phase (Fig. 3.7). The general texture of the rock shows phyllosilicate alignment as well as elongated porosity parallel to the basal planes of the crystals (Fig. 3.7a). The abundant presence of smectite helps to coat the coarse grains to maintain the fluent texture observed at lower magnification (Fig. 3.7b). High-resolution images of the rock matrix in a smectite-rich area show parallel to sub-parallel lattice fringes of smectite, the (001) spacing of smectite is here measured to be around 1.05 nm to 1.30 nm, due to the variable collapsing of its interlayer space in areas of poor impregnation (Fig. 3.7c, 3.7d). Lattice planes with spacing that vary from 2.00 to 2.30 nm were also observed within the smectite-rich matrix, that might correspond to mixed layer I/S with differente degree of collapse (Fig. 3.7d). The smectite crystals present broken and displaced lattice planes where the low crystallinity of the clay grains is evidenced by the absence of packets of more than two or three layers that never achieve a thickness of more than 10 nm (Fig. 3.7c, 3.7d). HR-images show crystals with diffuse regions that resemble the polysomes structures described by Krekeler et al. (2005) (Fig. 3.7f).

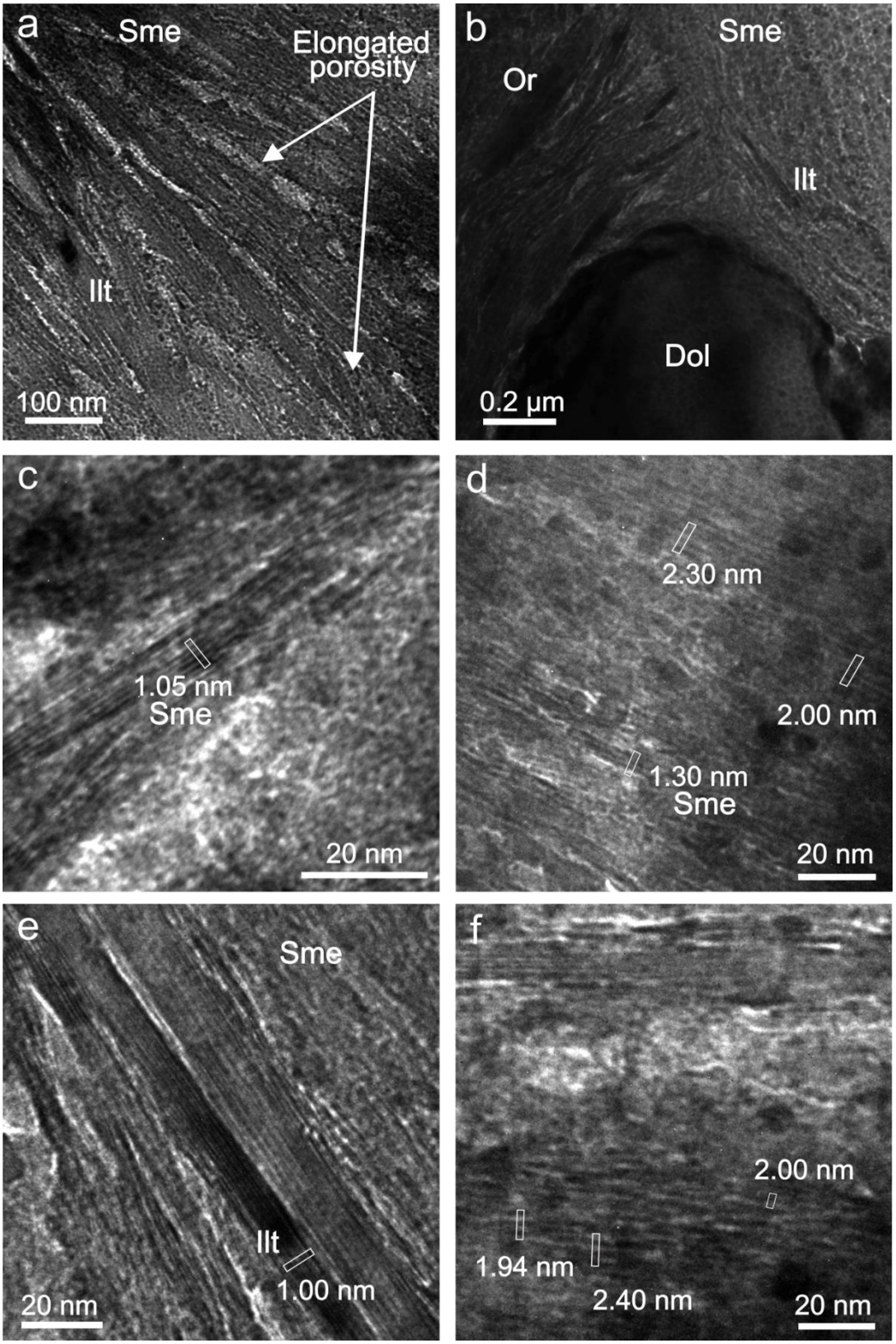


**Figure 3.7. a.** TEM image showing the general texture of the naturally deformed smectite and palygorskite fault rock. **b.** Smectite crystals coating coarse dolomite grain. **c.** High-resolution image of smectite crystals showing broken and displaced lattice fringes. **d.** Smectite-rich matrix shows smectite crystals with (001) spacing of 1.30 nm, and an area of unidentified phases with lattice fringes spaced 2.00 to 2.30 nm. **e.** HR-image of the matrix of the rock showing the proximity of the smectite and illite crystals. **f.** HR-image of crystals with discontinuos lattice fringes of variable d-spacing ranging from 1.9 to 2.4 nm.

b. Sepiolite fault rock

The general texture of the rock showed that the fibres have mainly three preferred orientations: orientations 1 and 2 have the c-axis (direction of the fibre) parallel to the imaged plane and are oriented almost perpendicular to each other; orientation 3 has the c-axis of the fibres oriented perpendicular to the imaged plane, showing a transversal section of the rods that appear in the image as small polygons (Fig. 3.8). These three orientations constitute a three-dimensional grid-like microfabric of the rock. The rock matrix is composed of fibre-aggregates (rods) with different sizes that vary from 1 μm to 100 nm (Fig. 3.8). The lack of fibre orientation in the rock matrix creates a large number of triangular to polygonal voids in the rock distributed throughout the matrix (Fig. 3.8). SAED patterns in the matrix are difficult to obtain, however, it is possible to observe reflections representing the 110 spacing of sepiolite at around 1.23 nm (Fig. 3.8b inset).

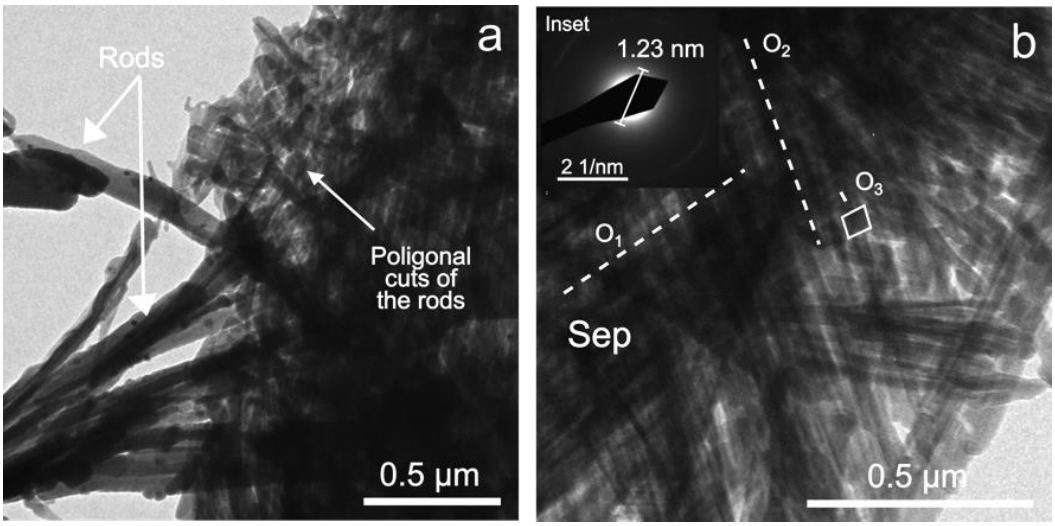


**Figure 3.8.** TEM images from a Cu-washer of the sepiolite fault rock. **a.** General fabric on the rock with variable rod sizes. **b.** Image of the rock matrix showing the disorientation of sepiolite fibres. Inset: SAED pattern on the rock matrix.

FIB-cut-lamellae extracted from the red rectangle shown in Figure 3.2.a allowed the identification of the general sense of deformation of the samples (Fig. 3.9a). Lamellae TEM observations show a consistent orientation for a set of feather-like structures that coincides with the general direction of shear of the sample (Fig. 3.9b, d and e). The feather structures show significant reduction of the grain size by bending and eventually breaking the fibres, creating an area of small oriented fibres that form the feather structure and are only recognisable at the TEM-scale (Fig. 3.9).

HR-TEM images show that the (110) lattice fringes in sepiolite crystals are continuous and no layer terminations were observed (Fig. 3.10). High-resolution images of the sepiolite crystals show lattice planes spacing that vary from 1.10 nm to 1.24 nm (Fig. 3.10). Some crystals (Fig. 3.10a) exhibit d-spacing closer to the ideal 1.20 and 1.21 nm. Meanwhile other sepiolite crystals show progressive decrease of the d-spacing (Fig. 3.10b and 3.10c).

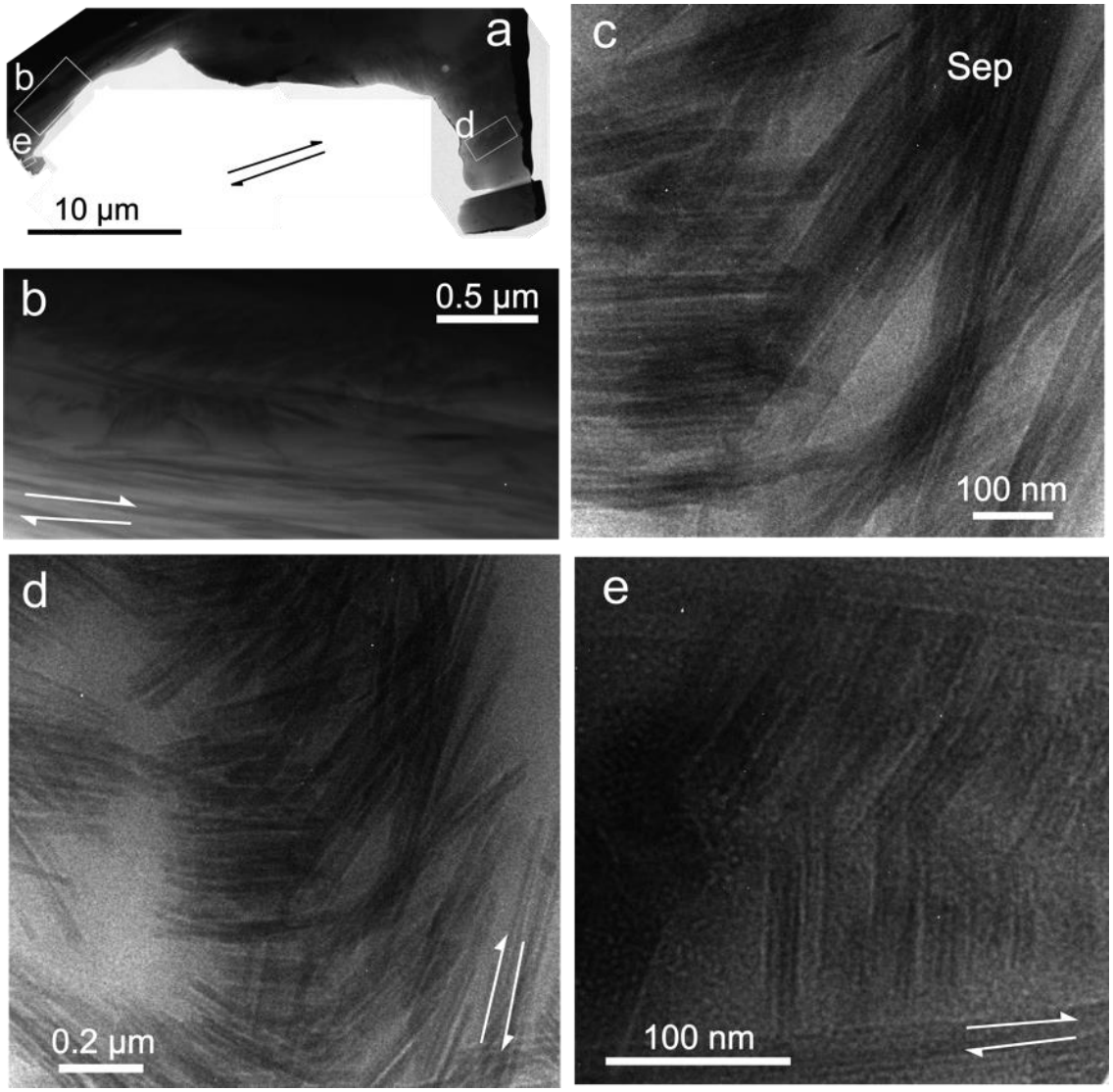


**Figure 3.9.** TEM images of a FIB-lamellae sample of a sepiolite fault rock **a.** General view of the lamellae extracted from the red rectangle shown in Fig. 3.2.a. **b.** Feather structure following the direction of shear. **c.** General texture of the naturally deformed sepiolite-rich fault rock. **d. and e.** Feather structures.

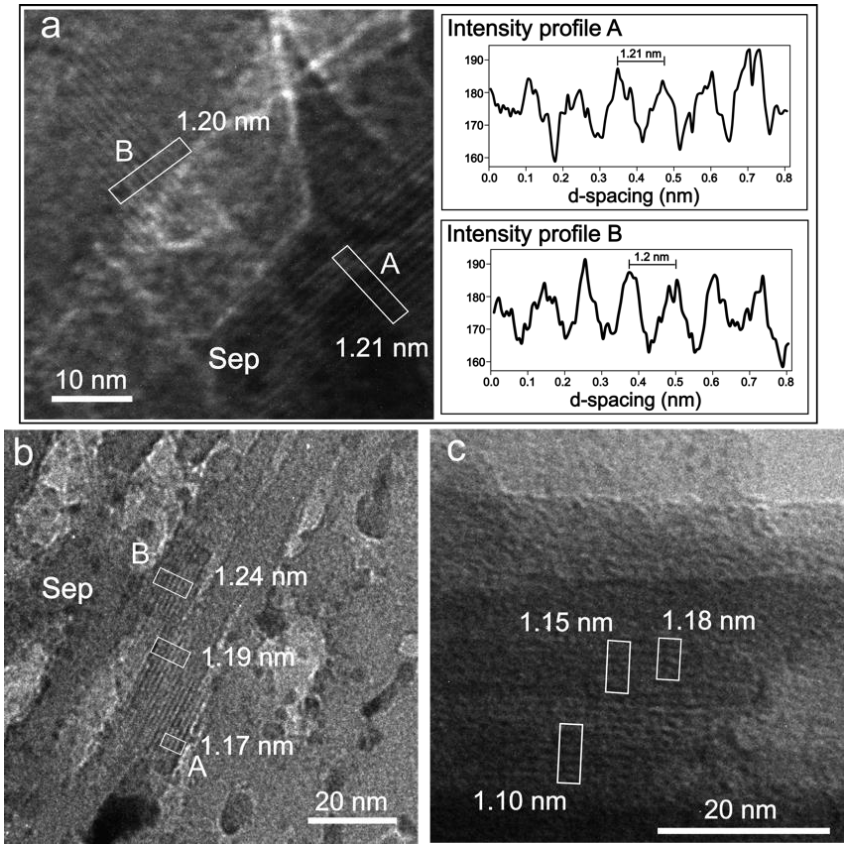


**Figure 3.10. a.** High-resolution TEM image of the sepiolite crystal lattice with close to ideal d-spacing 1.21 nm. Insets show the intensity profiles along crystals A and B and average d-spacing results. **b and c.** High-resolution images of the sepiolite crystal lattice with variable d-spacing from 1.10 nm to 1.24 nm.

High-resolution images on single fibres in the sepiolite-rich naturaly deformed samples showed multiple crystals with d-spacings intermediate between palygorskite and sepiolite showing a range of d-spacings from 1.03 nm to 1.18 nm (Fig. 3.11a). Furthermore the images show crystals with d-spacings of 1.04 to 1.06 nm which corresponds to the (110) plane of palygorskite, as well as lattice fringe spacings of 0.46 nm corresponding with the (400) plane of palygorskite with an ideal spacing of 0.45 nm. Crystal defects as dislocations were identified within these palygorskite crystals. (Fig. 3.11b).

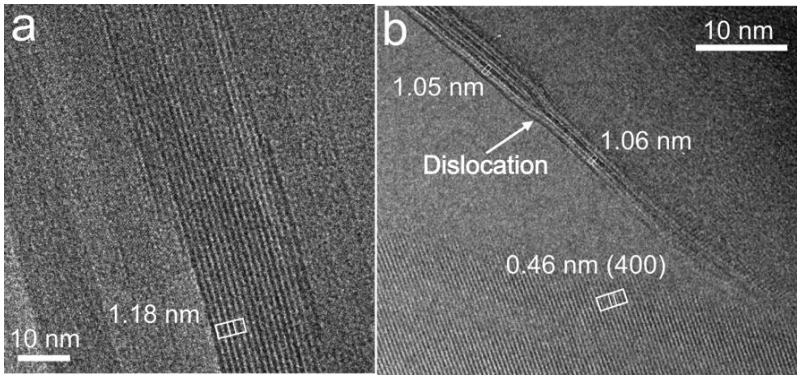


**Figure 3.11.** HR-TEM images of individual fibres in the sepiolite-rich gouge. **a.** Fibres with lattice spacing of 1.18 nm, slightly lower to those for ideal sepiolite. **b.** Fibre with lattice spacings corresponding with a palygorskite crystal.

4.2.2 Experimentally-deformed gouges

a. Smectite and palygorskite fault gouge material (wet and dry deformation)
Under wet conditions, low magnification images of the experimentally-deformed gouge fabric show two distinctively different textures of the rock (Fig. 3.12a). The first texture shows an oriented fabric constituted of laminar aggregates (Fig. 3.12b) that isolate the lenses of the second texture (Fig. 3.12a). Smectite and illite crystals constitute the matrix of texture 1 in the artificially fabricated gouge, these phyllosilicates are aligned on their basal planes, contrary to the initial random orientation of the crushed and powdered natural rock when placed on the sliders. Smectite spacing in these samples has been identified at around 1.02 nm and it is possible to recognise a number of deformation features including delamination of the phyllosilicates and shearing of phases with larger grain size, such as gypsum (Fig. 3.12b).

The second texture exhibits a more homogeneous aspect without visible crystals or any particular fabric orientation (Fig. 3.12c). High-resolution observations show that the origin of the two textures relates to the type of phyllosilicate in the area. Texture 1 is composed of smectite and illite, while texture 2 is entirely composed of the fibrous palygorskite (Fig. 3.12c).

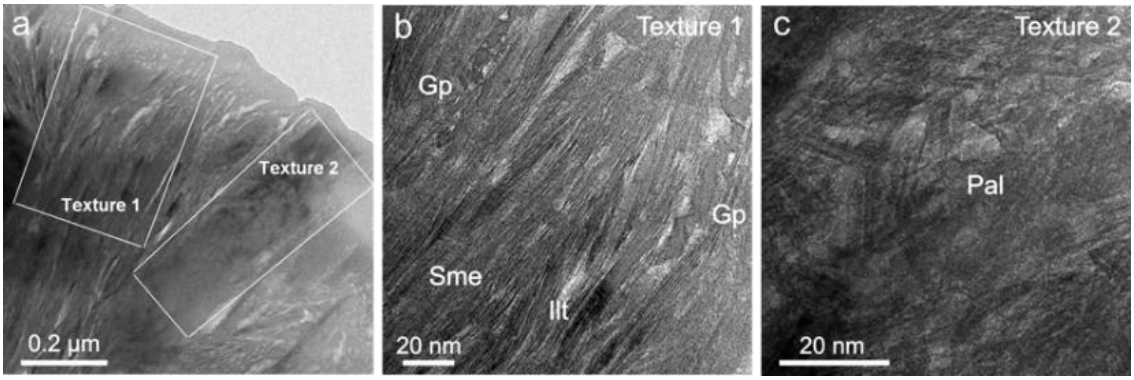


**Figure 3.12. a.** Low magnification image of the experimentally-deformed smectite and palygorskite gouge exhibiting two distinctively different textures of the rock. **b.** Magnification of texture 1 showing aggregates of smectite crystals. **c.** Magnification of texture 2 showing disoriented palygorskite fibres.

Samples deformed under the absence of water (dry deformation) show the same kind of phase segregation showed in the samples deformed under wet conditions (Fig. 3.13). Smectite-rich areas form sigmoidal structures and present large elongated pores that follow the orientation of the fluent deformation structure (Fig. 3.13a). SAED patterns are difficult to obtain for individual grains; however, the general SAED patterns in the matrix of both textures show significant differences confirming the segregation of mineral phases by habit. SAED pattern from areas rich in planar phyllosilicates are turbostratic, where the long axis represents d-spacings of 1.00 nm corresponding with the lattice spacing of the (001) plane of illite and possibly the collapsed smectite crystals, and the short axis represents d-spacings of 0.52 nm corresponding with the (003) plane of smectite (Fig. 3.13b inset). SAED

patterns from areas rich in fibrous phyllosilicates show a d-spacing of the first internal circle of 0.44 nm which corresponds with the (400) reflection of palygorskite (Fig. 3.13c inset).

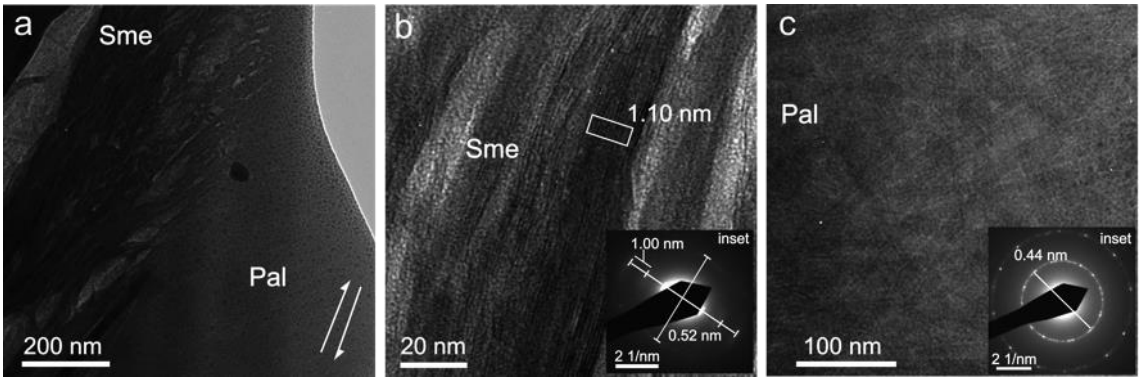


**Figure 3.13. a.** TEM image and general view of the lamellae extracted from the red rectangle shown in Fig. 3.6c **b.** Magnification of texture 1 showing aggregates of smectite crystals. **inset.** SAED patterns of texture 1. c. Magnification of texture 2 showing disoriented palygorskite fibres. **inset.** SAED patterns of texture 2.

b. Sepiolite fault gouge (wet and dry deformation)

The general texture in the gouge deformed under wet conditions shows a continuous feather structure or kinks (Fig. 3.14a and b). High-resolution images show (110) planes of sepiolite crystals with different d-spacing, varying from 1.14 to 1.20 nm (Fig. 3.14c), this particular image with angular edges is possibly viewing the crystals along the [100] direction. The parallelogram-shaped minerals could be the result of a cross-section of rod meso-crystals that resemble open channel defects described by Krekeler and Guggenheim (2008).

Very few images were obtained from the gouge deformed under dry conditions. The lattice fringe spacing of the sepiolite crystals measured in this preparation was 1.14 nm.

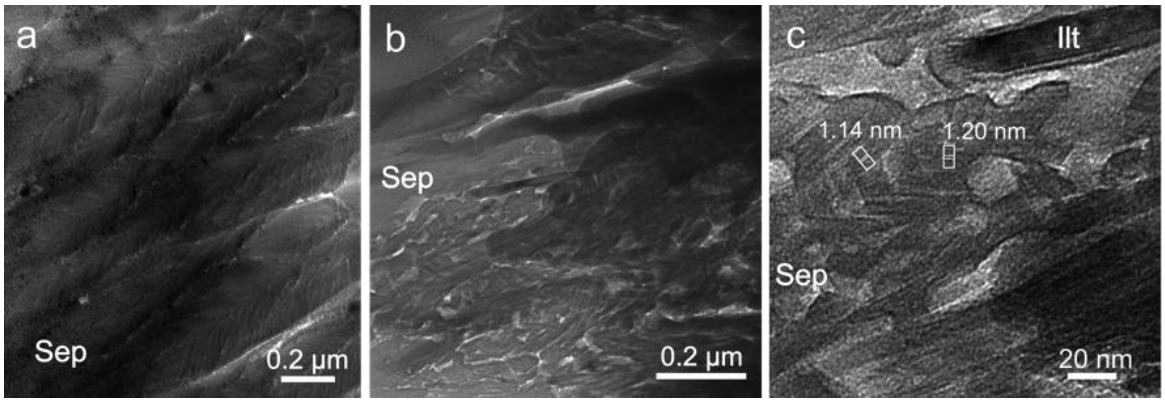


**Figure 3.14. a.** Low magnification TEM image showing the general texture of the sepiolite fault gouge under wet deformation and kinked sepiolite laths **b.** TEM image on the feather-like structures that form the matrix after deformation **c.** HR-TEM image of sepiolite crystals in the sepiolite fault gouge material under wet deformation.

### 4.3 Analytical Electron Microscopy

AEM analyses of single crystals from the two fault gouges in the Galera Fault Zone were collected to define the chemical compositions of sepiolite, palygorskite and smectite crystals and are presented in Figure 3.15 in the form of the main octahedral oxides to detect transitional compositions between sepiolite and palygorskite as well as between palygorskite and smectites. The fibrous samples plot continuously in all the compositional ranges discriminated in Suárez and García-Romero (2013), without mayor compositional gaps (Fig. 3.15). AEM analysis of smectite and palygorskite have great similitudes, palygorskite has a slightly higher Mg content than smectite, however the most significant feature to differentiate between them is their morphology.

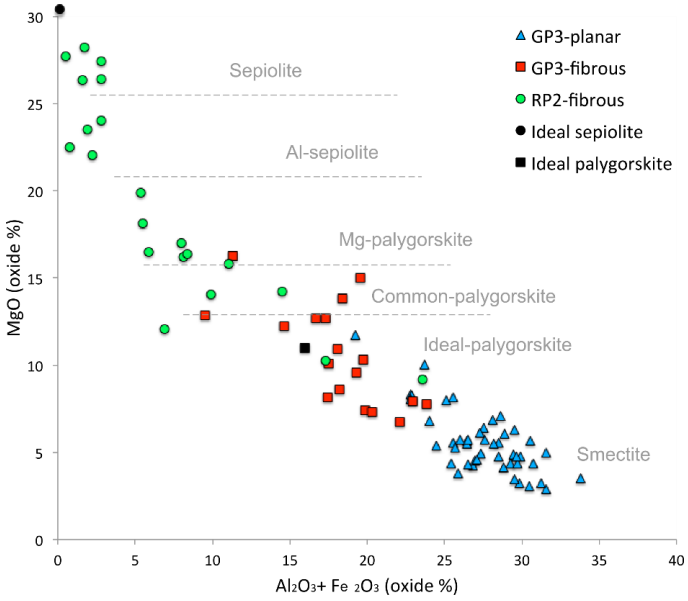


**Figure 3.15.** Variability in the octahedral cation content of the sepiolites, palygorskites and smectites of the study and their chemical classification according to Suárez and García-Romero (2013). Ideal octahedral cation oxide content for sepiolite and palygorskite are plotted according to García-Romero and Suárez (2010).

In order to identify whether or not the origin of the smectites present within the fault plane are authigenic, 89 smectite crystals were analysed including smectites collected from within the fault plane and smectites from the two principal lithologies in the sedimentary sequence of the wall-rock. The chemical composition of the major octahedral cations in the smectite crystals are presented in Figure 3.16. For the full list of normalised chemical formulas see Supplementary information, Table 3.S1.

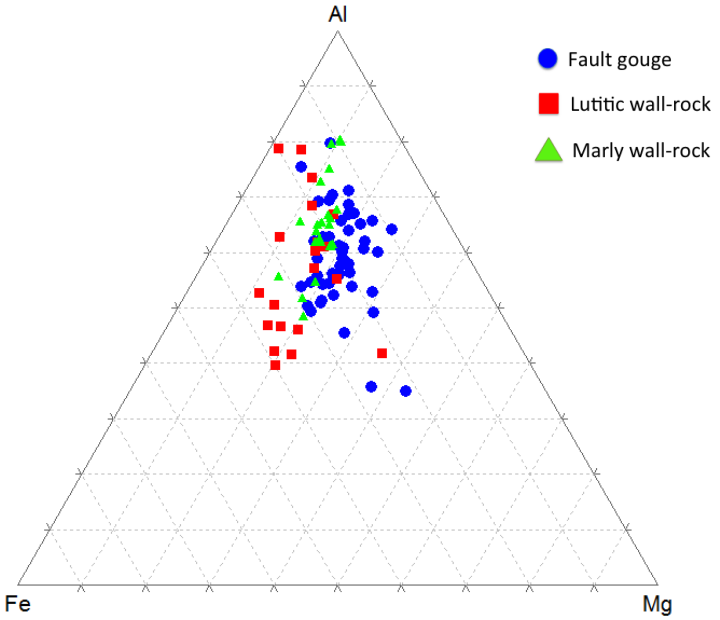


**Figure 3.16.** Ternary plot of major octahedral cations in smectite crystals form the fault rock in blue, lutitic wall rock in red and marly wall rock in green.

Most of the smectites analysed show a beidellite character. Smectites from the lutitic strata show a higher content of Fe, while those from the marly strata show a higher Al content. Smectites from the fault plane have chemical features similar to both the marls and the lutites from the wall rock, however their Mg content within the octahedral layer appears slightly higher than those from the wall rocks.

The identification of a small peak of palygorskite in XRD analysis motivated the exploration of the chemical composition of the sepiolite fibres in the sepiolite-rich gouge. A sequence of chemical analysis acquired within 46 individual fibres of sepiolite show small content of aluminium in 16 of the crystals. The highest Al content appears towards the edges of the crystals in 9 of the 16 crystals; while for the remaining 7 the Al content seems to be similarly distributed along the crystals. Differences in the Al content are noticeable within an individual fibre (Fig. 3.17), where the area of analysis 3 (in red) shows significantly higher Al content than areas 1 and 2.

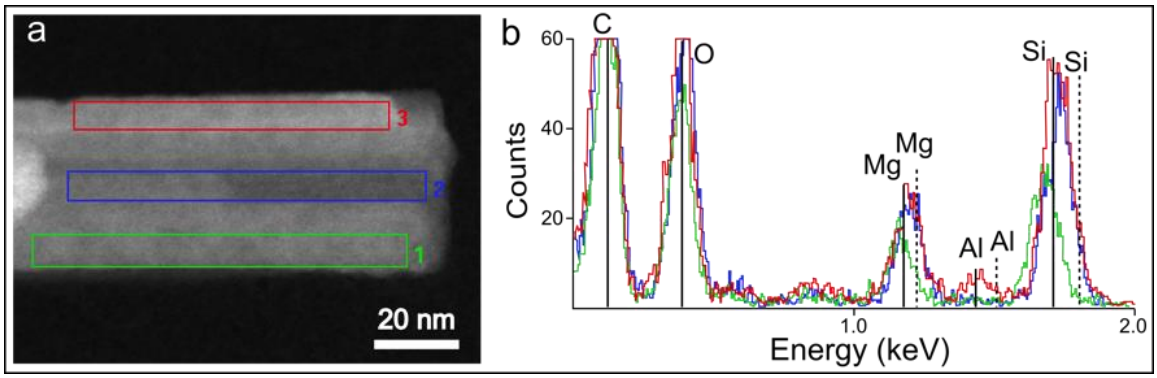


**Figure 3.17. a.** Sepiolite crystal and selected areas for microanalysis **b.** TEM-AEM analysis of three selected areas of sepiolite crystal.

### 4.4 Permeability

The values obtained from the permeability measurements on the smectite-rich fault gouge range between 1 $x10^{-20}$ to 1 $x10^{-21}$ $m^2$, which decrease almost linearly with a raise in confining pressure from 5 to 100 MPa, while results for the sepiolite-rich fault gouge range between 1 $x10^{-18}$ to 1 $x10^{-19}$ $m^2$ (Fig. 3.18).

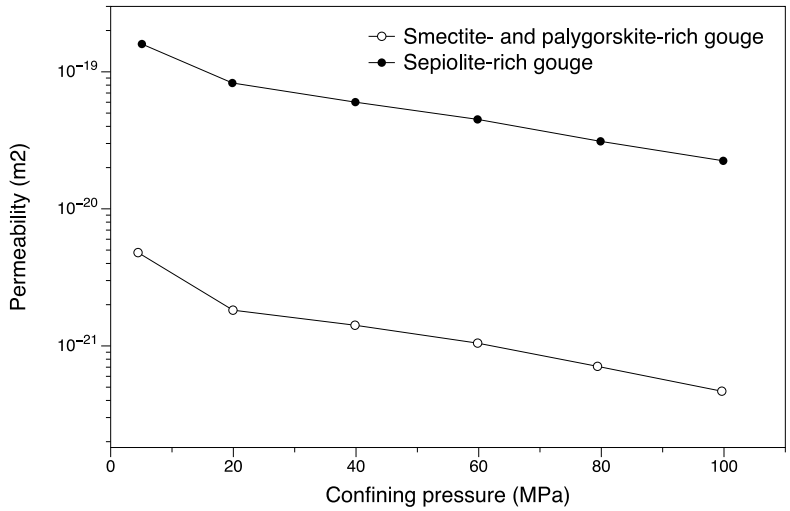


**Figure 3.18.** Permeability measurements on the two gouges with increasing confining pressure on a triaxial deformation apparatus.

## 5. Discussion

### 5.1 Deformation features in planar and fibrous clay minerals

Clay minerals are mayor constituents of many fault gouges (Haines and van der Pluijm, 2012; Rutter et al., 2012; Schleicher et al., 2013), reaching up to 99.5% in the Central Deforming Zone of the San Andreas Fault (Hadizadeh et al., 2012; Janssen et al., 2014), and constitute the majority of the fault gouge in the Galera Fault Zone (Sánchez-Roa et al., 2016). However, not all clay minerals have the same physical and chemical properties and possibly neither the same mode of deformation. In this section we aim to compare the deformation features from platy and fibrous clay minerals to identify possible differences on their behaviour under shear in both natural faults and friction experiments. The Galera Fault Zone is an ideal natural example for this study due to the presence of both platy and fibrous clay minerals within its main sliding planes (Sánchez-Roa et al., 2016).

Frictional deformation in phyllosilicates is facilitated by a series of micromechanisms including grain-grain sliding when the planar minerals are aligned on their basal planes, delamination, cataclasis, crystal plasticity, pressure-solution creep, etc. These processes are controlled by many factors including pressure and temperature (Beeler, 2007; French et al., 2015).

SEM observations on samples in this study do not show significant differences between the microstructures of wet and dry frictional experiments as has been previously described for microstructures of phyllosilicates sheared at low temperatures (Moore and Lockner, 2004;

Behnsen and Faulkner, 2013; Haines et al., 2013). In general all SEM observations in the experimentally-deformed samples show distributed deformation within the phyllosilicates of the matrix (Figs 1 to 6).

TEM observations on the smectite-rich gouge show how smectite crystals present broken and displaced lattice fringes in the rock matrix in order to accommodate deformation (Fig. 3.7). In this way smectite crystals ensure an uniform distribution of the shear in the rock. The quick alignment of the smectite and illite crystals of the matrix of the smectite- and palygorskite-rich samples in the experimentally-deformed gouges demonstrate that when the shear deformation starts, the platy minerals rapidly adopt a preferred orientation producing a very similar fabric to the one observed in the naturally deformed rocks. Smectite crystals aggregate together with the same orientation on their basal planes, and facilitate grain on grain sliding as well as delamination processes that accommodate deformation through creeping (Fig. 3.7).

On the other hand the fibrous phyllosilicate gouge shows mainly three different orientations of the fibres; this grid-like microfabric (Fig. 3.8) and the absence of weak cleavage planes for intragranular sliding result in the formation of feather structures that mark areas where the deformation processes have been localised producing the observed grain size reduction through a mechanical bending and breaking of the fibres. The orientation of the feather-like structures (Fig. 3.9), resemble the orientation of Riedel shears (Rutter et al., 1986). Indicating that deformation is localising by bending and breaking the fibres at a very small scale that is not visible until the clay fraction of the gouge is examined in detail (Fig. 3.9, 3.14).

In the case of the experimentally-deformed smectite- and palygorskite-rich gouge no feather structures were observed, a phenomenon that can be explained by the high amount of smectite in the sample that accommodates most of the deformation without the need to affect the stronger palygorskite-rich areas.

In HR-TEM observations, the delamination processes are visible in the smectite crystals, however in the fibrous materials the lattice fringes are mostly continuous and show no sign of delamination or layer termination, probably conditioned by the stronger bonds linking a TOT layer to the next. The higher strength of the fibrous structure hinders delamination processes accommodating the imposed deformation by breaking and bending of fibres resulting in a series of feather-like structures at the micro-scale (Fig. 3.9).

### 5.2 Permeability contrast

Permeability of fault zones is a relevant property that controls the subsurface fluid flow and plays an important role in coseismic fluid pressure changes, pore pressure build-ups and potential weakening of faults (Scuderi and Collettini, 2016). There is a difference of almost two orders of magnitude in the measured permeability for the two fault gouges in this study. This permeability contrast can be related to the gouge's texture and microfabric as well as to the nature of the dominant phyllosilicate for each gouge. Low magnification TEM observations show the porosity for the smectite-rich gouge as nanometer sized elongated

pores that extend with the same orientation as the crystals in the rock (Fig. 3.7); this porosity can possibly be related to the dehydration of the rock in ex-situ conditions, or be a real feature of the natural rock but remain isolated by the large continuity of the smectite crystals that create stacks of impermeable layers.

On the other hand, the fibre-rich gouge samples exhibits a more compact fabric without evidence of abundant porosity. TEM observations of areas with a strong grid-like microfabric reveal the development of a number of voids that will add nanoporosity to the rock and can be the reason for their highest permeability (Fig. 3.8).

Both gouges decrease their permeability with increasing confining pressure, however the smectite-rich fault gouge sustains greater decline in permeability for a given change in confining pressure (Fig. 3.18). The faster decrease in permeability for the smectite-gouge can be related to a much higher level of sheet alignment and lateral connectivity of the platy smectite crystals at medium to high pressures facilitated by the high particle mobility of this mineral (Behnsen and Faulkner, 2011). On the other hand, the grid-like microfabric in the fully fibrous material can leave room for a higher number of interconnected pores that add to the structural microporosity of the fibres, consequence of their internal channels. These results show how the permeability of the gouges in the Galera Fault is strongly affected by the mineralogy of the gouge and in particular by the shape of the grains and their microstuctural arrangement under shear.

### 5.3 Sepiolite to palygorskite phase transformation in the fault gounge

Sepiolite is the major phyllosilicate in one of the studied outcrops of the Galera Fault (Sánchez-Roa et al., 2016), as is supported by low- and high-resolution TEM images (Figs. 8, 9, 10 and 11). Nevertheless, significant contents in Al have been found in various of the analysed fibres, defining a continous trend between the compositional fields of sepiolite and palygorskite (Fig. 3.15). This Al is preferently associated to the border of the fibre, with a tendency to be absent in their centre (Fig. 3.17), and is expected to be associated to nanometer sized (less than 6 nm) discrete areas of palygorskite (Fig. 3.11b, 3.17). The d-spacing variation of lattice fringes on HR-TEM images of sepiolite ranges from 1.1 nm to 1.24 nm (Fig. 3.10). The presence of different d-spacings could suggest small contributions of palygorskite polysomes to the sepiolite structure (García-Romero and Suárez, 2013) that alter the regular (110) spacing of sepiolite ideally defined at 1.22 nm.

In nature, the progressive transformation from one phase to another, due to a changes in chemical and/or physical conditions, may occur via polysomatic reactions as it is the case of smectite to illite, through illite/smectite mixed-layers (Hower et al., 1976), or in the case of the transformation from piroxenes to amphiboles, through pyriboles (Veblen and Buseck, 1981). In both cases, high-resolution images display the new polysome as individual unit cells within the former phase showing their respective characteristic spacings, which allow the clear identification of the areas in which the new polysome is present (Bozhilov et al., 2007; Vázquez et al., 2014). In other cases, the new phase nucleates as discrete crystals, sometimes assisted by topotactic or epitactic mechanisms (Sánchez-Navas, 1999), but without the existence of intermediate stadiums (e.g chlorite to biotite transformation or the

transformation among the aluminium silicate polymorphs). Figure 3.11 could represent such a case or could be a more advanced stadium in the progresive development of polysomes. Contrarily from the layer silicates, the sepiolite- palygorskite polysomes would be individual chains. Taking into account that a lattice fringe in a high-resolution image would include at least 15.38 unit cells in depth, assuming an average width of 20 nm per fibre, the variability in the measured spacings could be the result of different proportions of the two types of chains, representing a weighted average of the spacings of the two polysomes. Nevertheless, we have not found individual lattice fringes corresponding to the palygorskite spacing in a matrix of sepiolite, as a difference with the case described for pyriboles by Bozhilov et al. (2007). Hence, our results cannot be considered conclussive in relation to the mechanism of transformation between sepiolite and palygorskite, but chemical analysis confirmed that the Al content appears often towards the edges of the crystals (Fig. 3.17). This suggests that the phase transformation starts affecting the edges of sepiolite fibres by including Al in palygorskite polysomes or directly producing the growth of individual crystals of palygorskite.

This phenomenon in the context of fault zones can be related to a higher fluid-rock interaction of the gouge with meteoric waters related to exhumation and deformation, which favour Al-contributions from the sedimentary sequence and, thus, the formation of palygorskite.

### 5.4 Paligorskite to Mg-smectite transformation in the fault gouge

Quantitative chemical analysis in paligorskite and smectite particles show mixed compositions in particular showing a compositional overlaping between fibrous and smectite crystals (Fig. 3.15). This chemical similarity of some palygorskite and smectites crystals suggest that either an epitaxial transformation or some mineral intergrowth between smectite and palygorskite crystals is taking place within the smectite- and palygorskite-rich sample (Fig. 3.15).

To further support this argument AEM analysis on 89 crystals of smectite from the two main levels of the sedimentary sequence of the wall rock and smectites from the fault plane are shown in Figure 3.16. The results of the normalised chemical formula for the major octahedral cations in the three groups of smectite show that the smectites with higher Mg content correspond to the smectites of the fault plane. The most common products of the transformation of fibrous clay minerals in experimental studies are Mg-rich smectites (Golden and Dixon, 1990). These results suggest that an important portion of the smectites within the fault plane have an authigenic origin, which is likely the result of a transformation reaction from palygorskite.

Previous studies on the transformation of fibrous clay minerals to smectites have experimentally showed that the product of hydrothermally transformed sepiolite is often constituted by lath-like morphology smectite (Guven and Carney, 1979), this phenomenon was again observed in the transformation from palygorskite to smectite and explained by smectite forming within the palygorskite laths prior to their physical disruption producing a palygorskite pseudomorph composed of smectite (Golden and Dixon, 1990).

According to the two well-defined textures in the experimentally-deformed rock (Fig. 3.12, 3.13) and the absence of the texture segregation in the naturally deformed rock (Fig. 3.7), we suggest that this textural difference could be an indication that the palygorskite crystals were indeed intergrown with smectite crystals in the natural rock. Segregation of mineral phases observed in the experimentally-deformed rocks can, on the other hand, occur as a result of the disaggregation of the rock during sample preparation and re-aggrupation of crystals by habit during the experiment (Fig. 3.12).

## 5.5 Geological implications

Transformations between fibrous and planar clay minerals in fault zones are important and occur in the Galera Fault. These mineral transformations could alter fault strength, affecting earthquake nucleation and propagation processes taking place in different materials. Based on our results we propose an evolution of the Mg-rich fault gouge in the Galera Fault with progressive exhumation and consequent increase of Al-activity product of the interaction of meteoric waters with the wall rocks. The evolution sequence starts with the precipitation of sepiolite from Mg-rich hydrothermal fluids (Sánchez-Roa et al., 2016). Sepiolite crystals start to incorporate palygorskite domains to produce a first evolution stage where both sepiolite and palygorskite are present as independent crystals as is the case of the studied gouge from the Galera Fault. Following this, we propose a second evolution stage intermediate between the two gouges studied, in which all sepiolite has been transformed to palygorskite. The smectite-palygorskite gouge from the Galera Fault constitutes a third stage of transformation in which part of the palygorskite has been transformed to smectite as a result of the large Al-availability forming Mg-rich smectite with a different chemical signature of the smectites in the wall rock. It is possible that further alteration of the fault gouge results in the complete disappearance of fibrous minerals by a full transformation to platy Mg-rich smectite. The strength of the two fault gouges in the Galera Fault are highly contrasting, the sepiolite-rich gouge has a higher friction coefficient ($\mu$=0.47 under wet deformation), while the gouge smectite and palygorskite-rich gouge has a lower friction coefficient ($\mu$=0.17 under wet deformation) (Sánchez-Roa et al., 2016). The presence of smectite has proven to have important effects on the strength of faults by contributing to a lower frictional strength and has been reported to have a weakening effect on concentrations as low as 10 wt% (Oohashi et al., 2015). Furthermore, previous studies comparing the strength of monomineralic fibrous clay minerals and the smectite saponite have shown that their frictional strength is dictated by their crystal structure showing that fibrous Mg-rich phyllosilicates are stronger than the platy smectite (Sánchez-Roa et al., 2017). Therefore, we suggest that the strength of the Galera Fault could be, to a great extent, controlled by the development of the palygorskite to smectite transformation within the fault planes.

Finally this type of transformation between fibrous and planar clay minerals (specifically smectite) could occur in other type of geological deposits under a variety of conditions. As a consequence these mineral transformations will drastically change important chemical and physical properties in the rock as surface area and cation exchange capacity that significantly alter the microfabric and permeability of the geological material.

## 6. Conclusions

The micro-scale deformation mechanisms of smectites and fibrous clay minerals differ significantly. The smectite-rich gouge shows a great number of layer terminations and delamination processes in the basal cleavage plane that contribute to a distributed mode of deformation in the gouge resulting in creeping. On the other hand, fibre disorientation and the random fabric of the sepiolite-rich gouge result in the localisation of deformation in punctual areas where sepiolite crystals are bent and broken without the presence of lattice distortions and finally producing feather-like structures.

Sample analysis shows higher porosity in the smectite-rich sample than in the smectite and palygorskite gouge. However permeability measurements show values of permeability for the sepiolite-rich gouge, which are one to two orders of magnitude higher than the smectite-rich gouge. The results can be explained assuming that pores in the smectite-rich gouge are completely isolated by impermeable smectite crystals, while a grid-like microfabric in the fibrous gouge and channel nanoporosity of the fibrous structures create a network of interconnected pores that allow higher permeability in the sepiolite-rich gouge. Furthermore particle alignment and connectivity in platy crystals increases faster with confining pressures producing a rapid decrease of permeability.

Habit segregation of the minerals in a gouge with mixed planar and fibrous clay minerals seems to be a common process in experimentally-deformed gouges. This process evidences how fast planar phyllosilicate interconnectivity develops in a deforming rock and the great effects they can have in facilitating distributed deformation. The absence of the segregation in the natural rock can be due to the fact that smectite is, at least in part, a transformation product of palygorskite and the two remain intergrown in the natural gouge. The segregation takes place during the mechanical grinding of the material where the intergrown minerals separate and reacomodate during the friction experiment.

A progressive transformation from sepiolite to palygorskite within the fault rock is suggested by chemical analysis acquired within individual fibres confirming the prescence of Al content towards the edges of the crystals. Furthermore, this observation is supported by the wide variability in the 110 d-spacing of sepiolite lattice fringes. This phenomenon can occur by including Al in palygorkite polysomes or by the growth of individual crystals of palygorskite on sepiolite crystals. The transformation from sepiolite to palygorskite can be triggered by a higher Al-input to the system and pore fluid chemistry disequilibrium, both product of exhumation and deformation.

The identification of authigenic smectites with a higher Mg content than smectites from the protolith in the smectite-rich gouge, suggests a mineral transformation between palygorskite and smectite. Transformations between fibrous and planar phyllosilicates can have important geological implications such as contrasting fault strength and stability, as well as industrial implications since partial or total transformations between the two mineral groups will drastically change important chemical and physical properties of the mineral, including surface area and cation exchange capacity.

The comparison of naturally- and experimentally-deformed samples in this study was a valuable tool in the identification of mineral authigenesis and microstructural features ocurring within the active Galera Fault Zone. Furthermore, the use of electron microscopy to explore fault rocks has permitted to recognise progresive mineral transformations and deformation microstructures otherwise undetectable.

## Acknowledgments

The authors would like to thank Dr.M.M. Abad-Ortega, A.Martinez-Morales and, Dr M. A. Laguna, Dr. A. Ibarra, Dr. R. Fernández-Pacheco for their support in electron microscopy data acquisition. This work has been financed by the research projects CGL2011-30153-C02-01,CGL2011-30153- C02-02, and CGL2013-46169-C2-1-P from MINECO, research project UJA2014/06/17 from the Universidad-Caja Rural de Jaén, Research Groups RNM-179 and RNM-325 of the Junta de Andalucía, UK NERC grant NE/J024449/1 and the F.P.I. Grant No. BES-2012-052 562 from the Spanish Government (Ministerio de Economía y Competitividad).

## References

Abad, I., Nieto, F., and Velilla, N., 2002, Chemical and textural characterisation of diagenetic to low-grade metamorphic phyllosilicates in turbidite sandstones of the South Portuguese Zone: A comparison between metapelites and sandstones: Schweizerische Mineralogische und Petrographische Mitteilungen, v. 82, p. 303–324.

Beeler, N.M., 2007, Laboratory-observed faulting in Intrinsically and Apparently Weak Materials: The Seismogenic Zone of Subduction Thrust Faults, p. 370–449.

Behnsen, J., and Faulkner, D.R., 2013, Permeability and frictional strength of cation-exchanged montmorillonite: Journal of Geophysical Research: Solid Earth, v. 118, no. 6, p. 2788–2798, doi: 10.1002/jgrb.50226.

Behnsen, J., and Faulkner, D.R., 2011, Water and argon permeability of phyllosilicate powders under medium to high pressure: Journal of Geophysical Research: Solid Earth, v. 116, no. 12, p. 1–13, doi: 10.1029/2011JB008600.

Bozhilov, K.N., Brownstein, D., and Jenkins, D.M., 2007, Biopyribole evolution during tremolite synthesis from dolomite and quartz in CO2-H2O fluid: American Mineralogist, v. 92, no. 5-6, p. 898–908, doi: 10.2138/am.2007.2376.

Brace, W.F., Walsh, J.B., and Frangos, W.T., 1968, Permeability of Granite under High Pressure: Journal of Geophysical Research, v. 73, no. 6.

Cliff, G. and Lorimer, G. W., 1975. The quantitative analysis of thin specimens: Journal of Microscopy, 103: 203-207. doi:10.1111/j.1365-2818.1975.tb03895.x

Faulkner, D.R., Jackson, C.A.L., Lunn, R.J., Schlische, R.W., Shipton, Z.K., Wibberley, C. a J., and Withjack, M.O., 2010, A review of recent developments concerning the structure, mechanics and fluid flow properties of fault zones: Journal of Structural Geology, v. 32, no. 11, p. 1557–1575, doi: 10.1016/j.jsg.2010.06.009.

French, M.E., Chester, F.M., and Chester, J.S., 2015, Micromechanisms of creep in clay-rich gouge from the Central Deforming Zone of the San Andreas Fault: Journal of Geophysical Research B: Solid Earth, v. 120, no. 2, p. 827–849, doi: 10.1002/2014JB011496.

García-Romero, E., and Suárez, M., 2010, On the chemical composition of sepiolite and palygorskite: Clays and Clay Minerals, v. 58, no. 1, p. 1–20, doi: 10.1346/CCMN.2010.0580101.

García-Romero, E., and Suárez, M., 2013, Sepiolite-palygorskite: Textural study and genetic considerations: Applied Clay Science, doi: 10.1016/j.clay.2013.09.013.

García-Tortosa, F.J., Alfaro, P., Sanz de Galdeano, C., and Galindo-Zaldívar, J., 2011, Glacis geometry as a geomorphic marker of recent tectonics: The Guadix-Baza basin (South Spain): Geomorphology, v. 125, no. 4, p. 517–529, doi: 10.1016/j.geomorph.2010.10.021.

Giese, R.F., 1978, Electrostatic Interlayer Forces of Layer Structure Minerals.: Clays and Clay Minerals, v. 26, no. 1, p. 51–57, doi: 10.1346/CCMN.1978.0260106.

Golden, D.C., and Dixon, J.B., 1990, Low-temperature alteration of palygorskite to smectite: v. 38, no. 4, p. 401–408.

Guven, N., and Carney, L.L., 1979, HYDROTHERMAL TRANSFORMATION OF SEPIOLITE TO STEVENSITE AND THE EFFECT OF ADDED CHLORIDES AND HYDROXIDES.: Clays and Clay Minerals, v. 27, no. 4, p. 253–260, doi: 10.1346/CCMN.1979.0270403.

Hadizadeh, J., Mittempergher, S., Gratier, J.P., Renard, F., Di Toro, G., Richard, J., and Babaie, H. a., 2012, A microstructural study of fault rocks from the SAFOD: Implications for the deformation mechanisms and strength of the creeping segment of the San Andreas Fault: Journal of Structural Geology, v. 42, p. 246–260, doi: 10.1016/j.jsg.2012.04.011.

Haines, S.H., Kaproth, B., Marone, C., Saffer, D., and Van der Pluijm, B., 2013, Shear zones in clay-rich fault gouge: A laboratory study of fabric development and evolution: Journal of Structural Geology, v. 51, p. 206–225, doi: 10.1016/j.jsg.2013.01.002.

Haines, S.H., and van der Pluijm, B.A., 2012, Patterns of mineral transformations in clay gouge, with examples from low-angle normal fault rocks in the western USA: Journal of Structural Geology, v. 43, p. 2–32, doi: 10.1016/j.jsg.2012.05.004.

Hickman, S., Sibson, R., and Bruhn, R., 1995, Mechanical involvement of fluids in faulting: Journal of Geophysical Research, v. 100, no. B7, p. 12831–12840, doi: 10.1029/94EO01059.

Houwers, M.E., Heijnen, L.J., Becker, A., and Rijkers, R., 2015, A Workflow for the Estimation of Fault Zone Permeability for Geothermal Production A General Model Applied on the Roer Valley Graben in the Netherlands: Proceedings World Geothermal Congress 2015, , no. April, p. 9.

Hower, J., Eslinger, E. V., Hower, M.E., and Perry, E. a., 1976, Mechanism of burial metamorphism of argillaceos sediment: Geological Society Of America Bulletin, v. 87, no. 60512, p. 725–737, doi: 10.1130/0016-7606(1976)87<725.

Ibanez, W.D., and Kronenberg, A.K., 1993, Experimental deformation of shale: Mechanical properties and microstructural indicators of mechanisms: International Journal of Rock Mechanics and Mining Sciences and, v. 30, no. 7, p. 723–734, doi: 10.1016/0148-9062(93)90014-5.

Janssen, C., Wirth, R., Wenk, H.R., Morales, L., Naumann, R., Kienast, M., Song, S.R., and Dresen, G., 2014, Faulting processes in active faults - Evidences from TCDP and SAFOD drill core samples: Journal of Structural Geology, v. 65, p. 100–116, doi: 10.1016/j.jsg.2014.04.004.

Kim, J.W., Peacor, D.R., Tessier, D., and Elsass, F., 1995, A technique for maintaining texture and permanent expansion of smectite interlayers for TEM observations: Clays and Clay Minerals, v. 43, no. 1, p. 51–57, doi: 10.1346/CCMN.1995.0430106.

Krekeler, M.P.S., and Guggenheim, S., 2008, Defects in microstructure in palygorskite-sepiolite minerals: A transmission electron microscopy (TEM) study: Applied Clay Science, v. 39, no. 1-2, p. 98–105, doi: 10.1016/j.clay.2007.05.001.

Logan, J.M., Friedman, M., Higgs, N., Dengo, C., and Shimamoto, T., 1979, Experimental studies of simulated gouge and their application to studies of natural fault zones: Proc. Conf. VIII - Analysis of Actual Fault Zones in Bedrock, p. 305–343.

Mares, V.M., and Kronenberg, a. K., 1993, Experimental deformation of muscovite: Journal of Structural Geology, v. 15, no. 9-10, p. 1061–1075, doi: 10.1016/0191-8141(93)90156-5.

Mitchell, T.M., and Faulkner, D.R., 2008, Experimental measurements of permeability evolution during triaxial compression of initially intact crystalline rocks and

implications for fluid flow in fault zones: Journal of Geophysical Research: Solid Earth, v. 113, no. 11, p. 1–16, doi: 10.1029/2008JB005588.

Moore, D.E., and Lockner, D.A., 2004, Crystallographic controls on the frictional behavior of dry and water-saturated sheet structure minerals: Journal of Geophysical Research, v. 109, no. B03401, p. 1–16, doi: 10.1029/2003JB002582.

Oohashi, K., Hirose, T., Takahashi, M., and Tanikawa, W., 2015, Dynamic weakening of smectite-bearing faults at intermediate velocities: Implications for subduction zone earthquakes: Journal of Geophysical Research-Solid Earth, v. 120, p. 11881, doi: 10.1002/2015JB011881.Received.

Overwijk, M.H.F., 1993, Novel scheme for the preparation of transmission electron microscopy specimens with a focused ion beam: Journal of Vacuum Science & Technology B: Microelectronics and Nanometer Structures, v. 11, no. 6, p. 2021–2024, doi: 10.1116/1.586537.

Peacor, D.R., 1992, Analytical electron microscopy, *in* Buseck, P.R. ed., Minerals and reactions at the atomic scale: Transmission electron microscopy., Mineralogical Society of America, p. 113–140.

Pluijm, B., Lee, J., and Peacor, D.R., 1988, Analytical Electron Microscopy and the Problem of Potassium Diffusion: Clays and Clay Minerals, v. 36, no. 6, p. 498–504.

Rutter, E.H., Faulkner, D.R., and Burgess, R., 2012, Structure and geological history of the Carboneras Fault Zone, SE Spain: Part of a stretching transform fault system: Journal of Structural Geology, v. 45, p. 68–86, doi: 10.1016/j.jsg.2012.08.009.

Rutter, E.H., Maddock, R.H., Hall, S.H., and White, S.H., 1986, Comparative microstructures of natural and experimentally produced clay-bearing fault gouges: Pure and Applied Geophysics, v. 124, no. 1-2, p. 3–30, doi: 10.1007/BF00875717.

Sakuma, H., and Suehara, S., 2015, Interlayer bonding energy of layered minerals: Implication for the relationship with friction coefficient: Journal of Geophysical Research: Solid Earth, p. 2212–2219, doi: 10.1002/2015JB011900.

Sanchez-Navas, A., 1999, Sequential kinetics of a muscovite-out reaction: A natural example: American Mineralogist, v. 84, no. 9, p. 1270–1286.

Sánchez-Navas, A., and Galindo-Zaldívar, J., 1993, Alteration and deformation microstructures of biotite from plagioclase-rich dykes (Ronda Massif, S. Spain): European Journal of Mineralogy, v. 5, no. 1987, p. 245–256.

Sánchez-Roa, C., Jiménez-Millán, J., Abad, I., Faulkner, D.R., Nieto, F., and García-Tortosa, F.J., 2016, Fibrous clay mineral authigenesis induced by fluid-rock interaction in the

Galera fault zone (Betic Cordillera, SE Spain) and its influence on fault gouge frictional properties: Applied Clay Science, doi: 10.1016/j.clay.2016.06.023.

Sánchez-Roa, C., Faulkner, D.R., Boulton, C., Jimenez-Millan, J., Nieto, 2017, How phyllosilicate mineral structure affects fault strength in Mg-rich fault systems: Geophysical Research Letters, doi: 10.1002/2017GL073055.

Schleicher, A.M., Hofmann, H., and van der Pluijm, B.A., 2013, Constraining clay hydration state and its role in active fault systems: Geochemistry, Geophysics, Geosystems, v. 14, no. 4, p. 1039–1052, doi: 10.1002/ggge.20077.

Schleicher, A.M., Van Der Pluijm, B. a., Solum, J.G., and Warr, L.N., 2006, Origin and significance of clay-coated fractures in mudrock fragments of the SAFOD borehole (Parkfield, California): Geophysical Research Letters, v. 33, no. 16, doi: 10.1029/2006GL026505.

Schleicher, A.M., van der Pluijm, B.A., and Warr, L.N., 2012, Chlorite-smectite clay minerals and fault behavior: New evidence from the San Andreas Fault Observatory at Depth (SAFOD) core: Lithosphere, v. 4, no. 3, p. 209–220, doi: 10.1130/L158.1.

Scuderi, M.M., and Collettini, C., 2016, The role of fluid pressure in induced vs. triggered seismicity: insights from rock deformation experiments on carbonates.: Scientific reports, v. 6, no. April, p. 24852, doi: 10.1038/srep24852.

Vázquez, M., Nieto, F., Morata, D., Droguett, B., Carrillo-Rosua, F.J., and Morales, S., 2014, Evolution of clay mineral assemblages in the Tinguiririca geothermal field, Andean Cordillera of central Chile: an XRD and HRTEM-AEM study: Journal of Volcanology and Geothermal Research, v. 282, p. 43–59, doi: 10.1016/j.jvolgeores.2014.05.022.

Veblen, D.R., and Buseck, P.R., 1981, Hydrous pyriboles and sheet silicates in pyroxenes and uralites: intergrowth microstructures and reaction mechanisms.: American Mineralogist, v. 66, no. 11-12, p. 1107–1134.

## Supplementary Material

Table 3.S1. Structural formulae calculated from AEM data for smectites normalised to $O_{10}(OH)_2$. All Fe as $Fe^{3+}$ and $^{IV}Al = (4 - Si)$.

| | Sample | Chemical formula | | | | | | | | | | | |
|---|---|---|---|---|---|---|---|---|---|---|---|---|---|
| | | Si | AlIV | AlVI | Fe | Mg oct | Ti | ∑ oct. | Ca | K | Na | Mg inter | ∑ inter. |
| 1 | GP-3-1 | 3.890 | 0.110 | 0.752 | 0.563 | 0.685 | 0.000 | 2.000 | 0.000 | 0.299 | 0.000 | 0.248 | 0.547 |
| 2 | GP-3-3 | 3.913 | 0.087 | 0.918 | 0.529 | 0.553 | 0.000 | 2.000 | 0.000 | 0.264 | 0.000 | 0.187 | 0.452 |
| 3 | GP-3-4 | 3.844 | 0.156 | 1.225 | 0.384 | 0.391 | 0.000 | 2.000 | 0.017 | 0.384 | 0.000 | 0.064 | 0.465 |
| 4 | GP-3-5 | 3.896 | 0.104 | 1.374 | 0.278 | 0.348 | 0.000 | 2.000 | 0.035 | 0.313 | 0.000 | 0.035 | 0.383 |
| 5 | GP-3-6 | 3.757 | 0.243 | 1.409 | 0.313 | 0.278 | 0.000 | 2.000 | 0.087 | 0.313 | 0.000 | 0.017 | 0.417 |
| 6 | GP-3-7 | 3.786 | 0.214 | 1.391 | 0.331 | 0.278 | 0.000 | 2.000 | 0.052 | 0.314 | 0.000 | 0.036 | 0.403 |
| 7 | GP-3-8 | 3.956 | 0.044 | 1.240 | 0.295 | 0.465 | 0.000 | 2.000 | 0.104 | 0.260 | 0.000 | 0.021 | 0.385 |
| 8 | GP-3-9 | 3.806 | 0.194 | 1.092 | 0.539 | 0.370 | 0.000 | 2.000 | 0.000 | 0.156 | 0.000 | 0.204 | 0.360 |
| 9 | GP-3-10 | 3.783 | 0.217 | 1.038 | 0.540 | 0.422 | 0.000 | 2.000 | 0.087 | 0.192 | 0.000 | 0.136 | 0.415 |
| 10 | GP-3-11 | 3.876 | 0.124 | 1.011 | 0.541 | 0.419 | 0.000 | 1.971 | 0.157 | 0.314 | 0.000 | 0.000 | 0.471 |
| 11 | GP-3-12 | 3.865 | 0.135 | 1.159 | 0.385 | 0.362 | 0.000 | 1.906 | 0.192 | 0.420 | 0.000 | 0.000 | 0.600 |
| 12 | GP-3-13 | 3.984 | 0.016 | 1.180 | 0.398 | 0.422 | 0.000 | 2.000 | 0.069 | 0.139 | 0.000 | 0.080 | 0.288 |
| 13 | GP-3-14 | 3.716 | 0.284 | 1.329 | 0.280 | 0.390 | 0.000 | 2.000 | 0.053 | 0.333 | 0.000 | 0.118 | 0.504 |
| 14 | GP-3-15 | 3.708 | 0.292 | 1.113 | 0.492 | 0.395 | 0.000 | 2.000 | 0.053 | 0.457 | 0.000 | 0.062 | 0.572 |
| 15 | GP-3-16 | 3.728 | 0.272 | 1.260 | 0.401 | 0.339 | 0.000 | 2.000 | 0.070 | 0.279 | 0.000 | 0.097 | 0.445 |
| 16 | GP-3-17 | 3.780 | 0.220 | 1.181 | 0.473 | 0.347 | 0.000 | 2.000 | 0.035 | 0.385 | 0.000 | 0.056 | 0.476 |
| 17 | GP-3-18 | 3.869 | 0.131 | 1.118 | 0.503 | 0.379 | 0.000 | 2.000 | 0.000 | 0.260 | 0.000 | 0.125 | 0.385 |
| 18 | GP-3-19 | 3.997 | 0.003 | 1.057 | 0.365 | 0.578 | 0.000 | 2.000 | 0.035 | 0.174 | 0.000 | 0.169 | 0.378 |
| 19 | GP-3-20 | 3.754 | 0.246 | 1.256 | 0.419 | 0.325 | 0.000 | 2.000 | 0.017 | 0.384 | 0.000 | 0.076 | 0.478 |
| 20 | GP-3-21 | 3.874 | 0.126 | 1.049 | 0.491 | 0.461 | 0.000 | 2.000 | 0.000 | 0.456 | 0.000 | 0.065 | 0.521 |
| 21 | GP-3-22 | 4.005 | 0.000 | 1.214 | 0.312 | 0.474 | 0.000 | 2.000 | 0.000 | 0.191 | 0.000 | 0.132 | 0.323 |
| 22 | GP-3-23 | 3.841 | 0.159 | 1.133 | 0.402 | 0.465 | 0.000 | 2.000 | 0.122 | 0.297 | 0.000 | 0.041 | 0.460 |
| 23 | GP-3-24 | 3.755 | 0.245 | 1.095 | 0.511 | 0.388 | 0.000 | 1.994 | 0.071 | 0.511 | 0.000 | 0.000 | 0.582 |
| 24 | GP-3-25 | 3.830 | 0.170 | 1.124 | 0.455 | 0.421 | 0.000 | 2.000 | 0.052 | 0.280 | 0.000 | 0.103 | 0.436 |
| 25 | GP-3-26 | 3.673 | 0.327 | 1.307 | 0.334 | 0.359 | 0.000 | 2.000 | 0.070 | 0.387 | 0.000 | 0.080 | 0.537 |
| 26 | GP-3-1 | 3.904 | 0.096 | 1.153 | 0.416 | 0.431 | 0.000 | 2.000 | 0.069 | 0.208 | 0.000 | 0.090 | 0.368 |
| 27 | GP-3-2 | 3.860 | 0.140 | 1.088 | 0.421 | 0.491 | 0.000 | 2.000 | 0.070 | 0.491 | 0.000 | 0.000 | 0.561 |
| 28 | GP-3-3 | 3.880 | 0.120 | 0.989 | 0.589 | 0.422 | 0.000 | 2.000 | 0.000 | 0.139 | 0.000 | 0.202 | 0.340 |
| 29 | GP-3-4 | 4.071 | 0.000 | 0.699 | 0.437 | 0.864 | 0.000 | 2.000 | 0.000 | 0.175 | 0.000 | 0.202 | 0.376 |
| 30 | GP-3-5 | 3.841 | 0.159 | 1.221 | 0.279 | 0.500 | 0.000 | 2.000 | 0.000 | 0.192 | 0.000 | 0.233 | 0.425 |

| | | | | | | | | | | | | | |
|---|---|---|---|---|---|---|---|---|---|---|---|---|---|
| 31 | GP-3-6 | 3.606 | 0.394 | 1.452 | 0.261 | 0.287 | 0.000 | 2.000 | 0.035 | 0.279 | 0.000 | 0.166 | 0.480 |
| 32 | GP-3-7 | 4.033 | 0.000 | 1.004 | 0.589 | 0.398 | 0.000 | 1.991 | 0.000 | 0.294 | 0.000 | 0.000 | 0.294 |
| 33 | GP-3-8 | 3.759 | 0.241 | 1.187 | 0.400 | 0.413 | 0.000 | 2.000 | 0.000 | 0.191 | 0.000 | 0.231 | 0.422 |
| 34 | GP-3-9 | 3.724 | 0.276 | 1.595 | 0.225 | 0.180 | 0.000 | 2.000 | 0.052 | 0.191 | 0.000 | 0.080 | 0.323 |
| 35 | GP-3-10 | 3.979 | 0.021 | 1.283 | 0.191 | 0.526 | 0.000 | 2.000 | 0.000 | 0.174 | 0.000 | 0.186 | 0.360 |
| 36 | GP-3-1 | 3.783 | 0.217 | 1.317 | 0.331 | 0.352 | 0.000 | 2.000 | 0.035 | 0.331 | 0.000 | 0.084 | 0.450 |
| 37 | GP-3-2 | 3.534 | 0.466 | 1.390 | 0.247 | 0.425 | 0.000 | 2.062 | 0.247 | 0.495 | 0.000 | 0.000 | 0.600 |
| 38 | GP-3-3 | 3.722 | 0.278 | 1.242 | 0.454 | 0.303 | 0.000 | 2.000 | 0.035 | 0.315 | 0.000 | 0.098 | 0.448 |
| 39 | GP-3-4 | 3.701 | 0.299 | 1.509 | 0.362 | 0.130 | 0.000 | 2.000 | 0.017 | 0.034 | 0.000 | 0.180 | 0.232 |
| 40 | GP-3-5 | 3.834 | 0.166 | 1.344 | 0.278 | 0.379 | 0.000 | 2.000 | 0.000 | 0.156 | 0.000 | 0.194 | 0.350 |
| 41 | GP-3-6 | 3.690 | 0.310 | 1.386 | 0.367 | 0.246 | 0.000 | 2.000 | 0.000 | 0.455 | 0.000 | 0.051 | 0.506 |
| 42 | GP-3-7 | 3.751 | 0.249 | 1.077 | 0.576 | 0.347 | 0.000 | 2.000 | 0.000 | 0.244 | 0.000 | 0.176 | 0.420 |
| 43 | GP-3-8 | 3.919 | 0.081 | 1.201 | 0.369 | 0.404 | 0.000 | 1.974 | 0.000 | 0.562 | 0.000 | 0.000 | 0.562 |
| 44 | GP-3-9 | 3.919 | 0.081 | 1.121 | 0.435 | 0.443 | 0.000 | 2.000 | 0.000 | 0.366 | 0.000 | 0.079 | 0.445 |
| 45 | GP-3-10 | 3.847 | 0.153 | 1.204 | 0.383 | 0.413 | 0.000 | 2.000 | 0.000 | 0.278 | 0.000 | 0.144 | 0.422 |
| 46 | GP-3-11 | 3.861 | 0.139 | 1.339 | 0.296 | 0.365 | 0.000 | 2.000 | 0.035 | 0.330 | 0.000 | 0.052 | 0.417 |
| 47 | GP-12-1 | 3.931 | 0.069 | 0.845 | 0.776 | 0.379 | 0.000 | 2.000 | 0.017 | 0.103 | 0.000 | 0.155 | 0.276 |
| 48 | GP-12-2 | 3.670 | 0.330 | 0.945 | 0.681 | 0.373 | 0.000 | 2.000 | 0.000 | 0.262 | 0.000 | 0.221 | 0.483 |
| 49 | GP-12-3 | 3.699 | 0.301 | 1.154 | 0.508 | 0.338 | 0.000 | 2.000 | 0.035 | 0.438 | 0.000 | 0.065 | 0.539 |
| 50 | GP-12-4 | 3.652 | 0.348 | 1.470 | 0.346 | 0.184 | 0.000 | 2.000 | 0.017 | 0.104 | 0.000 | 0.197 | 0.318 |
| 51 | GP-12-5 | 4.016 | 0.000 | 1.339 | 0.343 | 0.318 | 0.000 | 2.000 | 0.000 | 0.103 | 0.000 | 0.076 | 0.179 |
| 52 | GP-12-6 | 4.005 | 0.000 | 1.238 | 0.447 | 0.316 | 0.000 | 2.000 | 0.017 | 0.069 | 0.000 | 0.097 | 0.183 |
| 53 | GP-12-7 | 4.009 | 0.000 | 1.106 | 0.449 | 0.445 | 0.000 | 2.000 | 0.000 | 0.121 | 0.000 | 0.143 | 0.264 |
| 54 | GP-12-8 | 4.003 | 0.000 | 0.853 | 0.453 | 0.661 | 0.000 | 1.967 | 0.331 | 0.087 | 0.000 | 0.000 | 0.418 |
| 55 | GP-12-9 | 3.981 | 0.019 | 1.371 | 0.395 | 0.234 | 0.000 | 2.000 | 0.000 | 0.069 | 0.000 | 0.092 | 0.161 |
| 56 | GP-12-10 | 3.748 | 0.252 | 1.205 | 0.468 | 0.326 | 0.000 | 2.000 | 0.000 | 0.121 | 0.000 | 0.229 | 0.350 |
| 57 | GP12-1 | 3.831 | 0.169 | 1.010 | 0.693 | 0.296 | 0.000 | 2.000 | 0.000 | 0.191 | 0.000 | 0.137 | 0.328 |
| 58 | GP12-2 | 3.924 | 0.076 | 0.792 | 0.799 | 0.409 | 0.000 | 2.000 | 0.000 | 0.226 | 0.000 | 0.129 | 0.355 |
| 59 | GP12-3 | 3.488 | 0.512 | 1.578 | 0.397 | 0.025 | 0.000 | 2.000 | 0.000 | 0.035 | 0.000 | 0.251 | 0.286 |
| 60 | GP12-4 | 3.806 | 0.194 | 0.935 | 0.712 | 0.352 | 0.000 | 2.000 | 0.000 | 0.139 | 0.000 | 0.204 | 0.343 |
| 61 | GP12-5 | 3.879 | 0.121 | 1.259 | 0.552 | 0.190 | 0.000 | 2.000 | 0.000 | 0.172 | 0.000 | 0.069 | 0.241 |
| 62 | GP12-6 | 3.941 | 0.059 | 1.055 | 0.720 | 0.226 | 0.000 | 2.000 | 0.000 | 0.051 | 0.000 | 0.117 | 0.168 |
| 63 | GP12-7 | 3.809 | 0.191 | 0.939 | 0.748 | 0.313 | 0.000 | 2.000 | 0.017 | 0.191 | 0.000 | 0.139 | 0.348 |
| 64 | GP12-8 | 3.826 | 0.174 | 0.835 | 0.730 | 0.435 | 0.000 | 2.000 | 0.000 | 0.122 | 0.000 | 0.243 | 0.365 |
| 65 | GP12-9 | 3.618 | 0.382 | 1.574 | 0.329 | 0.098 | 0.000 | 2.000 | 0.035 | 0.087 | 0.000 | 0.162 | 0.283 |

| | | | | | | | | | | | | | |
|---|---|---|---|---|---|---|---|---|---|---|---|---|---|
| 66 | GP12-10 | 4.031 | 0.000 | 1.223 | 0.431 | 0.346 | 0.000 | 2.000 | 0.000 | 0.155 | 0.000 | 0.033 | 0.188 |
| 67 | GP1-2 | 3.873 | 0.127 | 1.234 | 0.436 | 0.330 | 0.000 | 2.000 | 0.035 | 0.349 | 0.000 | 0.019 | 0.403 |
| 68 | GP1-3 | 3.644 | 0.356 | 1.587 | 0.226 | 0.188 | 0.000 | 2.000 | 0.035 | 0.156 | 0.000 | 0.159 | 0.350 |
| 69 | GP1-4 | 3.725 | 0.275 | 1.604 | 0.191 | 0.204 | 0.000 | 2.000 | 0.052 | 0.296 | 0.000 | 0.040 | 0.388 |
| 70 | GP1-5 | 3.550 | 0.450 | 1.614 | 0.192 | 0.194 | 0.000 | 2.000 | 0.052 | 0.332 | 0.000 | 0.103 | 0.488 |
| 71 | GP1-6 | 3.767 | 0.233 | 1.306 | 0.467 | 0.228 | 0.000 | 2.000 | 0.000 | 0.156 | 0.000 | 0.152 | 0.308 |
| 72 | GP1-7 | 3.775 | 0.225 | 1.092 | 0.527 | 0.334 | 0.000 | 1.952 | 0.105 | 0.492 | 0.000 | 0.000 | 0.597 |
| 73 | GP1-8 | 3.759 | 0.241 | 1.500 | 0.278 | 0.222 | 0.000 | 2.000 | 0.000 | 0.313 | 0.000 | 0.074 | 0.388 |
| 74 | GP1-9 | 3.946 | 0.054 | 1.331 | 0.363 | 0.305 | 0.000 | 2.000 | 0.000 | 0.208 | 0.000 | 0.076 | 0.283 |
| 75 | GP1-10 | 3.756 | 0.244 | 1.452 | 0.329 | 0.219 | 0.000 | 2.000 | 0.035 | 0.208 | 0.000 | 0.093 | 0.335 |
| 76 | GP1-12 | 3.855 | 0.145 | 1.244 | 0.434 | 0.322 | 0.000 | 2.000 | 0.069 | 0.278 | 0.000 | 0.025 | 0.373 |
| 77 | GP1-13 | 3.623 | 0.377 | 1.058 | 0.613 | 0.329 | 0.000 | 2.000 | 0.123 | 0.455 | 0.000 | 0.003 | 0.581 |
| 78 | GP1-14 | 3.980 | 0.020 | 1.272 | 0.431 | 0.298 | 0.000 | 2.000 | 0.069 | 0.086 | 0.000 | 0.047 | 0.202 |
| 79 | GP1-15 | 3.582 | 0.418 | 1.004 | 0.650 | 0.346 | 0.000 | 2.000 | 0.140 | 0.334 | 0.000 | 0.075 | 0.549 |
| 80 | GP1-16 | 3.990 | 0.010 | 1.216 | 0.403 | 0.368 | 0.000 | 1.986 | 0.088 | 0.245 | 0.140 | 0.000 | 0.473 |
| 81 | GP1-17 | 3.849 | 0.151 | 1.218 | 0.416 | 0.366 | 0.000 | 2.000 | 0.052 | 0.243 | 0.000 | 0.085 | 0.380 |
| 82 | GP1-18 | 3.834 | 0.166 | 1.319 | 0.363 | 0.319 | 0.000 | 2.000 | 0.138 | 0.155 | 0.000 | 0.027 | 0.320 |
| 83 | GP1-19 | 3.716 | 0.284 | 1.296 | 0.417 | 0.287 | 0.000 | 2.000 | 0.104 | 0.313 | 0.000 | 0.025 | 0.442 |
| 84 | GP1-20 | 3.672 | 0.328 | 1.309 | 0.383 | 0.309 | 0.000 | 2.000 | 0.104 | 0.174 | 0.000 | 0.127 | 0.405 |
| 85 | GP1-21 | 3.843 | 0.157 | 1.349 | 0.329 | 0.323 | 0.000 | 2.000 | 0.069 | 0.121 | 0.000 | 0.110 | 0.301 |
| 86 | GP1-22 | 3.774 | 0.226 | 1.235 | 0.452 | 0.313 | 0.000 | 2.000 | 0.104 | 0.296 | 0.000 | 0.017 | 0.417 |
| 87 | GP1-23 | 3.762 | 0.238 | 1.305 | 0.399 | 0.296 | 0.000 | 2.000 | 0.069 | 0.191 | 0.000 | 0.102 | 0.362 |
| 88 | GP1-24 | 3.687 | 0.313 | 1.102 | 0.629 | 0.175 | 0.000 | 1.906 | 0.210 | 0.349 | 0.000 | 0.000 | 0.559 |
| 89 | GP1-25 | 3.640 | 0.360 | 1.251 | 0.420 | 0.280 | 0.000 | 1.951 | 0.228 | 0.333 | 0.000 | 0.000 | 0.560 |

# Chapter 4 Thermodynamic modelling of sepiolite dehydration

**Highlights:**

- Sepiolite standard-state thermodynamic properties were estimated and integrated in a new thermodynamic model in order to calculate its P-T stability conditions and water content.
- The stability field of sepiolite is ultimately limited by the reaction sepiolite → talc + quartz + $H_2O$, which is located at about 325°C at 1 to 500 MPa.
- The dehydration of sepiolite at T < 300°C is modest compared to that occurring during its breakdown, where 62% of water molecules leave the structure to form the association talc + quartz + $H_2O$. This reaction also involves the reduction of around 31% of the original solid volume.

# Implications of sepiolite dehydration for earthquake nucleation in the Galera Fault Zone: a thermodynamic approach

Catalina Sánchez-Roa[1], Olivier Vidal[2], Juan Jiménez-Millán[1], Fernando Nieto[3], Daniel R. Faulkner[4]

[1] Departamento de Geología and CEACTierra, Unidad Asociada IACT (CSIC-UGR), Universidad de Jaén, Campus Las Lagunillas s/n 23071, Jaén, Spain.
[2] CNRS, Université Joseph Fourier Grenoble, LGCA, 1381 rue de la piscine, BP 53, 38041 Grenoble Cedex, France.
[3] Departamento de Mineralogía y Petrología and IACT (CSIC-UGR), Facultad de Ciencias, Universidad de Granada, Avda. Fuentenueva s/n 18002, Granada, Spain.
[4] Rock Deformation Laboratory, Department of Earth and Ocean Sciences, University of Liverpool, Liverpool, UK.

**This manuscript has been sent for consideration to *Applied Geochemistry*.**
**Article received on: 18 April 2017**

## Abstract

A new thermodynamic model for the Mg-phyllosilicate sepiolite was developed and used to calculate its P-T stability conditions and water content for different bulk rock compositions. The standard-state thermodynamic properties, entropy (S°) and enthalpy (H°), were initially estimated by oxide summation taking into account the different entropic and enthalpic contributions of the three types of water in sepiolite: zeolitic water, bound water, and structural OH groups. The starting model was then refined with previously available synchrotron X-ray diffraction (XRD) data for dehydration of sepiolite and experimental data. The dehydration process follows a step function that allowed us to define "end-members" with decreasing hydration states in a theoretical solid solution.

The stability field of sepiolite is ultimately limited by the reaction sepiolite → talc + quartz + $H_2O$, which is located at about 325°C at 1 to 500 MPa. The large stability field of this clay mineral suggests that it could control the mechanical behaviour of crustal faults to 325°C. The refined model was then applied to the natural case of the Galera Fault Zone (SE Spain) using X-ray fluorescence (XRF) data of the bulk rock composition of the fault core gouge, which is mainly composed of sepiolite. The dehydration of sepiolite at T < 300°C is modest compared to that occurring during its breakdown, where 62% of water molecules leave the structure to form the association talc + quartz + $H_2O$; a reaction that also involves a reduction of around 31% of the original solid volume. These significant hydration and volume changes of sepiolite can have important implications on the strength and stability of the Galera Fault and other sepiolite-bearing gouges. We compare triaxial friction experiments on the natural sepiolite-rich gouge with a synthetic gouge to estimate strength changes on the gouge with depth. The synthetic gouge represents the breakdown association above 325°C, and was constructed following the mineral phases predicted by the thermodynamic model (93 wt% talc and 7 wt% quartz). The contrasting frictional strength and stability of sepiolite in comparison to talc could be one of the causes of fault instability and earthquake nucleation seen to be concentrated in the upper 10-13 km of the Galera Fault.

## 1. Introduction

The role of phyllosilicates within active fault systems and in relation to earthquake dynamics is a field of ongoing research. Clay mineral localization in fault zones is a common phenomenon (Haines and van der Pluijm, 2012; Morton et al., 2012; Richard et al., 2014; Schleicher et al., 2012; Yalçin and Bozkaya, 2004), which has been linked with processes controlling creep and facilitating slip in shallow sections of active faults due to their low friction coefficients and continuous layers of water on their main cleavage planes (Lockner et al., 2011; Schleicher et al., 2013).

Water release and dehydration of minerals in active fault systems are complex processes that include reorganization of water molecules, especially in clay minerals. Controlled humidity chamber experiments have shown that water layers in smectite occur at seismogenic depths, and that humidity in this context also affects particle orientation (Schleicher et al., 2013). The hydration state and particle orientation of clay minerals in active fault systems suggest higher mobility of the particles, which has important effects on frictional strength of fault gouges (Moore and Lockner, 2007; Schleicher et al., 2013). Furthermore, numerical simulations of pore pressure within fault zones have linked the onset of dehydration reactions in fault systems to instabilities on the fault plane that lead to a transient acceleration of the fault motion, which stops when the reaction is finished but can strongly modify the nucleation of unstable slip (Brantut et al., 2011). The evolution of fault strength and its relation to the seismic cycle requires the observation of natural systems to evaluate the extent of competing mechanisms such as fracturing and healing. These mechanisms are strongly dependent on the geological context, including the mineralogy and fluid flow in the area, which are in turn controlling factors on important processes within fault zones such as creep, mass transfer and pressure solution (Gratier, 2011).

As fibrous clay minerals are more commonly identified in fault gouges of active faults, the study of the role of fibrous phyllosilicates becomes crucial to understand their relationship to earthquake dynamics. Sepiolite is a fibrous clay mineral that can occur as a product of weathering of ophiolitic bodies (Gleeson et al., 2004; Ratié et al., 2015) and related to other Mg-rich minerals with important roles in fault stability such as saponite, minerals from the serpentine group, and talc (Manning, 1995; Yalçin and Bozkaya, 2004). Sepiolite is found associated with fault zones and fault planes (Haines and van der Pluijm, 2012; Sánchez-Roa et al., 2016). Therefore, the study and modelling of the hydration state, mineral reactions and stability of sepiolite is a step towards understanding the mechanical behaviour of sepiolite-rich fault gouges.

Sepiolite is composed of continuous silica tetrahedral sheets with the apical oxygen periodically inverted and a discontinuous octahedral layer between them (García-Romero and Suárez, 2013). Due to these periodical inversions, sepiolite has a fibrous morphology and channels containing $H_2O$ molecules. These channels can also accommodate some organic molecules and exchangeable cations (which are not bound to the structure) such as $Na^+$, $K^+$, and $Ca^{2+}$ (Krekeler and Guggenheim, 2008). Sepiolite is a hydrated Mg-rich fibrous phyllosilicate with formula: $Si_{12}Mg_8O_{30}(OH)_4(OH_2)_4 \bullet 8(H_2O)$. It contains three crystal-

chemical states of water molecules: zeolitic water in the channels; bounded water completing the coordination of $Mg^{+2}$ atoms in the edges of the octahedral layers; and hydroxyl groups ($OH^-$) in the octahedral layer bounded to the $Mg^{+2}$ atoms (Brauner and Preisinger, 1956). The dehydration of sepiolite in air therefore consists of various stages, which have been shown in experimental data to contain step functions due to different processes that occur during dehydration. First, most of the zeolitic water is lost when heated to 117°C or at room temperature under a vacuum of $1x10^{-6}$ torr. No change in the unit cell had been recognized until Rietveld refinements of temperature-resolved synchrotron powder X-ray diffraction data showed a slight decrease in the a and c unit cell parameters in this stage (Post et al., 2007). The loss of the bounded water takes place in two subsequent stages that are accompanied by the folding of the sepiolite structure and forming the experimentally achieved sepiol-$2H_2O$ and anhydrous sepiolite (Nagata et al., 1974).

The presence of sepiolite in the fault gouge of active faults and its hydration properties lead us to seek appropriate tools to discover the way sepiolite behaves under changing chemical and mechanical conditions. Currently there is a shortage of data on the evolution of this fibrous clay mineral in nature, including sepiolite interactions and compatibility relations with other phases in a wide range of pressure and temperature conditions. The scarcity of data on sepiolite stability and mineral transformations can be approached from a thermodynamic perspective, and thermodynamic models can then be used to assess the extent of sepiolite contribution to fault mechanics and earthquake nucleation.

This study presents the integration of a new thermodynamic model for sepiolite with frictional tests assessing fault strength, and the application of these methods to a natural example as a strategy to explore the relation between sepiolite dehydration and earthquake nucleation in the Galera Fault Zone.

## 2. Thermodynamic Model

### 2.1 Considered range of hydration states

Synchrotron XRD data show that the volume vs. temperature dehydration curve of sepiolite is a step function (Post et al., 2007), similar to that observed for smectite dehydration. In smectite, this step dehydration results from two different processes: i) continuous loss of interlayer water and constant decrease of volume for a fixed number of water layers, and ii) discontinuous loss of water layers and large volume changes associated with the collapse of the interlayer space at fixed temperatures (see Vidal and Dubacq, 2009 and references therein). Similarly, the step dehydration in sepiolite results from the progressive loss of interlayer water (zeolitic water), as well as the folding of the sepiolite structure that can be compared to the collapse of the interlayer space for smectites. Five end-members with different hydration states and four solid solutions between these end-members must be defined to cover the entire range of possible sepiolite hydration from 12 to 2 $H_2O$ p.f.u (Fig. 4.1). Given the low thermodynamic stability of the experimentally achieved sepiol-$2H_2O$ and anhydrous sepiolite and their absence in nature, we restricted our study and thermodynamic model to the "zeolitic water". Following the approach proposed for

smectite by Vidal and Dubacq (2009), the step dehydration of sepiolite was modelled with different solid solutions between the zeolitic-water-free end-member Sep-4$H_2O$ and the hydrated end-members Sep-12$H_2O$ or Sep-6$H_2O$. The Fe-Mg compositional variation in sepiolite was not included in this model due to the few occurrences of Fe-sepiolite and the lack of Fe-Mg exchange in the studied samples. The exchangeable cations within the channels were also excluded from the model because they are highly variable and not bound to the sepiolite structure or the water molecules in the channels, thus they are not expected to affect the dehydration temperatures of sepiolite.

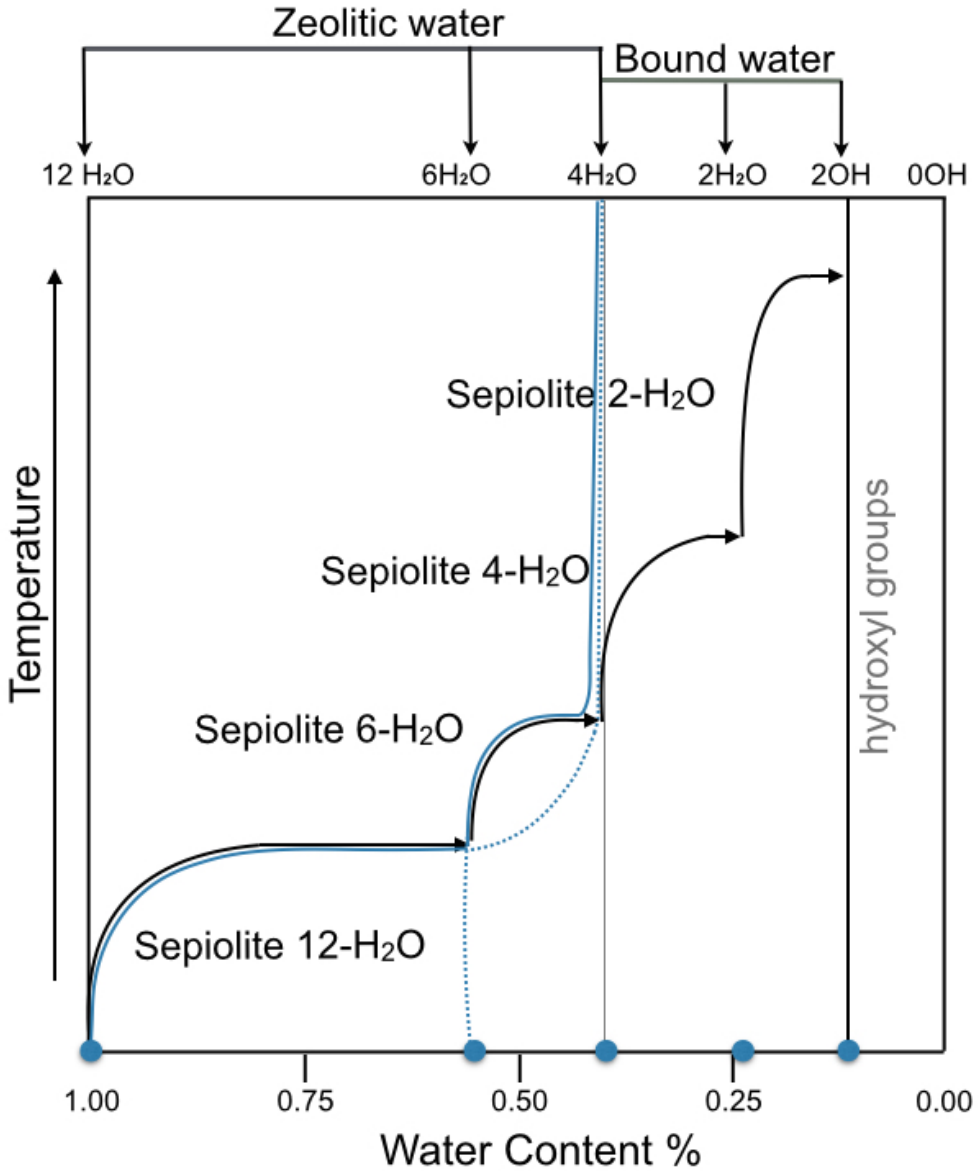


**Figure 4.1.** Dehydration model of sepiolite with temperature considering XRD data of the dehydration curve of sepiolite from Post et al. (2007) and the dehydration model proposed by Vidal and Dubacq (2009). The water content of the end-members is shown with circles in the horizontal axis both as water% and moles of water. The black lines indicate the experimentally proven transitions and the end-members initially considered. The blue lines indicate the solid solutions selected for the model, where the dashed parts of the line indicate the metastable parts.

## 2.2 Thermodynamic approach

In view of the strong similarities with smectite, the thermodynamic model developed for sepiolite in the present study is similar to that proposed for smectite by Vidal and Dubacq (2009). The hydration state of sepiolite is calculated by solving the conditions of the two following equilibria between two different hydrous end-members and the same anhydrous end-member at fixed P, T and $aH_2O$:

$$Sepiolite.12H_2O = Sepiolite.4H_2O + 8H_2O \quad (1)$$

$$Sepiolite.6H_2O = Sepiolite.4H_2O + 2H_2O \quad (2)$$

The conditions of equilibria 1) and 2) for $aH_2O = 1$ read:

$$RTln(aSepiolite.4H_2O/aSepiolite.12H_2O) = \Delta G(1)_f^{P,T} \quad (3)$$

$$RTln(aSepiolite.4H_2O/aSepiolite.6H_2O) = \Delta G(2)_f^{P,T} \quad (4)$$

Where a stands for activity and

$$\Delta G_f^{P,T} = G^{P,T}Sepiolite.4H_2O - G^{P,T}Sepiolite.12H_2O + 8G^{P,T}H_2O \quad \text{or}$$

$$= G^{P,T}Sepiolite.4H_2O - G^{P,T}Sepiolite.6H_2O + 2G^{P,T}H_2O$$

Where

$$\Delta G_f^{P,T} = \Delta H_f^{1,298} - T\Delta S^{1,298} + \int_{298}^{T} \Delta Cp\partial T - T\int_{298}^{T} \Delta Cp/T\,\partial T + \int_{1}^{P} \Delta V\partial P \quad (5)$$

The activities of the sepiolite end-members were assumed to be equal to their molar fraction (ideal solid solution model). Under this assumption, the molar fractions of $Sepiolite.4H_2O$ in the solid solution between $Sepiolite.4H_2O$ ($X_{4,1}$) and $Sepiolite.12H_2O$ or between $Sepiolite.4H_2O$ ($X_{4,2}$) and $Sepiolite.6H_2O$ can be calculated as:

$$X_{4,1}/(1-X_{4,1}) = \exp(\Delta G(1)_f^{P,T}/RT) \quad (6)$$

$$X_{4,2}/(1-X_{4,2}) = \exp(\Delta G(2)_f^{P,T}/RT) \quad (7)$$

The relative stability of the two solid solutions and the water content of sepiolite were calculated at given P and T from equilibria (6) and (7). Thermodynamic calculations of the stepwise dehydration of sepiolite, and its stability and compatibility relations were calculated by Gibbs free energy minimisation using Theriak-Domino (de Capitani, 1994, http://titan.minpet.unibas.ch/minpet/theriak/theruser.html) after implementation of the thermodynamic properties of sepiolite end-members discussed below, and with the

thermodynamic properties of common rock-forming minerals included in the internally consistent database jun92.bsc of Theriak-domino (de Capitani, 1994). The thermodynamic properties of smectitic phases included in Vidal and Dubaq (2009) were also incorporated to the calculations of selected natural samples.

### 2.3 Estimation of thermodynamic properties

The molar volume of sepiolite was calculated for its different hydration states based on the cell dimensions reported in the Rietveld refinement process for the sepiolite structure detailed in Post et al. (2007), who determined the cell parameters indicated in Table 4.1. The other thermodynamic properties of sepiolite-12$H_2O$, -6$H_2O$ and -4$H_2O$ end-members were first estimated using oxide summation techniques:

-The heat capacity functions of all sepiolite end-members were calculated according to the equation of Berman and Brown (1985), where in most cases only three or four parameters are used:

$$Cp = k_1 + k_2 \cdot T + \frac{k_3}{T^2} + \frac{k_4}{\sqrt{T}} + k_5 \cdot T^2 + \frac{k_6}{T} + k_7 \cdot \sqrt{T} + \frac{k_8}{T^3} + k_9 \cdot T^3 \ [J/mol]$$

The V(P, T) function of sepiolite was assumed to be to the same as that of muscovite.

- The standard-state third-law entropies (S°) of sepiolite end-members were estimated using the additivity of oxide components procedure (Holland, 1989). The value of $(S\text{-}V)_{H2O}$ was fixed for zeolitic water = 39 J/mol/K, which shows the best fit for the dehydration model in a binary system of water activity vs. temperature (Fig. 4.2). The OH groups from the octahedral sheet were assigned with a value of S° equals 7.44 J/mol/K according to Holland (1989), taking into account that sepiolite has a trioctahedral structure and the three full octahedral sites repel the proton equally (Bailey, 1984). Finally, the value for bounded water was fixed to 28 J/mol/K.

- A first estimation of the 1 bar, 25°C enthalpy of formation of sepiolite end-members was made according to the oxide summation technique of Chermak and Rimstidt (1989), which has been proven to give reliable results for clay minerals (Vidal and Dubacq, 2009).

The values of enthalpy of formation were then adjusted in order to 1) achieve the best possible fit of the dehydration vs. temperature evolution of Post et al. (2007) obtained by Rietveld refinements of temperature-resolved synchrotron powder X-ray diffraction data, and 2) create a realistic stability field for sepiolite while adjusting its stability conditions compared to talc in presence of quartz and water. Cold-seal pressure vessel experiments of Frank-Kamenetskiy et al. (1969) show that sepiolite breaks down into talc, quartz and water at 325°C for P between 1 and 300 MPa. These results constitute a valuable dataset and have been selected to refine the model.

a.

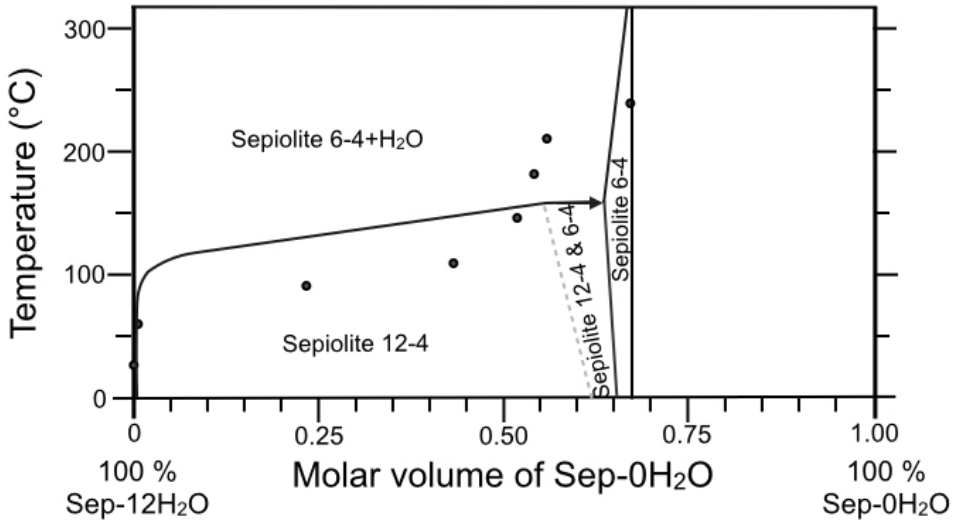


b.

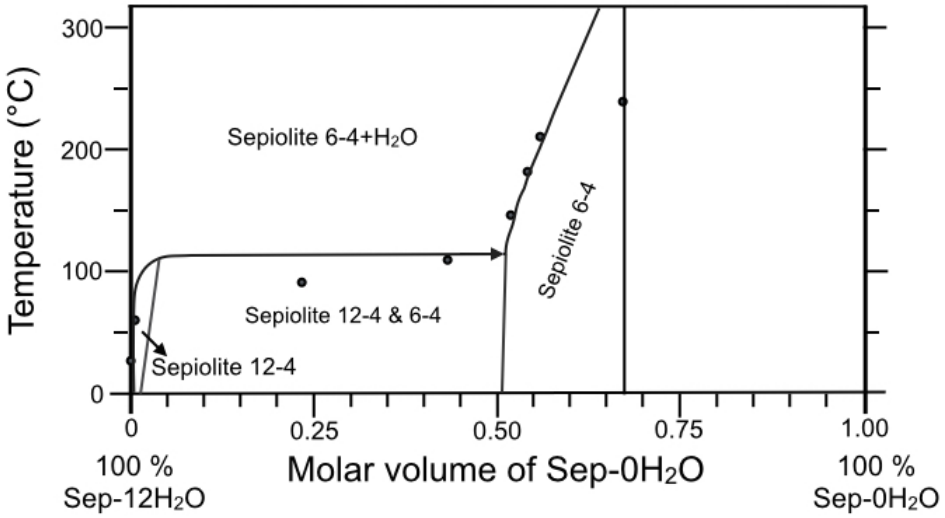


**Figure 4.2**. Binary diagrams of water content in the sepiolite structure versus temperature showing the progressive dehydration of sepiolite. Black dots represent the results of Rietveld refinement of the dehydration process (Post et al., 2007). The continuous black line is the output of this model. a. Using the standard-state thermodynamic properties from this study. b. Using adjusted standard-state thermodynamic properties to achieve a better agreement of the dehydration at low temperature.

## 3. Thermogravimetric Analysis

Validation of the model also requires a test of its capacity to reproduce the mineral assemblages observed in natural samples. The seismically active Galera Fault, SE Spain (Sánchez-Roa et al., 2016) presents a convenient example for this test. The Galera Fault has a sepiolite-rich fault gouge, produced by hydrothermal alteration of Mg-rich fluids during periods of fluid-rock interactions that concentrated on fault planes and fractures of the deformation area. XRD data limitations in determining the accurate percentage of sepiolite in the rock are mitigated by performing a thermogravimetric analysis of the fault rock that can confirm sepiolite is the major constituent of the gouge and an optimum candidate to assess the water release, volume changes and mineral reactions that can take place on Galera

Fault's active fault planes during ongoing deformation.

Decomposition of sepiolite-rich fault gouge from the Galera Fault Zone was analysed in a flowing (100 $cm^3$/min) air atmosphere using 851e Mettler Toledo equipment. The temperature was raised from 25 up to 1000°C at a heating rate of 20°C/min. For the measurement, a powder sample of ~23 mg was placed into an aluminium crucible, and weight loss data was collected at regular time intervals.

## 4. Strength Test

Previous experimental work on the Galera fault gouge showed the strength of the sepiolite-rich gouge to have friction coefficients around 0.47 under water-saturated conditions (Sánchez-Roa et al, 2016). To assess the changes on fault strength in the Galera Fault with changing pressure and temperature, we attempted to compare the experimentally-measured friction coefficient of the sepiolite-rich gouge with experimental strength measurements of the friction coefficient of a synthetic gouge mixture based on the mineral assemblage and proportions predicted by the new proposed thermodynamic model.

The friction test of the reaction products was carried out on a triaxial deformation apparatus with a servo-controlled axial loading system and fluid pressure system (Faulkner and Armitage, 2013; Mitchell and Faulkner, 2008). The servo-controlled fluid systems control the confining- and pore-fluid pressure to a resolution of 0.01 MPa, while the axial loading system has a resolution better than +/- 0.05 kN. Frictional sliding experiments were conducted on the mixture using a direct shear sample assembly (Sánchez-Roa et al., 2016). The test was performed on a crushed and sieved synthetic gouge comprised of 93 wt% talc and 7 wt% quartz, following the methods described in Sánchez-Roa et al. (2016), in order to compare strength results with those reported for the sepiolite gouge. The mixture was made into a paste using deionized water to construct a 2mm-thick layer. Experimental conditions include: confining pressure ($P_c$) = 100 MPa; pore pressure ($P_p$) = 5 MPa; effective normal pressure ($\sigma_{neff}$) = 95 MPa; initial sliding velocity for the 1.5 mm run-in 0.3 μm/s; after the run-in, sliding velocity steps were imposed every 0.5 mm (0.3-3.0-0.3 μm/s) until a total displacement of 4 mm. The friction coefficient values (μ) were determined for each experiment as the ratio of shear stress (τ) to effective normal stress ($\sigma_n$); ($\mu=\tau/\sigma_n$).

## 5. Results and Discussion

### 5.1. Estimation of standard-state thermodynamic properties

The thermodynamic properties estimated in the present study and those reported by Ogorodova et al. (2014) and Wolery and Jove-Colon (2004) are listed in Table 4.1. The comparison of our results for the fully-hydrated sepiolite end-member are in good agreement with values presented by Wolery and Jove-Colon (2004) for the V°, H° and G°, whereas the value of S° is slightly higher in our results. This small discrepancy could be attributed to slightly different values of the entropic contribution chosen in the two studies for the different oxides used to calculate the global S° of sepiolite.

The results for the Hf° of Sepiolite-8$H_2O$ by Ogorodova et al. (2014) are intermediate between our Hf° values for the sepiolite 12$H_2O$ and the sepiolite 6$H_2O$ end-members, which is expected for an intermediatly-hydrated member. Meanwhile, calculated values for the dehydrated member are in good agreement with those presented in Orgorodova et al. (2014). The values for intermediate members cannot be compared with previous results due to the lack of available data.

| | Formula | V° ($cm^3$/mol) | H°f (kJ/mol) | S° (J/mol-K) | K0 | K1 | K2 | K3 |
|---|---|---|---|---|---|---|---|---|
| Sepiolite 12$H_2O$[1] | $Mg_8 Si_{12} O_{30} (OH)_4.12H_2O$ | 575.0 | -20304.0 | 1349.2 | 696 | -4726 | -10394840 | 1377654000 |
| Sepiolite 6$H_2O$[1] | $Mg_8 Si_{12} O_{30} (OH)_4.6H_2O$ | 569.4 | -18468.0 | 1109.6 | 564 | -3589 | -10394840 | 1369717500 |
| Sepiolite 4$H_2O$[1] | $Mg_8 Si_{12} O_{30} (OH)_4.4H_2O$ | 567.6 | -17879.6 | 1030.0 | 520 | -3210 | -10394840 | 1367072000 |
| Sepiolite 2$H_2O$[1] | $Mg_8 Si_{12} O_{30} (OH)_4. 2H_2O$ | 422.8 | -17356.0 | 829.2 | 476 | -2830 | -10394840 | 1364426500 |
| Sepiolite dry[1] | $Mg_8 Si_{12} O_{30} (OH)_4$ | 415.3 | -16771.6 | 765.6 | 432 | -2451 | -10394840 | 1361781000 |
| Sepiolite 12$H_2O$[2] | $Mg_8 Si_{12} O_{30} (OH)_4.12H_2O$ | 570 | -20232.0 | 1226.7 | - | - | - | - |
| Sepiolite 8$H_2O$[3] | $Mg_8 Si_{12} O_{30} (OH)_4.(H_2O)_4. 4H_2O$ | - | -18773 ±28 | 1095 | - | - | - | - |
| Sepiolite dry[3] | $Mg_8 Si_{12} O_{30} (OH)_4$ | - | -16426 ±21 | 737 | - | - | - | - |

1: this study, 2: Wolery and Jove-Colon (2004), 3: Ogorodova et al. (2014)

**Table 4.1.** Standard-state thermodynamic properties. V° (molar volume), H°f (standard molar enthalpy of formation), S° (standard molar entropy), K0 to K3 (heat capacity function coefficients).

## 5.2 Dehydration

Figure 4.2 presents the interactions between the two extreme end-members of hydration (Sep-12$H_2O$ and Sep-4 $H_2O$) in a binary diagram versus T using two solid solutions—the first from Sepiolite-12$H_2O$ to Sepiolite-4$H_2O$ end-members and the second from Sepiolite-6$H_2O$ to Sepiolite-4$H_2O$ end-members (equations 1 and 2). Furthermore, it compares the results of this calculation with the experimental dehydration data reported in Post et al. (2007) for the progressive dehydration of sepiolite. The dehydration of zeolitic water (water molecules in the channels) takes place between 100 and 325°C as water progressively leaves the sepiolite structure without significant volume changes (Fig. 4.2a). Although the model in the binary diagram is not a perfect fit of the refinement data (Post et al., 2007), this study favoured the adjustment of the thermodynamic properties of the end-members to fit the experimental data from Frank-Kamenetskiy et al (1969). The achievement of a better fit of the dehydration data is possible by adjusting the thermodynamic properties of the sepiolite end-members (Fig. 4.2b). However in this study we prioritize the agreement with the experimental data for the sepiolite transformation into talc, quartz and $H_2O$.

## 5.3 Phase equilibrium, mineral evolution, water release and volume changes of sepiolite.

This thermodynamic model based on experimental dehydration data predicts phase amounts, volume changes and water release during mineral transformations for an initial

given bulk composition ($Mg_{(2)}Si_{(3)}O_{(11.5)}H_{(7)}$), corresponding to the ideal formula of sepiolite (Fig. 4.3). For this ideal case, a progressive decrease of Sepiolite-12 from the onset of dehydration is predicted at around 100°C and is coupled with an increase in the Sepiolite-4 end-member. This dehydration reaction continues to 325°C and is accompanied by the release of water from the solid phase. The amount of water released during this stage is strongly conditioned by the PT-path and can reach 29% of the water in sepiolite for high geothermal gradients such as 46°C/km (Fig. 4.3b) or 14% with a lower gradient of 25°C/km (Fig. 4.3c).

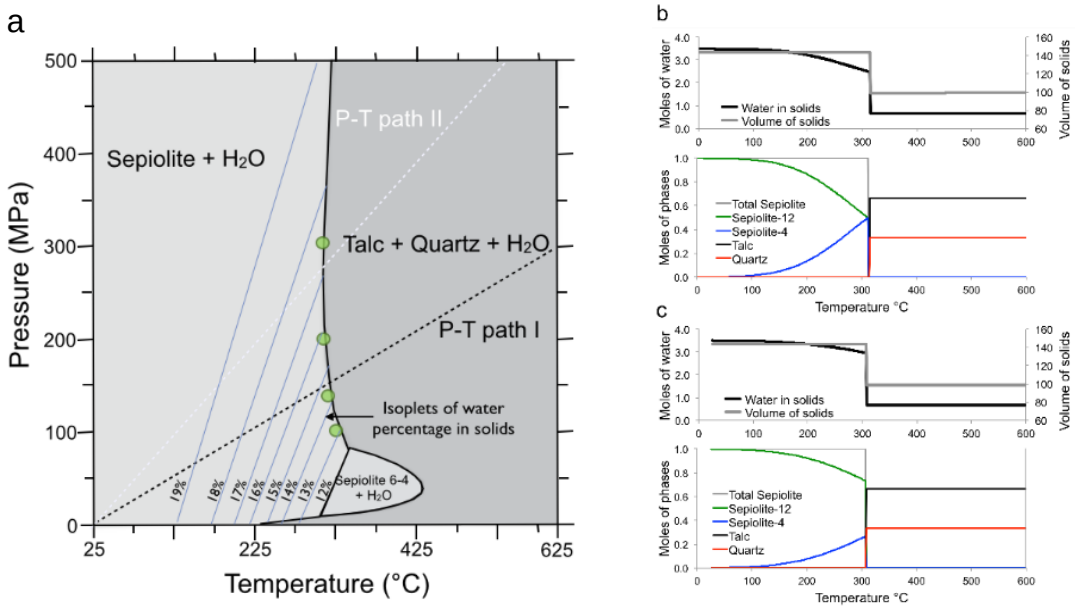


**Figure 4.3. a.** Equilibrium phase diagram of an initial ideal composition of pure sepiolite in excess of water. Green dots correspond to the experimentally determined limit of reaction sepiolite → talc + quartz + $H_2O$ by Frank-Kamenetskiy et al. (1969). Solid blue lines correspond to isoplets of equal H2O content indicating the percentage of water within the solid phases. **b.** Evolution of water content, volume of solids and mineral phases along PT-path I (46°C/km). **c.** Evolution of water content, volume of solids and mineral phases along PT-path II (25°C/km).

At 325°C both Sepiolite-12 and -4 disappear and further dehydration states of sepiolite such as "sepiol-2$H_2O$" and "sepiolite anhydrous" will therefore be preceded by the metamorphic reaction sepiolite → talc + quartz under hydrothermal conditions, due to the higher thermodynamic stability of the new mineral association. The two anhydrous phases, which are obtained after heating in air and vacuum atmospheres (Post et al., 2007; Nagata et al., 1994) are not present in natural samples, which validate the outcome of this model.

The amount of released zeolitic water is strongly dependent on the PT-path (Fig. 4.3). In the case of a high geothermal gradient, such as PT-path I in Fig. 4.3b, up to 4 water molecules per formula unit are lost with increasing temperature. A lower amount of zeolitic water is lost when the geothermal gradient is lower as is the case of PT-path II where only 2 water molecules are lost. Heat flow studies of the thermal structure of the crust in southern Spain, specifically in the Betic Cordilleras, predict projected geothermal temperatures

between 100 and 325°C at depths around 4 to 13 km (Soto et al., 2008). In this setting, the sepiolite dehydration reaction could occur at depths of around 4 km, potentially increasing pore pressure values, which could in turn affect the strength of the fault plane in shallow crustal faults (Leclère et al., 2016). Sepiolite is therefore predicted to be stable and without significant structural changes up to around 13 km depth, meaning that sepiolite physical properties such as strength (friction coefficient) may control fault gouge behaviour through most of the seismogenic depths in the Galera Fault.

The stable mineral association after 325°C is talc + quartz + $H_20$, including 0.66 moles of talc (93 wt%) and 0.33 moles of quartz (7 wt%) according to a Theriak (De Capitani and Petrakakis, 2010) calculation on conditions 200 MPa, 400°C (Table 4.2). This phase transformation is accompanied by a release of 57% of the water when following PT-path I (Fig. 4.3b), and 71% of the water when following PT-path II (Fig. 4.3c). In both cases, the volume decrease of the solid phases is 31.25%.

| Solid phases | N | Volume/mol | Vol (cm3) | vol% | Wt/mol | Wt (g) | Wt% | Density (g/cm3) |
|---|---|---|---|---|---|---|---|---|
| Talc | 0.6667 | 137.0299 | 91.353 | 92.3124 | 379.2657 | 252.8438 | 92.6603 | 2.7677 |
| Quartz | 0.3333 | 22.8231 | 7.607 | 7.687 | 60.0843 | 20.0281 | 7.3397 | 2.6326 |

**Table 4.2**. Stable phases according to Theriak calculation (de Capitani and Petrakakis, 2010) at conditions 200 MPa, 400 °C.

Our model reproduces the experimental results of Frank-Kamenetskiy et al. (1969) and allows prediction of the phase amounts, volume changes and water release during mineral transformations involving sepiolite (Fig. 4.3). The large amounts of water released during the transformation of sepiolite into talc and quartz (57% to 71% of the water in sepiolite) could have a significant impact on local pore pressures within the fault plane. In addition, the volume decrease in the fault gouge as a consequence of the transformation is substantial (31%) (Fig. 4.3b, 4.3c). Both competing processes could alter the state of stress of the fault and have important implications on the stability of these clay-bearing fault planes. Furthermore, differences in the rheological properties of the gouge and the mineral associations after mineral reactions in depth, can alter the strength of the fault plane (e.g. Leclère et al., 2016).

## 5.4 Thermogravimetric analysis of a sepiolite-rich gouge from the Galera Fault Zone

Figure 4.4 shows a thermogravimetric analysis of the sepiolite-rich fault gouge from the Galera Fault Zone to demonstrate the high content and dominance of sepiolite in the gouge sample. The analysis shows five major weight losses at around 100°C, 300°C and 525°C, 728°C and 905°C which show great similarity with sepiolite TG analysis. In agreement with previous TG interpretations of the dehydration of sepiolite, the first loss corresponds to the dehydration of zeolitic water; the second loss corresponds to the removal of half of the

water bound to the Mg atoms at the edges of the broken octahedral layer; the third loss relates to the remaining two molecules of water bound to the Mg atoms and the fourth represents the loss of the OH in the octahedral layer (Nagata et al., 1974). The poor definition of the dehydration stages after 500°C correspond to the onset of calcite and dolomite decomposition, also present in the sample, which makes the sepiolite dehydration stages slightly more difficult to identify. The last weight loss is likely to correspond to the amorphization of sepiolite and a final decomposition stage of the carbonatic minor phases.

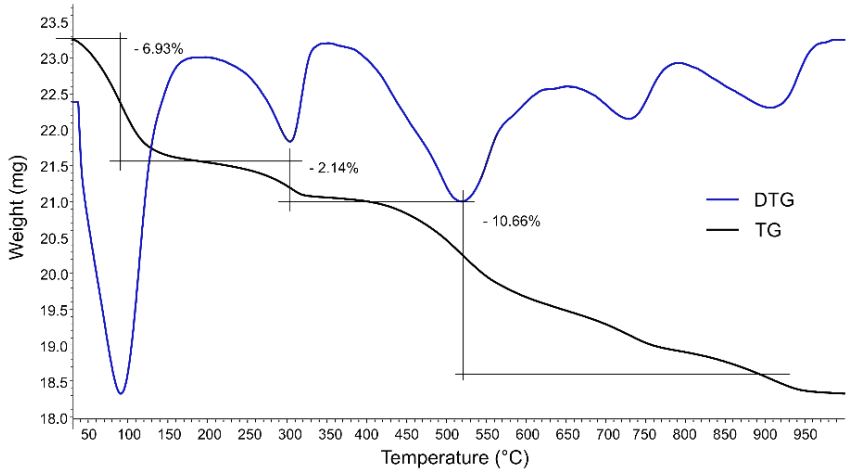


**Figure 4.4.** Thermogravimetric analysis of a natural gouge rich in sepiolite from the Galera Fault Zone (SE Spain).

## 5.5 Frictional strength of the predicted mineral assemblage

Results of the friction experiment for an assemblage made of 93 wt% talc and 7 wt% quartz are compared with those obtained for a sepiolite-rich gouge (Sánchez-Roa et al., 2016) in Figure 4.5. The representative friction coefficient of the experiment μ=0.3 was taken at 2.49 mm of axial displacement.

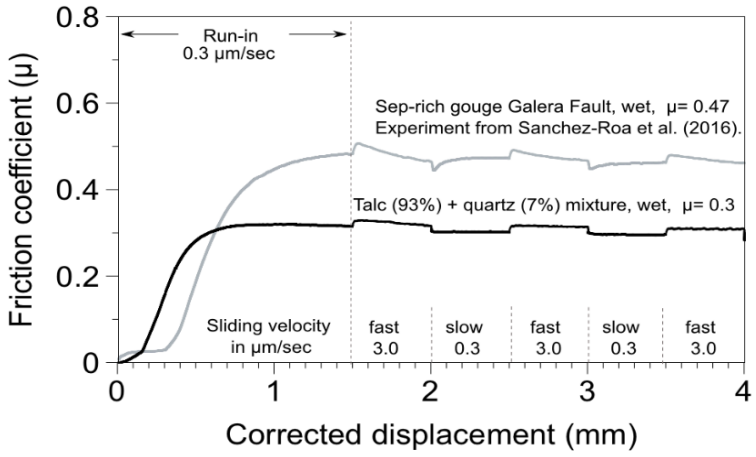


**Figure 4.5.** Experimental quantification of the frictional properties of the reaction products predicted by this model (93 wt% talc and 7 wt% quartz) under water-saturated conditions, 100 MPa confining pressure and 5 MPa pore pressure. The steps within the curves correspond to alternating changes in sliding velocity of one order of magnitude (0.3 to 3 µm/sec). An example of a strength test on a sepiolite-rich gouge (Sánchez-Roa et al., 2016) is plotted along with our results for comparison and discussion.

Friction coefficient values for the sepiolite-rich gouge (μ=0.472) and the synthetic mixture (μ=0.3) show a contrast in strength between reactants and products (Fig. 4.5). Strength results for the products mixture (93 wt% talc and 7 wt% quartz) are slightly higher than those reported by Moore and Lockner (2008) for a pure talc synthetic gouge. The higher friction coefficient in the modelled mixture could be related to the quartz fraction since quartz has much higher friction coefficients than talc (Moore and Lockner, 2011). The velocity-dependence of talc has shown to be velocity-strengthening and therefore stable under a wide range of temperature (25 to 400°C) and effective normal stresses (25 to 150 MPa) (Moore and Lockner, 2008). In contrast, results of the velocity dependency of strength for sepiolite-rich gouge show a neutral to velocity-weakening behaviour (Sánchez-Roa et al., 2016), which fulfils the prerequisite for earthquake nucleation (Marone, 1998). This difference in frictional strength between the two mineral assemblages is possibly enhanced by temperature according to friction experiments on talc that have shown friction coefficients ranging from 0.17 to 0.1 when talc is heated from 100 to 400°C (Moore and Lockner, 2008). Furthermore, experiments on quartz-talc mixtures have shown that the low strength of talc is dominant in mixtures containing more than 50% talc at temperatures of 200°C (Moore and Lockner, 2011), an effect that would increase with an increasing percentage of talc as is the case of the predicted gouge in the Galera fault containing 93 wt% talc. These results suggest a significant weakening of the fault plane after 325°C in a Mg-rich system where sepiolite is stable at temperatures below 325ºC and the association talc + quartz + $H_20$ predominates above this temperature.

### 5.6 Application to natural examples of sepiolite-rich rocks and fault gouges from the Galera Fault.

The dehydration of sepiolite is a step function that involves large and sudden volume changes related to the release of its three types of water. Figure 4.3 and experimental data (Frank-Kamenetskiy et al., 1969) show that these fibrous phyllosilicates can be stable at T°< 325°C. This relatively wide temperature-pressure range of stability implies that volume changes and water release involved both in the dehydration and phase transformations of sepiolite may occur at seismogenic depths. In a geological context and specifically for fault gouge evolution, calculations of mineral transformations, volume change and water release are particularly important to determine fault strength and stability as well as potential areas where pore fluid overpressure can develop (Brantut et al., 2011). The thermodynamic model presented in this study was used to quantify these processes in the Galera Fault area. The mineral assemblages of sepiolite-bearing rocks were calculated for bulk rock compositions measured by XRF analyses of the sepiolite-rich fault gouge from the Galera Fault Zone. The initial bulk compositions used in the calculations exclude carbonates in order to simplify the system. Nonetheless there is confidence on the model results given that water activity is not significantly affected by $CO_2$ at T < 375°C (Dubacq et al., 2013), and therefore the presence of carbonate in the calculation would not affect the temperature of the dehydration reaction. Figure 4.6 shows the phase equilibrium diagrams calculated with Theriyak-Domino and including our newly calculated and refined thermodynamic properties for sepiolite (table 1). The calculations were performed on three examples of natural rocks containing sepiolite as an abundant stable mineral phase within the fault gouge (Fig 6, 6b and 6c).

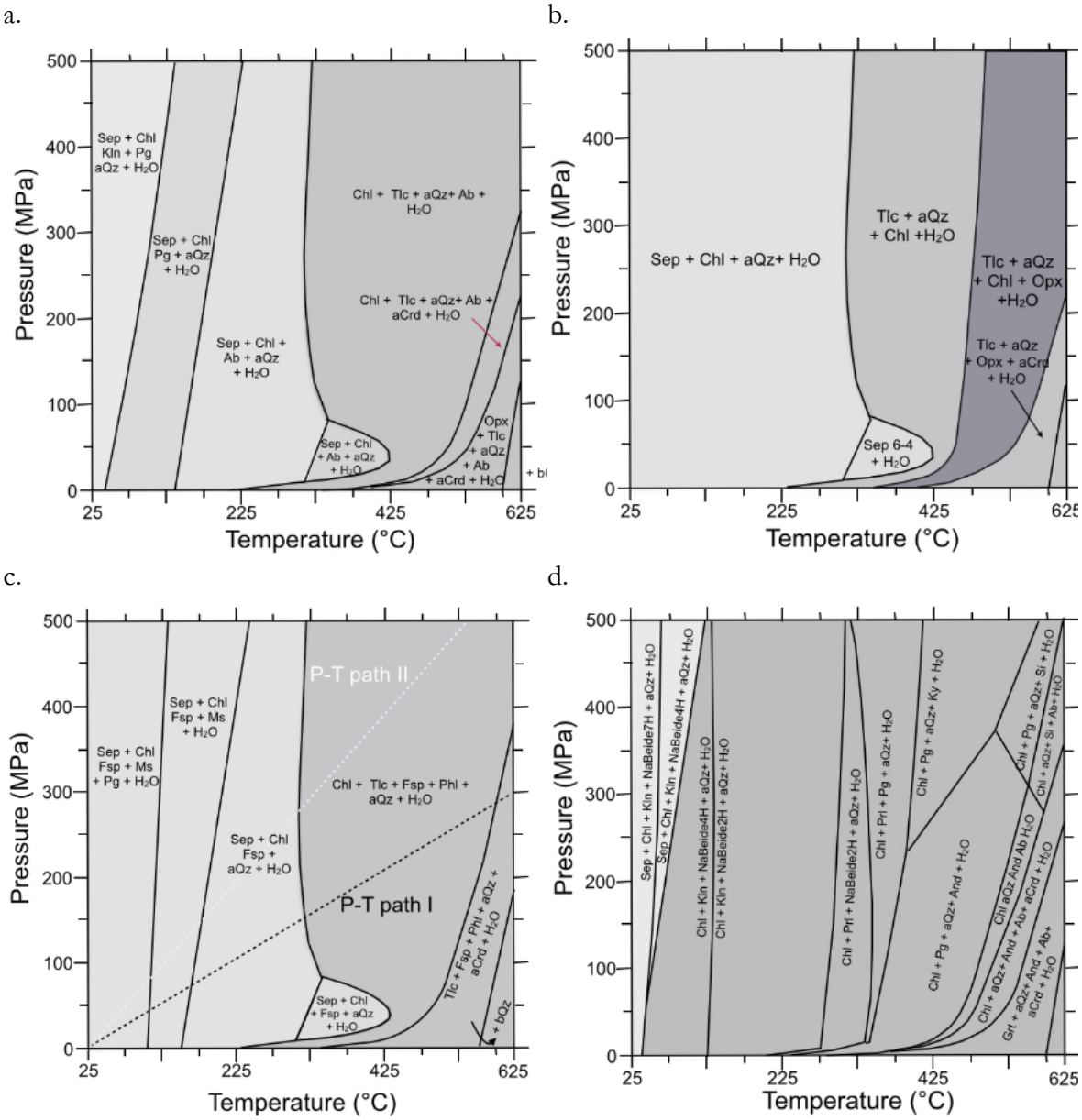


**Figure 4.6.** a. Equilibrium phase diagram for a natural lacustrine-sepiolite bulk composition, from a tertiary Spanish Basin, sample Cala-4 (Torres-Ruiz et al., 1994). b. Equilibrium phase diagram for natural sepiolite product of alteration of ultramafic rocks and seawater interactions within the Owen Transform Zone (Bonatti et al., 1983). c. Equilibrium phase diagram for the bulk rock composition of the sepiolite-rich gouge from the Galera Fault Zone. d. Equilibrium phase diagram for the bulk rock composition of the smectite-rich gouge from the Galera Fault Zone.

The evolution of mineralogy, volume and water content of the Galera Fault's gouge on two segments of the sliding surfaces are illustrated in Fig. 4.6. The main segment is primarily composed of sepiolite (Fig. 6a), while the secondary segment, contains a significant amount of smectite (Fig. 4.6d) (Sánchez-Roa et al., 2016). The evolution of starting rock composition is predicted with ongoing burial along a hypothetical P-T path from 25°C, 0.1 MPa to 600°C, 270 MPa. In the case of the sepiolite-rich gouge, the model predicts the presence of sepiolite as the main mineral phase followed by chlorite, feldspar, muscovite

and paragonite at temperatures less than 100°C, which correspond to those identified through XRD analysis (Fig. 4.6c). The agreement of the model prediction with the mineral associations of the natural gouge at low temperature suggests that the model is highly appropriate for sepiolite-rich bulk rock compositions.

The results of the calculation for the bulk composition representative of a natural gouge mainly composed of smectite indicate a very narrow stability field of sepiolite at temperatures < 50°C, while the most abundant phase predicted by the model is Na-beidellite, which is in agreement with the absence of sepiolite and the abundance of smectite occurring in the natural rock (Fig. 4.6d). This agreement suggests that the thermodynamic properties of sepiolite derived in the present study are consistent with the smectite model and thermodynamic data of Vidal and Dubacq (2009), and that these data reproduce natural observations from low-grade rocks.

The sepiolite-rich gouge, is thought to be the predominant mineral assemblage of the fault rocks in the Galera Fault (Sánchez-Roa et al., 2016), according to the model, the more significant dehydration stage for this fault gouge occurs at 325°C when sepiolite breaks down into talc+quartz+$H_2O$ (Fig. 4.6c). This variation is significant and could have important implications in the rheology of the gouge and the building of overpressures on the fault plane. Heat flow studies of the thermal structure of the crust in southern Spain predict temperatures of around 300°C for depths of 10 km (Soto et al., 2008), which corresponds to the most frequent depth of earthquake nucleation in the Galera Fault (Fig. 4.7). The distribution of earthquake depth in the Galera Fault could also partly reflect the temperature-dependent transition from frictional to viscous deformation regime for quartz, which has been indicated to occur at T° around 350°C (Kohlstedt et al., 1995; Scholz, 1998). However, the bulk composition of the fault gouges in the Galera Fault indicates high phyllosilicate- and Mg-content making the fault gouge mineral association less likely to contain significant amounts of quartz. The brittle to viscous transition in these gouges should therefore be related to the behaviour of Mg-rich mineral phases that prevail in the mineralogy of the fault gouge, which in this case is predicted to be talc at temperatures higher than 325ºC, according to this model, and up to ~700ºC (Escartín et al., 2008; Moore and Lockner, 2008).

Earthquake depth frequency and water release of the sepiolite-rich gouge from the Galera Fault Zone are presented in Figure 4.7. Earthquake nucleation depth in the Galera Fault can be correlated to (1) the presence of sepiolite (a stronger and potentially unstable mineral phase) and its breakdown into the association talc + quartz (a weaker and fully stable mineral phase) that can weaken the fault and could arrest the nucleation of earthquakes at depths greater than 10-13 km, and (2) the sudden water release linked to the phase transformation at around 10-13 km that could potentially create pore overpressures altering the state of stress on the fault plane. These two factors can perhaps contribute to decreasing the nucleation of earthquakes at depths greater than 13 km in the Galera Fault Zone.

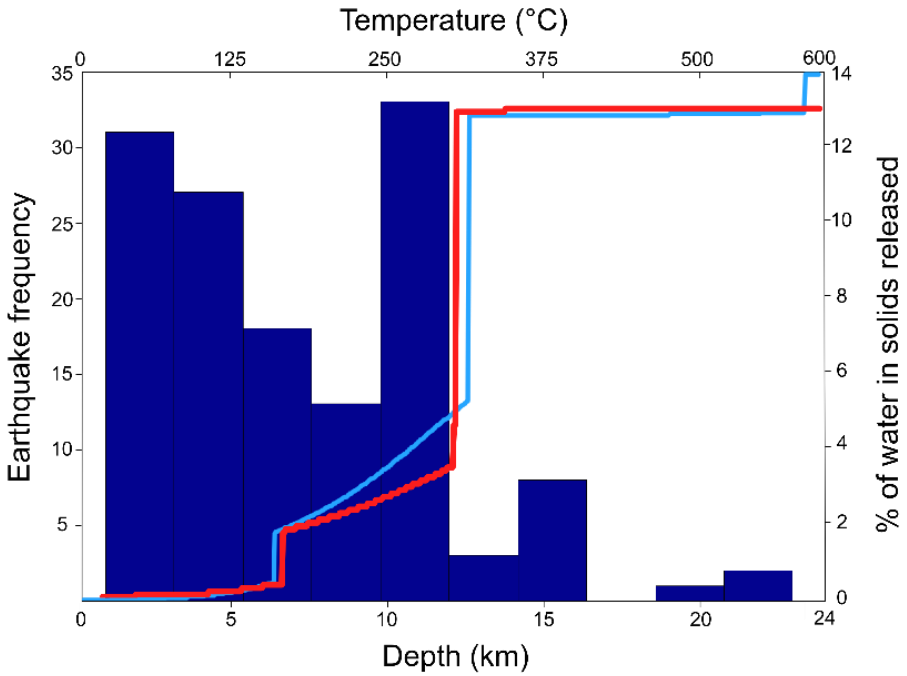


**Figure 4.7.** Frequency histogram of earthquake nucleation depth in the Galera Fault Zone. Constructed with data of depth from 136 earthquakes registered by the Instituto Geografico Nacional of Spain. The spatial constraints were reduced to coordinates: latitude 37.6 to 37.9 and longitude -2.8 to -2.3. The oldest event was registered in 1863 and the most recent in July 2016. The blue line represents the water release profile for the Galera Fault gouge initial bulk composition as a percentage of H2O in solids released by the calculated phases along P-T°-path I (46°C/km). The red line represents the water release profile for the Galera Fault gouge initial bulk composition as a percentage of H2O in solids released by the initial calculated phases, using a geothermal gradient of 25°C per km according to Soto et al. (2008) for the Central Betics.

## 6. Conclusions

The thermodynamic model presented in this study allows us to approach the dehydration of sepiolite in various geological contexts including fault gouges under active deformation.

According to this model and the estimated thermodynamic properties, sepiolite-2$H_2O$ and sepiolite anhydrite have a considerably lower thermodynamic stability than talc, indicating that the potential formation of the dehydrated sepiolite species will always be preceded by the metamorphic reaction sepiolite →talc + quartz, which is thermodynamically more stable than those anhydrous phases. The lack of natural occurrences of the two anhydrous phases validates the outcome of this model.

There could be two moments of special sensitivity when considering a fault gouge mainly composed of sepiolite; the first at the point of dehydration onset which will occur between 100 and 150°C (4 to 5 km) and will continue until the phase transformation starts. The second will take place at the onset of the mineral transformation of sepiolite into talc + quartz + $H_2O$ between 300 and 325°C (10-13 km).

There is a reasonable agreement between the output of our model and mineral paragenesis of natural rocks containing bulk rock compositions likely to yield sepiolite content in the rock. Without sepiolite as a stable phase in the model, the starting bulk composition for the

Galera Fault gouge would predict a mineral paragenesis mainly dominated by talc across the shallower 13 km of the crust that constitute the seismogenic zone in the Galera Fault Zone. Talc is one of the weakest minerals in the context of fault slip and not usually associated with seismicity. The addition of sepiolite thermodynamic properties in the calculations confirms the thermodynamic stability of sepiolite up to 325°C which, contrary to talc, has higher strength and the potential for mechanical instabilities that lead to earthquake nucleation. The presence of sepiolite in Mg-rich fault gouges could contribute to unstable regimes and earthquake nucleation in an otherwise fully stable regime dominated by talc.

## Acknowledgements

This work has been supported by research projects CGL2011-30153-C02-01 and -02 from MINECO, research project UJA2014/06/17 Universidad-Caja Rural de Jaén, Research Groups RNM-179 and 325 of the Junta de Andalucía, UK NERC grant NE/J024449/1, and the F.P.I. Grant BES-2012-052 562 from the Ministerio de Economía y Competitividad of Spain. Funding assistance was provided by the Junta de Andalucía (Research Group RNM-325), University of Jaén, and project "Complex rheologic behaviour of active fault zones in carbonate multilayer sequences: applications to the estimation of seismic hazard and the exploitation of water" (University of Jaén).

## References

Brantut, N., Sulem, J., Schubnel, A., 2011. Effect of dehydration reactions on earthquake nucleation: Stable sliding, slow transients, and unstable slip. J. Geophys. Res. 116, 1–16. doi:10.1029/2010JB007876

Brauner, K., Preisinger, A., 1956. Struktur und Entstehung des Sepioliths. Tschermaks Mineral. und Petrogr. Mitteilungen 6, 120–140. doi:10.1007/BF01128033

Chermak, J.A., Rimstidt, J.D., 1989. Estimating the thermodynamic properties (ΔG0f and ΔH0f) of silicate minerals at 298 K from the sum of polyhedral contributions. Am. Mineral. 74, 1023–1031.

De Capitani, C., 1994. Gleichgewichts-Phasendiagramme: Theorie und Software. Beihefte zum Eur. J. Miner. 72. Jahr. Deutsch. Miner. Gesell 48.

De Capitani, C., Petrakakis, K., 2010. The computation of equilibrium assemblage diagrams with Theriak/Domino software. Am. Mineral. 95, 1006–1016. doi:10.2138/am.2010.3354

Dubacq, B., Bickle, M.J., Evans, K. a., 2013. An activity model for phase equilibria in the H2O-CO2-NaCl system. Geochim. Cosmochim. Acta 110, 229–252. doi:10.1016/j.gca.2013.02.008

Escartín, J., Andreani, M., Hirth, G., Evans, B., 2008. Relationships between the microstructural evolution and the rheology of talc at elevated pressures and temperatures. Earth Planet. Sci. Lett. 268, 463–475. doi:10.1016/j.epsl.2008.02.004

Faulkner, D.R., Armitage, P.J., 2013. The effect of tectonic environment on permeability development around faults and in the brittle crust. Earth Planet. Sci. Lett. 375, 71–77. doi:10.1016/j.epsl.2013.05.006

Frank-Kamenetskiy, V.A., Kotov, N. V., Klochkova, G.N., 1969. Phase transformations in sepiolite and palygorskite at differrent pressures under hydrothermal conditions. Geokhimiya 14–21.

García-Romero, E., Suárez, M., 2013. Sepiolite-palygorskite: Textural study and genetic considerations. Appl. Clay Sci. doi:10.1016/j.clay.2013.09.013

Gleeson, S.A., Herrington, R.J., Durango, J., Velásquez, C.A., Koll, G., 2004. The mineralogy and geochemistry of the Cerro Matoso S.A. Ni Laterite deposit, Montelíbano, Colombia. Econ. Geol. 99, 1197–1213. doi:10.2113/gsecongeo.99.6.1197

Gratier, J.-P., 2011. Fault Permeability and Strength Evolution Related to Fracturing and Healing Episodic Processes (Years to Millennia): the Role of Pressure Solution. Oil Gas Sci. Technol. – Rev. d'IFP Energies Nouv. 66, 491–506. doi:10.2516/ogst/2010014

Haines, S.H., van der Pluijm, B.A., 2012. Patterns of mineral transformations in clay gouge, with examples from low-angle normal fault rocks in the western USA. J. Struct. Geol. 43, 2–32. doi:10.1016/j.jsg.2012.05.004

Holland, T.J.B., 1989. Dependence of entropy on volume for silicate and oxide minerals: A review and a predictive model. Am. Mineral. 74, 5–13.

Kohlstedt, D.L., Evans, B., Mackwell, S.J., 1995. Strength of the lithosphere: Constraints imposed by laboratory experiments. J. Geophys. Res. 100, 17,587–17,602. doi:10.1016/S0016-0032(16)90156-X

Krekeler, M.P.S., Guggenheim, S., 2008. Defects in microstructure in palygorskite-sepiolite minerals: A transmission electron microscopy (TEM) study. Appl. Clay Sci. 39, 98–105. doi:10.1016/j.clay.2007.05.001

Leclère, H., Faulkner, D., Wheeler, J., Mariani, E., 2016. Permeability control on transient slip weakening during gypsum dehydration: Implications for earthquakes in subduction zones. Earth Planet. Sci. Lett. 442, 1–12. doi:10.1016/j.epsl.2016.02.015

Lockner, D.A., Morrow, C., Moore, D., Hickman, S., 2011. Low strength of deep San Andreas fault gouge from SAFOD core. Nature 472, 82–85. doi:10.1038/nature09927

Manning, C.E., 1995. Phase-equilibrium controls on SiO2 metasomatism by acqueous fluid in subduction zones: reaction at constant preassure and temperature. Int. Geol. Rev. doi:10.1080/00206819509465440

Marone, C., 1998. Laboratory-Derived Friction Laws and Their Application To Seismic Faulting. Annu. Rev. Earth Planet. Sci. 26, 643–696. doi:10.1146/annurev.earth.26.1.643

Mitchell, T.M., Faulkner, D.R., 2008. Experimental measurements of permeability evolution during triaxial compression of initially intact crystalline rocks and implications for fluid flow in fault zones. J. Geophys. Res. Solid Earth 113, 1–16. doi:10.1029/2008JB005588

Moore, D., Lockner, D.A., 2007. Friction of the smectite clay montmorillonite: A review and interpretation of data, in: Dixon, T.H., Moore, C. (Eds.), The Seismogenic Zone of Subduction Thrust Faults, Margins Theor. Exp. Earth Sci. Ser., Vol 2. Columbia Univ. Press, New York, pp. 317–345.

Moore, D.E., Lockner, D.A., 2011. Frictional strengths of talc-serpentine and talc-quartz mixtures. J. Geophys. Res. Solid Earth 116, 1–17. doi:10.1029/2010JB007881

Moore, D.E., Lockner, D.A., 2008. Talc friction in the temperature range 25°-400°C: Relevance for Fault-Zone Weakening. Tectonophysics 449, 120–132. doi:10.1016/j.tecto.2007.11.039

Morton, N., Girty, G.H., Rockwell, T.K., 2012. Fault zone architecture of the San Jacinto fault zone in Horse Canyon, southern California: A model for focused post-seismic fluid flow and heat transfer in the shallow crust. Earth Planet. Sci. Lett. 329-330, 71–83. doi:10.1016/j.epsl.2012.02.013

Nagata, H., Shimoda, S., Sudo, T., 1974. On dehydration of bound water of sepiolite. Clays Clay Miner. 22, 285–293. doi:10.1346/CCMN.1974.0220310

Post, J.E., Bish, D.L., Heaney, P.J., 2007. Synchrotron powder X-ray diffraction study of the structure and dehydration behavior of sepiolite. Am. Mineral. 92, 91–97. doi:10.2138/am.2007.2134

Ratié, G., Jouvin, D., Garnier, J., Rouxel, O., Miska, S., Guimarães, E., Cruz Vieira, L., Sivry, Y., Zelano, I., Montarges-Pelletier, E., Thil, F., Quantin, C., 2015. Nickel isotope fractionation during tropical weathering of ultramafic rocks. Chem. Geol. 402, 68–76. doi:10.1016/j.chemgeo.2015.02.039

Richard, J., Gratier, J.-P., Doan, M.-L., Boullier, A., Renard, F., 2014. Rock and mineral transformations in a fault zone leading to permanent creep: Interactions between brittle and viscous mechanisms in the San Andreas Fault. J. Geophys. Res. Solid Earth 119, 8132–8153. doi:10.1002/2014JB011489.Received

Sánchez-Roa, C., Jiménez-Millán, J., Abad, I., Faulkner, D.R., Nieto, F., García-Tortosa, F.J., 2016. Fibrous clay mineral authigenesis induced by fluid-rock interaction in the Galera fault zone (Betic Cordillera, SE Spain) and its influence on fault gouge frictional properties. Appl. Clay Sci. doi:10.1016/j.clay.2016.06.023

Schleicher, A.M., Hofmann, H., van der Pluijm, B.A., 2013. Constraining clay hydration state and its role in active fault systems. Geochemistry, Geophys. Geosystems 14, 1039–1052. doi:10.1002/ggge.20077

Schleicher, A.M., van der Pluijm, B.A., Warr, L.N., 2012. Chlorite-smectite clay minerals and fault behavior: New evidence from the San Andreas Fault Observatory at Depth (SAFOD) core. Lithosphere 4, 209–220. doi:10.1130/L158.1

Scholz, C.H., 1998. Earthquakes and friction laws. Nature 391, 37–42. doi:10.1038/34097

Soto, J.I., Fernandez-Ibanez, F., Fernandez, M., Antonio, G.-C., 2008. Thermal structure of the crust in the Gibraltar Arc: Influence on active tectonics in the western Mediterranean. Geochemistry, Geophys. Geosystems 9. doi:10.1029/2007TC002192

Vidal, O., Dubacq, B., 2009. Thermodynamic modelling of clay dehydration, stability and compositional evolution with temperature, pressure and H2O activity. Geochim. Cosmochim. Acta 73, 6544–6564. doi:10.1016/j.gca.2009.07.035

Yalçin, H., Bozkaya, Ö., 2004. Ultramafic-rock-hosted vein sepiolite occurences in the Ankara ophiolitic mélange, Central Anatolia, Turkey. Clays Clay Miner. 52, 227–239. doi:10.1346/CCMN.2004.0520209

# Chapter 5 Mineral structure controls on fault strength

**Highlights:**

- The crystal structure of Mg-rich phyllosilicates has a strong influence on their frictional strength
- Water distribution in phyllosilicate mineral structure affects frictional behavior
- Pore fluid chemistry directly influences Mg-rich phyllosilicate distribution and fault strength

# How phyllosilicate mineral structure affects fault strength in Mg-rich fault systems

C. Sánchez-Roa [1], D. R. Faulkner[2], C. Boulton[2] J. Jimenez-Millan[1] and F. Nieto[3]

[1] Departamento de Geología y CEACTierra, Unidad Asociada IACT (CSIC-UGR), Universidad de Jaén, Campus Las Lagunillas s/n 23071, Jaén, Spain, [2] Rock Deformation Laboratory, Department of Earth and Ocean Sciences, University of Liverpool, Liverpool, UK, [3] Departamento de Mineralogía y Petrología e IACT (CSIC-UGR), Facultad de Ciencias, Universidad de Granada, Avda. Fuentenueva s/n 18002, Granada, Spain.

Corresponding author: Catalina Sánchez-Roa (catasroa@ujaen.es)

**This article has been published in *Geophysical Research Letters*, 2017**
**DOI: 10.1002/2017GL073055**
**Received: 12 February 2017; Accepted: 24 May 2017; Available online June 2017.**

## Abstract

The clay mineralogy of fault gouges has important implications for the frictional properties of faults, often identified as a major factor contributing to profound fault weakness. This work compares the frictional strength of a group of Mg-rich minerals common in the Mg-Al-Si-O compositional space (talc, saponite, sepiolite and palygorskite) by conducting triaxial frictional tests with water or argon as pore fluid. The studied minerals are chemically similar, but differ in their crystallographic structure. Results show fibrous Mg-rich phyllosilicates are stronger than their planar equivalents. Frictional strength in this group of minerals is highly influenced by strength of the atomic bonds, continuity of water layers within the crystals, and interactions of mineral surfaces with water molecules, all of which are dictated by crystal structure. The formation and stability of the minerals studied are mainly controlled by small changes in pore fluid chemistry, which can lead to significant differences in fault strength.

# 1 Introduction

Clay minerals are commonly significant components of fault gouges and have been found to play a significant role in controlling fault strength by facilitating shear localization in the weak clay matrix [*Shimamoto and Logan*, 1981; *Tembe et al.*, 2010]. Consequently, many studies have focused on determining what factors control clay mineral frictional strength [*Morrow et al.*, 2000; *Moore and Lockner*, 2004; *Behnsen and Faulkner*, 2012; *Sakuma and Suehara*, 2015], which is typically much lower than the Byerlee friction range ($0.6 \leq \mu \leq 0.85$) [*Byerlee*, 1978]. Several experimental studies have shown that the dominant microphysical processes operating during phyllosilicate deformation include rotation, delamination, and grain fracturing (involving breakage of bonds) during shear [*Ibanez and Kronenberg*, 1993; *Mares and Kronenberg*, 1993; *French et al.*, 2015]. Many factors influence these processes, including: normal stress, grain shape and grain strength (due to mineralogy) [*Guo and Morgan*, 2006]. In particular, strength is greatly affected by two factors: lubrication and adhesion [*Moore and Lockner*, 2004; *Sakuma and Suehara*, 2015]. Lubrication refers to the lubricating effect of adsorbed water (water molecules held on the mineral surfaces by electrochemical forces). Adhesion occurs within the interlayer space between phyllosilicate structural sheets, which are bonded by electrostatic forces, and may also have interlayer water molecules bonded via hydrogen bonds. Because it directly controls atomic arrangement, mineral crystallographic structure influences the atomic forces and interactions that can contribute to both lubrication and adhesion. Thus, identifying crystallographic controls on minerals present in fault zones can contribute to understanding fault strength.

Mg-bearing phyllosilicates have long been suggested to be implicated in lowering the strength of active faults [*Irwin and Barnes*, 1975; *Reinen et al.*, 1991; *Wintsch et al.*, 1995; *Lockner et al.*, 2011]. Fault zones enriched in magnesium (Mg) occur in the continental and oceanic crust. Mg-enrichment promotes the formation of Mg-rich phyllosilicates within fault rocks including: chlorite, talc, serpentine-group minerals, fibrous clay minerals (sepiolite and palygorskite), and Mg-rich smectites (i.e., saponite). Previous work on Mg-phyllosilicates under water-saturated conditions has shown very low friction coefficients, $\mu = 0.05$ for saponite [*Lockner et al.*, 2011] and $\mu = 0.16$ for talc [*Escartín et al.*, 2008; *Moore and Lockner*, 2008]. As a result of their low strength, the planar phyllosilicate minerals saponite and talc are thought to promote significant weakening and strain localization in various settings, including the oceanic lithosphere and the subduction interface [*Moore and Lockner*, 2008]. The frictional strength of serpentine minerals has also been investigated [*Dengo and Logan*, 1981; *Reinen et al.*, 1994; *Moore et al.*, 1996, 1997], with some studies showing significant differences in frictional behavior between minerals with the same chemical composition but different crystalline structures (polymorphs) [*Reinen et al.*, 1994]. In contrast to the relatively well-studied predominantly platy Mg-phyllosilicates above, the fibrous clay mineral group has not been studied in the context of faulting and friction. Thus, this study concentrates on the behavior of these less studied minerals and compares their frictional properties with their planar equivalents.

Sepiolite and palygorskite constitute a group of Mg-rich phyllosilicates with a fibrous (lath-like) morphology, which is dictated by their crystal structure. The frictional strengths of monomineralic samples of this mineral group have not previously been determined.

Sepiolite and palygorskite are Mg-rich phyllosilicates stable up to 325 °C under hydrothermal conditions [*Frank-Kamenetskiy et al.*, 1969]. They commonly form from reactions involving talc and Mg-rich smectites (i.e. saponite) which are chemically very similar and coexist under the same activity values of Mg and Si [*Birsoy*, 2002]. The serpentine-group minerals are also associated with the formation of fibrous clay minerals, but they are chemically less similar to the minerals in this study due to their significantly lower Si/Mg chemical ratio [*Peters*, 1993; *Yalçin and Bozkaya*, 2004]. Fibrous clay minerals commonly occur in fracture and fault zones [*Post and Crawford*, 2007; *Sánchez-Roa et al.*, 2016]. Thus, quantifying the frictional behavior of fibrous clay minerals constrains their contribution to the strength of Mg-rich fault gouges and facilitates comparison of the strength of chemically similar but structurally different minerals.

In this study, the results of friction experiments on planar and fibrous Mg-phyllosilicates at nucleation velocities (0.3 to 3 μm/s) are used to investigate the possible effects of crystal structure on the frictional strength and stability of chemically similar and structurally different minerals. A comparison between water- and argon-saturated experiments is used to explore the role water plays in their frictional behavior. Finally, we present the thermodynamic controls on the distribution of these Mg-rich phyllosilicates in fault zones to describe the implications of the results on fault strength.

## 2 Materials and Methods

The materials selected for the study are: palygorskite (PIF-1) (79% purity) [*Chipera and Bish*, 2001]; sepiolite (SV) (91% purity) [*Viseras et al.*, 1999]; saponite (78% purity) [*Boulton et al.*, 2017]; and talc item-468003 from Ward's Scientific. All samples were sieved to obtain the <53 μm fraction, with the exception of the saponite sample in which the <2 μm separate was obtained. For more details on the selected materials see supporting information (Figure 5.S1). The main phyllosilicate in each of the samples constitutes more than 75% of the tested gouge, thus, they are expected to control the bulk frictional properties. However, to some extent, sample impurities could affect sample strength and their contributions cannot be fully disregarded. In particular, the palygorskite gouge contains ~11% smectite; hence our measurements may present a lower bound on the strength for this phase.

Friction tests were carried out using a triaxial deformation apparatus with a servo-controlled axial loading system and fluid pressure pump [*Faulkner and Armitage*, 2013]. Frictional sliding experiments were conducted on 1.5 mm-thick gouge layers using a direct shear sample assembly and methods documented in *Sánchez-Roa et al.* [2016]. For more details on experimental methods see supporting information (Figure 5.S2 and 5.S3).

For the argon tests, the pore pressure lines were connected to a vacuum pump to ensure that water (including air humidity) was removed from the system. The samples were kept in a vacuum oven at 80 °C overnight to ensure complete evaporation of the ethanol used during sample preparation and introduced in the pressure vessel while warm to limit adsorption of water. The use of water as pore fluid during the experiments more closely resembles the conditions found in natural faults, while the use of argon gas as pore fluid is designed to understand the mechanisms of friction and identify the effects on the frictional

behavior caused by the physicochemical interactions between water and each of the phyllosilicates studied.

The initial sliding velocity for the 1.5 mm displacement run-in was 0.3 μm/s. A low loading rate was chosen specifically to avoid the development of pore fluid effects, such as overpressure development due to a combination of compaction and low hydraulic diffusivity that could influence the measured strength. The starting permeability was ~$10^{-19}$ $m^2$, reducing to ~$10^{-20}$ $m^2$ during shear. Permeability measurements were conducted using the pore pressure oscillation technique [*Fischer*, 1992] and processed following the methods in *Faulkner and Rutter* [2000]. For details on the permeability measurements, see supporting information (Figure 5.S2). The values of normal stress and fluid pressure were set at $\sigma_n$=100 MPa and $P_p$=5 MPa for all experiments. After the run-in, sliding velocity steps were imposed every 0.5 mm (0.3-3.0-0.3 μm/s) to a total displacement of 4 mm.

Friction coefficient values ($\mu$) were calculated for each experiment as the ratio of shear stress ($\tau$) and effective normal stress ($\sigma_n$) = normal stress ($\sigma_n$) – pore fluid pressure ($P_p$); ($\mu=\tau/\sigma_n-P_p$). The "true shear stress" was calculated as the force *(F)* per unit area *(A)*; $\tau=F/A$. The area was calculated based on the initial dimensions of the assembly's sliders, which increases in the direction of shearing during displacement; [$\tau=F/width.(length+displacement)$]. Fitting of the velocity steps using the rate and state formulation with the ageing law [*Dieterich*, 1979] was conducted for all samples through a least squares numerical fitting routine including apparatus stiffness [*Noda and Shimamoto*, 2009], with the aim of finding the friction rate parameter (*a-b*), which describes the stability of the sliding surface [*Scholz*, 1998]. For a description of the methods used in the modeling, see supporting information Text S1.

Scanning electron microscope (SEM) observations were made on polished impregnated samples using a Merlin Carl Zeiss SEM in back-scattered electron (BSE) mode and secondary electron (SE) mode. Transmission electron microscope (TEM) images on individual particles were obtained with a Philips CM20 (STEM) microscope operated at 200 kV.

## 3 Results

Results of friction experiments on samples of palygorskite, sepiolite, saponite and talc at 95 MPa effective normal stress, 5 MPa pore pressure and 25 °C are presented in Figure 5.1a and 1b. Test reproducibility was good with differences in $\mu$<0.05 for duplicate experiments. Differences between duplicates are much smaller than the relative strengths between the different minerals. The primary source of error between duplicate experiments likely results from sample preparation.

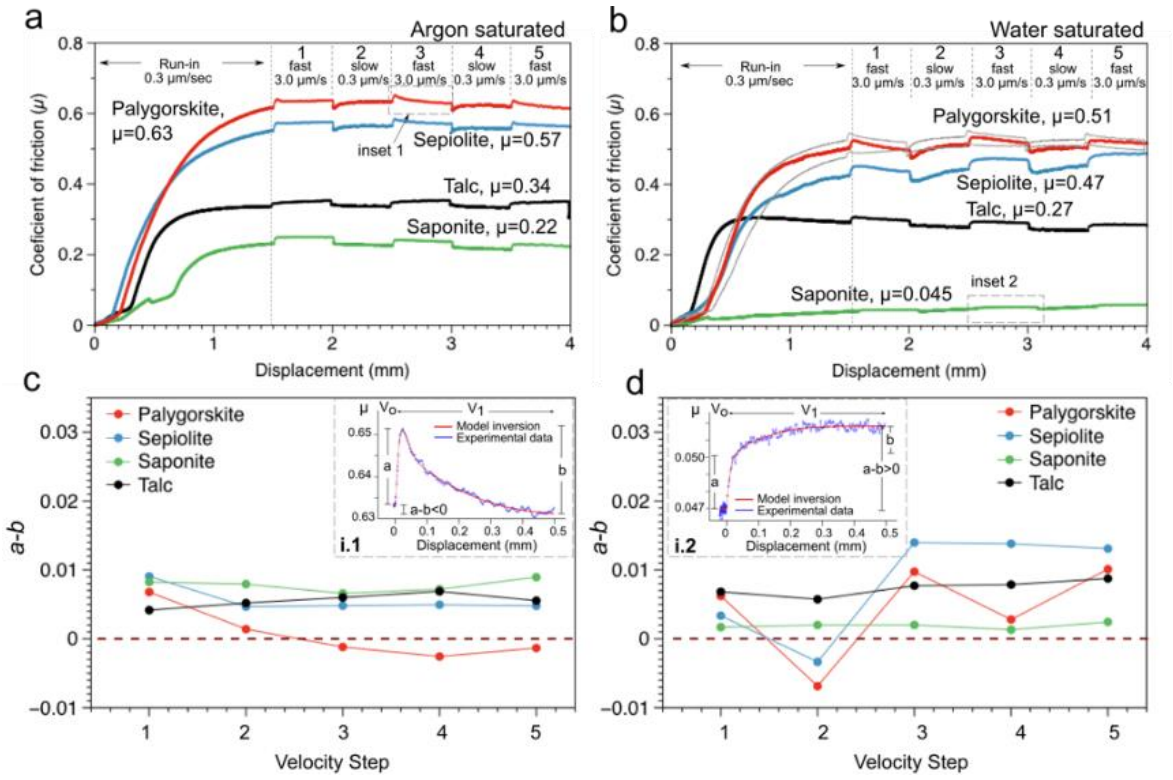


**Figure 5.1. a. and b.** Experimental quantification of the frictional properties of palygorskite, sepiolite, talc and saponite under a. argon and b. water-saturated conditions. The steps within the curves correspond to alternating changes in sliding velocity of one order of magnitude (0.3 to 3 µm/sec). Grey curves on palygorskite water-saturated runplot are duplicate experiments c. and d. Values of the friction stability parameter (a-b) for positive and negative velocity steps under c. argon-saturated and d. water-saturated conditions. Inset: Enlargement of two individual positive velocity steps at 2.5 mm of axial displacement from: inset 1. Palygorskite under argon conditions, and inset 2. Saponite under water-saturated conditions. The insets illustrate the model inversion fitting of the experimental data with the aging law and the resulting values of a, b and a-b.

All samples experienced yield during the initial run-in, before the first positive velocity step. For comparison, the representative friction coefficient of each experiment is taken at 2.49 mm displacement at the end of a slow-sliding velocity segment (0.3 µm/s). Sepiolite shows values of friction coefficient ($\mu$) of 0.57 with argon and 0.47 for water-saturated experiments whereas the palygorskite values of $\mu$ are higher, 0.63 with argon and 0.51 for water (Fig. 5.1). Talc $\mu$ values of 0.34 and 0.27 show the smallest difference between argon and water-saturated experiments, respectively. Experiments run on saponite show considerably lower friction coefficients ($\mu$) of 0.22 with argon and 0.045 for water-saturated experiments. Saponite under water-saturated conditions also exhibits the largest displacement-hardening effects. For all samples, friction coefficients in water-saturated experiments were lower than in the argon experiments run under the same conditions of effective normal stress and velocity. However, the extent of this effect is variable between the saponite, talc and the fibrous clay minerals. Saponite exhibited the greatest effect of water on $\mu$, and talc exhibited the smallest water effect.

All samples tested show strong rate dependency of the friction coefficient. Figure 5.1c and 5.1d show the results of changes in sliding velocity imposed during the experiments to

determine the rate dependence of the strength. Results of the frictional stability parameter *a-b* for experiments on talc and saponite show a consistent velocity-strengthening behavior for both positive and negative velocity steps (Fig. 5.1c and 5.1d). Meanwhile, the frictional stability parameter *a-b* obtained for the fibrous clay minerals palygorskite and sepiolite shows predominantly velocity-strengthening and velocity-neutral behavior. However, negative values of the *a-b* parameter can be observed in the first positive velocity steps after yield in the water-saturated experiments, and in the palygorskite experiment with argon as pore fluid, which is the only experiment that shows consistent velocity-weakening (Fig. 5.1c and 5.1d). For more details on the constitutive parameters for the velocity steps see supporting information (Table 5.S1).

TEM images of the contrasting morphology of the studied planar and fibrous Mg-rich phyllosilicates are presented in Figure 5.2a. SEM observations on the deformed samples (Fig. 5.2b and 2c) show a homogeneous matrix with the development of typical clay-bearing fault gouge microstructures [*Rutter et al.*, 1986] including P foliation, poorly developed $R_1$ Riedel shears, and shear-parallel Y-shears (Fig. 5.2b 1 to 4). Under higher magnification (Fig. 5.2c) on a cut parallel to the slip direction and perpendicular to the shear plane, different arrangements of the individual crystals were observed. Crystals in the planar phyllosilicates talc and saponite (5.2c 1 and 2) are aligned on their basal planes and appear to show the start of delamination and folding of the grains (Fig. 5.2c 1 and inset 1). The fibers of sepiolite and palygorskite are not aligned within the shears. Instead, samples appear to show multiple fiber orientations forming a grid-like network visible within the $R_1$ Riedel shears (Fig. 5.2c 3 and 4).

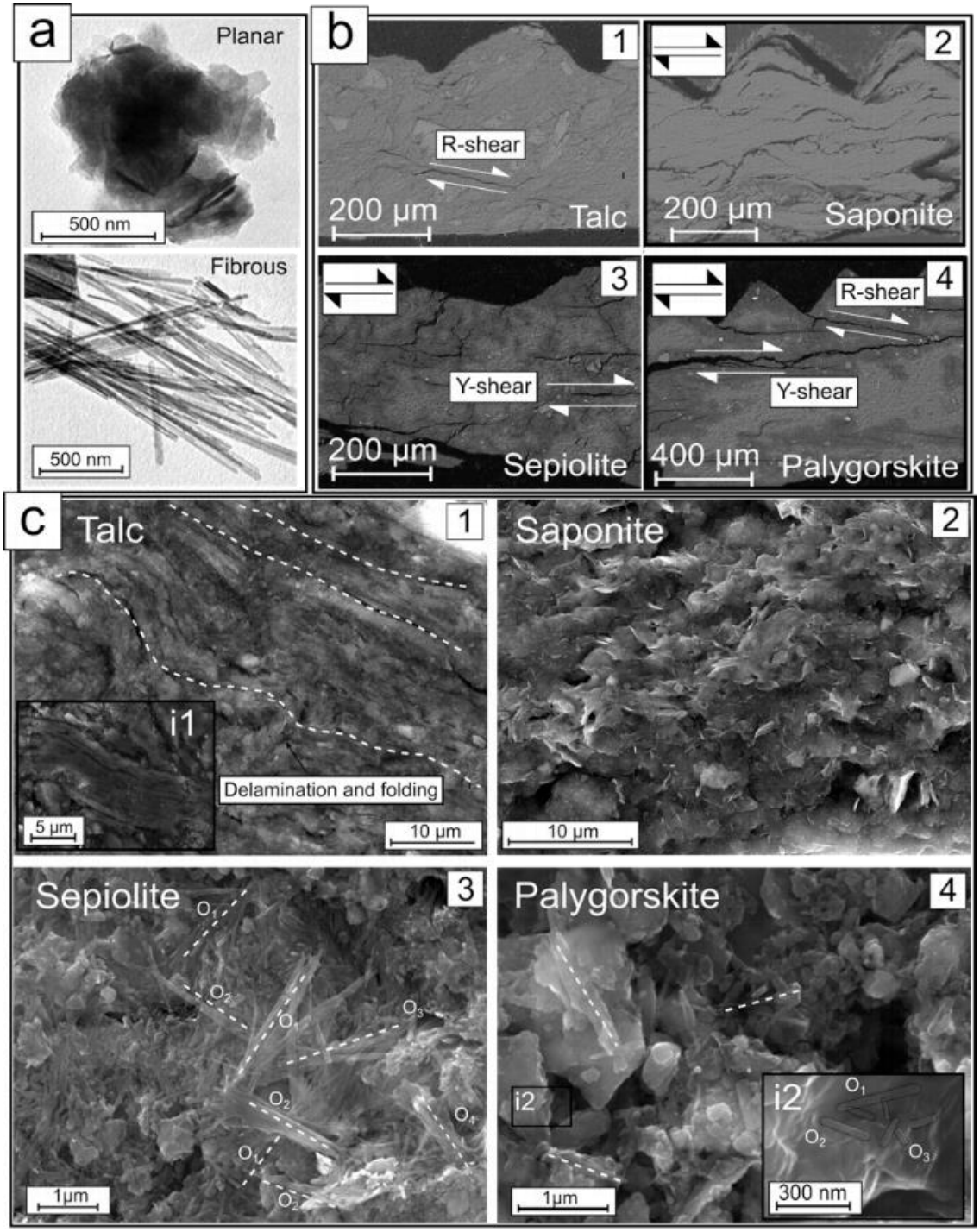


**Figure 5.2. a.** TEM images illustrating the planar morphology (smectite) and fibrous morphology (sepiolite) of the minerals studied. **b.** Microstructural comparison of planar and fibrous phyllosilicate gouges recovered at the end of the experiments. BSE images showing poorly developed Y-shears and R-shears for 1. Talc 2. Saponite 3. Sepiolite 4. Palygorskite **c.** SEM images of the deformed gouges were taken with a combination of in-lens secondary electrons detector (66%) and secondary electrons detector (33%). White dashed lines indicate the general orientation of the crystals. 1. SEM image of talc gouge showing an interconnected network of talc crystals oriented on their basal planes with signs of delamination and folding. Inset-1. Folded talc crystal 2. Saponite crystals oriented on their basal planes 3. SEM image of sepiolite gouge showing the needle-like morphology of the crystals and the representative microstructure with multiple orientations of the acicular crystals after shearing ($O_1$, $O_2$, $O_3$, etc.). 4. SEM image of the palygorskite gouge Inset-2. Higher magnification image showing how the planar-like grains within the palygorskite gouge are aggregates of palygorskite fibers.

# 4 Discussion

## 4.1 Crystallographic control on the frictional strength and stability

The results of the experiments performed show significantly higher friction coefficients for the fibrous clay minerals sepiolite and palygorskite than for the planar clay minerals talc and saponite, despite their chemical similarity. The actual differences could be still higher than those shown by the experiments due to the presence of minor impurities of planar minerals in the fibrous samples investigated. Planar phyllosilicates are well known for their perfect (001) cleavage, a consequence of their continuous interlayer spacing between one T-O (1 tetrahedral sheet: 1 octahedral sheet) or T-O-T (2 tetrahedral sheets:1 octahedral sheet) layer and the next (Fig 3). The lower bonding energy of the adhesive forces that bind the layers together makes the interlayer the most likely place to localize shear deformation. Consequently, the frictional strength of phyllosilicates has previously been compared to the strength of their (001) interlayer bond energy [*Moore and Lockner*, 2004; *Behnsen and Faulkner*, 2012].

In the case of fibrous clay minerals, periodic inversions of the apical oxygen atoms in the Si-tetrahedra create discontinuous alumino-magnesic-silicate ribbons, which dictate the fibrous morphology of the minerals. The discontinuous ribbons remain together through Si-O-Si covalent bonds which serve as "bridges" [*Yariv*, 1986] (Fig. 5.3). The presence of these strong "bridges" forces the fibrous structures to shift the cleavage planes to the octahedral-planes (O-planes), where deformation (delamination) must involve the breaking of the ionic bonds of the octahedral layer. The breaking of ionic bonds requires higher shear stresses than those involved in shearing of weakly-bonded planar structures in this study and partly explains the difference in frictional strength between these planar and fibrous Mg-rich clay minerals.

This case of crystallographic control can be compared to that of serpentine polymorphs, where experiments at room temperature show higher friction coefficients for the fibrous polymorph antigorite (0.5-0.85) [*Reinen et al.*, 1994], and low friction coefficients for the polymorph chrysotile [*Moore et al.*, 1996]. Antigorite has the same Si-O-Si covalent bridging bonds as palygorskite and sepiolite [*Yariv*, 1986], which can explain its higher strength. Chrysotile, while also fibrous in morphology due to its tubular structure, does not have periodic inversions or connections between the tubes and therefore lacks the strong Si-O-Si bridging group. This difference in strength for phyllosilicates with fibrous morphologies implies that crystal structure has a stronger influence on the frictional strength than particle morphology.

With regards to the frictional stability parameter *a-b*, the minerals studied are predominantly velocity strengthening, with sepiolite and palygorskite sometimes exhibiting velocity-neutral or even velocity-weakening behavior. Results of the stability parameter *a-b* for talc agree with results from previous experiments, showing a consistent velocity-strengthening behavior for both positive and negative velocity steps [*Moore and Lockner*, 2008]. Similarly, our velocity-strengthening results for the saponite gouge agree with stability parameter *a-b* for a gouge with high saponite content yielding velocity-strengthening results [*Moore et al.*, 2016]. Most of the positive velocity steps (where sliding velocity is increased) for saponite

and talc were modeled using negative values of the state parameter *b*, the microphysical basis for the occurrence of negative *b* can be related to grain-scale contact saturation [*Ikari et al.*, 2009; *Smith and Faulkner*, 2010], changes in viscosity of the water phase in the contacts [*Niemeijer and Collettini*, 2013], or transient pore pressure changes [*Samuelson et al.*, 2009]. In contrast, *b* values for sepiolite and palygorskite were always positive (supporting information, Table 5.S1), possibly indicating that the microphysical processes involved in the friction of the fibrous and planar minerals in this study are different or have a different dependence on velocity. The stability parameter (*a*-b) results for the lowest-displacement positive velocity steps in the water-saturated fibrous clay minerals show velocity-weakening behavior, and thus the potential for earthquake nucleation [*Scholz*, 1998]. However, exploration of a wider range of velocities, temperatures and normal stresses is required for extrapolation of the data to crustal-scale conditions, which is outside the scope of this study.

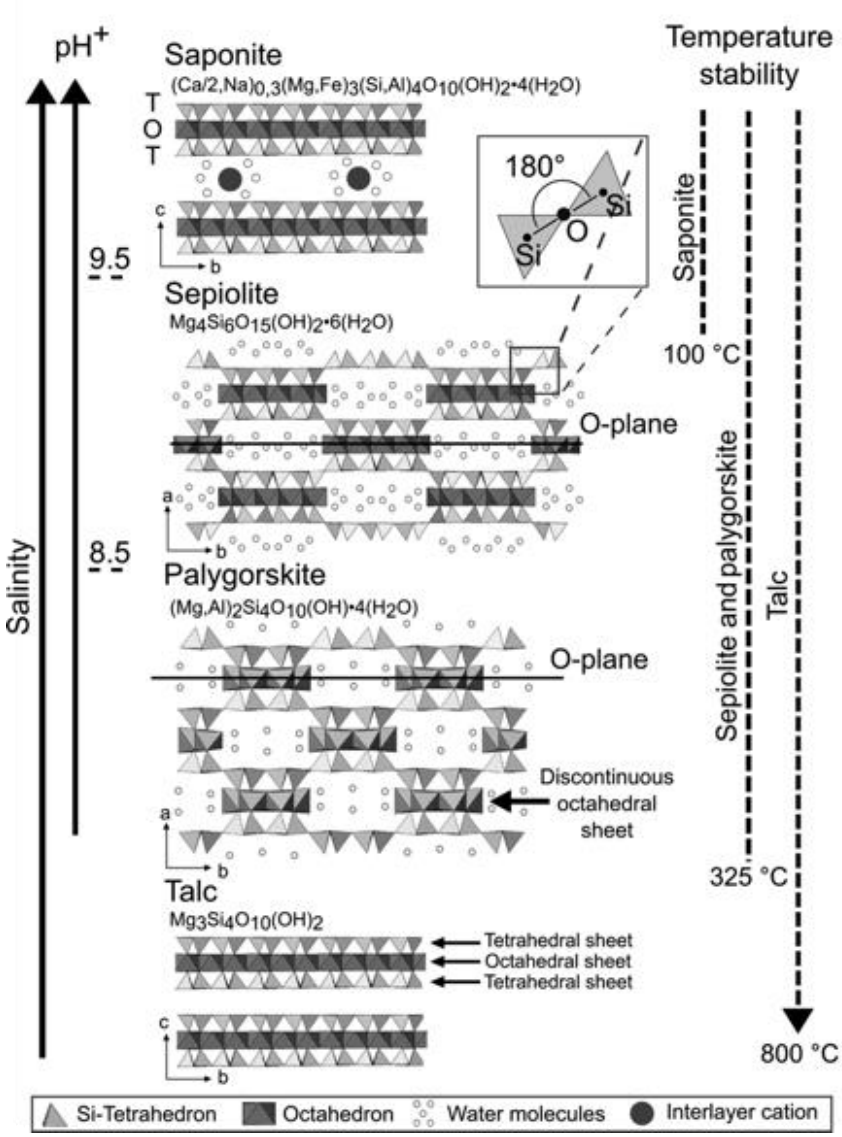


**Figure 5.3.** Schematic diagram illustrating the different crystal structures, as well as $pH^+$, salinity and temperature stability of the Mg-rich phyllosilicate minerals in the study. Mineral structures after Guggenheim and Krekeler (2011).

### 4.2 Strength results and effects of water distribution

The results of talc friction experiments using argon as pore fluid ($\mu$=0.34) are in good agreement with those reported for the dry frictional strength of talc in previous studies ($\mu$=0.35-0.36) [*Moore and Lockner*, 2004; *Moore and Rymer*, 2007]. The results of this study for wet talc ($\mu$=0.27) show values slightly higher than previously reported ($\mu$=0.18-0.20) [*Moore and Lockner*, 2004; *Behnsen and Faulkner*, 2012], but this small discrepancy is within the experimental variability. Talc exhibits the smallest difference between frictional properties under argon- and water-saturated conditions, whereas all the other minerals tested show a significant reduction in friction with the addition of water (Fig. 5.1). Talc crystal structure has no cation substitutions in either the tetrahedral or octahedral layers resulting in an electrostatically neutral T-O-T structure [*Meunier*, 2005]. The lack of electrostatic charge prevents water molecules from bonding in the interlayer space (unlike other platy phyllosilicates) and therefore would not be expected to produce any difference in friction coefficient with water or argon as the pore fluid (Fig. 5.1, 3). Adsorbed water on mineral surfaces might be expected to produce a difference in frictional behavior but talc can only adsorb one monolayer of water to its surface [*Wang et al.*, 2006]. However, removal of this monolayer of water may be the primary factor responsible for the small difference in friction coefficients measured during the argon- and water-saturated experiments.

The results of saponite friction coefficient using argon as pore fluid ($\mu$=0.22) are lower than those reported for the dry frictional strength of montmorillonite in previous studies, which range from $\mu$=0.39 to $\mu$=0.8 [*Moore and Lockner*, 2007; *Behnsen and Faulkner*, 2012]. However, a direct comparison cannot be drawn given that all reported friction experiments on saponite have been conducted using water as pore fluid. Meanwhile, the results of this study for wet saponite ($\mu$=0.045) show very good agreement with the values reported for a highly-pure saponite sample ($\mu$=0.05) [*Lockner et al.*, 2011]. The planar phyllosilicate saponite shows the largest difference between water-saturated and argon-saturated friction coefficients in this study (Fig 1). For phyllosilicates such as smectites, substitutions in the tetrahedral layers (common in saponite, where $Si^{4+}$ is replaced by $Al^{3+}$) and substitutions in the octahedral layers result in a deficit of positive charge in the structure, leading to the need for interlayer cations to balance the excess of negative charges. The cations within the interlayer space have the ability to hydrate [*Norrish*, 1954], resulting in continuous sheets of hydrogen-bonded water molecules that decrease tetrahedral-layer contact area and reduce shear strength [*Schleicher et al.*, 2013; *Behnsen and Faulkner*, 2013]. Furthermore, smectites can adsorb multiple (two to six) monolayers of water to their surface [*Clausen et al.*, 2009], Thus, the effect of water in smectite friction is strongly related to both adsorbed water on the mineral surface [*Moore and Lockner*, 2004] and to bound water in the interlayer.

The fibrous clay minerals show a difference between their water-saturated and argon-saturated friction coefficients of around 0.1, a value between that for talc and saponite. Water distribution in fibrous clay minerals differs from the planar phyllosilicates. Due to their crystallographic structure, and the discontinuity of the octahedral sheet, the interlayer space in these fibrous minerals is made of channels parallel to the c axis of the fiber [*García-Romero and Suárez,* 2013]. Two water molecules bond to the edges of the discontinuous octahedral sheets to complete the octahedral coordination of the Mg atoms. In addition,

non-structurally-bound water occurs within the channels. This interlayer water may affect fibrous-mineral friction by decreasing direct contact between surfaces, thus decreasing their friction coefficient under water-saturated conditions (Fig. 5.3). Adsorbed water may play a less significant role in the friction of fibrous phyllosilicates. Unlike talc and smectite surfaces, which can adsorb one or multiple (two to six) monolayers of water respectively, sepiolite has a 3Å void space on the basal plane that repels the adsorption of water molecules directly on the sepiolite surface due to the absence of hydrogen bonding sites in the hydrophobic basal plane [*Benli et al.*, 2012]. Thus, the interlayer water (water in the channels, both bound and unbound) likely influences the friction of fibrous clay minerals more than adsorbed water.

The observed differences in the strength, stability, and microstructures of fibrous and planar clay minerals indicate that gouge microstructures influence the deformation mechanisms operating during frictional sliding. In particular, the stronger fibrous clays are influenced by the observed lack of fiber alignment that result in the grid-like microfabric seen in electron microscope images (Fig. 5.2c 3 and 4). This microfabric can be related to the exposed crystal surfaces of the fibrous minerals, which have numerous atomic-scale barriers; these barriers create rough surfaces that resist alignment and exhibit relatively high frictional strength. Fibrous phyllosilicates have specific surface areas that vary from 95 to 400 $m^2/g$ for sepiolite [*Hibino et al.*, 1995] and 173 $m^2/g$ for palygorskite [*Dogan et al.*, 2006]. These surface areas are considerably larger than those of the planar phyllosilicates in this study, around 65.2 $m^2/g$ for smectites [*Dogan et al.*, 2006] and 7.4 $m^2/g$ for talc [*Huang and Fuerstenau*, 2001]. A combination of a strong mineral structure, high contact area, and a grid-like microfabric explain the higher friction coefficients found for fibrous clay minerals compared to their planar equivalents.

### 4.3 Thermodynamic controls on the distribution of Mg-rich phyllosilicates

Given the marked difference between the frictional properties of planar and fibrous Mg-phyllosilicates, the thermodynamic stability and conditions necessary for transformation from one mineral group to another in natural faults become a key question. In terms of thermodynamic stability, smectite minerals as pure phases are restricted to the upper 3-4 km and are generally unstable at temperatures >100 °C, when the smectite transformation to illite-smectite and chlorite-smectite mixed layered minerals is noticeable [*Inoue and Utada*, 1991; *Vazquez et al.*, 2016]. Sepiolite and palygorskite are stable to higher temperatures (~325 °C) than smectites, and break down to talc and quartz at these high temperatures independent of pressure conditions [*Frank-Kamenetskiy et al.*, 1969]. Talc is the most stable Mg-rich phyllosilicate over a wide range of temperature-pressure conditions ranging from surficial environments to temperatures of ~800 °C and pressures of 1-2 GPa [*Moore and Lockner*, 2008].

Talc, saponite, sepiolite and palygorskite are chemically similar minerals that occupy the same equilibrium field on Mg-Si activity diagrams [*Birsoy*, 2002]. Their formation and stability relate primarily to Al activity, changes in $pH^+$, salinity of the water, and reaction kinetics. Chemical stability studies on sepiolite and palygorskite indicate that their occurrence is mainly dictated by $pH^+$ and temperature [*Guggenheim and Krekeler*, 2011]. A high (Mg+Si)/Al ratio, $pH^+$ between 8 to 9.5, and moderate salinity favor precipitation of

fibrous clay minerals instead of the Mg-rich smectites (saponite and stevensite), which are favored by a $pH^+$ higher than 9.5 and high salinity waters [*Jones and Galán*, 1988].

Transformations between fibrous and planar phyllosilicates are likely important processes that affect fault strength and stability. Natural cases of this transformation include epitaxial overgrowth of smectite on palygorskite [*Krekeler et al.*, 2005]. Meanwhile, experimental studies exploring transformation of palygorskite and sepiolite to smectites (at conditions found in shallow, brittle portions of fault zones) have obtained well-developed transformation reactions at $T$=22 to 180 °C; pressures $P$= atmospheric pressure to 30 MPa; and $pH^+$ = 6 to 12 [*Golden et al.*, 1985; *Wang et al.*, 2015]. Once again, pore fluid chemistry is the most important factor controlling the transformation.

The scarcity of fibrous clay minerals in surface fault rock outcrops does not rule out their stability and abundance in depth. Evidence of sepiolite and palygorskite transformation to smectites as a result of fluid-rock interaction in surface outcrops indicates that they could exist widely in their fibrous configuration at seismogenic depths [*Callen*, 1984; *Krekeler et al.*, 2005]. Sepiolite and palygorskite have been observed in cores recovered from the Mariana Fore-arc region [*Natland and Mahoney*, 1982] and minor amounts of palygorskite were recognized in cores recovered from the San Andreas Fault [*Bradbury et al.*, 2011, 2015], demonstrating that fibrous clay minerals can indeed constitute important amounts of fault gouges in Mg-rich fault systems and influence frictional sliding at seismogenic depths.

## 5. Concluding remarks

The distribution of chemically similar Mg-rich phyllosilicates can significantly influence fault strength depending on the abundance of either weak platy minerals ($\mu$=0.045-0.22) or stronger fibrous clay minerals ($\mu$=0.44-0.63) (Fig. 5.1). This strength variation may also be accompanied by a transition in the stability regime of crustal faults, which can vary from a velocity-strengthening, stable regime when planar phyllosilicates are present to a velocity-neutral regime when fibrous clay minerals dominate (Fig. 5.1). Subtle changes in pore-fluid chemistry within fault zones control the formation of Mg-rich mineral phases with markedly different crystallographic structures and frictional behaviors.

## Acknowledgments

The authors thank Dr. H. Noda for his code used in the numerical fitting of the experimental data. We thank Dr. T. Tesei, two anonymous reviews and Associate Editor Ake Fagereng for their comments that led to significant improvements. Dr. Diane Moore is thanked for valuable comments on a previous version of this manuscript. This work was supported by MINECO research projects CGL2011-30153-C02-01 and -02, Universidad-Caja Rural de Jaén research project UJA2014/06/17, Junta de Andalucía Research Groups RNM-179 and 325, UK NERC grant NE/J024449/1, and Spanish Ministerio de Economía y Competitividad F.P.I. Grant BES-2012-052-562.

# Supporting Information

## Text S1. Numerical fitting of the velocity steps

The velocity steps were modeled with an iterative non-linear least squares numerical fitting routine on the experimental data [*Noda and Shimamoto*, 2009], using the constitutive friction equation [*Dieterich*, 1979] with two state variables that provided a much better fit to the data than a single state variable:

$$\mu_{ss} = \mu_0 + a \ln\left(\frac{V}{V_0}\right) + b_1 \ln\left(\frac{V_0\theta_1}{D_{c_1}}\right) + b_2 \ln\left(\frac{V_0\theta_2}{D_{c_2}}\right)$$

$V_0$ and $V$ are the initial and final load point velocities, respectively, $\mu_0$ and $\mu_{ss}$ are the initial and final (steady-state) friction coefficients, *a, b,* and *Dc* are empirical constants, and $\theta$ is the state variable that evolves according to the ageing law [*Dieterich*, 1979]:

$$\frac{d\theta_i}{dt} = 1 - \left(\frac{V\theta_i}{D_{c_i}}\right), (i = 1, 2)$$

For the numerical fitting, the data are first de-trended based on the averaged displacement-hardening rates in the sections of the run-plot where a steady state is recognized. The routine finds the best-fit values for the empirical constants, *a* (related to the direct effect), *b* (related to the evolution effect), $D_c$ (critical distance) and *k* (machine stiffness) [*Noda and Shimamoto*, 2009]. The rate-and-state frictional properties of fault materials help determine fault stability. The friction rate parameter (*a-b*) describes the stability of the sliding surface. A positive value of (*a-b*) indicates rate-strengthening leading to fault creep. Negative values of (a-b) correspond to velocity weakening that may result in earthquake nucleation [*Scholz*, 1998]. Two state variables were used for the fitting because the use of one state variable underestimates the values of *a* (Fig. 5.1 inset 1 and 2). Negative values of the parameter *b* (Fig. 5.1 inset 2) were introduced into the model fitting procedure for materials showing strong velocity-strengthening behavior (planar minerals). Meanwhile, the fibrous clay minerals palygorskite and sepiolite were modeled with positive values for the *b* parameter.

## Figure 5.S1. Selected Materials

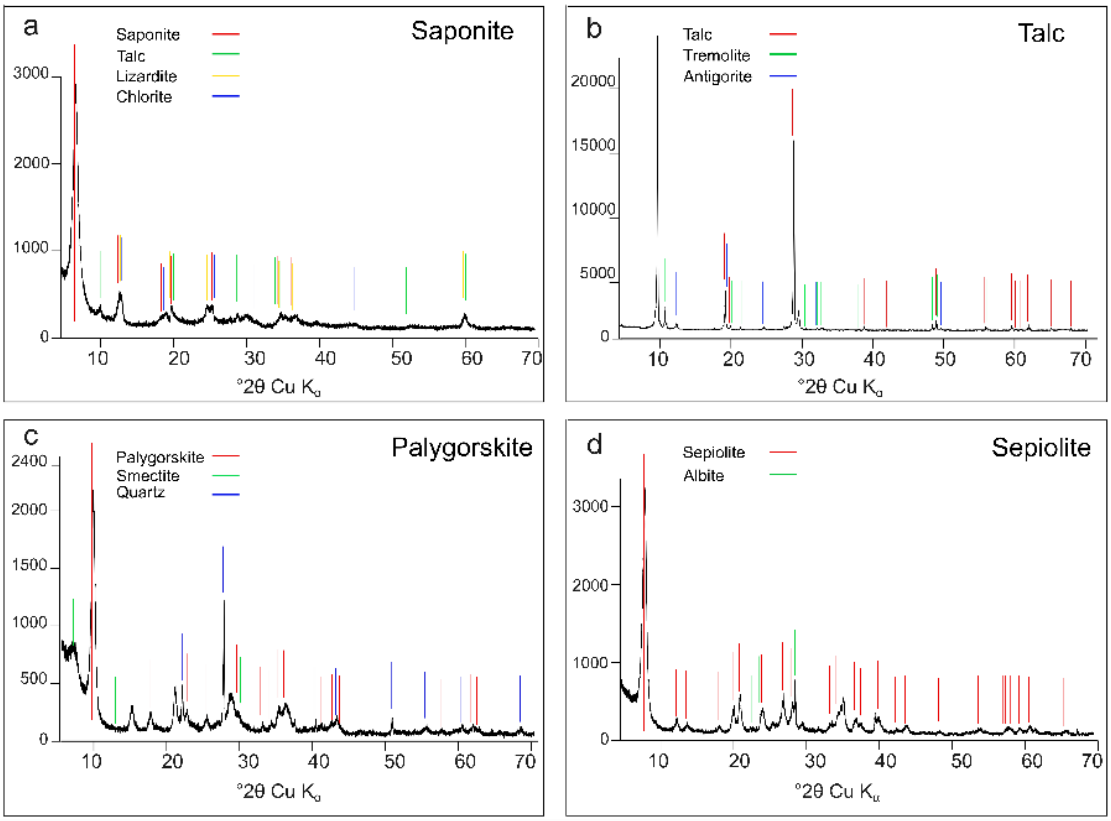


**Figure 5.S1.** X-ray diffraction patterns of randomly oriented powdered samples were obtained in a PANalytical X'Pert Pro diffractometer (CuKα radiation, 45 kV, 40 mA) equipped with an X'Celerator solid-state linear detector (Department of Mineralogy and Petrology, University of Granada). A sweep between 3° and 70° 2 $\theta$ was performed using a step increment of 0.008° 2 $\theta$ and a counting time of 10 s/step. **a.** Planar saponite separated from sample 34116 from the Alpine Fault Zone at Hokuri Creek, New Zealand (78% saponite, impurities include lizardite, talc and chlorite) [*Boulton et al.*, 2017]. **b.** Planar talc item-468003 from Ward's Scientific used as a standard for strength tests for interlab comparisons, XRD analysis of the talc sample shows that impurities include tremolite and antigorite, impurities where not recognized in SEM imaging (Fig 2c1). **c.** Fibrous palygorskite (PIF-1) from the Clay Mineral Society standards (79% palygorskite, 11% smectite, 6% quartz, 4% feldspar, 1% other) [*Chipera and Bish*, 2001]. **d.** Fibrous sepiolite sample (SV) from the Vicalvaro deposit, Spain (91% sepiolite; impurities include 2% quartz, 2% illite, 2% feldspar and 3% smectite) [*Viseras et al.*, 1999], the only impurity detected through XRD analysis in this study was a small content of albite. All samples were sieved to obtain the <53 μm fraction, with the exception of the saponite sample in which the <2μm separate was obtained. Further grain size separation on the other samples was not conducted to avoid the concentration of impurities that are favored in the <2μm separate due to their clay size (<2μm) such as smectite, illite and antigorite.

## Figure 5.S2. Sample assembly

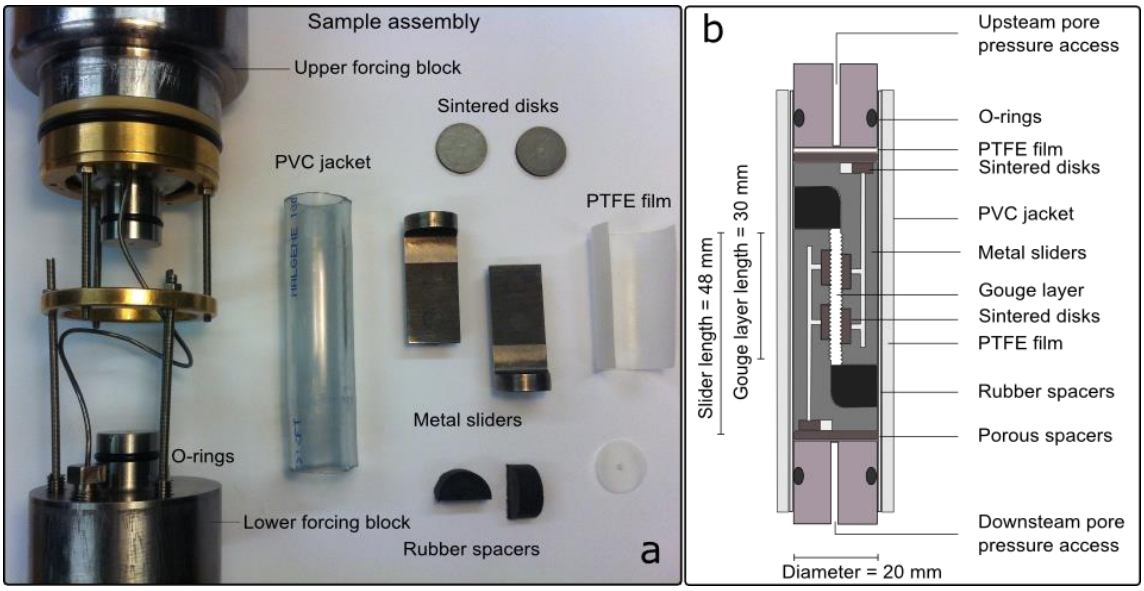


**Figure 5.S2.** a. Photograph of the sliders and other elements included in the direct-shear sample assembly used for the friction tests b. Schematic cross section of the direct-shear sample assembly used in friction tests in a triaxial deformation apparatus with a servo-controlled axial loading system and fluid pressure pump [*Mitchell and Faulkner*, 2008]. The servo-controlled fluid system controls the confining and pore fluid pressure to a resolution of 0.01 MPa, the force is measured to +/- 0.05 kN, and the axial loading system controls the displacement rate. During sample preparation, a fixed mass of one gram of the powdered samples was made into a paste using deionized water for water-saturated experiments and ethanol as bonding agent for experiments using argon as the pore fluid. The layers were then prepared on the sliders using a precision leveling jig to ensure a uniform thickness of around 1.5 mm. Test reproducibility was good with differences in $\mu<0.05$ for duplicate experiments, at least one and up to 5 duplicate test were run for water-saturated tests, argon test were then run with confidence in the sample preparation and apparatus calibrations. Measurements monitoring permeability evolution during deformation experiments were carried out using the pore pressure oscillation technique (Fischer, 1992). This technique applies a sinusoidal pore-fluid pressure oscillation in the up-stream reservoir using a servo-controlled pump. The up- and down-stream reservoirs are separated from each other by the sample, therefore the attenuation (A) and phase offset ($\theta$) of the sinusoidal pressure wave recorded in the downstream reservoir reflect the properties of the sample. The amplitude and period of the imposed oscillation were fixed to 1 MPa and 2000 s, respectively. Further details on the technique and the processing of the signal can be found in Faulkner and Rutter (2000).

**Figure 5.S3. Triaxial deformation apparatus**

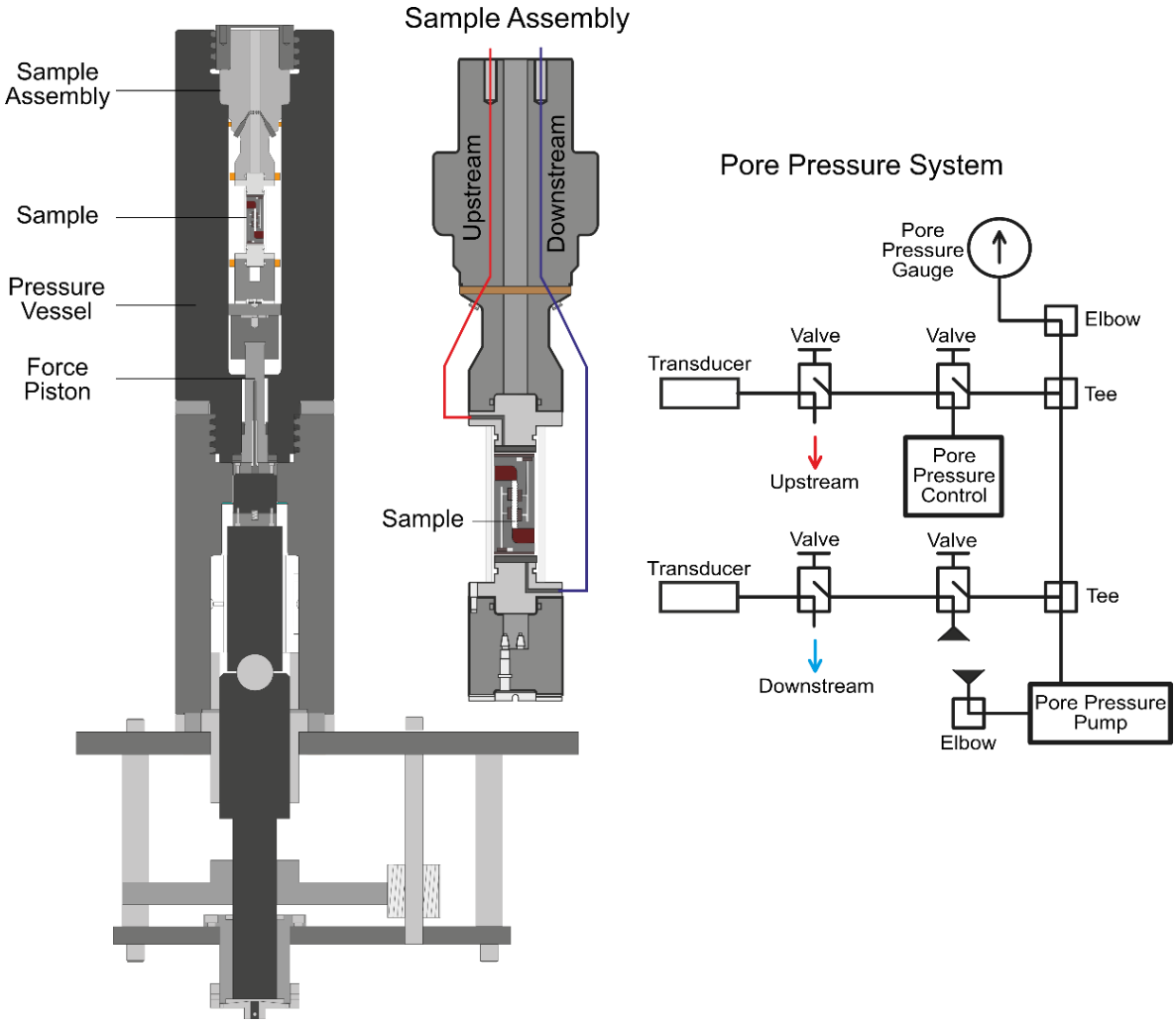


**Figure 5.S3.** General configuration of the triaxial deformation apparatus, sample assembly and pore pressure system used in frictional sliding experiments and permeability measurements.

TABLE S1. VELOCITY DEPENDENCE OF μ FOR EXPERIMENTS CONDUCTED AT Pc=100 MPa Pp=5 MPa AND 25°C

| Experiment | Peak (μm) | $V_o$ (μm/s) | V (μm/s) | k | a | $b_1$ | $Dc_1$ (mm) | $b_2$ | $Dc_2$ (mm) | a-b | $\mu_{ss}$ | $\mu_0$ | Error 2σ (k) | 2σ (a) | 2σ ($b_1$) | 2σ ($Dc_1$ (mm)) | 2σ ($b_2$) | 2σ ($Dc_2$ (mm)) | 2σ (fo) | Total error (a-b) |
|---|---|---|---|---|---|---|---|---|---|---|---|---|---|---|---|---|---|---|---|---|
| Sepiolite (water) | | | | | | | | | | | | | | | | | | | | |
| | 1.5 | 0.3 | 3.0 | 1027.43 | 0.014237 | 0.010475 | 0.000192 | 0.000402 | 0.000001 | 0.003360 | 0.453000 | 0.424250 | 3.41E-01 | 3.95E+00 | 1.03E-01 | 1.41E+02 | 1.48E-01 | 6.80E+01 | 3.11E-04 | 0.05623089 |
| | 2.0 | 3.0 | 0.3 | 1139.39 | 0.015699 | 0.018714 | 0.001865 | 0.000337 | 0.000001 | -0.003352 | 0.441740 | 0.436890 | 5.46E+00 | 1.25E+02 | 1.11E-01 | 5.85E+03 | 4.43E-01 | 2.82E+03 | 9.02E-04 | 1.96802775 |
| | 2.5 | 0.3 | 3.0 | 824.45 | 0.014311 | 0.000023 | 0.000005 | 0.000315 | 0.000001 | 0.013974 | 0.469240 | 0.441740 | 6.42E-01 | 2.10E+01 | 1.86E+03 | 8.80E+02 | 7.41E+02 | 7.79E+02 | 3.66E-04 | 0.38293528 |
| | 3.0 | 3.0 | 0.3 | 856.16 | 0.016756 | 0.002532 | 0.000852 | 0.000429 | 0.000002 | 0.013796 | 0.453520 | 0.469240 | 2.72E+00 | 4.63E+01 | 2.53E-01 | 1.81E+03 | 7.58E-01 | 9.71E+02 | 8.49E-04 | 0.77545126 |
| | 3.5 | 0.3 | 3.0 | 685.20 | 0.013455 | 0.000017 | 0.000018 | 0.000352 | 0.000002 | 0.013086 | 0.486590 | 0.453520 | 3.30E-01 | 7.84E+00 | 1.33E+02 | 2.97E+02 | 9.11E+01 | 1.87E+02 | 3.58E-04 | 0.11030453 |
| Sepiolite (argon) | | | | | | | | | | | | | | | | | | | | |
| | 1.5 | 0.3 | 3.0 | 1723.17 | 0.010197 | 0.000183 | 0.000008 | 0.000956 | 0.000008 | 0.009058 | 0.573500 | 0.551460 | 1.29E-01 | 1.53E-01 | 9.29E+01 | 1.80E+01 | 3.40E+02 | 6.66E+01 | 3.84E-04 | 0.32557409 |
| | 2.0 | 3.0 | 0.3 | 1862.92 | 0.012005 | 0.007281 | 0.000096 | 0.000047 | 0.000005 | 0.004678 | 0.565000 | 0.575520 | 2.22E-01 | 5.80E-01 | 6.59E-02 | 1.54E+02 | 7.06E-02 | 1.18E+02 | 4.67E-04 | 0.00697473 |
| | 2.5 | 0.3 | 3.0 | 1464.21 | 0.019914 | 0.002812 | 0.000068 | 0.012296 | 0.000001 | 0.004806 | 0.571280 | 0.564890 | 1.80E-01 | 1.06E+00 | 6.13E-02 | 1.72E+00 | 1.03E-01 | 1.60E+00 | 3.92E-04 | 0.02119106 |
| | 3.0 | 3.0 | 0.3 | 3805.88 | 0.010181 | 0.005127 | 0.000056 | 0.000099 | 0.000010 | 0.004955 | 0.557470 | 0.571280 | 1.75E-01 | 1.38E-01 | 1.97E-01 | 1.15E+01 | 1.44E-01 | 2.71E+01 | 3.62E-04 | 0.00172842 |
| | 3.5 | 0.3 | 3.0 | 1556.56 | 0.009896 | 0.001243 | 0.000100 | 0.003865 | 0.000005 | 0.004788 | 0.570100 | 0.557470 | 1.26E-01 | 1.30E-01 | 1.19E-01 | 3.24E-01 | 2.67E-01 | 3.80E-01 | 3.49E-04 | 0.00165968 |
| Palygorskite (water) | | | | | | | | | | | | | | | | | | | | |
| | 1.5 | 0.3 | 3.0 | 1154.67 | 0.013187 | 0.004250 | 0.000070 | 0.002717 | 0.000004 | 0.006220 | 0.497690 | 0.503410 | 6.29E-02 | 1.62E-01 | 2.55E-02 | 7.83E-01 | 3.82E-02 | 6.29E-01 | 2.80E-04 | 0.00214063 |
| | 2.0 | 3.0 | 0.3 | 961.12 | 0.014194 | 0.001087 | 0.000266 | 0.019973 | 0.000260 | -0.006866 | 0.511860 | 0.497590 | 3.93E-02 | 2.88E-02 | 3.53E+02 | 1.92E+01 | 1.68E+02 | 9.19E+00 | 9.04E-04 | 3.36840118 |
| | 2.5 | 0.3 | 3.0 | 1130.84 | 0.074711 | 0.001573 | 0.001047 | 0.063388 | 0.000000 | 0.009750 | 0.517650 | 0.511860 | 1.11E-01 | 1.54E+01 | 1.98E+01 | 1.69E+01 | 2.19E+01 | 1.62E+01 | 1.85E-04 | 1.80034085 |
| | 3.0 | 3.0 | 0.3 | 934.72 | 0.028664 | 0.009416 | 0.000535 | 0.016448 | 0.000003 | 0.002800 | 0.503060 | 0.517650 | 4.12E-01 | 3.57E+00 | 3.26E-02 | 6.24E+00 | 7.65E-02 | 5.26E+00 | 6.63E-04 | 0.10236161 |
| | 3.5 | 0.3 | 3.0 | 1074.75 | 0.038974 | 0.000005 | 0.000003 | 0.028857 | 0.000000 | 0.010112 | 0.525890 | 0.503060 | 4.51E-01 | 2.47E+01 | 2.73E+03 | 3.31E+01 | 1.10E+03 | 3.12E+01 | 5.63E-04 | 31.63037385 |
| Palygorskite (argon) | | | | | | | | | | | | | | | | | | | | |
| | 1.5 | 0.3 | 3.0 | 1501.74 | 0.011443 | 0.000804 | 0.000067 | 0.003852 | 0.000013 | 0.006787 | 0.637270 | 0.616590 | 6.49E-02 | 4.12E-02 | 4.55E-01 | 1.19E-01 | 4.56E-01 | 2.06E-01 | 3.64E-04 | 0.00185444 |
| | 2.0 | 3.0 | 0.3 | 1752.65 | 0.015091 | 0.008643 | 0.000141 | 0.005041 | 0.000011 | 0.001407 | 0.633710 | 0.637270 | 5.77E-02 | 8.06E-02 | 3.06E-02 | 2.15E-01 | 4.44E-02 | 3.65E-01 | 3.07E-04 | 0.00126408 |
| | 2.5 | 0.3 | 3.0 | 1676.32 | 0.008806 | 0.006769 | 0.000111 | 0.003216 | 0.000017 | -0.001179 | 0.629580 | 0.633710 | 8.50E-02 | 3.53E-02 | 2.87E-02 | 9.91E-02 | 6.27E-02 | 1.66E-01 | 3.54E-04 | 0.00041830 |
| | 3.0 | 3.0 | 0.3 | 2157.06 | 0.012382 | 0.010383 | 0.000256 | 0.004565 | 0.000010 | -0.002566 | 0.619140 | 0.629580 | 1.21E-01 | 1.38E-01 | 1.97E-02 | 3.45E-01 | 6.61E-02 | 5.52E-01 | 5.14E-04 | 0.00174661 |
| | 3.5 | 0.3 | 3.0 | 1969.99 | 0.008116 | 0.006865 | 0.000144 | 0.002584 | 0.000016 | -0.001333 | 0.617500 | 0.619140 | 1.51E-01 | 5.47E-02 | 4.56E-02 | 1.71E-01 | 1.30E-01 | 2.79E-01 | 5.19E-04 | 0.00063865 |
| Saponite (water) | | | | | | | | | | | | | | | | | | | | |
| | 1.5 | 0.3 | 3.0 | 168.34 | 0.001728 | 0.000003 | 0.000020 | 0.000031 | 0.000002 | 0.001694 | 0.043969 | 0.039837 | 4.67E-01 | 4.94E+00 | 1.10E+02 | 2.75E+02 | 8.99E+01 | 1.85E+02 | 1.45E-03 | 0.00896486 |
| | 2.0 | 3.0 | 0.3 | 141.72 | 0.003160 | 0.001134 | 0.000131 | 0.000017 | 0.000011 | 0.002009 | 0.047093 | 0.043969 | 7.50E-01 | 3.73E+00 | 2.78E-01 | 7.03E+02 | 3.35E-01 | 5.46E+02 | 2.03E-03 | 0.01179926 |
| | 2.5 | 0.3 | 3.0 | 233.28 | 0.001198 | -0.000213 | 0.000008 | -0.000599 | 0.000058 | 0.002009 | 0.051168 | 0.047093 | 3.44E-01 | 3.66E-01 | 1.84E+00 | 2.08E-01 | 1.89E+00 | 2.12E-01 | 9.57E-04 | 0.00127671 |
| | 3.0 | 3.0 | 0.3 | 123.83 | 0.003186 | 0.001808 | 0.000382 | 0.000055 | 0.000004 | 0.001323 | 0.052928 | 0.051168 | 1.86E+00 | 2.93E+01 | 4.22E-01 | 1.72E+03 | 6.29E-01 | 1.02E+03 | 1.75E-03 | 0.09345487 |
| | 3.5 | 0.3 | 3.0 | 221.10 | 0.001673 | -0.000080 | 0.000010 | -0.000693 | 0.000135 | 0.002446 | 0.058450 | 0.052928 | 2.56E-01 | 2.73E-01 | 5.34E+00 | 1.75E-01 | 5.34E+00 | 4.52E-01 | 1.06E-03 | 0.00374885 |
| Saponite (argon) | | | | | | | | | | | | | | | | | | | | |
| | 1.5 | 0.3 | 3.0 | 1342.16 | 0.008551 | 0.000007 | 0.000008 | 0.000303 | 0.000001 | 0.008241 | 0.249290 | 0.231050 | 3.20E-01 | 2.73E+00 | 1.78E+02 | 7.80E+01 | 1.31E+02 | 4.27E+01 | 8.17E-04 | 0.04590281 |
| | 2.0 | 3.0 | 0.3 | 3025.09 | 0.008026 | 0.000070 | 0.000425 | 0.000019 | 0.000001 | 0.007936 | 0.225740 | 0.249290 | 8.16E-01 | 3.15E+00 | 5.39E-01 | 1.30E+03 | 3.17E+00 | 1.90E+02 | 5.43E-04 | 0.02530290 |
| | 2.5 | 0.3 | 3.0 | 2185.95 | 0.006383 | -0.000201 | 0.000001 | -0.000002 | 0.000035 | 0.006586 | 0.236830 | 0.225740 | 7.72E-01 | 2.81E+00 | 8.91E+01 | 1.92E+02 | 5.42E+01 | 2.53E+02 | 1.20E-03 | 0.02535720 |
| | 3.0 | 3.0 | 0.3 | 3427.59 | 0.005612 | -0.001535 | 0.000026 | -0.000042 | 0.000026 | 0.007189 | 0.214880 | 0.236910 | 2.02E-01 | 8.19E-02 | 9.52E+01 | 3.44E+03 | 8.48E+01 | 3.10E+03 | 7.93E-04 | 0.14618175 |
| | 3.5 | 0.3 | 3.0 | 2159.42 | 0.006246 | -0.002590 | 0.000101 | -0.000123 | 0.000055 | 0.008959 | 0.235800 | 0.214880 | 2.56E-01 | 5.01E-02 | 3.18E+00 | 6.88E+01 | 1.32E+00 | 2.21E+01 | 1.34E-03 | 0.00823411 |
| Talc (water) | | | | | | | | | | | | | | | | | | | | |
| | 1.5 | 0.3 | 3.0 | 1484.48 | 0.006930 | 0.000007 | 0.000009 | 0.000088 | 0.000001 | 0.006835 | 0.297760 | 0.291830 | 5.85E-01 | 3.33E+00 | 1.44E+02 | 2.62E+02 | 1.19E+02 | 1.46E+02 | 5.76E-04 | 0.02537368 |
| | 2.0 | 3.0 | 0.3 | 1502.61 | 0.005930 | 0.000153 | 0.000098 | 0.000042 | 0.000002 | 0.005735 | 0.277720 | 0.297760 | 7.94E-01 | 2.46E+00 | 1.20E+00 | 3.48E+02 | 1.89E+00 | 1.95E+02 | 7.95E-04 | 0.01457687 |
| | 2.5 | 0.3 | 3.0 | 957.70 | 0.007755 | 0.000013 | 0.000005 | 0.000037 | 0.000002 | 0.007705 | 0.290170 | 0.277720 | 5.10E-01 | 3.50E+00 | 3.11E+03 | 4.21E+02 | 8.27E+02 | 1.18E+03 | 7.68E-04 | 0.05792249 |
| | 3.0 | 3.0 | 0.3 | 738.24 | 0.007966 | 0.000024 | 0.000022 | 0.000072 | 0.000006 | 0.007870 | 0.268550 | 0.290170 | 1.02E+00 | 5.25E+00 | 5.78E+02 | 4.42E+02 | 2.20E+02 | 6.32E+02 | 1.01E-03 | 0.04685046 |
| | 3.5 | 0.3 | 3.0 | 1672.28 | 0.005826 | -0.001575 | 0.000083 | -0.001353 | 0.000011 | 0.008754 | 0.285750 | 0.268550 | 1.72E-01 | 1.04E-01 | 1.48E-01 | 4.23E-01 | 2.21E-01 | 5.21E-01 | 6.18E-04 | 0.00071581 |
| Talc (argon) | | | | | | | | | | | | | | | | | | | | |
| | 1.5 | 0.3 | 3.0 | 519.42 | 0.005085 | 0.000001 | 0.000001 | 0.000916 | 0.000000 | 0.004167 | 0.352040 | 0.336100 | 1.26E+01 | 7.26E+02 | 2.32E+04 | 4.01E+03 | 4.93E+03 | 2.11E+03 | 3.66E-04 | 5.83633007 |
| | 2.0 | 3.0 | 0.3 | 426.81 | 0.005306 | 0.000059 | 0.000002 | 0.000049 | 0.000003 | 0.005198 | 0.335990 | 0.352040 | 1.01E+01 | 1.59E+02 | 4.87E+06 | 5.91E+06 | 2.45E+05 | 2.40E+05 | 7.17E-04 | 288.06355799 |
| | 2.5 | 0.3 | 3.0 | 1688.93 | 0.004314 | -0.001581 | 0.000034 | -0.000102 | 0.000010 | 0.005997 | 0.353060 | 0.335990 | 2.35E-01 | 1.10E-01 | 5.62E-01 | 8.01E+00 | 3.26E-01 | 9.60E+00 | 3.24E-04 | 0.00100638 |
| | 3.0 | 3.0 | 0.3 | 5983.81 | 0.003875 | -0.003011 | 0.000086 | -0.000009 | 0.000081 | 0.006895 | 0.332520 | 0.353040 | 4.41E-01 | 5.10E-02 | 2.20E+01 | 7.77E+03 | 2.17E+00 | 7.73E+02 | 4.93E-04 | 0.06613691 |
| | 3.5 | 0.3 | 3.0 | 1529.58 | 0.004520 | -0.000888 | 0.000010 | -0.000130 | 0.000010 | 0.005538 | 0.345800 | 0.332520 | 2.96E-01 | 2.00E-01 | 2.38E+02 | 1.63E+03 | 5.64E+01 | 3.72E+02 | 4.36E-04 | 0.21173384 |

$V_o$: sliding velocity before the velocity step
V: sliding velocity of the step
k: machine stiffness
a: empirical constant related to the direct effect
$b_1$ and $b_2$: empirical constants related to the evolution effect for the first and second state variables respectively
$Dc_1$ and $Dc_2$: critical distance for the first and second state variables respectively
$\mu_{ss}$: final coeficient of friction after the velocity step
$\mu_0$: coeficient of friction before the velocity step
2σ: standard deviation

**Table 5.S1.** Results of the numerical fitting of the empirical constants *a, $b_1$, $b_2$, $Dc_1$, $Dc_2$* for all experiments used to calculate the friction rate parameter (*a-b*).

## References


Behnsen, J., and D. R. Faulkner (2012), The effect of mineralogy and effective normal stress on frictional strength of sheet silicates, *J. Struct. Geol.*, *42*, 49–61, doi:10.1016/j.jsg.2012.06.015.

Benli, B., H. Du, and M. S. Celik (2012), The anisotropic characteristics of natural fibrous sepiolite as revealed by contact angle, surface free energy, AFM and molecular dynamics simulation, *Colloids Surfaces A Physicochem. Eng. Asp.*, *408*, 22–31, doi:10.1016/j.colsurfa.2012.04.018.

Birsoy, R. (2002), Formation of sepiolite-palygorskite and related minerals from solution, *Clays Clay Miner.*, *50*(6), 736–745, doi:10.1346/000986002762090263.

Boulton, C. J., C. D. Menzies, V. G. Toy, J. Townend, and R. Sutherland (2017), Geochemical and microstructural evidence for interseismic changes in fault zone permeability and strength, Alpine Fault, New Zealand, *Geochemistry, Geophys. Geosystems*, *18*, 238–265, doi:10.1002/2016GC006588.

Bradbury, K. K., J. P. Evans, J. S. Chester, F. M. Chester, and D. L. Kirschner (2011), Lithology and internal structure of the San Andreas fault at depth based on characterization of Phase 3 whole-rock core in the San Andreas Fault Observatory at Depth ( SAFOD ) borehole, *Earth Planet. Sci. Lett.*, *310*(1-2), 131–144, doi:10.1016/j.epsl.2011.07.020.

Bradbury, K. K., C. R. Davis, J. W. Shervais, S. U. Janecke, and J. P. Evans (2015), Composition, Alteration, and Texture of Fault-Related Rocks from Safod Core and Surface Outcrop Analogs: Evidence for Deformation Processes and Fluid-Rock Interactions, *Pure Appl. Geophys.*, *172*(5), 1053–1078, doi:10.1007/s00024-014-0896-6.

Byerlee, J. (1978), Friction of rocks, *Pure Appl. Geophys.*, *116*(4-5), 615–626, doi:10.1007/BF00876528.

Callen, R. A. (1984), Clays of the palygorskite-sepiolite group: depositional environment, age and distribution, in *Developments in Sedimentology*, vol. 37, edited by A. Singer and E. Galan, pp. 1–37.

Chipera, S. J., and D. L. Bish (2001), Baseline studies of the clay minerals society source clays: Powder X-ray diffraction analyses, *Clays Clay Miner.*, *49*(5), 398–409, doi:10.1346/CCMN.2001.0490511.

Clausen, P., W. Andreoni, A. Curioni, E. Hughes, and C. J. G. Plummer (2009), Water adsorption at a sodium smectite clay surface: An ab initio study of the first stage, *J. Phys. Chem. C*, *113*(34), 15218–15225, doi:10.1021/jp901162s.

Dengo, C. A., and J. M. Logan (1981), Implications of the Mechanical and Frictional Behavior of Serpentinite to Seismogenic Faulting, *J. Geophys. Res.*, *86*(B11), 10771–10782.

Dieterich, J. H. (1979), Modeling of rock friction 1. Experimental results and constitutive equations, in *Journal of Geophysical Research: Solid Earth*, vol. 84, pp. 2161–2168.

Dogan, a. U., M. Dogan, M. Onal, Y. Sarikaya, a. Aburub, and D. E. Wurster (2006), Baseline studies of the Clay Minerals Society source clays: Specific surface area by the BET method, *Clays Clay Miner.*, *54*(1), 62–66, doi:10.1346/CCMN.2006.0540108.

Escartín, J., M. Andreani, G. Hirth, and B. Evans (2008), Relationships between the microstructural evolution and the rheology of talc at elevated pressures and temperatures, *Earth Planet. Sci. Lett.*, *268*(3-4), 463–475, doi:10.1016/j.epsl.2008.02.004.

Faulkner, D. R., and P. J. Armitage (2013), The effect of tectonic environment on permeability development around faults and in the brittle crust, *Earth Planet. Sci. Lett.*, *375*, 71–77, doi:10.1016/j.epsl.2013.05.006.

Faulkner, D. R., and E. H. Rutter (2000), Comparisons of water and argon permeability in natural clay-bearing fault gouge under high pressure at 20°C, *J. Geophys. Res.*, *105*(B7), 16415, doi:10.1029/2000JB900134.

Fischer, G. J. (1992), The determination of permeability and storage capacity: Pore pressure oscillation method BT - Fault Mechanics and Transport Properties of Rocks, *Fault Mech. Transp. Prop. Rocks*, (8), 1–13.

Frank-Kamenetskiy, V. A., N. V. Kotov, and G. N. Klochkova (1969), Phase transformations in sepiolite and palygorskite at differrent pressures under hydrothermal conditions, *Geokhimiya*, (1), 14–21.

French, M. E., F. M. Chester, and J. S. Chester (2015), Micromechanisms of creep in clay-rich gouge from the Central Deforming Zone of the San Andreas Fault, *J. Geophys. Res. B Solid Earth*, *120*(2), 827–849, doi:10.1002/2014JB011496.

García-Romero, E., and M. Suárez (2013), Sepiolite-palygorskite: Textural study and genetic considerations, *Appl. Clay Sci.*, doi:10.1016/j.clay.2013.09.013.

Golden, D. C., J. B. Dixon, and L. A. Kippenberger (1985), Palygorskite and sepiolite alteration to smectite under alkaline conditions, , *33*(I), 44–50.

Guggenheim, S., and M. P. S. Krekeler (2011), The structures and microtextures of the palygorskite-sepiolite group minerals, in *Developments in Clay Science*, vol. 3, edited by E. Galan and A. Singer, pp. 3–32, Elsevier B.V.

Guo, Y., and J. K. Morgan (2006), The frictional and micromechanical effects of grain comminution in fault gouge from distinct element simulations, *J. Geophys. Res. Solid Earth*, *111*(12), 1–21, doi:10.1029/2005JB004049.

Hibino, T., A. Tsunashima, A. Yamazaki, and R. Otsuka (1995), Model calculation of sepiolite surface areas, *Clays Clay Miner.*, *43*(4), 391–396.

Huang, P., and D. W. Fuerstenau (2001), The effect of the adsorption of lead and cadmium ions on the interfacial behavior of quartz and talc, *Colloids Surfaces A Physicochem. Eng. Asp. 177*, 147–156.

Ibanez, W. D., and A. K. Kronenberg (1993), Experimental deformation of shale: Mechanical properties and microstructural indicators of mechanisms, *Int. J. Rock Mech. Min. Sci.*, *30*(7), 723–734, doi:10.1016/0148-9062(93)90014-5.

Ikari, M. J., D. M. Saffer, and C. Marone (2009), Frictional and hydrologic properties of clay-rich fault gouge, *J. Geophys. Res. Solid Earth*, *114*(5), 1–18, doi:10.1029/2008JB006089.

Inoue, A., and M. Utada (1991), Smectite-to-chlorite transformation in thermally metamorphosed volcanoclastic rocks in the Kamikita area, northern Honshu, Japan, *Am. Mineral.*, *76*(3-4), 628–640, doi:10.1144/GSL.SP.1986.019.01.17.

Irwin, W. P., and I. Barnes (1975), Effect of geologic structure and metamorphic fluids on seismic behavior of the San Andreas fault system in central and northern California, *Geology*, *3*(12), 713–716, doi:10.1130/0091-7613(1975)3<713:EOGSAM>2.0.CO;2.

Jones, B. F., and E. Galán (1988), Sepiolite and palygorskite, *Bailey, S.W. (Ed.), Hydrous Phyllosilicates (Exclusive Micas). Rev. Mineral.*, *19*(Mineralogical Society of America, Washington, DC), 631–674.

Krekeler, M. P. S., E. Hammerly, J. Rakovan, and S. Guggenheim (2005), Microscopy studies of the palygorskite-to-smectite transformation, *Clays Clay Miner.*, *53*(1), 92–99, doi:10.1346/CCMN.2005.0530109.

Lockner, D. A., C. Morrow, D. Moore, and S. Hickman (2011), Low strength of deep San Andreas fault gouge from SAFOD core, *Nature*, *472*(7341), 82–85, doi:10.1038/nature09927.

Mares, V. M., and a. K. Kronenberg (1993), Experimental deformation of muscovite, *J. Struct. Geol.*, *15*(9-10), 1061–1075, doi:10.1016/0191-8141(93)90156-5.

Meunier, A. (2005), *Clays*, Springer, Berlin.

Moore, D., and D. A. Lockner (2007), Friction of the smectite clay montmorillonite: A review and interpretation of data, in *The Seismogenic Zone of Subduction Thrust Faults,*

*Margins Theor. Exp. Earth Sci. Ser., vol 2*, edited by T. H. Dixon and C. Moore, pp. 317–345, Columbia Univ. Press, New York.

Moore, D. E., and D. A. Lockner (2004), Crystallographic controls on the frictional behavior of dry and water-saturated sheet structure minerals, *J. Geophys. Res.*, *109*(B03401), 1–16, doi:10.1029/2003JB002582.

Moore, D. E., and D. A. Lockner (2008), Talc friction in the temperature range 25°-400°C: Relevance for Fault-Zone Weakening, *Tectonophysics*, *449*(1-4), 120–132, doi:10.1016/j.tecto.2007.11.039.

Moore, D. E., and M. J. Rymer (2007), Talc-bearing serpentinite and the creeping section of the San Andreas fault., *Nature*, *448*(7155), 795–797, doi:10.1038/nature06064.

Moore, D. E., D. A. Lockner, R. Summers, M. Shengi, and J. D. Byerlee (1996), Strength of crisolite-serpentinite gouge under hydrothermal conditions: Can it explain a weak San Andreas fault?, *Geology*, *24*(11), 1041–1044, doi:10.1130/0091-7613(1996)024<1041.

Moore, D. E., D. A. Lockner, M. Shengli, R. Summers, and J. D. Byerlee (1997), Strengths of serpentinite gouge at elevated temperatures, *J. Geophys. Res.*, *102*, 14787 – 14801.

Moore, D. E., D. a. Lockner, and S. Hickman (2016), Hydrothermal frictional strengths of rock and mineral samples relevant to the creeping section of the San Andreas Fault, *J. Struct. Geol.*, *89*, 153–167, doi:10.1016/j.jsg.2016.06.005.

Morrow, C. a, D. E. Moore, and D. a Lockner (2000), The effect of mineral bond strength and absorved water on fault gouge frictional strength, *Geophys. Res. Lett.*, *27*(6), 815–818.

Natland, J. H., and J. J. Mahoney (1982), Alteration in igneous rocks at Deep Sea Drilling Project Sites 458 and 459, Mariana fore-arc region: relationship to basement structure, *Initial reports Deep Sea Drill. Proj.*, *60*, 769–788, doi:10.2973/dsdp.proc.60.145.1982.

Niemeijer, A. R., and C. Collettini (2013), Frictional properties of a low-angle normal fault under in situ conditions: thermally-activated velocity weakening, *Pure Appl. Geophys.*, *171*(10), 2641–2664, doi:10.1007/s00024-013-0759-6.

Noda, H., and T. Shimamoto (2009), Constitutive properties of clayey fault gouge from the Hanaore fault zone, southwest Japan, *J. Geophys. Res. Solid Earth*, *114*(4), 1–29, doi:10.1029/2008JB005683.

Norrish, K. (1954), The swelling of montmorillonite, *Discuss. Faraday Soc.*, *18*, 120, doi:10.1039/df9541800120.

Peters, E. K. (1993), D-18O enriched waters of the Coast Range Mountains, northern California: Connate and ore-forming fluids, *Geochim. Cosmochim. Acta*, *57*(5), 1093–1104, doi:10.1016/0016-7037(93)90043-V.

Post, J. L., and S. Crawford (2007), Varied forms of palygorskite and sepiolite from different geologic systems, *Appl. Clay Sci.*, *36*(4), 232–244, doi:10.1016/j.clay.2006.10.003.

Reinen, L. A., J. D. Weeks, and T. E. Tullis (1991), Fault in which the subscripts faults, , *18*.

Reinen, L. A., J. D. Weeks, and T. E. Tullis (1994), The frictional behavior of lizardite and antigorite serpentinites: Experiments, constitutive models, and implications for natural faults, *Pure Appl. Geophys. PAGEOPH*, *143*(1-3), 317–358, doi:10.1007/BF00874334.

Rutter, E. H., R. H. Maddock, S. H. Hall, and S. H. White (1986), Comparative microstructures of natural and experimentally produced clay-bearing fault gouges, *Pure Appl. Geophys.*, *124*(1-2), 3–30, doi:10.1007/BF00875717.

Sakuma, H., and S. Suehara (2015), Interlayer bonding energy of layered minerals: Implication for the relationship with friction coefficient, *J. Geophys. Res. Solid Earth*, 2212–2219, doi:10.1002/2015JB011900.

Samuelson, J., D. Elsworth, and C. Marone (2009), Shear-induced dilatancy of fluid-saturated faults: Experiment and theory, *J. Geophys. Res. Solid Earth*, *114*(12), 1–15, doi:10.1029/2008JB006273.

Sánchez-Roa, C., J. Jiménez-Millán, I. Abad, D. R. Faulkner, F. Nieto, and F. J. García-Tortosa (2016), Fibrous clay mineral authigenesis induced by fluid-rock interaction in the Galera fault zone (Betic Cordillera, SE Spain) and its influence on fault gouge frictional properties, *Appl. Clay Sci.*, doi:10.1016/j.clay.2016.06.023.

Schleicher, A. M., H. Hofmann, and B. A. van der Pluijm (2013), Constraining clay hydration state and its role in active fault systems, *Geochemistry, Geophys. Geosystems*, *14*(4), 1039–1052, doi:10.1002/ggge.20077.

Scholz, C. H. (1998), Earthquakes and friction laws, *Nature*, *391*(6662), 37–42, doi:10.1038/34097.

Shimamoto, T., and J. M. Logan (1981), Effects of simulated clay gouges on the sliding behavior of tennessee sandstone, *Tectonophysics*, *75*, 243–255.

Smith, S. A. F., and D. R. Faulkner (2010), Laboratory measurements of the frictional properties of the Zuccale low-angle normal fault, Elba Island, Italy, *J. Geophys. Res.*, *115*(B2), B02407, doi:10.1029/2008JB006274.

Tembe, S., D. A. Lockner, and T. F. Wong (2010), Effect of clay content and mineralogy on frictional sliding behavior of simulated gouges: Binary and ternary mixtures of quartz, illite, and montmorillonite, *J. Geophys. Res. Solid Earth*, *115*(3), 1–22, doi:10.1029/2009JB006383.

Vazquez, M., B. Bauluz, F. Nieto, and D. Morata (2016), Illitization sequence controlled by temperature in volcanic geothermal systems: The Tinguiririca geothermal field, Andean Cordillera, Central Chile, *Appl. Clay Sci.*, *134*, 221–234, doi:10.1016/j.clay.2016.04.011.

Viseras, C., G. H. Meeten, and a. Lopez-Galindo (1999), Pharmaceutical grade phyllosilicate dispersions: The influence of shear history on floc structure, *Int. J. Pharm.*, *182*(1), 7–20, doi:10.1016/S0378-5173(99)00075-7.

Wang, J., A. G. Kalinichev, and R. J. Kirkpatrick (2006), Effects of substrate structure and composition on the structure, dynamics, and energetics of water at mineral surfaces: A molecular dynamics modeling study, *Geochim. Cosmochim. Acta*, *70*(3), 562–582, doi:10.1016/j.gca.2005.10.006.

Wang, W., Z. Zhang, G. Tian, and A. Wang (2015), From nanorods of palygorskite to nanosheets of smectite via a one-step hydrothermal process, *RSC Adv.*, *5*, 58107–58115, doi:10.1039/C5RA05187H.

Wintsch, R. P., R. Christoffersen, and a. K. Kronenberg (1995), Fluid-rock reaction weakening of fault zones, *J. Geophys. Res.*, *100*(B7), 13021, doi:10.1029/94JB02622.

Yalçin, H., and Ö. Bozkaya (2004), Ultramafic-rock-hosted vein sepiolite occurences in the Ankara ophiolitic mélange, Central Anatolia, Turkey, *Clays Clay Miner.*, *52*(2), 227–239, doi:10.1346/CCMN.2004.0520209.

Yariv, S. (1986), Infrared evidence for the occurrence of SiO groups with double-bond character in antigorite, sepiolite and palygorskite, *Clay Miner.*, (21), 925–936.

# Chapter 6 Conclusiones

Este capítulo resume los aportes más significativos realizados en esta tesis doctoral en relación con la presencia de minerales fibrosos de la arcilla en zonas de falla. En particular, se describen los hallazgos obtenidos en tres áreas específicas: (i) la formación de minerales fibrosos de la arcilla en zonas de falla, (ii) su estabilidad termodinámica dentro de la roca de falla, y (iii) el comportamiento mecánico de los minerales fibrosos de la arcilla.

**i. Origen de los minerales fibrosos de la arcilla en zonas de fallas geológicas**

El estudio mineralógico de la Falla de Galera reveló que la presencia de minerales fibrosos de la arcilla se concentra y está limitada a la zona de falla, mientras que el análisis geoquímico de las rocas mostró enriquecimientos en elementos asociados con la circulación de fluidos calientes, tales como arsénico y berilio. Según estos datos, la precipitación de las asociaciones mineralógicas que contienen minerales fibrosos de la arcilla en la Falla de Galera ha sido interpretada como el resultado de la precipitación de minerales desde un fluido hidrotermal rico en magnesio, canalizado preferentemente a través de la roca fallada. La precipitación directa desde el fluido conduce a la formación de sepiolita, mientras que la asociación mineralógica rica en esmectita y palygorskita es posiblemente el resultado de la interacción entre las rocas afectadas por el fluido hidrotermal y fluidos meteóricos que interactúan con la roca de caja rica en aluminio.

La determinación de las relaciones genéticas de las asociaciones minerales en las rocas de falla por medio de microscopia electrónica analítica, demostró que algunas fibras individuales de sepiolita contienen pequeñas cantidades de aluminio en los bordes y presentan variaciones de las distancias reticulares de sus planos (110). Estos hallazgos sugieren el inicio de una transformación progresiva de sepiolita a palygorskita. Por otra parte, la identificación de esmectitas autigénicas ricas en magnesio en las rocas de falla ricas en esmectita y palygorskita sugiere el desarrollo de una transformación entre ambas. Además, existe continuidad química entre estos tres minerales, puesta de manifiesto por una disminución progresiva del contenido en magnesio y el aumento correspondiente del contenido en aluminio de las sepiolitas, palygorskitas y esmectitas presentes en las rocas de falla. Esta continuidad indica una secuencia de transformaciones minerales que vinculan las diferentes asociaciones minerales en la Zona de Falla de Galera a diferentes etapas de evolución de una roca de falla alterada hidrotermalmente por un fluido rico en Mg, sometida a una interacción progresiva con la roca de caja y con fluidos meteóricos.

El estudio de preparaciones extraídas mediante FIB de las rocas de falla, analizadas mediante microscopía electrónica de transmisión, demostraron una diferencia significativa en la alineación de los granos de los dos tipos de rocas de falla seleccionadas. Los cristales de esmectita se encuentran claramente alineados y muestran un gran número de terminaciones de capa y delaminación a favor de sus planos basales, propiciando una distribución homogénea de la deformación. En cambio, las rocas de falla ricas en sepiolita muestran una microfábrica con apariencia enrejada, consecuencia de la falta de alineación de las fibras, que conduce a una deformación localizada, limitada a áreas pequeñas, donde los cristales fibrosos se doblan y se fragmentan produciendo estructuras en forma de pluma, sin presencia de terminaciones de capa u otros signos de deformación interna de los granos. La permeabilidad de la rocas de falla ricas en minerales fibrosos de la arcilla es, al menos, un orden de magnitud mayor que la permeabilidad de las rocas de falla ricas en esmectitas. Las

observaciones obtenidas mediante el estudio de las muestras a escala micro y nanométrica resaltan la importancia de la composición mineralógica y las microestructuras de las rocas de falla, como factores que afectan a la permeabilidad y el tipo de deformación que tiene lugar en las zonas de falla.

### ii. Estabilidad termodinámica de los minerales fibrosos de la arcilla en zonas de falla

El modelo termodinámico desarrollado en este estudio permite considerar la deshidratación de la sepiolita en diferentes contextos geológicos, incluyendo rocas de falla bajo deformación activa. Los cálculos termodinámicos realizados permiten identificar dos momentos de especial importancia al considerar una roca de falla compuesta principalmente por sepiolita. La primera es el punto de inicio de la deshidratación que ocurre entre los 100 y 150°C (4 a 5 km de profundidad) y continúa hasta el comienzo de la fase de transformación. La segunda tendrá lugar al inicio de la transformación mineral de sepiolita a la asociación talco + cuarzo + $H_2O$, que ocurre entre los 300 y 325 °C (10 a 13 Km de profundidad).

De acuerdo con este modelo, la estabilidad termodinámica de las fases experimentales sepiolita-2$H_2O$ y sepiolita anhidra, es considerablemente más baja que la del talco. Por lo tanto, la formación de las especies de sepiolita deshidratada en la naturaleza es inhibida por la reacción metamórfica sepiolita → talco + cuarzo + $H_2O$, que es termodinámicamente más estable. La ausencia de estas fases anhidras en la naturaleza valida los resultados de este modelo.

La estabilidad de la sepiolita supera la estabilidad termodinámica del talco a temperaturas menores de 325°C en sistemas ricos en magnesio. Este resultado sugiere que las rocas de falla de los 13 kilómetros más superficiales de la corteza pueden contener sepiolita; esta profundidad constituye la zona sismogénica en la Zona de la Falla de Galera.

### iii. Comportamiento ante la fricción y estabilidad mecánica de los minerales fibrosos de la arcilla

Los ensayos de fricción de muestras monominerálicas de filosilicatos fibrosos y planares indica que la distribución de diferentes tipos de filosilicatos en los segmentos de fallas activas puede influir de manera significativa en su resistencia al desplazamiento, dependiendo de la abundancia de minerales laminares más débiles, con bajos coeficientes de fricción ($\mu$=0.045-0.22) o minerales fibrosos de la arcilla con coeficientes de fricción más elevados ($\mu$=0.44-0.63). Los efectos en la resistencia al desplazamiento de fallas activas podrían, a su vez, estar acompañados por una transición en el régimen de estabilidad de las fallas de la corteza, que puede variar de un régimen completamente estable, cuando hay presencia abundante de filosilicatos planares, a un régimen de estabilidad neutral a inestable cuando predominan los minerales fibrosos de la arcilla.

Los cambios en la mineralogía de las rocas de falla de la Zona de Falla de Galera influyen decisivamente en el comportamiento de fricción de sus segmentos de falla. Las rocas de falla

ricas en esmectita y palygorskita muestran bajos coeficientes de fricción y un régimen friccional estable. Este comportamiento contrasta con los mayores coeficientes de fricción y el régimen neutral a inestable para las rocas de falla ricas en sepiolita. Estos resultados indican que existe mayor probabilidad de que los terremotos en la Falla de Galera sean nucleados en áreas de la falla ricas en sepiolita, lo cual destaca la importancia de los estudios de la mineralogía de arcillas para la evaluación del riesgo sísmico relacionado con áreas de fallas activas.

La transformación de sepiolita en profundidad, donde las condiciones de presión y temperatura son elevadas, conduce a la formación de talco. El talco es uno de los minerales más débiles y con mayor estabilidad mecánica en el contexto del deslizamiento de fallas activas, por lo que no suele asociarse con sismicidad. Las propiedades termodinámicas de la sepiolita, integradas en cálculos termodinámicos para la roca de falla de la Zona de Falla de Galera, confirman su estabilidad a temperaturas menores que 325°C. La sepiolita, contrariamente al talco, presenta mayor resistencia a la fricción y tiene el potencial de producir inestabilidades mecánicas que conducen a la nucleación de terremotos. La presencia de sepiolita en rocas de falla ricas en Mg podría contribuir a regímenes inestables y a la nucleación de terremotos en zonas que, de lo contrario, estarían dominadas por talco y exhibirían un régimen mecánico totalmente estable, en el que los terremotos no podrían nuclearse.

# Conclusions

This chapter summarises the main contributions of this doctoral dissertation regarding the presence of fibrous clay minerals in fault zones. In particular, we outline the main findings obtained from the study of the Galera Fault Zone considering: (i) the formation of fibrous clay minerals in fault zones; (ii) their thermodynamic stability within fault rocks; and, (iii) the frictional behaviour of fibrous clay minerals.

**i. Origin of fibrous clay minerals in fault zones**

The mineralogical study of the Galera Fault revealed the occurrence of fibrous clay minerals limited to the fault planes. Geochemical analysis of the rocks show enrichments in As and Be, elements typically associated with hot fluid circulation. The precipitation of mineral assemblages that include fibrous clay minerals in the Galera Fault result from a thermal Mg-rich fluid channelled through the faulted rock. Direct precipitation from the fluid leads to the formation of sepiolite, while the palygorskite- and smectite- rich gouge is most likely the result of the interaction of the fluid with the Al-rich wall-rock.

Exploration of the genetic relationships of the mineral assemblages in the fault gouges through AEM revealed Al content towards the fibre edges and $d_{110}$ variability across single fibres of sepiolite. These findings suggest the existence of a progressive transformation from sepiolite to palygorskite. Furthermore, the identification of authigenically-formed Mg-enriched smectite in the smectite and palygorskite -rich gouge, suggests an ongoing transformation between palygorskite and smectite. In addition, chemical continuity of Mg-decrease and Al-increase in the octahedral cation content of the sepiolites, palygorskites and smectites analysed within the gouges indicates a sequence of mineral transformations that link the mineral assemblages of the smectite- and palygorskite-rich gouge as the evolution of the sepiolite-rich gouge with increasing fluid rock interaction.

TEM study of FIB-extracted impregnated gouges evidenced a significant difference in grain alignment between the two kinds of gouges. Smectite crystals are aligned on the same orientation and show a great number of layer terminations and delamination on the basal planes that contribute to a distributed mode of deformation. In contrast, the sepiolite-rich gouge exhibits a grid-like microfabric that results in localised deformation limited to small areas where the needle-like crystals are bent and broken producing "feather-like" structures, without the presence of lattice distortions. In addition, the measured permeability of the fibrous-rich gouge is at least one order of magnitude higher than the smectite-rich gouge. These findings highlight the importance of mineral composition and microstructures of fault gouges as factors controlling the permeability and mode of deformation of fault zones.

**ii. Thermodynamic stability of the fibrous clay minerals in fault zones**

According to the newly built thermodynamic model of sepiolite dehydration, sepiolite-$2H_2O$ and anhydrous sepiolite have a considerably lower thermodynamic stability than talc. Thus, the potential formation of the dehydrated sepiolite species in nature will always be preceded by the metamorphic reaction sepiolite → talc + quartz, which produces

thermodynamically more stable phases. The lack of natural occurrences of the two anhydrous phases validates the outcome of this model.

The thermodynamic model developed in this study permits to consider sepiolite dehydration in various geological contexts including fault gouges under active deformation. Based on thermodynamic calculations, two moments of special sensitivity can be identified when considering a fault gouge mainly composed of sepiolite; the first at the point of dehydration onset which will occur between 100 and 150°C (4 to 5 km depth) and will continue until the phase transformation starts. The second will take place at the onset of the mineral transformation from sepiolite to talc + quartz + H2O between 300 and 325°C (10-13 km).

The stability of sepiolite instead of talc, at temperatures less than 325°C in Mg-rich systems is an important finding that suggests the mineralogy of the fault gouge could indeed be composed of sepiolite across the shallower 13 km of the crust, which is the area that constitutes the seismogenic zone in the Galera Fault Zone.

**iii. Frictional strength and stability of fibrous clay minerals**

The study of nearly pure standards of planar and fibrous clay minerals indicate that the distribution of chemically similar Mg-rich phyllosilicates can significantly influence fault strength depending on the abundance of either weak platy minerals ($\mu$=0.045-0.22) or stronger fibrous clay minerals ($\mu$=0.44-0.63). This strength variation may also be accompanied by a transition in the stability regime of crustal faults, which can vary from a velocity-strengthening, stable regime when planar phyllosilicates are present to a velocity-neutral regime when fibrous clay minerals dominate.

The change in mineralogy within the fault core of the Galera Fault results in low friction coefficients and a stable frictional regime for the smectite- and palygorskite-rich gouge, which contrasts with the stronger friction coefficients and neutral to unstable frictional regime for the sepiolite-rich gouge. These results indicate that earthquakes in the Galera Fault are more likely to nucleate in sepiolite-rich areas of the fault, and highlights the importance of clay mineralogy studies for the evaluation of seismic risk linked to fault areas.

Talc is the main mineral produced by sepiolite transformation at increasing temperature and pressure and it is also one of the weakest minerals in the context of fault slip and not usually associated with seismicity. The integration of sepiolite thermodynamic properties to the thermodynamic calculations of the Galera Fault gouge confirm the thermodynamic stability of sepiolite up to 325°C which, contrary to talc, has higher frictional strength and potential for mechanical instabilities that lead to earthquake nucleation. The presence of sepiolite in Mg-rich fault gouges could contribute to unstable regimes and earthquake nucleation in an otherwise fully stable regime dominated by talc.

# Universidad de Jaén

## Departamento de Geología

Centro de Estudios Avanzados en Ciencias de la Tierra